Design and Development of Aggregation-Induced Emission based Probes

A Dissertation Submitted in Partial Fulfilment of Requirements for the Degree of

Doctor of Philosophy

By

Laxmi Raman Adil

(Roll No. 146122032)

Department of Chemistry

Indian Institute of Technology Guwahati, Guwahati

Assam-781039

Feb, 2022

PhD Thesis

Department of Chemistry,

IIT Guwahati, Assam,

India, 781039.

Design and Development of Aggregation-Induced Emission based Probes

By

Laxmi Raman Adil

(Roll No. 146122032)

Supervisor

Prof. Parameswar Krishnan Iyer

Feb, 2022

Dedicated To

I dedicate my dissertation work to my Teachers

Department of Chemistry,
Indian Institute of Technology Guwahati,
Guwahati.
Assam-781039

STATEMENT

*I do hereby declare that the work contained in the thesis entitled "**Design and Development of Aggregation-Induced Emission based Probes**" is the result of investigations carried out by me in the Department of Chemistry, Indian Institute of Technology Guwahati, Guwahati, Assam, India under the supervision of Prof. Parameswar Krishnan Iyer, Professor, Department of Chemistry, Indian Institute of Technology, Guwahati, Guwahati, Assam India.*

This work has not been submitted elsewhere for the award of any degree.

Feb, 2022
IIT Guwahati

Laxmi Raman Adil
Roll No. 146122032

Department of Chemistry,
Indian Institute of Technology Guwahati,
Guwahati.
Assam-781039

CERTIFICATE

*This is to certify that the work contained in the thesis entitled "***Design and Development of Aggregation-Induced Emission based Probes***" by Laxmi Raman Adil, PhD. Student in the Department of Chemistry, Indian Institute of Technology Guwahati, Guwahati, Assam for the award of degree of Doctor of Philosophy has been carried out under my supervision and this work has not been submitted elsewhere for the award of any degree.*

Feb, 2022
IIT Guwahati

Prof. Parameswar Krishnan Iyer
Thesis Supervisor
Department of Chemistry,
Indian Institute of Technology Guwahati,
Guwahati, 781039,
Assam, India.

Acknowledgements

At this stage of ending overwhelming and truly memorable journey towards my intellectual destination, I would like to express my sincere gratitude to my thesis supervisor Prof. Parameswar Krishnan Iyer for his kind support, great encouragement and excellent guidance to be creative and introducing me to an interdisciplinary area of research. I earnestly thank him for helping me to learn Chemistry, freedom to work, inspiration, scientific ideas and always believing on me, that enhance my confidence in my scientific abilities.

I sincerely thank and would like to acknowledge my sincere gratitude to my doctoral committee members, Prof. Subhas Chandra Pan, Prof. Aditya Narayan Panda, Dr Sachin Kumar, Prof. Subhendu Sekhar Bag for their suggestions, insightful advices and crucial comments which certainly helped me for betterment of my thesis.

I am thankful to Prof Siddhartha Sankar Ghosh for his kind support for and extending his laboratory facilities and valuable suggestions in our collaborative works.

The completion of this thesis became possible only with the help of my collaborators, who had provided strong support and guidance along with lab facilities. I sincerely thank my collaborators Dr Anil Bidkar, Rajib Shome, Hirakjyoti Roy.

I am thankful to all faculty members in the Department of Chemistry, IIT Guwahati for encouragement and also non-teaching staff for their support.

I wants to thank Department of Chemistry for allowing me to use instrument facilities like NMR HRMS, UV vis and florescence spectrophotometer and CIF for providing me instruments facility like AFM, FESEM, SCXRD.

I want to thank my extremely cooperative and friendly senior Muthu bhaiya, Subbarao bhaiya, Priyanka mam, Himani di, Jupitara mam, Ekta di, Radha bhaiya, Bhim bhaiya, Suresh bhaiya, Anamika mam, Ashish bhaiya , Sameer bhaiya, Akhtar bhaiya, Arvin bhaiya, Sayan bhaiya, Dipjyoti bhaiya, Adil bhaiya, Gopi bhaiya, Niranjan bhaiya, Rahul bhaiya who made my experience unforgettable with their help and care. I want to thank my present labmates Subrata, Ramesh ji, Maimur, Debasish, Rabindra, Nehal, Ritesh, Retwik, Anwesha, Nasima, Biki, Anita, Kavita, Rajdikshit, Paromita, Geetmani bhaiya, Tamal, Priyam, Debika, Dibash for their hands of support and their valuable suggestion whenever needed. I would also like to thank them for

creating a pleasant and vibrant laboratory atmosphere and making my days memorable. I especially thank Sameer bhaiya, Adil bhaiya and Gopi bhaiya for sharing their enormously broad knowledge and showing endless patience. They taught me all the basics, experiments and techniques that were needed.

I am grateful to acknowledge my all teachers specially Aashish Kumar Tiwari, Subhash Banerjee, Prashant Kumar Sahu, Kherari Ram Dewangan, Santosh Kumar Verma for constant motivations and precious advices which are of great impact on me

I feel pleased to express my sincere gratitude and appreciation to those who have supported me and contributed to this thesis during this truly overwhelming and memorable journey. It is really hard to list all who sincerely helped me, and I would like to thank all of them who have made this thesis possible.

Finally, my PhD endeavor could not be completed without the endless love unending support blessing from my family. I would like to express my sincere gratitude to my family members.

Laxmi Raman Adil

Synopsis

"A whole formed by combining several separate elements'' is called aggregates. Traditional organic luminogens have a planar structure, they have intense emission in the soluble state but shows less or nearly no emission at a higher concentration, aggregated and in the solid-state. The emission was quenched due to a higher concentration called concentration quenching (CQ), and this phenomenon is also referred to as aggregation caused quenching (ACQ). Typically, all classical aromatic compounds have suffered from the notorious ACQ effect. *Tang et al* reported a non-planar aromatic material, having precise opposite emissive properties as compared to classical materials. These non-planar (non-classical) compounds have extensively bright fluorescence in the aggregated state due to the restriction of intramolecular motions, this phenomenon is termed as aggregation-induced emission (AIE). In the individual (soluble) state, the non-planar molecules were weakly emissive due to the intramolecular rotation or vibration. (IR or IV).

AIE materials have a widespread application viz. chemo-sensing, bio-imaging, photodynamic therapy, drug delivery and in OLED devices. Hence, designing and synthesis of conceptually new AIE materials are exciting research themes. The development of color-tunable with higher quantum yield AIE active materials with novel applications have led us to significant leaps in the field of imaging, diagnosis, sensors and in optoelectronics devices.

The content of the synopsis report entitled "***Design and Development of Aggregation-Induced Emission based Probes***" is divided into five chapters. Chapter 1 describes the world of aggregation-induced emission (AIE) and its scopes in various applications. Chapter 2 discussed the design and synthesis of pyrene-based AIE luminogens by push-pull, planar-rotor, a multi-responsive probe and photodynamic therapy. Chapter 3 described the synthesis of aggregation-induced enhance emission (AIEE) active monomer **TPBZ** for AIEE active copolymer **PFTPBZ** synthesis. It was further used for selective and sensitive receptor-free detection of picric acid (PA) and 2,4,6-trinitrotoluene (TNT). Chapter 4 highlighted the effects of incorporating regioisomers and flexible rotors to direct aggregation-induced emission luminogen and stimuli-responsive emission-based security ink. The pressure-responsive membrane was developed and used in the selective and sensitive detection of chemical warfare agent (CWAs) sensing. Chapter 5 discussed the aggregation-induced emission active luminogens for wash free imaging and antimicrobial application against pathogenic bacteria and fungus.

Chapter 1 Introduction

Current developments in organic AIE materials and their mechanistic perspective have been discussed in this chapter. Limitation of the conventional fluorophore towards the recent technologies, whereas astonishing usage of AIE fluorescent materials have been highlighted in this section. Organic fluorescent materials those are exhibiting condense state emission and their working mechanism is also discussed. Along with the structure-photophysical property relationships the various potential and applications have been summarized in this chapter.

Chapter 2

AIE modulation in pyrene via push-pull, planar-rotor architecture: sensing hydrazine, water traces in organic solvents and photodynamic therapy applications

Pyrene is a classical molecule which has a disc-like shape; therefore, it suffered with ACQ in aggregated and solid state. To prevent it from diminishing ACQ we have decorated pyrene with various π rotor groups. We have synthesized **PP**, **PBA**, **PBT** and **PBM** including impact of push-pull rotor groups on the photophysical properties were studied carefully. **PBM** material has environment-dependent emission hence it is employed to detect trace water (0.1%) present in the various organic solvents. Hydrazine (N_2H_4) is used extensively in the chemical industry as a reagent. Hydrazine is carcinogenic in nature and is extremely toxic to aquatic animals but hydrazine was used as reagent in various industries and also used in rockets and satellites as a propellant hence detection of hydrazine has tremendous important. There were many probes for hydrazine detection with higher

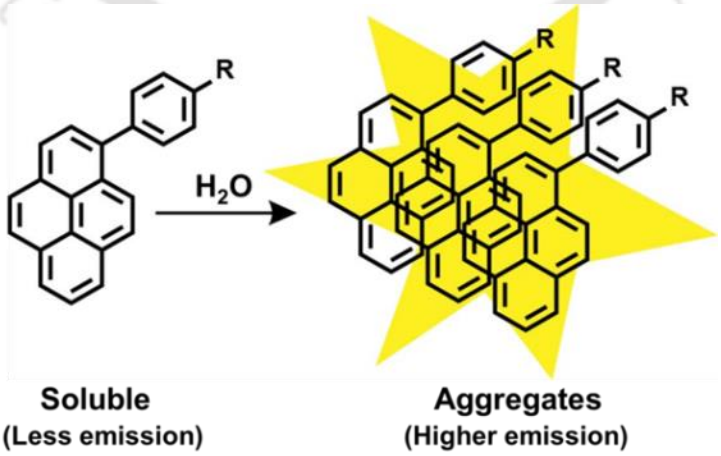

Scheme 1: Pictorial representation to design AIE dye from ACQ pyrene molecule.

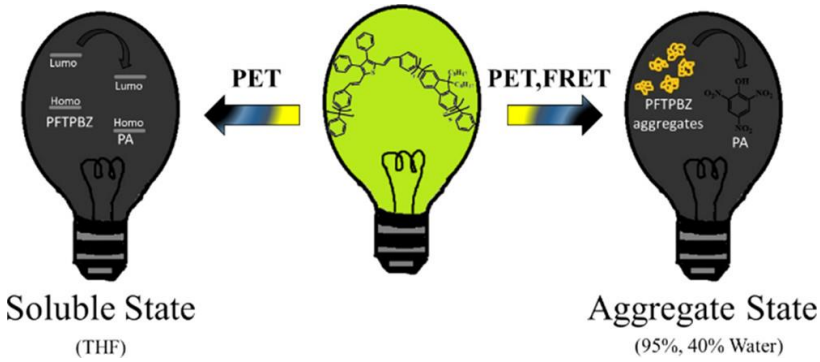

Scheme 2: Pictorial representation of sensing of PA by PFTPBZ in soluble states.

sensitivity and selectivity, but most of them required organic solvents that create hurdles in analysis in an aqueous medium. We have used **PBM** for sensitive and selective hydrazine detection in the 99% water fraction (f_w) (44.14 nM). **PBM** can further generate ROS hence it was used in photodynamic therapy to kill MCF-7 and MDAMB231 cancer cells (Scheme 1).

Chapter 3

Receptor-free detection of picric acid: a new structural approach for designing aggregation-induced emission probes

In this work, we have synthesized aggregation-induced enhanced emission (AIEE) active monomer 2,5-bis((E)-4-bromostyryl)-3,4-diphenylthiophene (**TPBZ**) and its copolymer (**PFTPBZ**) via Suzuki coupling polymerization. **PFTPBZ** is devoid of any receptor showed AIEE emission and performed sensitive and selective fluorometric recognition of TNT in aggregated state (aqueous medium) and PA in aggregated state and solution state (organic solvent) as well as in vapor phase via **PFTPBZ** dip-coated Whatman filter paper on a solid-phase platform in 1.86 ng level (naked eye). The limit of detection (LOD) for TNT in 95% f_w was 53.74 µM, and at 40% f_w, it was 1.42 µM. PA detection in tetrahydrofuran solution was possible with a LOD of 2.81 µM, 95% f_w with LOD of 10.47 µM, and in 40% f_w with LOD of 0.47 µM. Detection of PA in the presence of various metal analytes and inorganic acids in real water samples (lakes, rivers, and seawater) was also demonstrated using the receptor-free conjugated polymer probe (Scheme 2).

Chapter 4

Effects of incorporating regioisomers and flexible rotors to direct aggregation-induced emission to achieve stimuli-responsive luminogens, security inks and chemical warfare agent sensors

Efficient transformation of ACQ materials to AIE luminogens using simple design principles of positional isomerization and C-C bond exclusion is presented here. In the present work, three new non-planar materials **1PN**, **1PON** and **3PN** was designed and synthesized. The relation between **1PN** and **1PON** is regioisomers, while **3PN** is an analogue of **1PN** which has one C–C bond less between C_{10}, C_{11}. This difference lead to altering their packing arrangement that further caused diverse photophysical properties. Out of them **3PN** has higher brightness and used as a CWAs sensing.

Consequently, **1PON** has shown mechanoresponsive emission hence we demonstrated **1PON** as an erasable secret ink for encrypted messages and also pressure responsive membrane was fabricated with the **1PON** doped PDMS film (Scheme 3).

Chapter 5

Aggregation-induced emission active luminogens for wash free imaging and antimicrobial application against pathogenic bacteria and fungus

Microbes have increasing resistance to conventional antibiotics that raised a demand to design new antimicrobial agents. In the present work, we have synthesized non-planar non-ionic AIE material **PNH** & non-planar but ionic materials **PNM** and **PNB**. However, the non-planar nature of the synthesized materials provides amplified emissive behaviour in the aggregated state and the ionic characteristic of **PNM** and **PNB** triggers the membrane anchoring property *via* electrostatic interaction between cationic pyridinium unit and potential negative pathogens cell membrane.

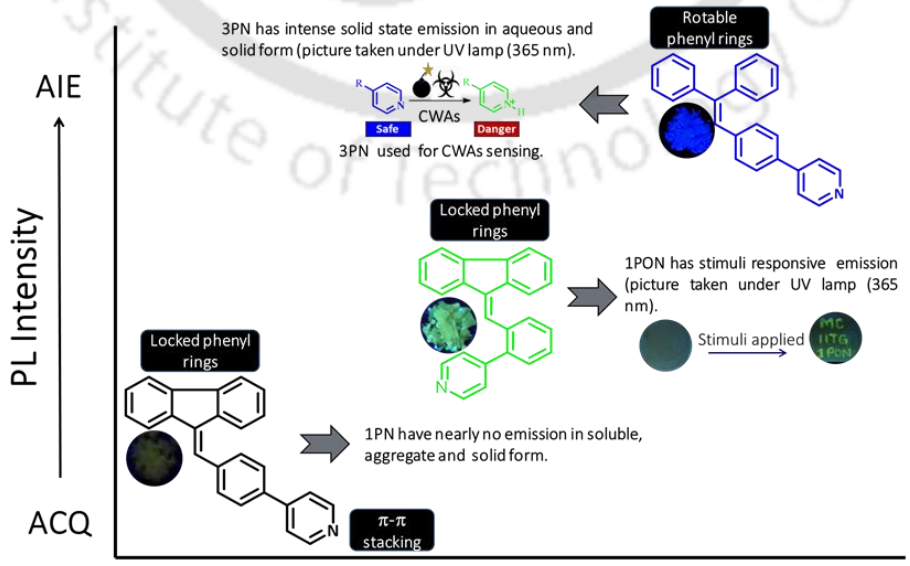

Scheme 3: Strategically designed molecules to get AIE property.

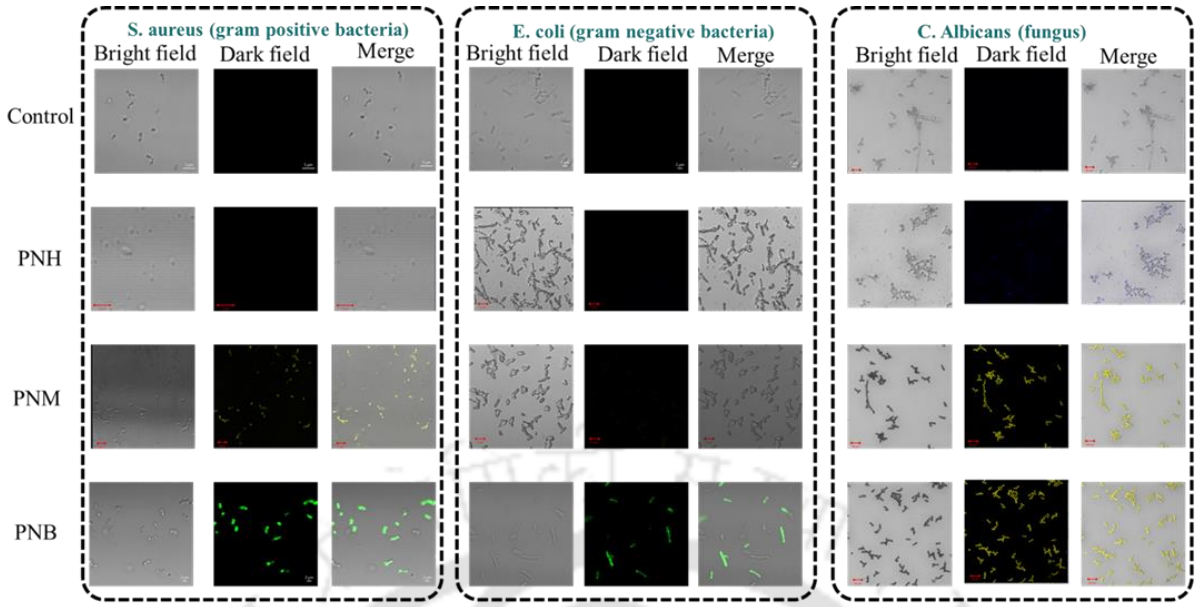

Figure 1: Confocal laser scanning microscopy (CLSM) images of S. aureus, E. coli. and C. albicans using AIE active **PNH**, **PNM** and **PNB**.

From the confocal microscopic studies, it is observed that **PNH** is unable to interact with the pathogens, whereas **PNM** exhibits efficient interaction with the Staphylococcus aureus (S. aureus) bacteria and Candida albicans (C. albicans) respectively, which could be energized by the proficient interaction between the cationic pyridinium congener and the negative charge of the pathogen's membrane. Interestingly, it is also showing the negligible interaction between the Escherichia coli (E. coli) a gram-negative bacteria. These above results suggested that the **PNM** is selective towards the S. aureus bacteria and C. albicans. Whereas, **PNB** displayed emissive behaviour towards the S. aureus, E. coli bacteria and C. albicans respectively. Most remarkably, it is can also concluded that these **PNM** and **PNB** luminogens exhibit wash free fluorescence imaging characteristics towards pathogens (Figure 1).

Further, selective killing was performed and observed by the 3-(4,5-dimethylthiazol-2-yl)-2,5-diphenyltetrazolium bromide (MTT) experiment, which has been demonstrated that the **PNM** selectively killed the S. aureus bacteria and C. albicans, whereas **PNB** exhibited killing effect towards all types of pathogens (S. aureus, E. coli and C. albicans) by disrupting the cellular membrane of the pathogens, confirmed by the field emission scanning electron microscope (FESEM) studies. Hence minor alteration in the AIE luminogens lead to drastic difference in their imaging and killing behaviour of pathogens.

Conclusion and thesis overview

In conclusion, step-by-step designing of AIE luminogen have been demonstrated *i.e.* incorporation of planar and non-planar rotor groups, regioisomers and flexible rotors. We have synthesized different types of AIE luminogens for trace water, organic solvents, hydrazine, PA, TNT, CWAs, and also developed invisible ink, pressure-responsive membrane. The PDT on MCF07, MDAMB cancer cells line have been performed. Aggregation-induced emission active luminogens have established for wash free imaging and antimicrobial application against pathogenic bacteria and fungus. Furthermore, mentioned strategies can also be employed for designing new AIE luminogens for several applications to serve humankind.

Contents

Abbreviations

ACQ	aggregation caused quenching
AIE	Aggregation-induced emission
AIEE	aggregation-induced enhance emission (AIEE)
C. albicans	Candida albicans
CWAs	Chemical warfare agent
CQ	Concentration quenching
CLSM	Confocal laser scanning microscopy (CLSM)
COF	Covalent organic frameworks (COF)
CIEE	Crystallization induced emission (CIEE)
CIE	Crystallization induced emission enhancement (CIE)
DNA	Deoxyribonucleic acid (DNA)
DMSO	Dimethyl sulfoxide
DSE	Dual state emission (DSE)
E. coli	Escherichia coli
ESIPT	Excited state intramolecular proton transfer
FESEM	Field emission scanning electron microscope
FRET	Förster resonance energy transfer
HOMO	Highest occupied molecular orbital
IR	Intramolecular rotation
IV	Intramolecular vibration
LFP	Latent fingerprint visualization
LED	Light-emitting diode
LD	lipid droplet
LOD	Limit of detection
LUMO	lowest unoccupied molecular orbital
MCF-7	Michigan cancer foundation-7
MDAMB231	Human mammary carcinoma
MOF	Metal organic frameworks
µM	Micromolar
NPs	Nanoparticles

ng	Nanogram
nM	Nanomolar
NMR	Nuclear magnetic resonance
OFET	Organic field effect transistors
OLED	Organic light-emitting diode
OLET	Organic light-emitting transistor
PDMS	Polydimethylsiloxane
PET	Photoinduced electron transfer
PDT	Photodynamic therapy
PL	Photoluminescence
(ROS)	Reactive oxygen species
RIM	restriction of intramolecular motions
RIR	Restriction of intramolecular rotations
RIV	Restriction of intramolecular vibration
SCXRD	Single crystal X-ray diffractometer
S. aureus	Staphylococcus aureus
THF	Tetrahydrofuran
TPE	Tetraphenylethene
TICT	Twisted intramolecular charge transfer
f_w	Water fraction
XRD	X-ray crystallography

CHAPTER 1

Introduction

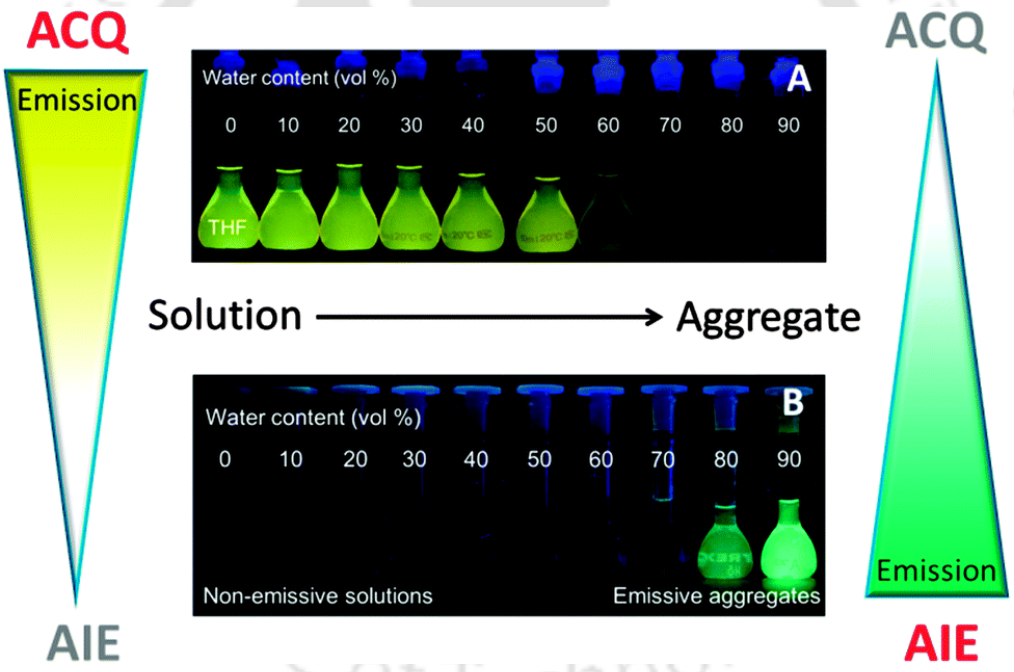

1.1 World of fluorescence

The process of light-generation from any substance without generating or obtaining heat, is called luminescence. It originates from electronically excited states, and there are various types of luminescence *viz.* electroluminescence,[1] chemiluminescence,[2] crystalloluminescence,[3] mechanoluminescence,[4] photoluminescence,[5] radioluminescence,[6] sonoluminescence[7] but generally it categorized into phosphorescence[8] and fluorescence.[9] Many nature creatures, such as fireflies, bigfin reef squid, ctenophore and anglerfish have bioluminescence to attract and catch foods and protect themselves against aggressors. Human beings are inspired by nature and employ luminous materials for biomedical applications, displays and illumination devices for making our brighter and colorful life events. The development in the field of fluorescence technique is lowering the cost and complexity of the previous techniques. Fluorescence-based sensing and imaging are applied to the broad area of problems in biological and chemical science. [10,11]

1.2 Classical luminogens: aggregation caused quenching (ACQ)

Light-emitting organic materials have (electron conjugation) been trending in the research area for their prominent broad applications. Technological requirements have created higher interest in the development of novel materials with higher luminescence. Fluorescent materials have magnificent advantages such as fast response time, high resolution, low background noise, quick response and superior selectivity hence it has been broadly used in sensing and biological imaging.[12-15] Photophysical studies of fluorescent materials are performed in dilute solution, because of solvent molecules obstructed intermolecular interactions of luminogens. For the real-world applications, fluorescent materials were used in thin-film or solid-state like in organic light-emitting diode (OLED), organic light-emitting transistor (OLET). However, classical fluorescent molecules have some disadvantages as well that limit their various applications. The conventional fluorescent materials tend to form aggregates in the aqueous medium and lead to π-π stacking in the solid and thin-film state that caused decreasing of fluorescence of materials this phenomenon is termed as concentration quenching or aggregation caused quenching (ACQ).[16] The device performance is profoundly dependent upon the intrinsic property of emissive material, especially the material's emission efficiency in the thin-film or solid-state. Hence the fluorescence from the aggregated state has countless importance in our real-world applications.[17]

1.3 Trailblazing novel luminogens: condense state emission and its types

Luminescence materials whose emissions intensity are brightened by aggregate formation are termed as aggregation-induced emission materials (AIE). In AIE photophysical phenomenon molecular aggregates exhibited intense emission AIE materials are smart materials we can employed it as chemical probe, bio-imaging and optoelectronic device.[18]

1.3.1 Aggregation-induced emission (AIE)

AIE term describes the behavior of molecule with no emission in diluted solution and/or higher emission in the solid or aggregate state. AIE phenomenon is not new to us firstly Sir George Gabriel stokes (1853) has discussed similar fluorescent properties in inorganic salts.[19] but slight more attention was paid. The immense interest it attracted since 2001 after Tang *et al* rediscovered and proposed the concept of AIE is notworthy.[20]

1.3.2 Aggregation-induced enhanced emission (AIEE)

After the term AIE discovery, Park *et al.* reported a new abnormal observation in the fluorescence that is aggregation-induced emission enhancement (AIEE). They studied emission pattern of cyano-substituted 1,2-bis(pyridylphenyl)ethene (CNPPE). These luminogens fall in this category have less emission in soluble form but have intense emission in fraction of bad solvent. Strong emission in these materials was due to formation of *J* aggregates and the synergetic effect of intramolecular planarization.[21]

1.3.3 Dual state emission (DSE)

Wherein these materials can have emission in both soluble and in the aggregated state. AIE and AIEE materials have lack or less emission in solution but have intense emission in the aggregated form, but DSE materials can show emission in the solid as well as the solution state. DSE materials have some advantages than AIEE and AIE materials such as higher quantum yield, tunable fluorescence emission etc.[22]

1.3.4 Crystallization induced emission enhancement (CIE) and crystallization induced emission (CIEE)

For optoelectronic devices like an organic laser, OLETs, OLEDs fabrication organic material was used as an emissive layer in the thin film or crystal form. Crystallization is a tedious process for traditional luminogens because the emission wavelength will generally shift and intensity will be weakend due to robust π-π interactions. To prevent decrement phenomenon many chemical and physical methods were performed but all these attempts have seen limited success moreover it turns increasingly complex and the device becomes costlier. If twisted and

bulky molecules are loosely packed in the amorphous form that allows the material to perform intramolecular motions but in the crystalline form, due to rigidification intramolecular motion was prevented that resulted in intense emission in the crystal state.[23]

1.4 Working mechanisms

Decipherment of solid/ aggregate state emission and enhanced mechanism knowledge have prodigious importance to the quest for photophysics basic knowledge to further design novel luminogens for practical technological innovations. AIE concept was coined in 2001 and after that scientists has shown indefatigable thirst to know the reason behind the unprecedented emission property therefore several mechanistic pathways have been hypothesized like planarization, E/Z isomerization, J-aggregate formation, twisted intramolecular charge transfer (TICT) etc. Luminescence is a robust tool using many fields its understanding of photophysical mechanism has permitted us to synthesize new efficient materials for detection, imaging and electroluminescent devices.

However, none of these mechanisms can fully explain all AIE systems with experimental data. The most accepted hypotheses for the AIE phenomenon's mechanistic cause with the experimental and theoretical proof are restriction of intramolecular rotations (RIR), restriction of intramolecular vibration (RIV) and restriction of intramolecular motions (RIM) (Figure 1.1).

1.4.1 Restriction of intramolecular rotations (RIR)

Restriction of intramolecular rotations was currently the most accepted mechanistic model used to explain the main reason for the AIE's origin. Most of the AIE materials contain an aromatic ring that can revolve in a solvated state, it consumes excited state energy permitting energy to decay and the decline of emission rapidly. Intermolecular interactions between AIE molecules were restricted upon the formation of aggregates that caused the molecules to decay by radiative pathway.[24,25]

1.4.2 Restriction of intramolecular vibration (RIV)

The RIR model explained several AIE systems that were observed however AIEgen family continues growing. Some of the AIE systems exhibit AIE phenomenon, although it lacks rotor group systems like 10,10′,11,11′-Tetrahydro-5,5′-bidibenzo[a,d][7]annulenylidene (THBA)**.** There is no rotatable unit in THBA as its rotor phenyl ring was locked by ethylene tethers, yet it displays AIE activity. Due to locked rotation motion, it should have bright emission but its excited-state energy was consumed by intramolecular vibration. Hence in THBA**,** RIV is the reason for the AIE phenomenon.[26,27]

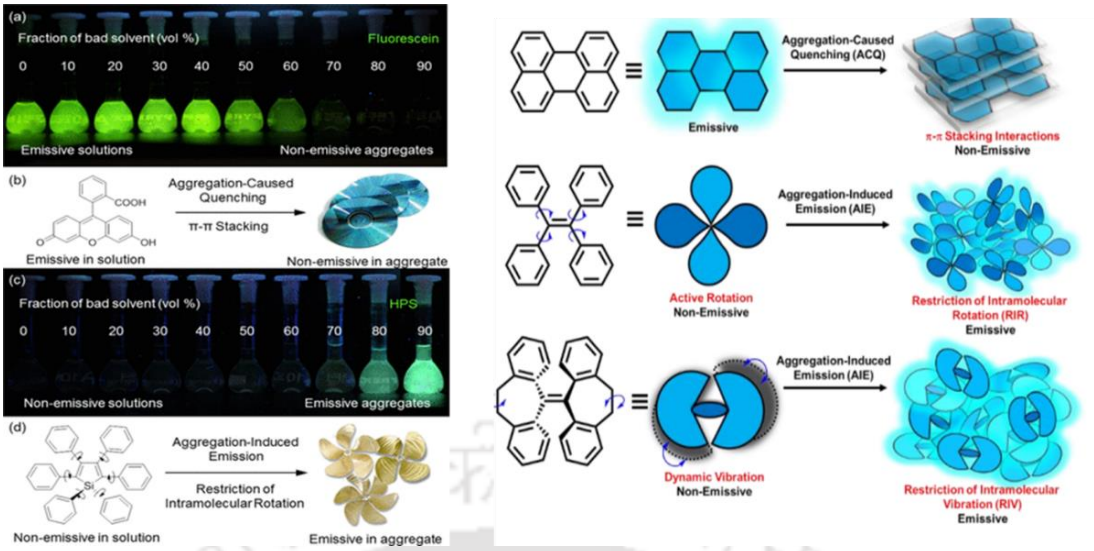

Figure 1.1: Disk shaped ACQ materials emissive in soluble but quenched in aggregated form but propeller shaped luminogen have non-emission in the dissolved but becomes emissive when aggregated, owing to restriction in intramolecular motions (RIM).

1.4.3 Restriction of intramolecular motions (RIM)

Rotational twisting and swinging motion in-plane and out-plane also act as a pathway to consume the excited state energy. The restriction of intramolecular rotation and vibration collectively summaries as RIM.

1.5 Types of AIE materials

The year 2022 marks 22 years since the concept of AIE was coined by Ben Zhong Tang. The AIE concept broke the conventional dogma of ACQ and guided researchers to design and synthesize brighter fluorophores. In literature varieties of AIE systems are published ranging from their chemical, electronic, energy, optical properties for different applications such as OLED, chemical sensors, cellular imaging, cancer theranostics and other biomedical applications.

1.5.1 Small molecule

1-Methyl-1,2,3,4,5-pentaphenylsilole(HPS) is the first molecule which showed AIE phenomenon. HPS is non-emissive in the dissolved state but gets intense emission in the aggregation state. after this molecule, so many small molecules based numerous AIEgen have been reported and used for different applications. The traditional small molecule mainly consists of aromatic non-planar rotors. Functionalized acrylonitrile **1** achieves AIE properties with efficient red emission by reaction condition varioations.[29] Triphenylamine based donor-acceptor based **2** and **3** materials with bright red AIE emission was reported for multifunctional

cancer therapy.Excited state intramolecular proton transfer (ESIPT) based AIE fluorophore **4** was synthesized and it showed intense yellow emission in aqueous medium (Figure 1.2).[31]

1.5.2 Polymer (conjugated and non-conjugated)

Polymer is a macromolecule or large molecule made up of repeating ones or several small units. Contrary to traditional polymers that generally faced the ACQ phenomenon, the incorporation of AIE monomers yielded AIE characteristics into the polymer. Polymer morphology, composition and structure can be tuned to meet the requirements and also easily functionalized via covalent and noncovalent interactions for different applications. AIE active polymers can be constructed by various strategies such as coupling method (Suzuki, Stille), reversible addition fragmentation chain (RAFT), step-growth polymerization etc. Non-conjugated AIE polymer **5** was synthesized using poly(acrylate) with a Tetraphenylethene (TPE) pendant. [32] AIE active conjugated polymer **6** has showed color tunable nanoparticles (NPs) and it was used for self-indicating cancer therapy (Figure 1.3a,b). [33]

1.5.3 Metal organic frameworks (MOF)

MOF is inorganic-organic a new type of material, that display a wide range of tunable fluorescence behavior. The fluorescence properties are systematically tuned by changing the metal ion framework, organic linkers and by a change in the guest species etc. Introduction of AIE active organic linker into the MOF tune the electronic transition energies that leads to enhanced fluorescence. Gold metal based **7** was reported by integration of Au (I) with an AIE active N,N-diphenyl-4-(7-(pyridin-4-yl)benzo[c][1,2,5]thiadiazol-4-yl)aniline (TBP) and it

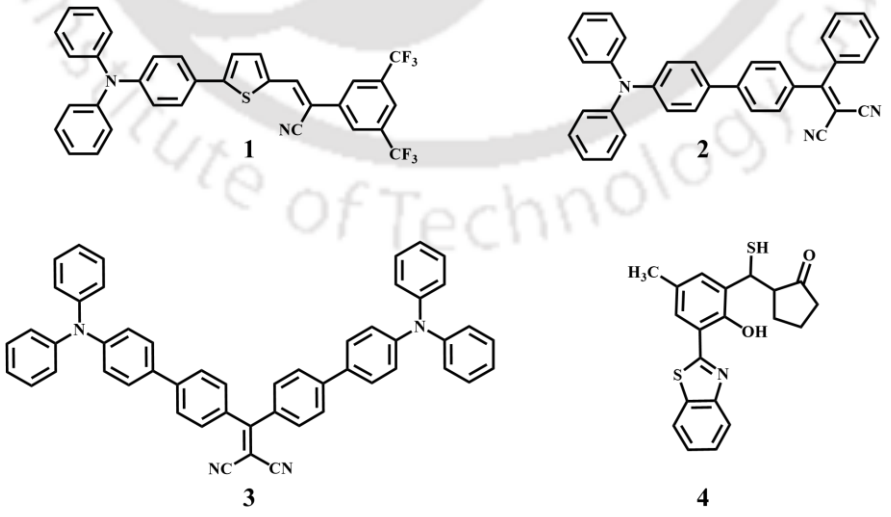

Figure 1.2: Chemical structures of AIE active small molecules.

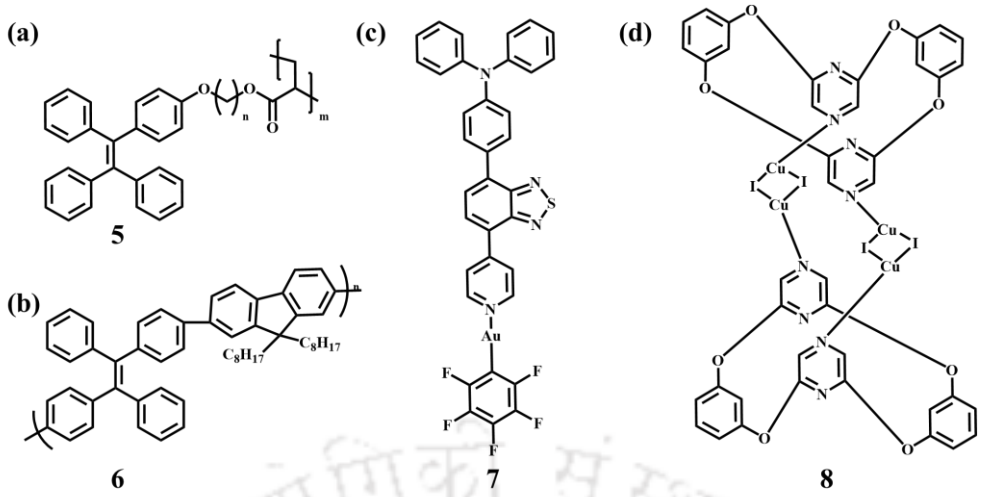

Figure 1.3: Chemical structures of (a,b) AIE active polymers and (c,d) MOFs.

showed enhanced anticancer properties by thioredoxin reductase activity suppression.[34] Butterfly like MOF **8** was prepared and and it has 1D chain structures and its ligands are connected by Cu_2I_2 clusters and it exhibited multiple potential applications in white Light-emitting diode (LED) and encrypted information storage(Figure 1.3c,d). [35]

1.5.4 Covalent organic frameworks (COF)

Covalent organic frameworks (COF) have structural diversity, it emerged as a fascinating class of organic materials. It has a periodic crystalline framework with assembled molecular chromophore *via* covalent bonds. The diverse types of molecular ligands allow us to include most of the organic ligands. Different functional groups can modify these ligands to tune the required photophysical properties. Highly emissive COF are rare due to ACQ of π-π stacked layer. AIE active TPE unit integration in COF **9** yields exceptional intense fluorescence in solid and solutions.[36] Triazine core based COF **10** with unsubstituted olefin linkages was reported. Vertically stacked triazine cored Two-dimensional (2D) sheets extended π electron delocalization and tune the energy levels(Figure 1.4a,b).[37]

1.6 Applications of AIE materials

The AIE materials have given scientists a more powerful tool for versatile strategies to design novel sensor systems. A wide variety of AIEgens have been successfully synthesized and many innovative probes are reported every day. AIE probes can be used as explosive, pH, ions, amines and biological probes for amino acid, nucleic acid, glucose etc. In contrast to conventional probes AIE based system has excellent photostability, higher signal to noise ratio and low detection limit. In contrast to classical ACQ fluorophores the recently introduced AIEgen have high emission efficiency featured which provide exceptional advantages such as

high photostability, high signal to noise ratio, hence AIE fluorescent materials are best candidates for chemical and biosensing.[38]

1.6.1 Chemical and biological sensors

Fluorescent probes with advantages of rapid response, easy operation and excellent sensitivity are emerging as potent tools for biological sensing, disease diagnosis and environment monitoring. Prodigious efforts have been devoted for developing cost effective and rapid fluorescence probe to design chemical and biological sensors. According to Cambridge definition, "Chemical sensors are miniaturized devices that can deliver real time and on-line information on the presence of specific compounds or ion in even complex samples". Quantification and detection of toxic or essential metal ions is most important for environmental and biological inspection. The detection of environmentally significant analytes has emerged substantial goal in the field of chemical and biological sensor area. Numerous methods, such as mass spectrometry, high performance liquid chromatography, electrochemical sensing etc., have been employed for sensing application. Nevertheless, these methods are costly and time-consuming process and limits the use of sophisticated techniques. Whereas fluorescence-based sensing is nondestructive, highly sensitive, easy to operate and can be rapidly performed. TPE based probe **11** was designed for thiol specific biomolecular probing via thiol-ene click mechanism.[39] Probe **12** showed selective and activatable fluorescent AIE characteristics for peroxynitrite generation.[40] Fluorescent turn-on amine vapors detection was performed by probe **13** through aminolysis reaction, a portable sensor was also prepared

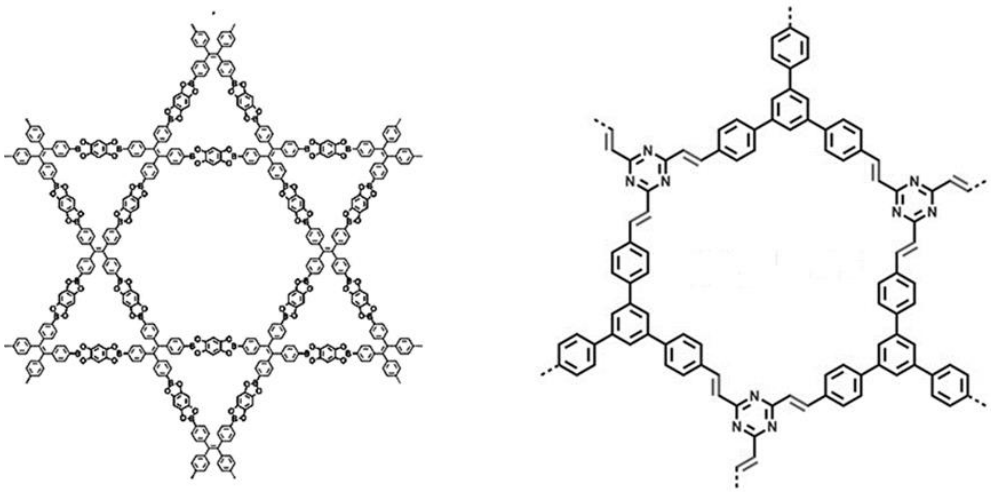

(9) **(10)**

Figure 1.4: Chemical structure of AIE active COF materials.

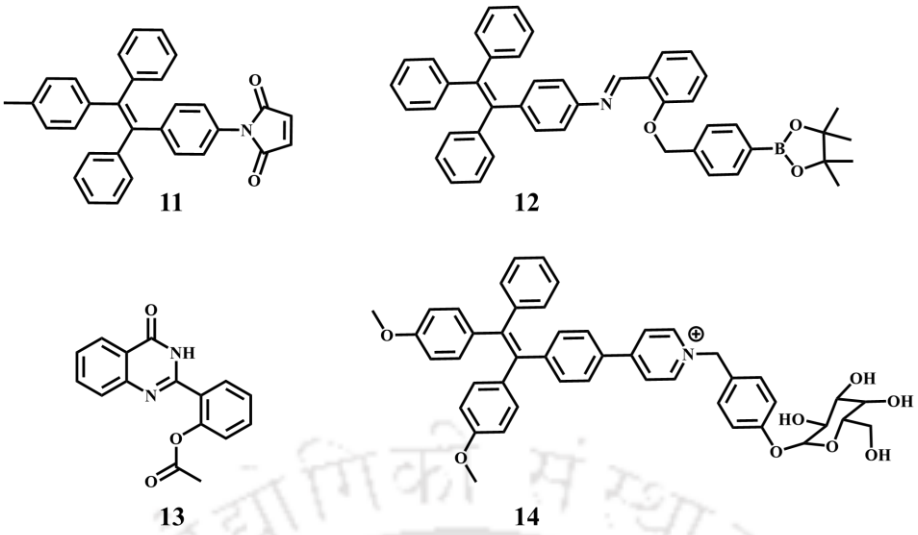

Figure 1.5: Chemical structure of AIE probes for chemical and biological sensors.

by depositing on filter paper and also food spoilage detection was performed.[41] AIE probe **14 was** developed for *β*-galactosidase activity detection in living cells, it has great potential in cancer diagnosis and chemotherapy (Figure 1.5).[42]

1.6.2 *In-vivo, in-vitro* imaging

Fluorescence *in-vivo* and *in-vitro* imaging has become an integral part of modern research. Fluorescent live cell dyes, protein tags and other techniques provide a various cellular process. Optical imaging with AIE materials has been revolutionized due to exceptional photophysical properties such as less toxicity, high bioaccumulation, high signal to noise ratio and low background interference. Live cell imaging techniques give scientist the access to see insight into the various cell process furthermore the high-resolution microscopy open new gateway to observe subcellular structures. Probe **15** showed bright AIE emission and it was used for two photon imaging and localized cancer therapy.[43] For image guided surgery and in-vivo imaging near infrared II (NIR-II) fluorescence imaging have immense potential due to deep penetration and high resolution images. Novel NIR-II AIE material **16** was synthesized and used for visualizing tumor feeding blood vessels and breast tumor imaging. This was used as proof of concept for first time non invasive and real time NIR-II gastrointestinal tract imaging (Figure 1.6a,b).[44]

1.6.3 Theranostics based on AIEgens

The materials with AIE characteristics have emerged as a source of tremendous scope in the research area of theranostics. AIE materials have several distinct advantages *viz.* simple synthesis method, easy modification and higher biocompatibility etc. are encouraged for

application in photodynamic therapy. In cancer therapy integrated diagnosis and therapy are in higher demand therefore **17** was reported, it demonstrated novel strategy of traceable cancer therapy. It has been incorporated with AIE active molecule TPS and photosensitizer pheophorbide A(PheA).[45] Far red and near infrared (NIR) fluorescent materials **18** showed two photon absorption and it demonstrated lipid driplet (LD), mitochondria targeting and efficient PDT of cancer cells ablation (Figure 1.6c,d).[46]

1.6.4 AIE based smart materials

AIEgens fluorescent materials are intelligent materials, their emission changes in response towards external stimulant and environment variance such as mechanical force, solvent polarity, temperature (heating/cooling), fuming (vapor), photonic irradiation, etc. The change in fluorescence due to mechanical force leads to chromic effect and such materials have prodigious potential in security ink, information storage and pressure sensors.

(a) Stimuli responsive

The mechanochromic effect is associated with a change in the molecular arrangement and phase transition of AIEgen. The non-planar AIE molecule's loose packing morphology is sensitive towards external force, thus it will lead to chromic response. Diphenyldibenzofulvenes based AIE material **19** reportedly showed reversible switching of the emission by mechanical and thermal stimuli.[47] TPE based benzothiazolium functionalized molecule **20** reportedly it demonstrated tunable solid state emission via grinding, heating and solvent fuming(Figure 1.7a,b).[48]

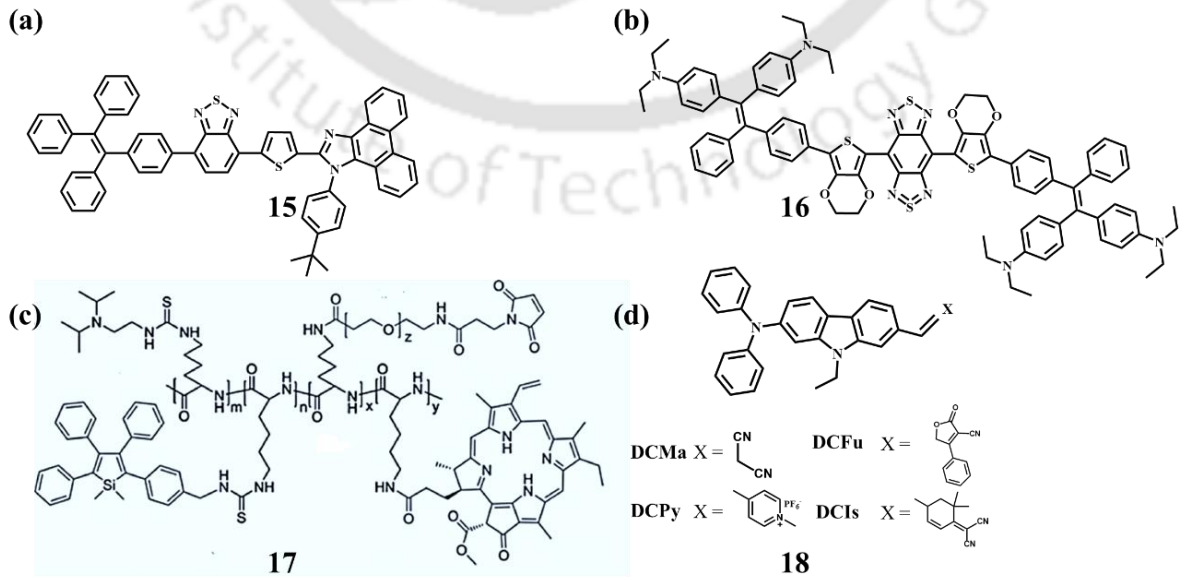

Figure 1.6: Chemical structure of AIE active materials for (a,b) imaging and (c,d) theranostics applications.

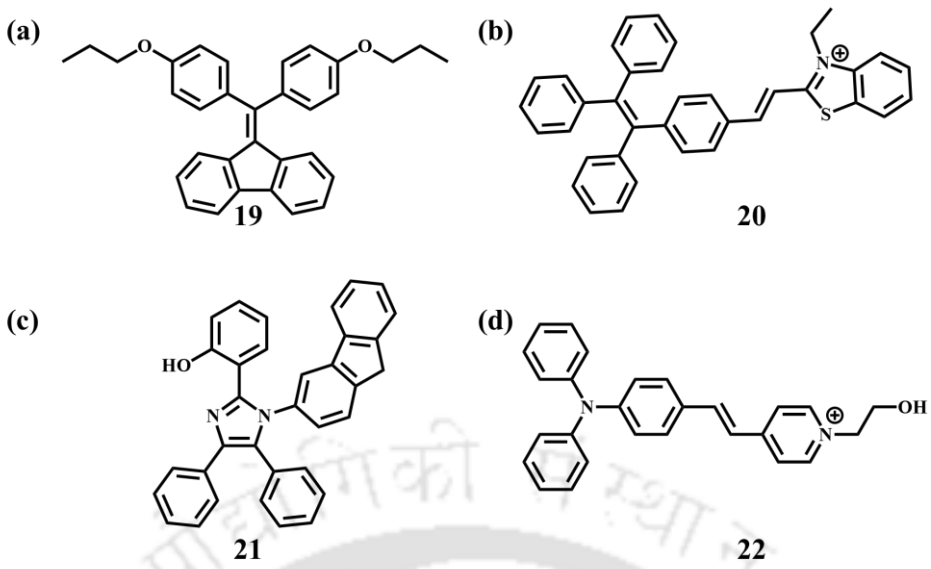

Figure 1.7: Chemical structure for AIE meterials for (a,b) stimuli responsive and LFP (c,d) imaging.

(b) Latent fingerprint visualization (LFP)

Fluorescent materials are widely used for bio-sensing and chemo-sensing but utilization in imaging of LFP was prohibited due to ACQ. AIE active imidazole-based molecule **21** was developed for latent fingerprints visualization and anticounterfeiting applications.[49] For visualization of LFP exceeding level 3, Probe **22** was synthesized. The LFP developed by the probe showed real time in situ fluorescence imaging and it demonstrated relationship between LFP fluorescence intensity and its deduced time (Figure 1.7c,d).[50]

1.7 Conclusion and future aspects

The discovery of fluorescence materials has given access to the vast knowledge that lead us to many innovations for the benefit for the whole humankind. Theoretically fluorescent materials can be employed in any state *i.e.* solution, solid. However classical fluorescent materials suffered with the ACQ phenomenon. Therefore, in practical applications such as organic field effect transistors (OFET) and OLED classical materials have shown lesser performance. ACQ luminogens are planar in structure and they have strong intermolecular π- π interactions that lead to reduction in the fluorescence in the aggregated or solid state. In contrast AIE luminogens have non-planar, propeller shaped rotor groups that prevent π- π stacking results intense emission in aggregated and solid state. In the past few years scientist have fascinating interest for design and development of AIE luminogens for various real world (biomedical and optoelectronic applications. In this thesis work, design and development of AIE materials from ACQ luminophore have been unveiled by various strategies. Various environmentally toxic,

nitro explosive, nerve agents, hydrazine detection and imaging (cell, bacteria and fungi) demonstrated. Overall the present thesis focuses on the design and development of the AIE luminogens and applied for various sensing and imaging applications.

1.8 References

(1) Usta, H.; Alimli, D.; Ozdemir, R.; Dabak, S.; Zorlu, Y.; Alkan, F.; Tekin, E.; Can, A. *ACS Appl. Mater. Interfaces* **2019,** *11* (47), 44474-44486.

(2) Lan, Y.; Yuan, F.; Fereja, T. H.; Wang, C.; Lou, B.; Li, J.; Xu, G. *Anal. Chem.* **2019,** *91* (3), 2135-2139.

(3) Safonov, G. P.; Shlyapintokh, V. Y.; Entelis, S. G. *Nature* **1965,** *205* (4977), 1203-1204.

(4) Zhuang, Y.; Xie, R.-J. *Adv. Mater.* **2021,** *33* (50), 2005925-2005958.

(5) Algar, W. R.; Massey, M.; Rees, K.; Higgins, R.; Krause, K. D.; Darwish, G. H.; Peveler, W. J.; Xiao, Z.; Tsai, H.-Y.; Gupta, R. •Lix, K.; Tran M.V.; Kim, H. *Chem. Rev.* **2021,** *121* (15), 9243-9358.

(6) Cooper, D. R.; Capobianco, J. A.; Seuntjens, J. *Nanoscale* **2018,** *10* (16), 7821-7832.

(7) Harvey, E. N. *J. Am. Chem. Soc.* **1939,** *61* (9), 2392-2398.

(8) Baryshnikov, G.; Minaev, B.; Ågren, H. *Chem. Rev.* **2017,** *117* (9), 6500-6537.

(9) Warner, I. M.; Soper, S. A.; McGown, L. B. *Anal. Chem.* **1996,** *68* (12), 73-92.

(10) Lin, W.; Yuan, L.; Long, L.; Guo, C.; Feng, J. *Adv. Funct. Mater.* **2008,** *18* (16), 2366-2372.

(11) Stenken, J. A. *J. Am. Chem. Soc.* **2009,** *131* (30), 10791-10794.

(12) Tagit, O.; Hildebrandt, N. *ACS Sens.* **2017,** *2* (1), 31-45.

(13) Liu, S.; Pestano, J. P. C.; Wolf, C. *J. Org. Chem.* **2008,** *73* (11), 4267-4270.

(14) Bao, Y.; De Keersmaecker, H.; Corneillie, S.; Yu, F.; Mizuno, H.; Zhang, G.; Hofkens, J.; Mendrek, B.; Kowalczuk, A.; Smet, M. *Chem. Mater.* **2015,** *27* (9), 3450-3455.

(15) Wang, Q.; Wang, W.; Lei, J.; Xu, N.; Gao, F.; Ju, H. *Anal. Chem.* **2013,** *85* (24), 12182-12188.

(16) Kim, H. S.; Park, S.-R.; Suh, M. C. *J. Phys. Chem. C* **2017,** *121* (26), 13986-13997.

(17) Siu, H.; Duhamel, J. *Macromolecules* **2005,** *38* (16), 7184-7186.

(18) Würthner, F. *Angew. Chem. Int. Ed.* **2020,** *59* (34), 14192-14196.

(19) Stokes, G. G. Philos. Trans. R. Soc. 1852, 142, 463-562.

(20) Luo, J.; Xie, Z.; Lam, J. W. Y.; Cheng, L.; Chen, H.; Qiu, C.; Kwok, H. S.; Zhan, X.; Liu, Y.; Zhu, D. Tang, B. Z. *Chem. Commun.* **2001**, 1740-1741.

(21) An, B.-K.; Kwon, S.-K.; Jung, S.-D.; Park, S. Y. *J. Am. Chem. Soc.* **2002,** *124* (48), 14410-14415.

(22) Chen, G.; Li, W.; Zhou, T.; Peng, Q.; Zhai, D.; Li, H.; Yuan, W. Z.; Zhang, Y.; Tang, B. Z. *Adv. Mater*. **2015**, *27 (30)*, 4496-4501.

(23) Crocker, R. D.; Pace, D. P.; Zhang, B.; Lyons, D. J. M.; Bhadbhade, M. M.; Wong, W. W. H.; Mai, B. K.; Nguyen, T. V. *J. Am. Chem. Soc.* **2021,** *143* (48), 20384-20394.

(24) Padalkar, V. S.; Seki, S. *Chem. Soc. Rev.* **2016,** *45* (1), 169-202.

(25) Pina, J.; B. Rodrigues, A. C.; Alnady, M.; Dong, W.; Scherf, U.; Seixas de Melo, J. S. *J. Phys. Chem. C* **2020,** *124* (25), 13956-13965.

(26) Wang, Y.; Nie, J.; Fang, W.; Yang, L.; Hu, Q.; Wang, Z.; Sun, J. Z.; Tang, B. Z. *Chem. Rev.* **2020,** *120* (10), 4534-4577.

(27) Zhao, Z.; Zheng, X.; Du, L.; Xiong, Y.; He, W.; Gao, X.; Li, C.; Liu, Y.; Xu, B.; Zhang, J.et al. *Nat Commun* **2019,** *10* (1), 2952-2951.

(28) Suman, G. R.; Pandey, M.; Chakravarthy, A. S. J. *Mater. Chem. Front.* **2021**, 5 (4), 1541-1584.

(29) Niu, G.; Zheng, X.; Zhao, Z.; Zhang, H.; Wang, J.; He, X.; Chen, Y.; Shi, X.; Ma, C.; Kwok, R. T. K.et al. *J. Am. Chem. Soc.* **2019,** *141* (38), 15111-15120.

(30) Zhang, L.; Che, W.; Yang, Z.; Liu, X.; Liu, S.; Xie, Z.; Zhu, D.; Su, Z.; Tang, B. Z.; Bryce, M. R. *Chem. Sci.* **2020,** *11* (9), 2369-2374.

(31) Chen, L.; Wu, D.; Lim, C. S.; Kim, D.; Nam, S.-J.; Lee, W.; Kim, G.; Kim, H. M.; Yoon, J. *Chem. Commun.* **2017,** *53* (35), 4791-4794.

(32) Zhou, H.; Li, J.; Chua, M. H.; Yan, H.; Tang, B. Z.; Xu, J. *Polym. Chem.* **2014,** *5* (19), 5628-5637.

(33) Wang, Z.; Wang, C.; Fang, Y.; Yuan, H.; Quan, Y.; Cheng, Y. *Polym. Chem.* **2018,** *9* (23), 3205-3214.

(34) Zou, H.; Zhang, J.; Wu, C.; He, B.; Hu, Y.; Sung, H. H. Y.; Kwok, R. T. K.; Lam, J. W. Y.; Zheng, L.; Tang, B. Z. *ACS Nano* **2021,** *15* (5), 9176-9185.

(35) Liu, Y. Y.; Zhang, X.; Li, K.; Peng, Q. C.; Qin, Y. J.; Hou, H. W.; Zang, S. Q.; Tang, B. Z. *Angew. Chem. Int. Ed.* **2021,** *60* (41), 22417-22423.

(36) Dalapati, S.; Jin, E.; Addicoat, M.; Heine, T.; Jiang, D. Highly Emissive Covalent Organic Frameworks. *J. Am. Chem. Soc.* **2016,** *138* (18), 5797-5800.

(37) Wei, S.; Zhang, F.; Zhang, W.; Qiang, P.; Yu, K.; Fu, X.; Wu, D.; Bi, S.; Zhang, F. *J. Am. Chem. Soc.* **2019**, *141*, *36*, 14272–14279.

(38) Zhu, Z.; Wang, Q.; Chen, X.; Wang, Q.; Yan, C.; Zhao, X.; Zhao, W.; Zhu, W.-H. *Adv Mater.* **2022,** *34* (3), 2107444-2107453.

(39) Liu, Y.; Yu, Y.; Lam, J. W. Y.; Hong, Y.; Faisal, M.; Yuan, W. Z.; Tang, B. Z. *Chemistry-A European Journal* **2010,** *16* (28), 8433-8438.

(40) Song, Z.; Mao, D.; Sung, S. H. P.; Kwok, R. T. K.; Lam, J. W. Y.; Kong, D.; Ding, D.; Tang, B. Z. *Adv. Mater.* **2016,** *28* (33), 7249-7257.

(41) Gao, M.; Li, S.; Lin, Y.; Geng, Y.; Ling, X.; Wang, L.; Qin, A.; Tang, B. Z. *ACS Sens.* **2016,** *1* (2), 179-184.

(42) Jiang, G.; Zeng, G.; Zhu, W.; Li, Y.; Dong, X.; Zhang, G.; Fan, X.; Wang, J.; Wu, Y.; Tang, B. Z. *Chem. Commun.* **2017,** *53* (32), 4505-4508.

(43) Li, Y.; Tang, R.; Liu, X.; Gong, J.; Zhao, Z.; Sheng, Z.; Zhang, J.; Li, X.; Niu, G.; Kwok, R. T. K.et al. *ACS Nano* **2020,** *14* (12), 16840-16853.

(44) Lin, J.; Zeng, X.; Xiao, Y.; Tang, L.; Nong, J.; Liu, Y.; Zhou, H.; Ding, B.; Xu, F.; Tong, H.. *Chem. Sci.* **2019,** *10* (4), 1219-1226.

(45) Yuan, Y.; Kwok, R. T. K.; Tang, B. Z.; Liu, B. *Small* **2015,** *11* (36), 4682-4690.

(46) Zheng, Z.; Zhang, T.; Liu, H.; Chen, Y.; Kwok, R. T. K.; Ma, C.; Zhang, P.; Sung, H. H. Y.; Williams, I. D.; Lam, J. W. Y.; Wong K. S.; Tang B. Z. *ACS Nano* **2018,** *12* (8), 8145-8159.

(47) Luo, X.; Li, J.; Li, C.; Heng, L.; Dong, Y. Q.; Liu, Z.; Bo, Z.; Tang, B. Z. *Adv. Mater.* **2011,** *23* (29), 3261-3265.

(48) Zhao, N.; Yang, Z.; Lam, J. W. Y.; Sung, H. H. Y.; Xie, N.; Chen, S.; Su, H.; Gao, M.; Williams, I. D.; Wong, S. K.; Tang, B. Z. *Chem. Commun.* **2012,** *48* (69), 8637-8639.

(49) Ravindra, M. K.; Darshan, G. P.; Lavanya, D. R.; Mahadevan, K. M.; Premkumar, H. B.; Sharma, S. C.; Adarsha, H.; Nagabhushana, H. *Sci. Rep.* **2021,** *11* (1), 16748.

(50) Wang, Y.-L.; Li, C.; Qu, H.-Q.; Fan, C.; Zhao, P.-J.; Tian, R.; Zhu, M.-Q. *J. Am. Chem. Soc.* **2020,** *142* (16), 7497-7516.

CHAPTER 2

AIE modulation in Pyrene via Push-Pull, Planar-Rotor Architecture: Sensing Hydrazine, Water Traces in Organic Solvents and Photodynamic Therapy Applications

Adil, L. R.; Bidkar, A. P.; Ghosh, S. S.; Iyer, P. K. (under communication)

Abstract

Aggregation-induced emission (AIEgens) luminogens, owing to their excellent optical performances in their condensed state, have emerged as unique class of materials in many interdisciplinary research areas. However, there is still in high demand for the advancement of novel AIEgens with tunable-emission, easy functionalization and synthesis. Thus, in this contribution, a simple and precise design strategy of four color-tunable smart luminogens **PP**, **PBA**, **PBT,** and **PBM** have been developed, which potentially transform the notorious aggregation-caused quenching (ACQ) effect in a planar disc shaped pyrene fluorophore, which subsequently tuned the photophysical properties of this pyrene scaffold due to the push-pull effect of its donor-acceptor structural engineering. Interestingly, one of these strategically designed luminogens, **PBM** showed environmental dependent fluorescence multitasking behavior due to its distinct donor-acceptor AIE architecture, and have been employed for the detection of trace water (0.1%) in the presence of broad range of organic solvents as well as identification and discrimination of various solvents. Besides, this **PBM** AIEgen accomplished the selective detection of hydrazine in aqueous environment, a highly toxic substance, with a limit of detection (LOD) of 44.71 nM. Herein, the fluorescence quenching response ensued due to the spontaneous formation of reaction-based non-fluorescent **PBM-NNH$_2$** congener, which was further confirmed via the ^{1}H NMR and MALDI-TOF experiments. This highly fluorescent **PBM** AIEgen also demonstrated the reactive oxygen species (ROS) generation ability, and additionally employed as the heavy atom free photosensitizer in image-guided photodynamic therapy of cancer cells in vitro. These intriguing outcomes propose that **PBM** AIEgen exhibits a huge potential for multiplatform futuristic applications through the rational modulation of the pyrene core.

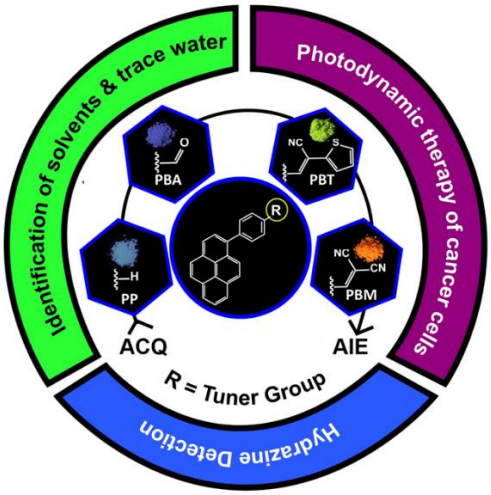

2.1 Introduction

Luminescent compounds have attracted considerable attention since the discovery of fluorescence (1565) by Nicolás Monardes. Although fluorescent compounds were developed over centuries, this dynamic research area is still in growing stage and are now indispensable tools for structural enginering as were never observed previously, which has been recognized by Nobel Prizes in 2008 for green fluorescent proteins, and in 2014 for super-resolved fluorescent microscopy.[1,2] Engineering a new conjugated organic π-materials with intense emission are in high demand due to their wide range of applications in sensing, for example metal ion sensing, bio-sensing, and gas sensing as well as it has high stipulation in biological environment *viz*. cell imaging, fluorescence-guided therapy and shows extensive application in the optoelectronic devices such as OLED etc.[3-7] In recent years, pyrene derivatives have been studied extensively due to their remarkable photophysical properties such as higher lifetime, quantum yield, and higher charge carrier mobilities. However, the planar structure of pyrene core leads to π-π stacking and restrict its futuristic practical applications.[8-12] Most of the traditional fluorescence materials have strong emission in dilute solution or lesser concentration, but are quenched at higher concentration due to the robust intermolecular interactions, and are termed as ACQ.[13,14] Therefore, these ACQ materials-based sensors limited their practical applications, for example to detect the biological analytes in physiological conditions. To prevent the fluorescence molecules from the notorious ACQ phenomenon, few chemical and physical engineering methods have been adopted, but achieved limited success. Organic molecules consisting of condensed state emission are enduring in huge consideration owing to its multifaceted real-world applications. In this aspect, an unusual photophysical phenomenon AIE was formulated by *Luo et al*.[15], reporting emission enhancement of some fluorophores in the solid, thin film, and aggregated-state unlike the classical fluorophores. In contrast to the existing dyes, newly designed aggregate forming materials have constructive effects on the fluorescence in their condensed state and, are termed as AIE materials, which have common characteristics of non-planarity and propeller shaped with free rotatable aromatic rings. This novel anomalous behavior in the aggregated-state is observed due to the result of RIR and RIV.[16] Till date, numerous AIE and AIEE active core based on distyryl, anthracenes, cyanostilbenes, siloles, and tetraphenylethenes (TPE) have been developed. However, most of the AIE/AIEE luminogens restrict their real-world

applications due to the emission fall in the region of blue/UV visible range. Hence, there is a high necessity of designing new AIE/AIEE fluorophores, which can be easily tuned to blue or UV region window by appropriate and precise modifications.[17-20] It has been well established that blue light has harmful effect towards mammalian cells, and has been well studied by various researchers. In the electromagnetic spectrum, every color has different energy and wavelength region. Out of these, blue color consisting of higher energy, covered the 400 to 490 nm wavelength window. Effect of the blue light to the eye was first studied in 1966.[21] Exposure to blue light leads to a higher risk to human health such as human eye inflammatory apoptosis, Deoxyribonucleic acid (DNA) damage, and chronic disease etc. Beside this, the blue light exposure to children causes sleep disorders by disruption of the internal clock and suppression of melatonin secretion.[22] Thus, the above remarkable destructive disastrous effect of blue light attracted immense research interest to the design of far blue fluorescent materials.[23-26] Identification and discrimination of organic solvents requires sophisticated and cost-effective approaches. However, in industry or laboratory usually the conventional methods such as nuclear magnetic resonance (NMR), mass spectrometry and chromatographic technique, which are highly expensive and time-consuming are used. Thus, along with the detection of trace water in the presence of organic solvents, the identification and discrimination of various organic solvents gain huge attention in the field of analytical and synthetic chemistry, which is a crucial for quality control in industries.[27] Similarly, hydrazine (N_2H_4) has been listed as a carcinogen and its huge toxicity causes severe threats to human and marine life, yet it is used unceasingly as a chemical reagent for various synthetic experiments and in rocket fuel. Furthermore, hydrazine has been considered as life-threatening for human health, leading to harmful kidney, liver and lungs diseases, subsequently it exhibits harmful effects for the aquatic animals due to its highly solubility in water, and its huge potential application as a reagent and fuel for long space missions that makes it a very poisonous and harmful molecule. Hence, the development of the highly robust and advanced platform for its detection has attracted immense attention.[28-29] In this respect, many fluorescent probes for the detection of hydrazine with higher sensitivity and selectivity have been devised. Yet, most of the sensing systems require organic solvents that seldom can be used for analysis in aqueous medium. Near blue color fluorescent AIEgen such as TPE[30] and

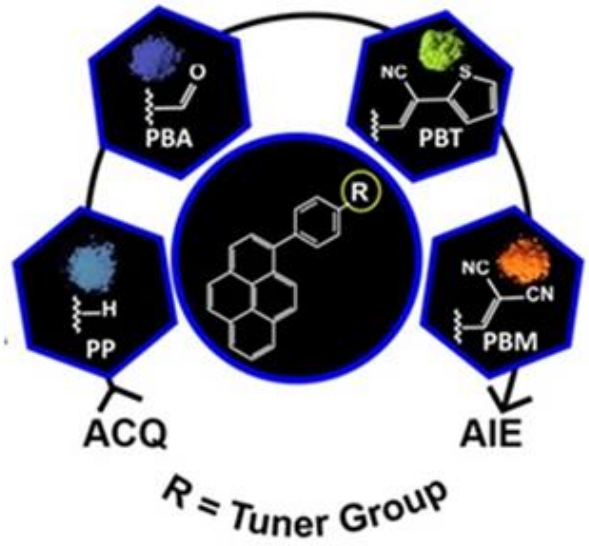

Figure 2.1: Chemical structures of pyrene derivatives with different electron deficient rotor groups and photos of luminescent powder of **PP**, **PBA**, **PBT** and **PBM** under UV lamp.

naphthalene diimides[31] etc. dyes have suffered with light scattering as well as autofluorescence in the biological environment. As stated by the Mie theory for light scattering from the formula $(1/\lambda)\ \alpha$, higher the wavelength of light resulted in lower light scattering (α = 0.2-4 for biological tissue, λ is the wavelength).[32] Thus, fluorescence bioimaging with the help of higher wavelength dye has demonstrated advantages over common blue color fluorescent dye. Correspondingly, the detection of trace water or moisture content in organic solvent has remained challenging and creates hindrance for using these solvents in crucial moisture sensitive reactions. This challenge has been persisting both in academic setup and industrial operations as presence of water hampers in several major chemical conversion steps. Therefore, development of a new probe with multi-tasking ability such as, detection of trace water present in organic solvents and toxic hydrazine in an aqueous medium as well as discriminating this toxic hydrazine in natural and competitive environment would be very challenging. Further, the development of efficient photosensitizers, with enhanced PDT efficiency is an interesting topic gaining tremendous attention in the area of nano-theranostics materials. [33,34]

2.2 Results and Discussion

2.2.1 Design and synthesis of pyrene derivatives

In this chapter, four color tunable pyrene based luminogens **PP**, **PBA**, **PBT** and **PBM** (Figure 2.1) have been designed and synthesized by Suzuki coupling and Knoevenagel condensation reactions. The synthesis route to pyrene derivatives is shown in Scheme 2.1.

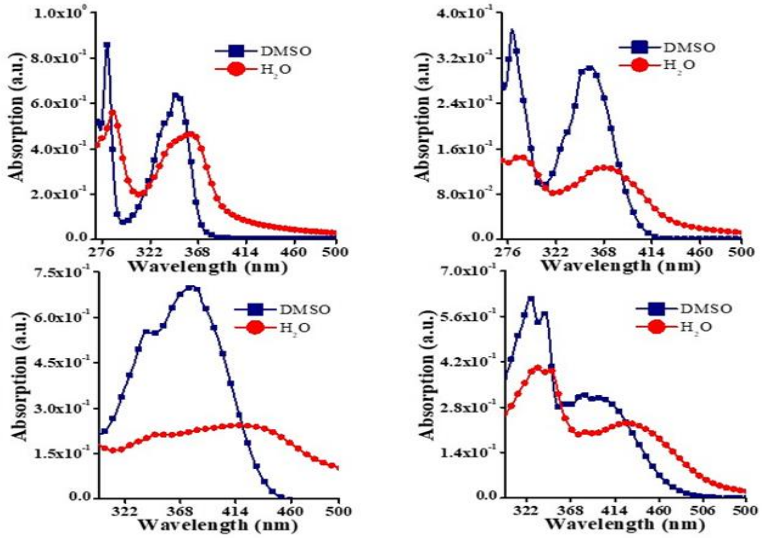

Figure 2.2: UV-vis. spectra of **PP, PBA, PBT** and **PBM** in DMSO and 99% f_w in room temp (10 µM).

2.2.2 Photophysical studies

The photophysical behaviors were strategically tuned by carefully functionalizing with specific rotor groups. Their absorption spectra (Figure 2.2) showed λ_{max} ranging from 279 to 397 nm. These pyrene luminogens possess donor-acceptor (D-A) system except **PP**, where pyrene acts as a donating moiety and the rest part of the molecule acts as an acceptor. This D-A system in pyrene luminogens affects the photophysical properties in both solution and aggregated-state. Their UV-vis. (Figure A2.1) and fluorescence (PL) studies (Figur 2.3) were performed by varying (dielectric constant) the solvents (Toluene to DMSO) to study the solvent polarity effect on their optical properties. Except for **PP**, the other luminogens **PBA**, **PBT** and **PBM** showed solvent dependent

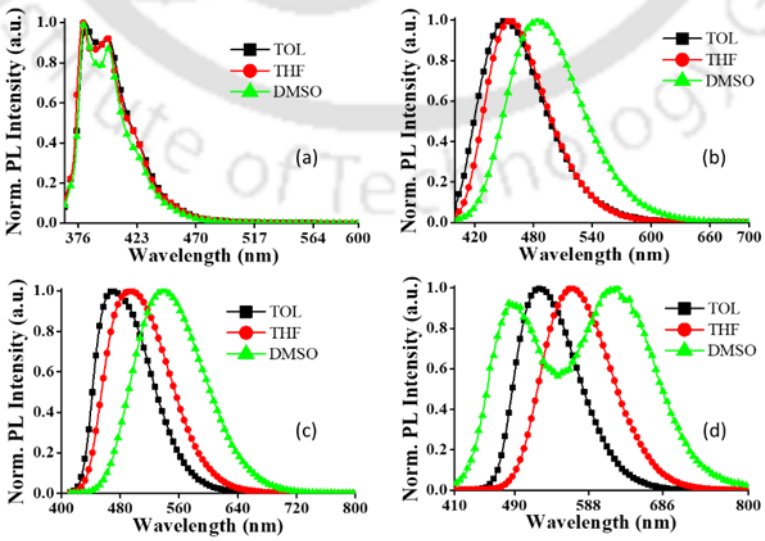

Figure 2.3: PL emission spectra of (a) **PP** (b) **PBA** (c) **PBT** and (d) **PBM** in different polar solvents, all spectra were taken at room temperature.

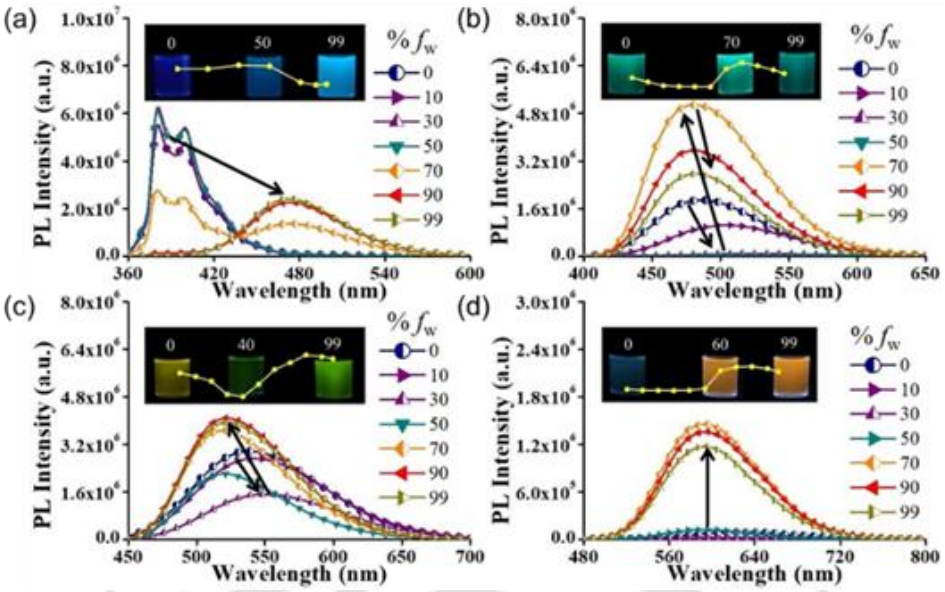

Figure 2.4: Emission intensity plot of (a) **PP** (b) **PBA** (c) **PBT** and (d) **PBM** with the increasing water fraction (f_w) in DMSO-water mixture (10 µM).

UV-vis and emission PL variation with a notable bathochromic shift due to electron push-pull architecture. The detailed photophysical data of these luminogens are mentioned in Table 2.1.

2.2.3 AIE studies

Luminogens **PP**, **PBA**, **PBT** and **PBM** contain two parts (a) the planar pyrene moiety having high emitting properties in dilute solution, but responsible for emission quenching in the aggregated-state or solid-state (b) non-planar rotor group that influence the photophysical behavior. Their AIE and solid-state emission properties are dependent on the RIR and RIV of these non-planar rotors. Although all **PP**, **PBA**, **PBT** and **PBM** luminogens were insoluble in water, they are highly soluble in most organic solvents. Their aggregation dependent studies were performed in DMSO/water mixture system

Table 2.1: **PP**, **PBA**, **PBT** and **PBM** (a) UV-vis. spectra in DMSO and in 99% f_w & PL spectra in DMSO, 99% f_w at room temperature at 10 µM concentration.

Compound	λ_{max} Abs DMSO (nm)	λ_{max} Abs 99% f_w (nm)	λ_{max} PL DMSO (nm)	λ_{max} PL 99% f_w (nm)
PP	279, 349	289, 361	381,400	471
PBA	281, 353	290, 372	484	482
PBT	338, 377	350, 420	537	523
PBM	326, 341, 397	330, 347, 430	481, 615	595

considering the miscibility of DMSO and water. **PP** had intense emission in DMSO and when water fraction (f_w) was increased up to 70%, its emission intensity remained constant. Beyond 70% and up to 99% f_w the formation of less fluorescent aggregates were observed. **PBA** has extra rotatable formyl groups functionalized to the phenyl compared to **PP**. Due to the RIR effect, **PBA** emission is less in DMSO but emission was enhanced with increasing f_w and was highest at 70% f_w, beyond which the **PBA** fluorescence also decreased due to the formation of less fluorescent aggregates. **PBT** showed dual emission, with an intense emission in DMSO but this emission was quenched at 40% f_w and was enhanced with the highest being at 80% f_w. **PBM** had less emission in DMSO because of intramolecular motions of malonitrile group, however, its emission was enhanced with increasing f_w due to RIM, hence, **PBM** displayed AIE property (Figure 2.4). **PP** molecule showed ACQ characteristics because of the inefficiency of the phenyl core to consume the excitation energy in solution state through rotation.

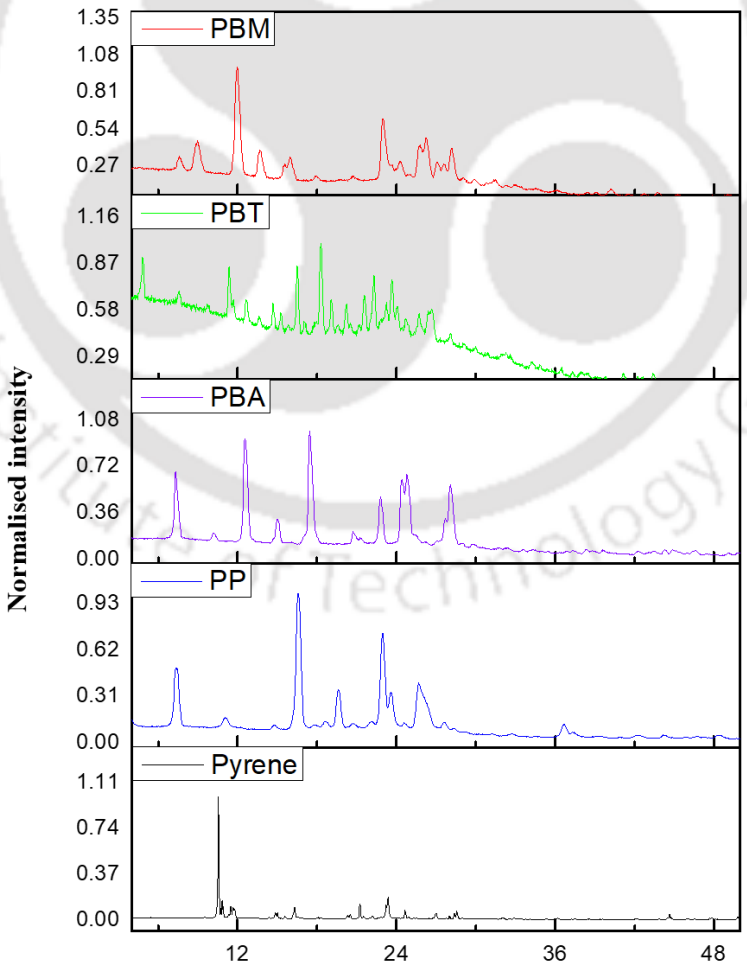

Figure 2.5:Wide angle XRD diffractograms of **PP**, **PBA**, **PBT** and **PBM** in powder state.

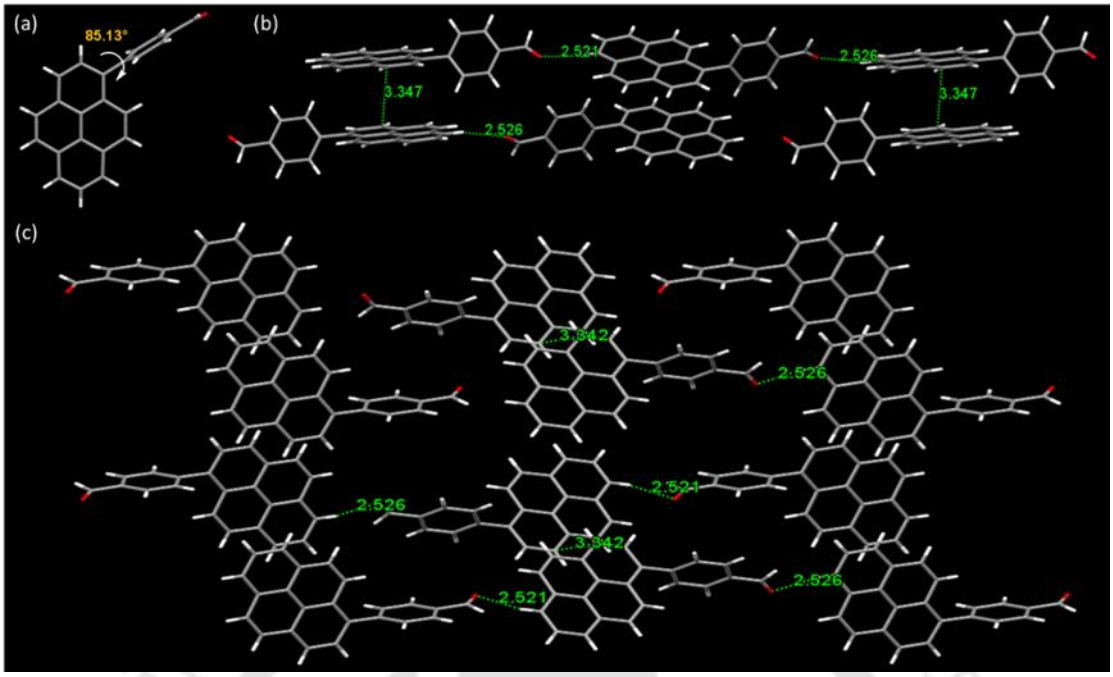

Figure 2.6: (a) Torsional angle in **PBA** with pyrene and phenyl aldehyde (b) prevention of dimer formation in pyrene due to introduction of rotor group (side view) (c) the crystal packing structures of **PBA**.

2.2.4 Packing arrangement

In powder XRD experiments pyrene showed a sharp peak at 2θ =10.54° for dimer, which after introduction of rotor groups (in **PP**, **PBA**, **PBT** and **PBM**) displayed several peaks owing to regular packing arrangements due to hindrance of dimer formation (Figure 2.5).

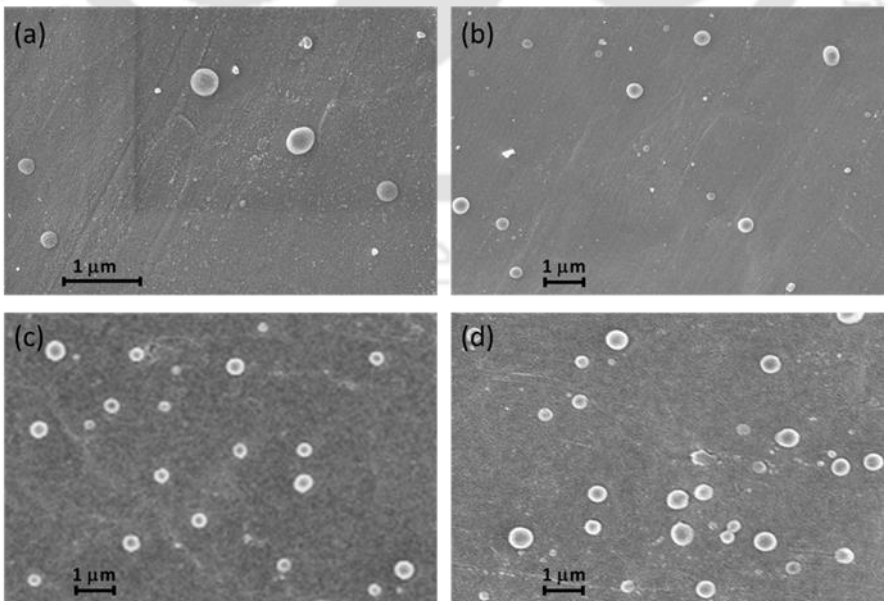

Figure 2.7: FESEM images of (a) **PP** (b) **PBA** (c) **PBT** and (d) **PBM** nanoparticles formed in 99% f_w by simple drop-casting technique.

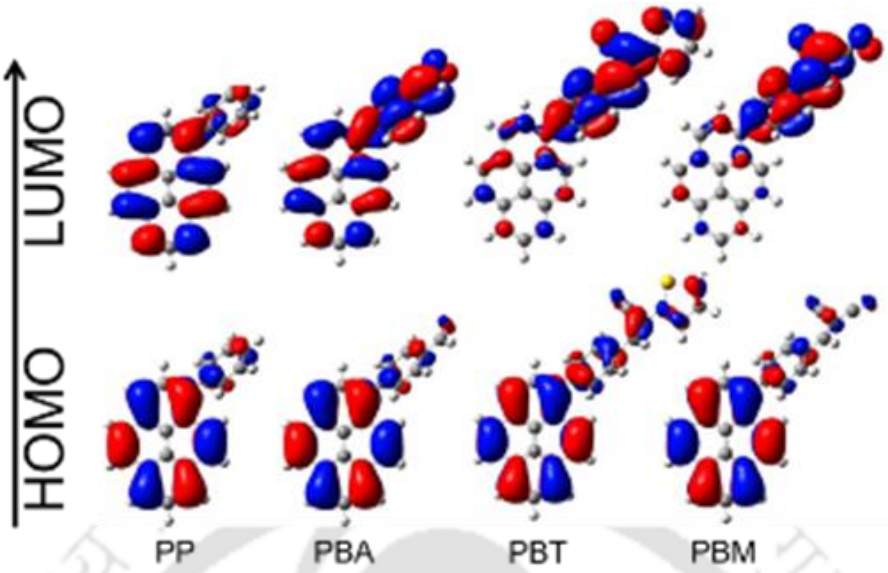

Figure 2.8: Theoretical calculation of electron cloud distribution of frontier molecular orbitals of **PP, PBA, PBT** and **PBM** by using B3LYP/6-31G (d,p) basis set (Gaussian 09 software)

Single crystals of **PBA** grown successfully in chloroform and methanol (9:1) solvent, was subjected to X-ray diffraction experiment to get the intermolecular interaction and arrangements. The **PBA** has non-planar conformation with higher torsional angle of 85.13° between pyrene core and phenyl aldehyde part (Figure 2.6a). The packing arrangement showed a head to head arrangement with π–π distance of 3.347 Å and C-H…O hydrogen bond distance of 2.521 and 2.526 Å. It is noteworthy that pyrene has the tendency to form dimers, which on introduction of rotor groups prevented the π-π stacking, as also confirmed by Single Crystal X-ray Diffractometer (SCXRD) of **PBA** (Figure 2.6 b,c). SCXRD measurement data of **PBA** is summarized in Table A2.1.

2.2.5 Studies of nanoparticles formation

Pyrene derivatives that were insoluble in water, readily formed NPs when introduced to aqueous medium and were confirmed by dynamic light scattering (DLS) experiments (Figure A2.2). In DLS experiment z-average of **PP**, **PBA**, **PBT** and **PBM** were found to be 295.2, 231.5, 256.1, 299.7 nm respectively. For obtaining the morphology of luminogen NPs, the FESEM images recorded for the luminogen NPs were found to be spherically shaped (Figure 2.7) with size distribution of 60-100 nm.

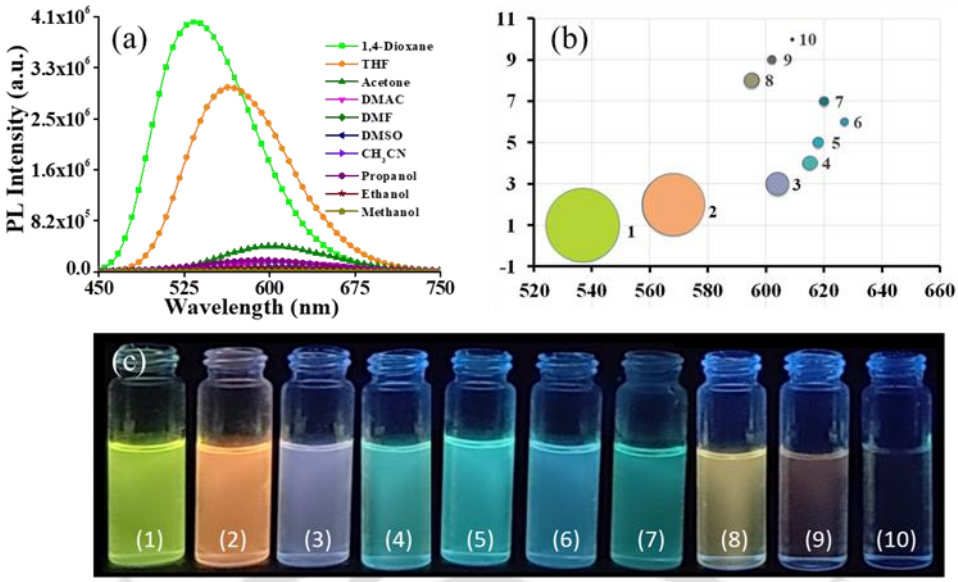

(1) 1-4 dioxane (2) THF (3) Acetone (4) DMAc (5) DMF (6) DMSO (7) Acetonitrile (8) Propanol (9) Ethanol (10) Methanol

Figure 2.9: Fluorescence spectra of **PBM** (10 μM) in (a) in various solvents (b) **PBM** emission in various solvents vs wavelength (spherical size is related to **PBM** emission intensity) (c) The picture of **PBM** in different solvents (increasing polarity) under 365 nm UV excitation.

2.2.6 Theoretical calculations

To understand the electronic distribution in pyrene derivatives, theoretical calculation was performed by the density functional theory (DFT) using B3LYP/6-311G (d,p) method by Gaussian 09 software program. The D-A system was theoretically reproduced with the help of DFT calculations showed narrowing the band gap after introducing electron withdrawing groups.[35] The highest occupied molecular orbital (HOMO) is found towards the pyrene molecule while lowest unoccupied molecular orbital (LUMO) was found towards the acceptor group except for **PP** molecule, where both the HOMO and LUMO orbitals were located on pyrene core, since this is not a D-A system. The presence of more electron withdrawing rotor group leads to more separation of HOMO and LUMO orbitals in these luminogens as seen from the electron clouds (Figure 2.8).

2.2.7 Solvent detection and discrimination

Fluorescence behavior of **PBM** was studied in various widely used organic solvents. **PBM** emission was very sensitive to its environment, displaying drastic fluorescence changes in the florescence behavior of **PBM** studied in various solvents with changes in presence of different solvents (Figure 2.9a-c) such as 1,4-dioxane, tetrahydrofuran, acetone, DMAc, DMF, DMSO, acetonitrile, propanol, ethanol and methanol, while easily discriminating alcohols with increasing % f_w (Figure 2.10) showed huge

fluorescence quenching responses in presence of 0.1 % f_w (Figure A2.3) in organic solvents. This was due to the enhancement in the non-radiative deactivation rate in more polar solvents, arising by twisted intramolecular charge transfer (TICT), attributed to solvatochromic and solvent effect.[36,37] These remarkable changes indicates the unique ability of **PBM** to be utilized for distinguishing a large number of solvents as well as verifying the presence of even very trace amounts of water in them.

2.2.8 Hydrazine Detection

Since **PBM** showed intense emission in solid as well as aqueous medium, its ability for the detection of hydrazine was pursued carefully. For this purpose, 10 µM of **PBM** was taken in aqueous medium and hydrazine was subsequently added, incubated for 10 minutes and the emission spectra were recorded. Additionally, competitive sensing was also performed by adding different amine analytes to observe florescence quenching only in the presence of hydrazine (Figure 2.11a,b). For instant detection and real-world applications, a portable device for the detection of hydrazine was fabricated by using Whatman filter paper. A 1 cm X 1 cm Whatman filter paper was dipped in **PBM** solution in THF and exposed to different concentrations of hydrazine to observe a distinct color change from bright orange to brown with a LOD achieved to be 44.76 nM (Figure A2.4

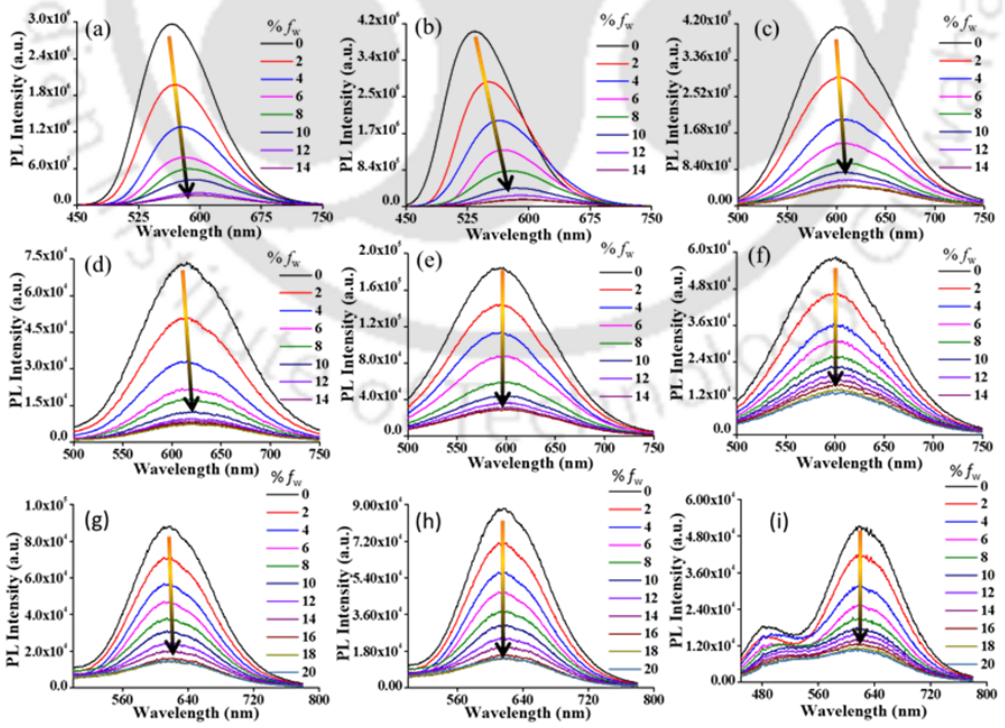

Figure 2.10: Fluorescence quenching response of **PBM** in presence of trace water (from 0% to 20% f_w) present in (a) THF (b) 1,4-dioxane (c) acetone (d) acetonitrile (e) propanol (f) ethanol (g) dimethylacetamide (h) dimethylformamide (i) dimethyl sulfoxide.

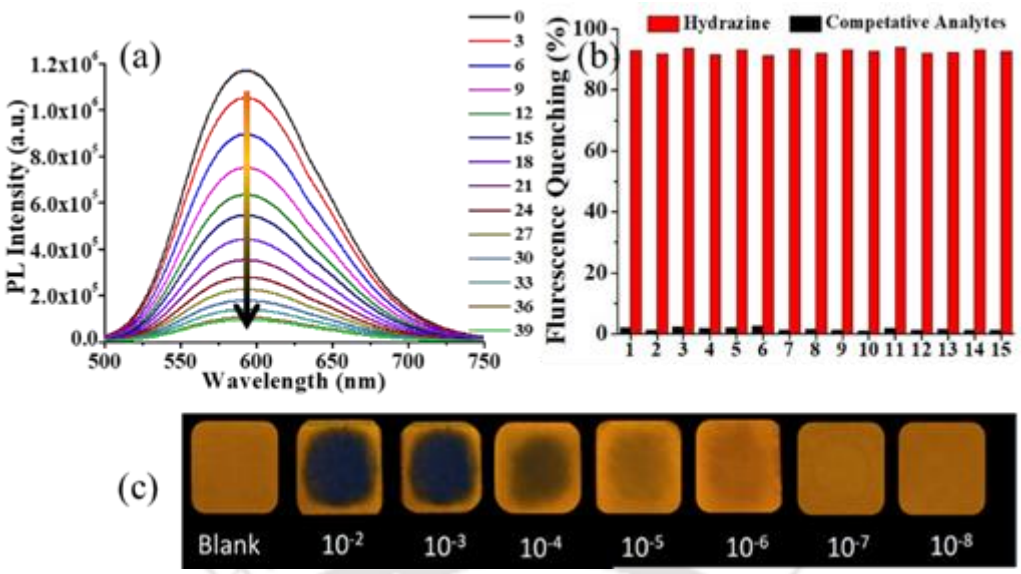

Figure 2.11: (a) Fluorescence quenching of **PBM** after addition of hydrazine in aqueous medium (b) selective sensing of hydrazine by **PBM** in presence of competitive analysts (c) on-spot whatman paper based sensing device after addition of different concentration of hydrazine solution (photographs taken under 365 nm UV lamp) (1. Thiourea 2. urea 3. cysteine 4. homocystein 5. leucine 6. glutathione 7. glycine 8. dimethylamine 9. diethylamine 10. triethylamine 11. tripropylamine 12. triphenyl amine 13. ethylenediamine 14. ammonium, hydroxide 15. hydroxylamine).

and Equation A2.1) in aqueous medium and 3.5 µM in Whatman paper based on-spot device (Figure 2.11c).The detection mechanism for hydrazine was studied by MALDI-TOF (Figure 2.12a,b**)** and ^{1}H NMR spectra (Figure 2.12c,d**)** that suggested **PBM** is involved in the formation of non-fluorescent hydrazine complex **PBM-NNH$_2$**.

2.2.9 Photodynamic therapy

Taking advantage of the intense emission of **PBM** in aqueous medium, it was used for cancer cell imaging and PDT therapy. **PBM** molecule was tracked inside the MCF-7 and MDAMB231 cells. CLSM results for MDAMB231 (triple negative breast cancer) cells (Figure 2.13a) and MCF-7 (breast cancer) (Figure 2.13b) confirm the permeation of **PBM** inside metastatic cells. More precisely, the fluorescence of the **PBM** as well as DAPI panel (for nucleus staining) denoted that most of the **PBM** were localized in the cytoplasm. To confirm the presence of **PBM** inside the cells, reddish green coloration of the **PBM** treated cells during Z-stacking analysis (Figure A2.5) confirmed that the **PBM** was internalized inside the cells. The cell viability results by MTT assay revealed interesting photochemical properties of the **PBM** molecules. MCF-7 and MDAMB231 were treated with increasing concentrations of **PBM** for 6 hours, followed by white light irradiation for 10 minutes. The results (Figure 2.13c,d) for MCF-7 and MDAMB231 cells showed significant increase in the anti-cell proliferative activity of the **PBM**

molecules after light irradiation. The **PBM** molecules alone were able to induce the cell death at low amounts with the IC50 concentration of 139.8± 1.4 µM and 166.2±13.4 µM for MCF7 and MDAMB231 cells, respectively. Remarkably, the IC50 of **PBM** molecules were found to be significantly reduced (83.5± 0.5 µM and 87.4± 2.5 µM for MCF-7 and MDAMB231 cells) when the cells were exposed to white light. The $^1O_2$ generation by pyrene derivatives was evaluated by 9,10-anthracenediyl-bis(methylene) dimalonic acid (ABDA) as an indicator.[38] As shown in the Figure 2.13e and Figure A2.6 the absorbance of ABDA in the presence of **PBM** decreased sharply, indicating the decomposition of ABDA by the generation of $^1O_2$ solely by **PBM** molecule.[39,40]

2.3 Conclusions

In this work, four pyrene derivatives with ACQ-to-AIE transformation design strategy comprising of different rotor group, have been developed using simple Suzuki coupling and Knoevenagel condensation synthetic procedures. The attached rotor groups

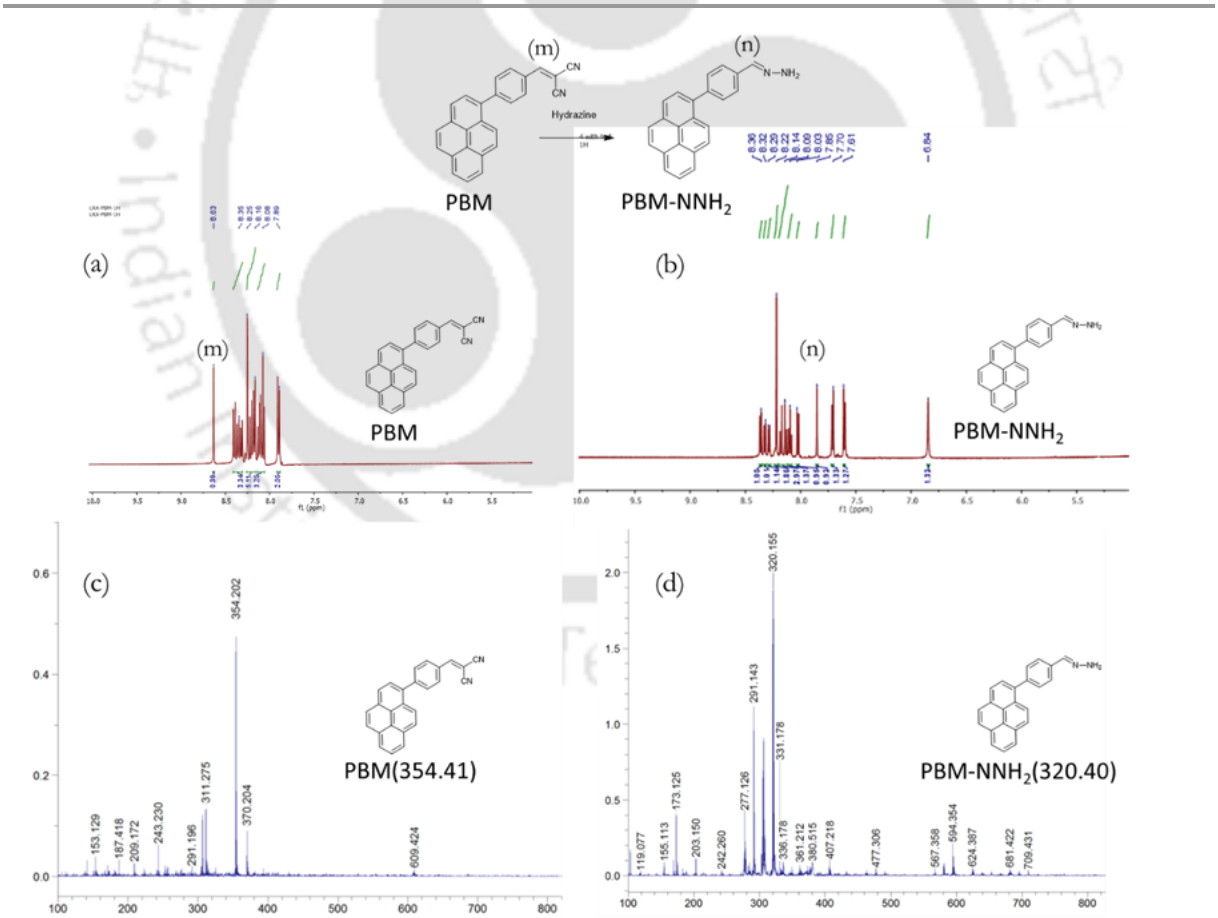

Figure 2.12: Detection mechanism of hydrazine by **PBM** (a) MALDI-TOF before hydrazine addition (b) MALDI-TOF after hydrazine addition (c) ^{1}H NMR spectra before hydrazine addition (c) ^{1}H NMR spectra after hydrazine addition.

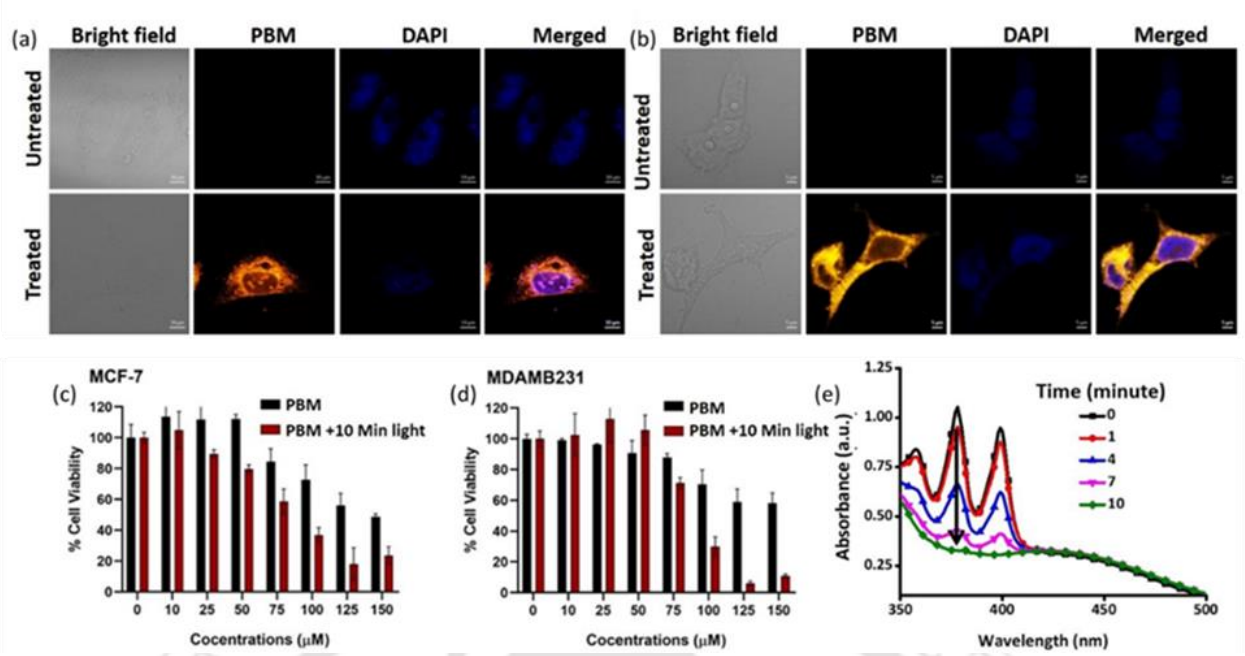

Figure 2.13: CLSM imaging of the MCF7 and MDAMB231 cells after **PBM** treatment and DAPI staining (a) MDAMB231 and (b) MCF7 cells. Antiproliferative activity of the **PBM** in (c) MCF7 and (d) MDAMB231 cells by MTT assay (e) UV-vis absorbance spectra of ABDA upon irradiation in the presence of **PBM.**

supported efficient RIM process and prevent notorious dimer formation in their aggregated-state, thereby enabling AIEE features in **PBA**, **PBT** as well as AIE phenomenon in **PBM. PP** showed ACQ characteristics owing to inadequate RIM process of the donor phenyl unit. Apart from the proficient design strategy of distinct donor group incited morphology and ACQ-to-AIE transformation phenomenon, the **PBM** showed strong solvatochromic effects, which was utilized to detect the trace water (0.1 % f_w) as well as identify and discriminate various organic solvents. This luminogen has been further employed for the highly selective detection of toxic hydrazine (LOD-44.71 nM). Besides, **PBM** luminogens generated elevated ROS, could be utilized for the photodynamic therapy in the killing of cancer cells, while its fluorescence could be useful in bioimaging. Thus, these multifunctional simple design strategy could be promising for the development of advanced materials for high-tech applications through the simply manipulation of the parent pyrene core.

2.4 Experimental section

2.4.1 Chemicals and reagents

Pyrene, N-bromosuccinimide, phenylboronic acid, 4-formylphenylboronic acid, 2-thiopheneacetonitrile, Tetrakis(triphenylphosphine)palladium(0), Malononitrile, Potassium tert-butoxide, Potassium carbonate were purchased from Sigma Aldrich.

Tetrahydrofuran (THF), 1,4-dioxane, methanol, ethanol and propanol etc. were bought from Zenith India. All mentioned chemicals were received commercially and used without any further purification.

2.4.2 Preparation of standard solutions

The standard solution of **PP**, **PBA**, **PBT** and **PBM** were prepared at a 1 mM concentration in DMSO solvent. All the photophysical experiments were performed by using HPLC grade solvents (DMSO, THF, 1,4-Dioxane etc.) and Milli-Q water. Photophysical property studies

2.4.3 General Synthesis Procedure

Synthesis procedure for **PP**, **PBA**, **PBT** and **PBM** are summurised in scheme 2.1.

The synthesis procedure of 1-phenylpyrene (**PP**)

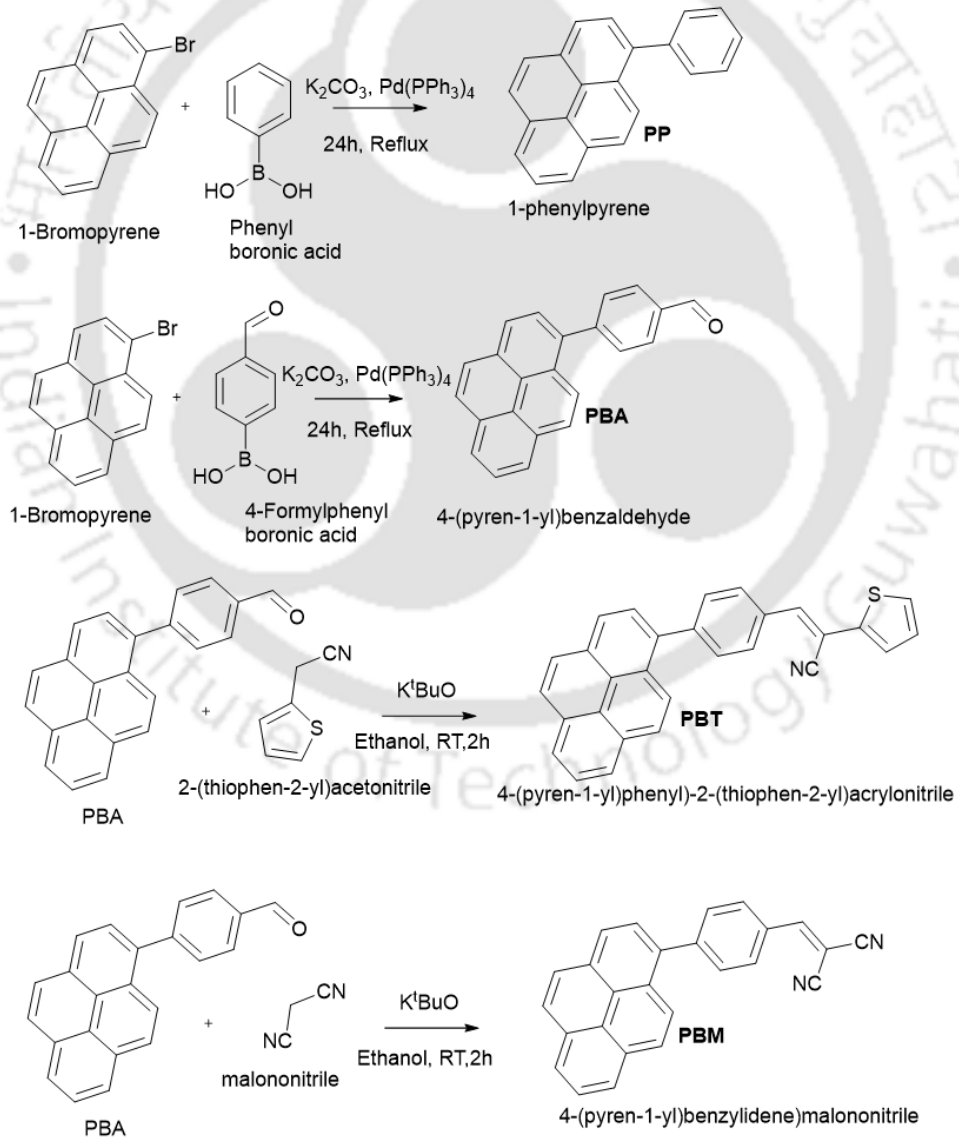

Scheme 2.1: Pyrene luminogens synthesis schemes, Suzuki coupling reaction was followed by Knoevenagel condensation reaction.

1-Bromopyrene (0.281 g, 1 mmol), Phenylboronic acid (0.122 g, 1 mmol), $Pd(PPh_3)_4$ (5 mg) and K_2CO_3 (2M aq. solution) in 5 mL dry THF was added and made it inert by argon. The mixture was refluxed at 80 °C for 24 h. The reaction mixture was quenched and it was extracted with chloroform and water. The organic solvent was dried over sodium sulfate it was removed by rotary evaporator. Pure product of **PP** was collected by silica gel column chromatography (hexane) to give white solid (0.216g, 76% yield).
^{1}H NMR ($CDCl_3$, 400 MHz) ppm: 8.20 (m, 4H), 8.11 (s, 2H), 8.02 (m, 3H), 7.64 (d, 2H), 7.57 (t, 2H), 7.50 (t, 1H)
^{13}C NMR ($CDCl_3$, 100 MHz) ppm: 141.38, 137.91, 131.65, 131.14, 130.74, 128.66, 128.52, 127.75, 127.60, 127.56, 127.39, 126.15, 125.44, 125.24, 125.12, 125.08, 124.97, 124.78.
MALDI TOF m/z calcd for ($C_{23}H_{14}O$): 278.354, Found: 278.340.

Synthesis of 4-(pyren-1-yl)benzaldehyde (PBA)

1-Bromopyrene (0.281 g, 1 mmol), 4-Formylphenylboronic acid (0.149 g, 1 mmol), $Pd(PPh_3)_4$ (5 mg) and K_2CO_3 (2M aq. solution) in 5 mL dry THF was added and made it inert by argon gas. The mixture was refluxed at 80°C for 24 h. The reaction mixture was quenched and it was extracted with chloroform and water. The organic solvent was dried over sodium sulfate it was removed by rotary evaporator. Pure product of **PBA** was collected by silica gel column chromatography (hexane:DCM = 7:3) to give white solid powder(0.205g, 72% yield).
^{1}H NMR ($CDCl_3$, 400 MHz) ppm: 10.17 (s, 1H), 8.24 (m, 3H), 8.07 (m, 7H), 7.97 (m, 1H), 7.81 (m, 2H).
^{13}C NMR ($CDCl_3$, 100 MHz) ppm: 192.14, 147.83, 136.16, 135.37, 131.57, 131.40, 131.33, 130.00, 129.92, 128.46, 128.19, 128.07, 127.46, 127.39, 126.35, 125.65, 125.31, 125.09, 124.96, 124.84, 124.70.
MALDI TOF m/z calcd for ($C_{23}H_{14}O$): 306.364, Found: 306.458.

Synthesis of 4-(pyren-1-yl)phenyl)-2-(thiophen-2-yl)acrylonitrile (PBT)

To a suspension of **PBA** (1 mmol) in absolute ethanol potassium butoxide (1 mmol) and 2-thiopheneacetonitrile (1 mmol) was added. The mixture was stirred for 2 hours under inert medium. Solid formed was filtered and workup was performed by using chloroform and water. The organic layer was separated and dried using sodium sulfate

and concentrated with rotary evaporator. Pure product of **PBT** was collected by silica gel chromatography to give yellow solid.

^{1}H NMR ($CDCl_3$, 400 MHz) ppm: 8.19 (m, 4H), 8.03 (M, 7H), 7.72 (m, 2H), 7.50 (m, 1H), 7.43 (m, 1H), 7.10 (m, 1H)

^{13}C NMR ($CDCl_3$, 100 MHz) ppm: 143.66, 143.30, 139.39, 139.27, 136.49, 132.39, 131.55, 131.29, 131.06, 131.02, 130.03, 129.53, 129.28, 128.48, 128.29, 127.97, 127.85, 127.47, 127.43, 126.42, 126.24, 125.45, 125.16, 125.09, 124.94, 124.84, 117.12, 106.14.

MALDI TOF m/z calcd for ($C_{23}H_{14}O$): 411.522, Found: 411.916.

Synthesis of 4-(pyren-1-yl)benzylidene)malononitrile (PBM)

To a suspension of **PBA** (1 mmol) in absolute ethanol potassium butoxide (1 mmol) and malononitrile (1 mmol) was added. The mixture was stirred for 2 hours under inert medium. Solid formed was filtered and workup was performed by using chloroform and water. The organic layer was separated and dried using sodium sulfate and concentrated with rotary evaporator. Pure product of **PBM** was collected by silica gel chromatography to give orange color solid.

^{1}H NMR (DMSO-d^6, 400 MHz) ppm: 8.63 (s, 1H), 8.35 (m,3H), 8.18 (m, 5H), 8.08 (m, 3H), 7.89 (d,2H).

^{13}C NMR ($CDCl_3$, 100 MHz) ppm: 159.45, 148.19, 131.89, 130.98, 128.49, 128.36, 127.45, 127.34, 126.49, 125.50, 124.96, 124.39, 114.03, 112.93.

MALDI TOF m/z calcd for ($C_{23}H_{14}O$): 354.115, Found: 354.689.

2.5 References

1. Lakowicz, J. R. Principles of Fluorescence Spectroscopy, *Springer Science & Business Media*, **2007**.
2. Miranda, A.; Gómez-Varela, A. I.; Stylianou, A.; Hirvonen, L.M.; Sánchez, H.; Beule, P. A. A. D. *Nanoscale*, **2021**,*13*, 2082-2099.
3. Adil, L. R.; Gopikrishna, P.; Iyer, P. K. *ACS Appl. Mater. Interfaces*, **2018**, *10*, 27260-27268.
4. Khan, F.; Urbonas, E.; Volyniuk, D.; Grazulevicius, J. V.; Mobin, S. M.; Misra, R. *J. Mater. Chem. C*, **2020**, *8*, 13375-13388.
5. Ma, W.; Iyer, P. K.; Gong, X.; Liu, B.; Moses, D.; Bazan, G. C.; Heeger, A. J. *Adv. Mater.*, **2005**, *17*, 274-277.

6. Khatun, M. N.; Tanwar, A. S.; Meher, N.; Iyer, P. K. *Chem. Asian J.*, **2019**, *14*, 4725-4731.
7. Gopikrishna, P.; Das, D.; Adil, L. R.; Iyer, P. K. *J. Phys. Chem. C*, **2017**, *121*, 18137-18143.
8. Xing, C.; Liu, J.; Chen, F.; Li, Y.; Lv, C.; Peng, Q.; Hou, H.; Li, K. *Chem. Commun.*, **2020**, *56*, 4220-4223.
9. Huang, Y.; Xing, J.; Gong, Q.; Chen, L.-C.; Liu, G.; Yao, C.; Wang, Z.; Zhang, H.-L.; Chen, Z.; Zhang, Q. *Nat Commun*, **2019**, *10*, 169-177.
10. Zhang, M.; Chen, J.; Wang, M.; Yuan, M.; Feng, R. Li, X.; He, Y.; Mao, X.; Li, Y.; Xiong, Z.; Xing, Z.; Hu, J.; Wu, G. *ACS Appl. Mater. Interfaces*, **2021**, *13*, 9036-9042.
11. Suman, G. R.; Pandey, M.; Chakravarthy, A. S. J. *Mater. Chem. Front.*, **2021**, *5*, 1541-1584.
12. Tang, Y.; Zhang, D.; Zhang, Y.; Liu, Y.; Cai, L.; Plaster, E.; Zheng, J. *J. Mater. Chem. B*, **2022**, DOI: 10.1039/D1TB01942B.
13. Zhang, Z.; Liu, X.; Feng, Y. Yu, Z.-Q.; Wang, L.; Ren, X.-K.; Liu, Y. *J. Mater. Chem. C*, **2021**, *9*, 975-981.
14. Yan, S.; Gao, Z.; Yan, H.; Niu, F.; Zhang, Z. *J. Mater. Chem. C*, **2020**, *8*, 14587-14594.
15. Luo, J.; Xie, Z.; Lam, J. W. Y.; Cheng, L.; Chen, H.; Qiu, C.; Kwok, H. S.; Zhan, X.; Liu, Y.; Zhu, D.; Tang, B. Z. *Chem. Commun.*, **2001**, 1740-1741.
16. Adil, L. R.; Iyer, P. K. *Chem. Commun.*, **2020**, *56*, 7633-7636.
17. Feng, X.; Xu, Z.; Hu, Z.; Qi, C.; Luo, D.; Zhao, X.; Mu, Z.; Redshaw, C.; Lam, J. W. Y.; Ma, D.; Tang, B. Z. *J. Mater. Chem. C*, **2019**, *7*, 2283-2290.
18. Kenry; Tang, B. Z.; Liu, B.; *Chem*, **2020**, *6*, 1195-1198.
19. Gu, X.; Zhang, D. *Chem*, **2020**, *6*, 1199-1200.
20. Yu, W.; Zhang, H.; Yin, P.-A.; Zhou, F.; Wang, Z.; Wu, W.; Peng, Q.; Jiang, H.; Tang, B. Z. *iScience*, **2020**, *23*, 101587-101624.
21. Li, H.; Zhang, M.; Wang, D.; Dong, G.; Chen, Z.; Li, S.; Sun, X.; Zeng, M.; Liao, H.; Chen, H.; Xiao, S. Li, X. *Biomed Res Int*, **2021**, 3236892-3236892.
22. Touitou, Y.; Point, S. *Environmental Research*, **2020**, *190*, 109942-109956.
23. Ouyang, X.; Yang, J. Hong, Z.; Wu, Y.; Xie, Y.; Wang, G. *Biomedicine & Pharmacotherapy*, **2020**, *130*, 110577-110584.

24. Noell, W. K.; Walker, V. S.; Kang, B. S.; Berman, S. *Investig. Ophthalmol.* **1966**, *5*, 450-473.
25. Ham, W. T.; Mueller, H. A.; Sliney, D. H. *Nature*, **1976**, *260*, 153-155.
26. Zhao, Q.; Sun, J. Z. *J. Mater. Chem. C*, **2016**, *4*, 10588-10609.
27. Yoo, H.; Kim, H. S. *J. Mater. Chem. C*, **2019**, *7*, 7336-7343.
28. Teng, M.; Zhou, Z.; Qin, Y.; Zhao, Y.; Zhao, C.; Cao, J. *Sens Actuators B*, **2020**, *311*, 127914-127920.
29. Cao, Y.; Zhang, L.; Yang, J.; Zhang, J.; Si, W.; Wang, J. Iqbal, A.; Qin, W.; Liu, Y. *Sens Actuators B*, **2021**, *346*, 130472-130478.
30. Zanotti, K. J.; Silva, G. L.; Creeger, Y.; Robertson, K. L.; Waggoner, A. S.; Berget, P. B.; Armitage, B. A. *Org. Biomol. Chem.*, **2011**, *9*, 1012-1020.
31. Meher, N.; Panda, S.; Kumar, S.; Iyer, P. K. *Chem. Sci.*, **2018**, *9*, 3978-3985.
32. Hong, G.; Diao, S.; Chang, J.; Antaris, A. L.; Chen, C.; Zhang, B.; Zhao, S.; Atochin, D. N.; Huang, P. L.; Andreasson, K. I.; Kuo, C. J.; Dai, H. *Nature Photon*, **2014**, *8*, 723-730.
33. Y. Feng, C. Coradi Tonon, S. Ashraf and T. Hasan, *Advanced Drug Delivery Reviews*, 2021, **177**, 113941-113952.
34. Hu, J.-J.; Lei, Q.; Zhang, X.-Z. *Progress in Materials Science*, **2020**, *114*, 100685-100722.
35. Frisch, M. J.; Trucks, G. W.; Schlegel, H. B.; Scuseria, G. E.; Robb, M. A.; Cheeseman, J. R.; Scalmani, G.; Barone, V.; Mennucci, B.; Petersson, G. A.; Nakatsuji, H.; Caricato, M.; Li, X.; Hratchian, H. P.; Izmaylov, A. F.; Bloino, J.; Zheng, G.; Lonnenberg, J.; Hada, M.; Ehara, M.; Toyota, K.; Fukuda, R.; Hasegawa, J.; Ishida, M.; Nakajima, T.; Honda, Y.; Kitao, O.; Nakai, H.; Vreven, T.; Montgomery, J. A.; Peralta, J. E.; Ogliaro, F.; Bearpark, M.; Heyd, J. J.; Brothers, E.; Kudin, K. N.; Staroverov, V. N.; Keith, T.; Kobayashi, R.; Normand, J.; Raghavachari, K.; Rendell, A.; Burant, J. C.; Iyengar, S. S.; Tomasi, J.; Cossi, M.; Rega, N.; Millam, J. M.; Klene, M.; Knox, J. E.; Cross, J. B.; Bakken, V.; Adamo, C.; Jaramillo, J.; Gomperts, R.; Stratmann, R. E.; Yazyev, O.; Austin, A. J.; Cammi, R.; Pomelli, C.; Ochterski, J. W.; Martin, R. L.; Morokuma, K.; Zakrzewski, V. G.; Voth, G. A.; Salvador, P.; Dannenberg, J. J.; Dapprich, S.; Daniels, A. D.; Farkas, O.; Foresman, J. B.; Ortiz, J. V.; Cioslowski, J.; Fox, J. *Gaussian, Inc., Wallingford CT*, **2013**.

36. Wang, C.; Qiao, Q.; Chi, W.; Chen, J.; Liu, W.; Tan, D.; McKechnie, S.; Lyu, D.; Jiang, X.-F.; Zhou, W. Xu, N.; Zhang, Q.; Xu, Z.; Liu, X. *Angew. Chem. Int. Ed.*, **2020**, *59*, 10160-10172.
37. Liu, S.; Zhou, X.; Zhang, H.; Ou, H.; Lam, J. W. Y.; Liu, Y.; Shi, L.; Ding, D.; Tang, B. Z. *J. Am. Chem. Soc.*, **2019**, *141*, 5359-5368.
38. Yuan, Y.; Zhang, C.-J.; Kwok, R. T. K.; Xu, S.; Zhang, R.; Wu, J.; Tang, B. Z.; Liu, B. *Adv. Funct.Mater.*, **2015**, *25*, 6586-6595.
39. Wu, W.; Mao, D.; Cai, X.; Duan, Y.; Hu, F.; Kong, D.; Liu, B. *Chem. Mater.*, **2018**, *30*, 3867-3873.
40. Wang, X.; Song, Y.; Pan, G.; Han, W.; Wang, B.; Cui, L.; Ma, H.; An, Z.; Xie, Z.; Xu, B.; Tian, W. *Chem. Sci.*, **2020**, *11*, 10921-10927.

Appendix

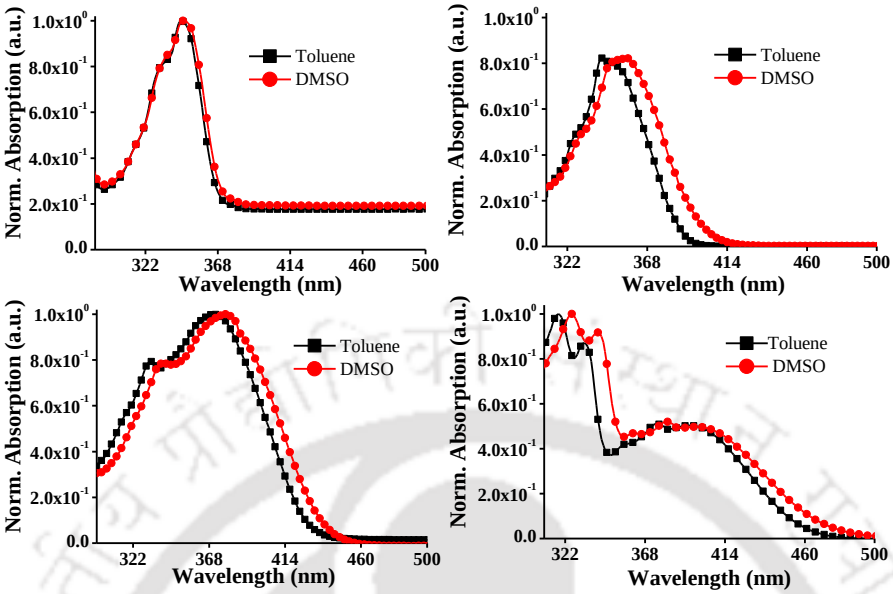

Figure A2.1: UV-vis. spectra of (a) **PP** (b) **PBA** (c) **PBT** and (d) **PBM** in different polar solvents, all spectra were taken at room temperature.

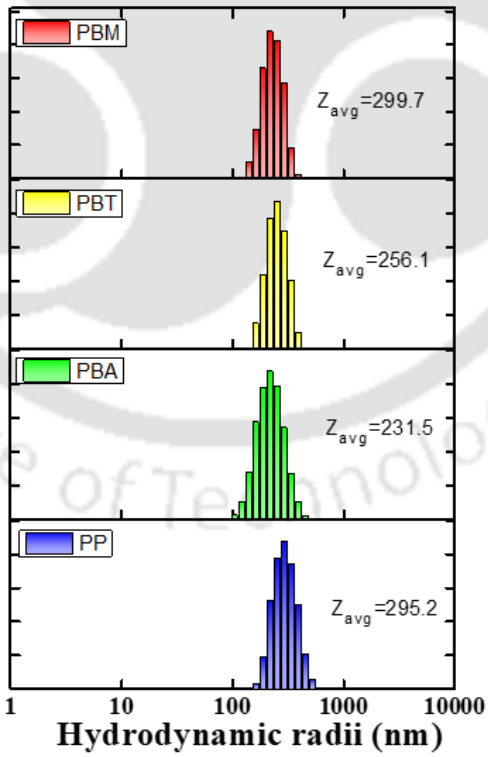

Figure A2.2: Study of nanoparticle (NP) formation of **PP**, **PBA**, **PBT** and **PBM** by DLS spectroscopy 99 % f_w (10 µM solution).

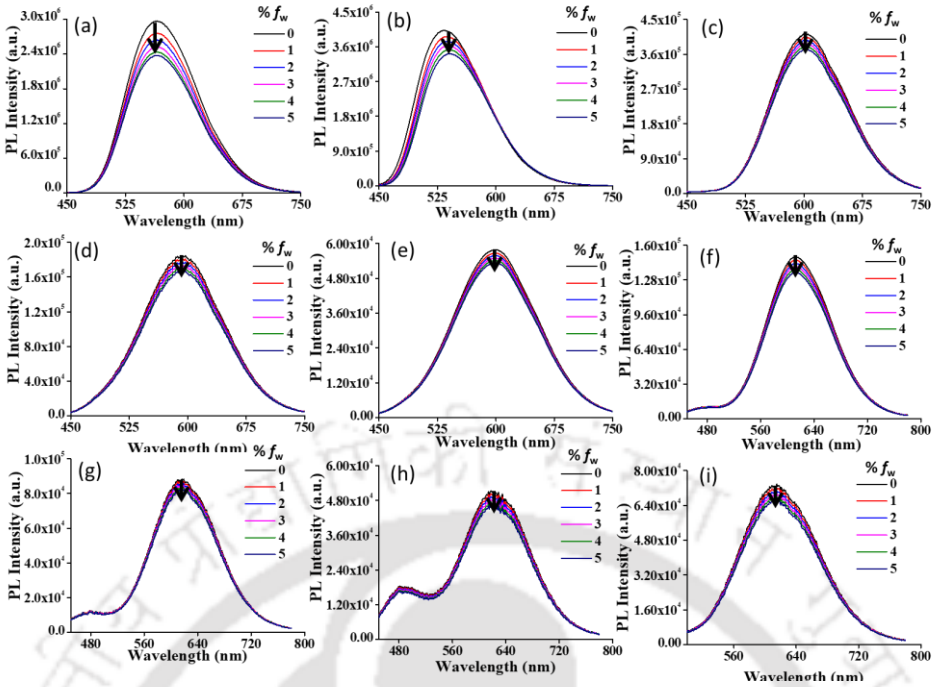

Figure A2.3: Fluorescence limit of detection for trace water by **PBM** (a) THF (b) 1,4 Dioxane (c) acetone (d) acetonitrile (e) propanol (f) ethanol (g) dimethylacetamide (h) dimethyl sulfoxide (i) dimethylformamide.

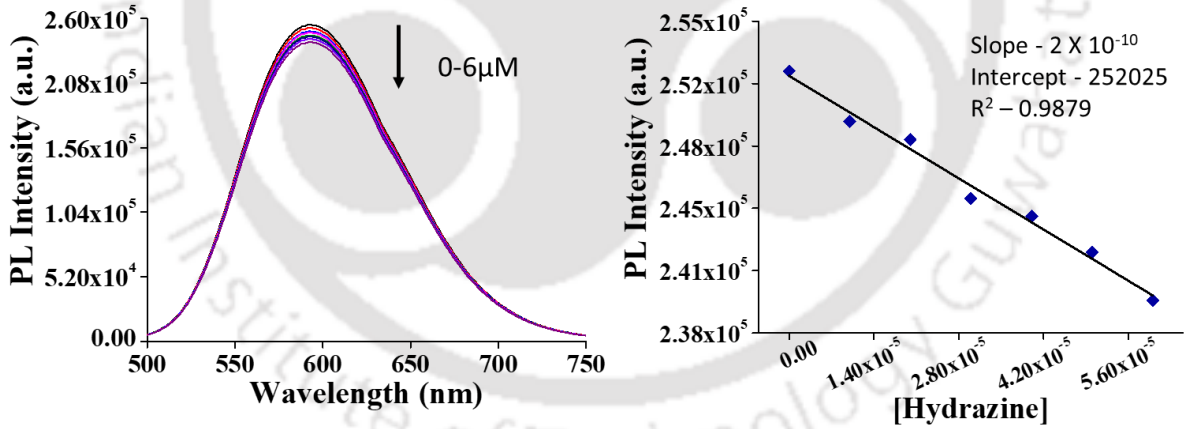

Figure A2.4: Change of fluorescence intensity of **PBM** in lower concentration of Hydrazine (µM) in 99% f_w.

Equation A2.1 LOD = 3 × S.D. / k

LOD for Hydrazine = $3 \times 1192.30 / 2 \times 10^{10}$

$= 44.71 \times 10^{-9}$ M

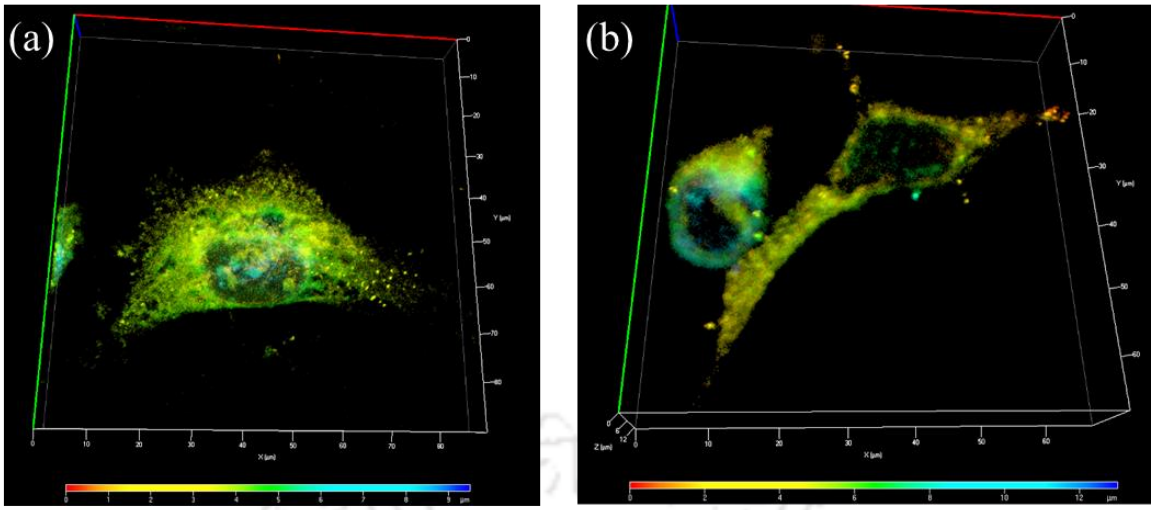

Figure A2.5: Z-stacking analysis of the (a) MDAMB231 and (b) MCF-7, confirming the internalization and localization of the **PBM** in the cytoplasm. (Scale bar: 10 µm).

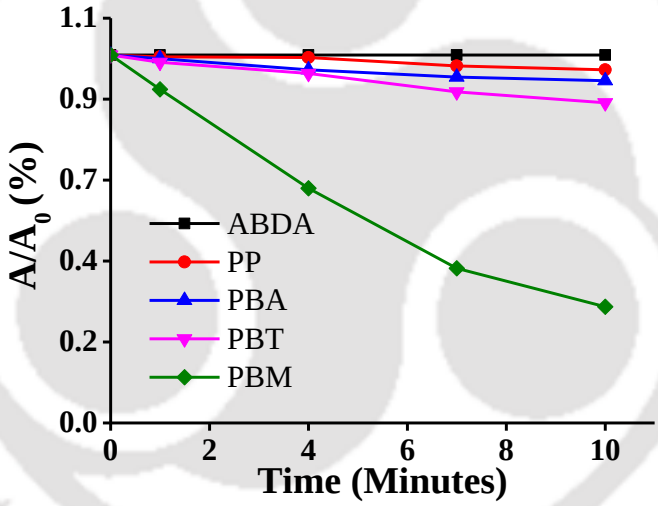

Figure A2.6: Normalized degradation percentages of ABDA in the presence of **PP**, **PBA**, **PBT** and **PBM** in aqueous media upon white light irradiation (350−500 nm, (Pyrene derivatives = 5 µM; [ABDA] = 20 µM.

Table A2.1: Single crystal X-ray diffraction data of **PBA**.

S No.	**Compound**	**PBA**
1	Empirical formula	$C_{23}H_{14}O$

2	CCDC NO	1938844
3	Formula weight	306.36
4	Temperature/K	296 K
5	Crystal system	triclinic
6	Space group	P -1
7	a/Å	9.970
8	b/Å	11.910
9	c/Å	13.394
10	α/°	90.003
11	β/°	101.077
12	γ/°	90.102
13	Volume/$Å^3$	1560.9
14	Z	4
15	ρ**calc**mg/mm^3	1.467
16	m/mm^{-1}	3.088
17	F(000)	2400.0
18	Crystal size/mm^3	0.28 × 0.23 × 0.17
19	2Θ range for data collection	1.34 to 47.78°
20	Index ranges	$-11 \leq h \leq 11$, $-14 \leq k \leq 14$, $-15 \leq l \leq 15$
21	Reflections collected	51077
22	Independent reflections	5489 [R(int) = 0.0239]
23	Data/restraints/parameters	5489/0/433
24	Goodness-of-fit on F2	1.259
25	Final R indexes [I>=2σ(I)]	R1 = 0.0794, wR2 = 0.2087
26	Final R indexes [all data]	R1 = 0.1201, wR2 = 0.2591

Table A2.2: Comparison table for detection of solvent and trace water present in organic solvents by **PBM**

S. N.	Material Used	Trace Water detection	Detection Range	Solvent Detection/ Discrimination	Publication
1	Indole-boron trifluoride complex	1 solvent (0.25%)	2-40%	No	*Dalton Trans.*, 2019,**48**, 2086-2092
2	Cyanostilbene derivatives	2 solvents (.02%)	0-20%	No	*New J. Chem.*, 2017,**41**, 8644-8649
3	Coumarin based	2 solvents (0.011%)	0-20%	No	*Anal. Methods*, 2019,**11**, 3079-3084
4	Benzothiophene based	3 solvents (0.02%)	0-20%	No	*Dyes and Pigments* 2020, **177**, 108300-108309
5	Triphenylimidazole-based	4 solvents (2%)	0-95%	No	*Chem. Commun.*, 2020,**56**, 10702-10705
6	Quinizarin based	4 solvents (~0.001%)	0-2.5%	No	*Analyst*, 2019,**144**, 594-601
7	Copper complex based	4 solvents (0.003-0.448%)	0-3.16%	No	*Anal. Chem.* 2016, **88**, 11314-11318
8	1,4-diketo-3,6-diphenylpyrrolo[3,4-c]pyrrole (DPP)	4 solvents (0.0027-0.0153%)	0-30%	No	*Sensors and Actuators B*, 2017, **245**, 845-852
9	4-amino-1,8-naphthalimide Tröger's base	No	No	Yes	*Chem. Commun.*, 2019,**55**, 12140-12143
10	***Pyrene based AIEgen***	***9 solvents (0.1%)***	***0-20%***	***Yes***	***Present Work***

Table A2.3: Comparison table for detection of solvent and trace water present in organic solvents by **PBM**

S. N.	Material Used	Hydrazine Detection Limit	Detection medium	Publication

1	Hemicyanine based probe	0.17 μM	HEPES buffer-DMSO (8/2, v/v)	*Anal. Chem.* 2015, **87**, 9101-9107
2	ESIPT-based fluorescent	0.147 μM	PBS buffer-ethanol (99/1, v/v)	*Org. Biomol. Chem.*, **2015**, 13, 5344-5348
3	Phthalimide based probe	0.1 μM	H_2O/DMSO (v/v, 3:7)	*Anal. Chem.* 2014, **86**, 4611-4617
4	Benzo[*d*] oxazole	84 nM	CH_3CN–HEPES buffer (1/2, v/v)	*RSC Adv.*, 2014, **4**,41807-41811
5	Naphthalimide moiety	100 nM	CH_3CN	*Chem. Sci.*, 2013, **4**, 4121-4126
6	Benzothiazole based probe	66 nM	CH_3CN:H_2O (2/3, v/v)	*Org. Lett.*, 2013, **15**, 5412-5415
7	Carbazole based probe	1.02 μM	CH_3CN:H_2O (8 : 2, v/v)	*RSC Adv.*, 2013, **3**, 18872-18877
8	Coumarin dye	2.46 μM	DMSO–Acetate buffer (7/3, v/v)	*Org. Lett.*, 2011, **13**, 5260-5263
9	**Pyrene based AIE probe**	**44.76 nM**	**99% aqueous medium**	***Present Work***

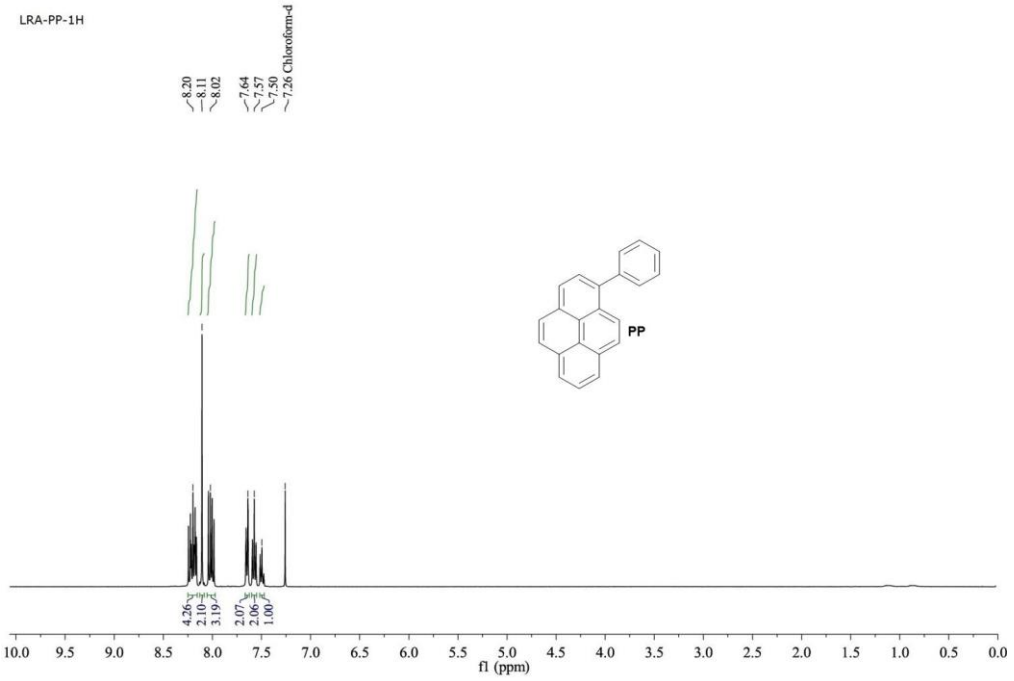

^{1}H NMR spectra of **PP** in $CDCl_3$ solvent.

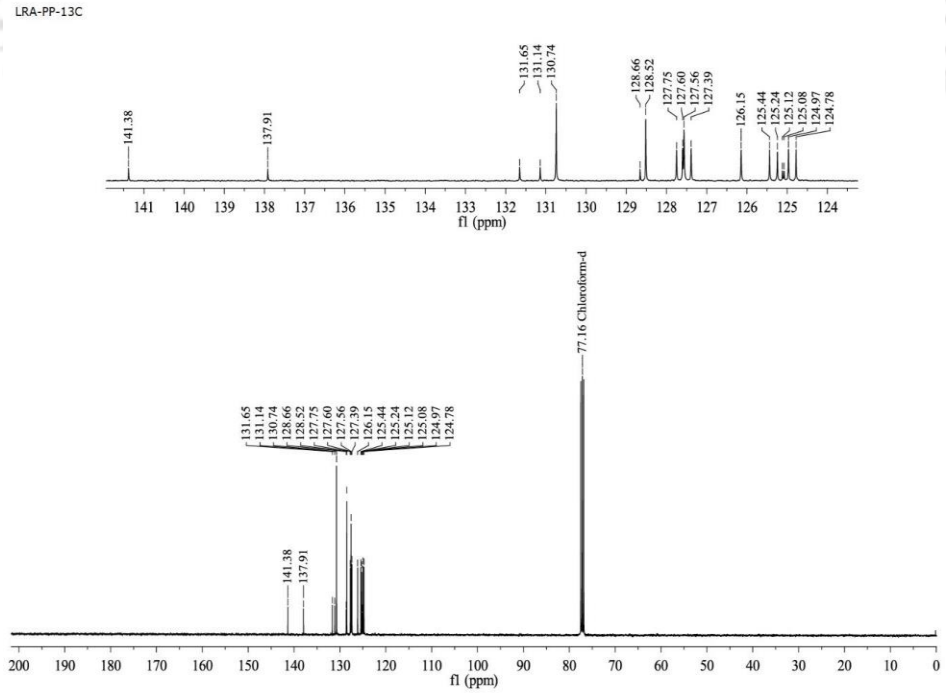

^{13}C NMR spectra of **PP** in $CDCl_3$ solvent.

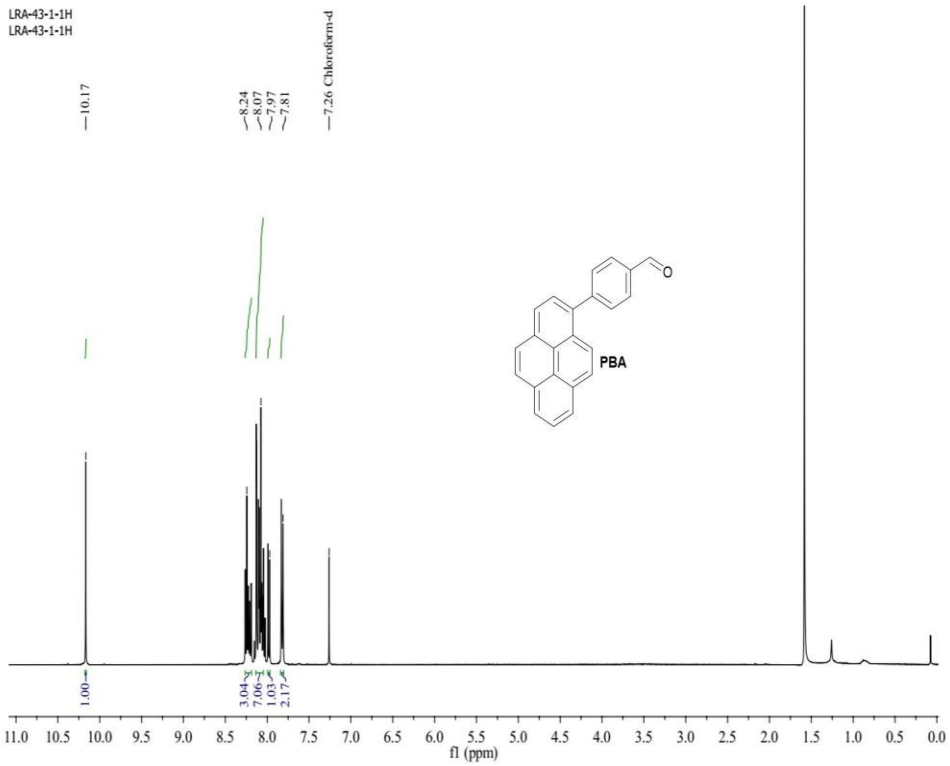

^{1}H NMR spectra of **PBA** in $CDCl_3$ solvent.

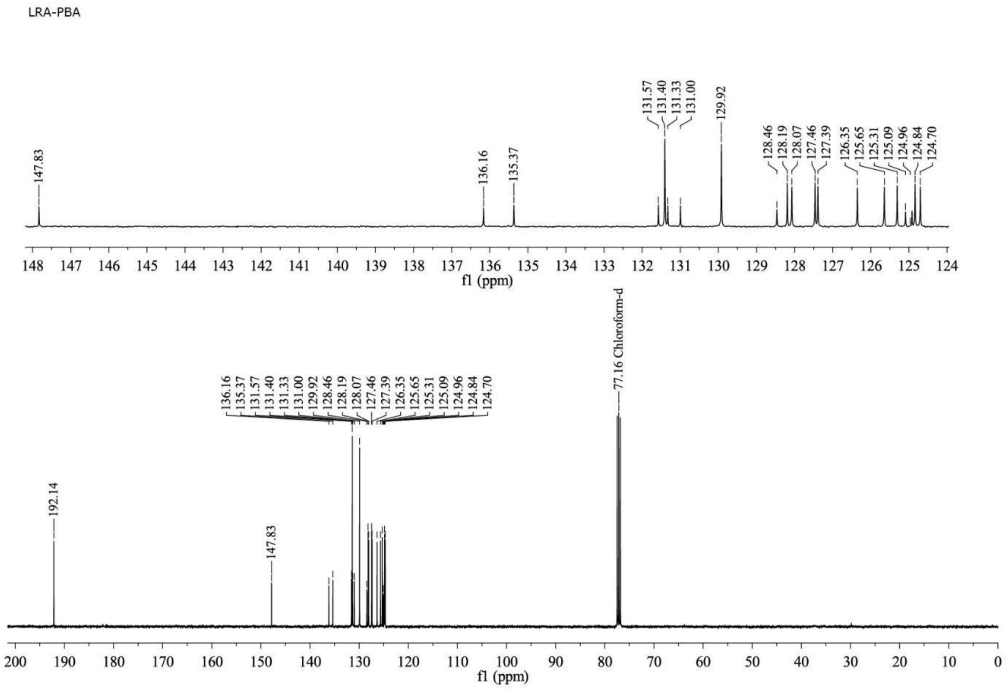

^{13}C NMR spectra of **PBA** in $CDCl_3$ solvent.

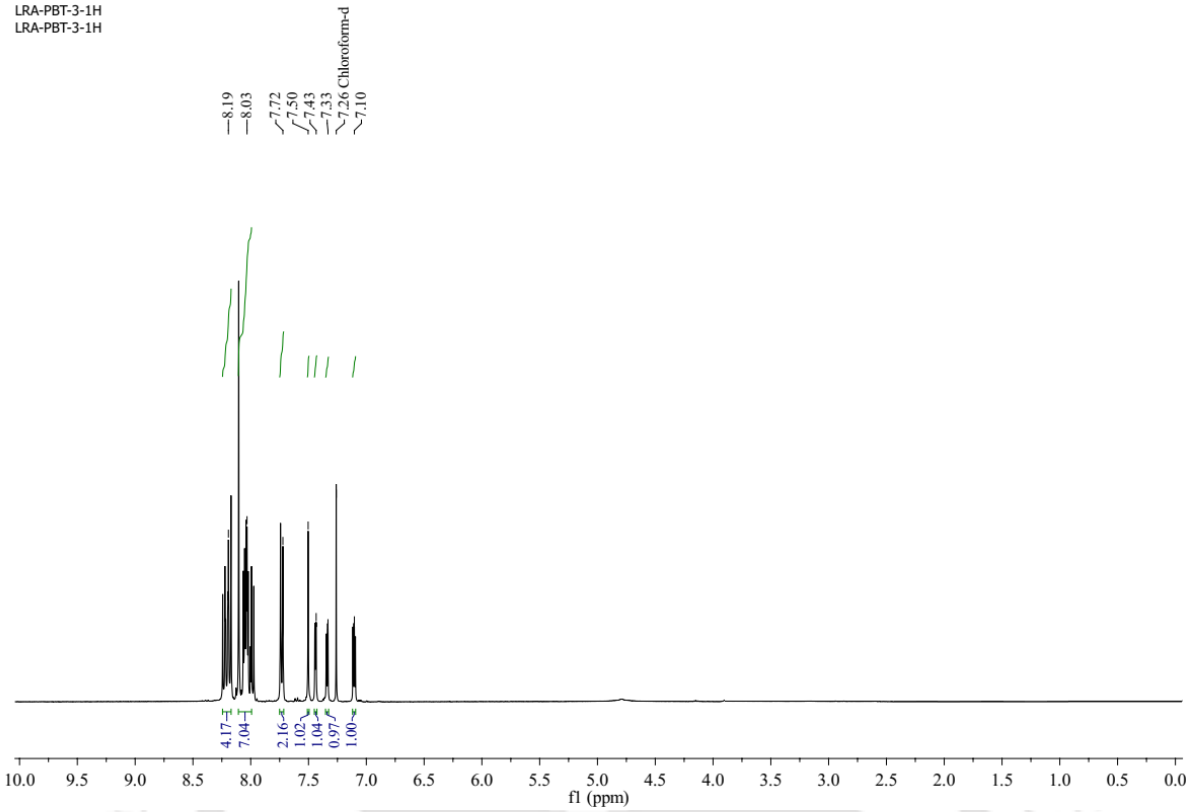

^{13}C NMR spectra of **PBT** in $CDCl_3$ solvent.

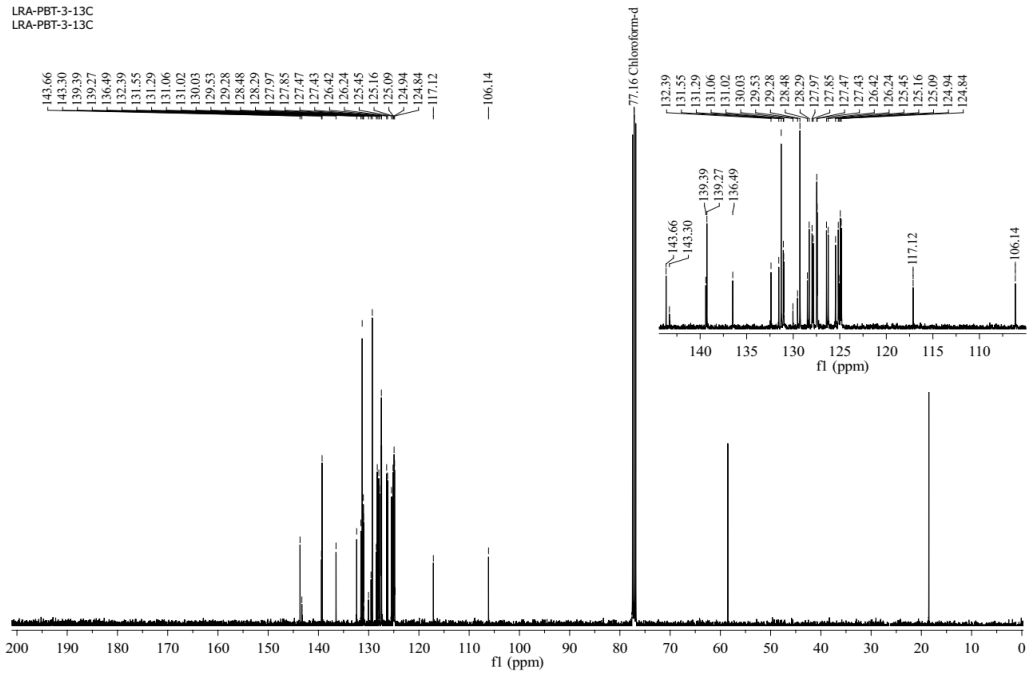

^{13}C NMR spectra of **PBT** in $CDCl_3$ solvent.

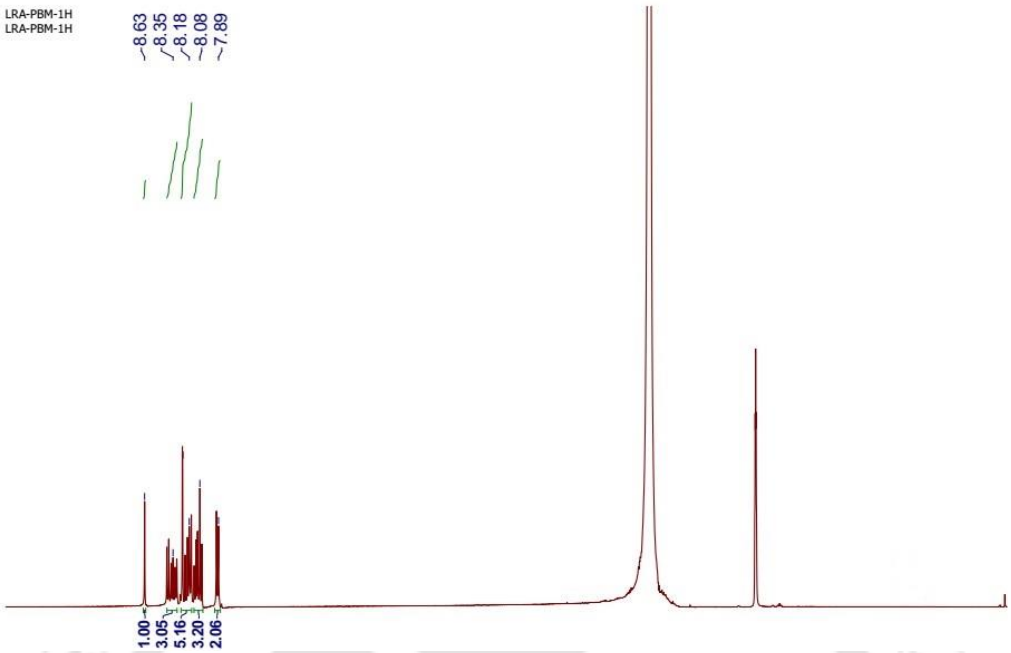

^{1}H NMR spectra of **PBM** in $CDCl_3$ solvent.

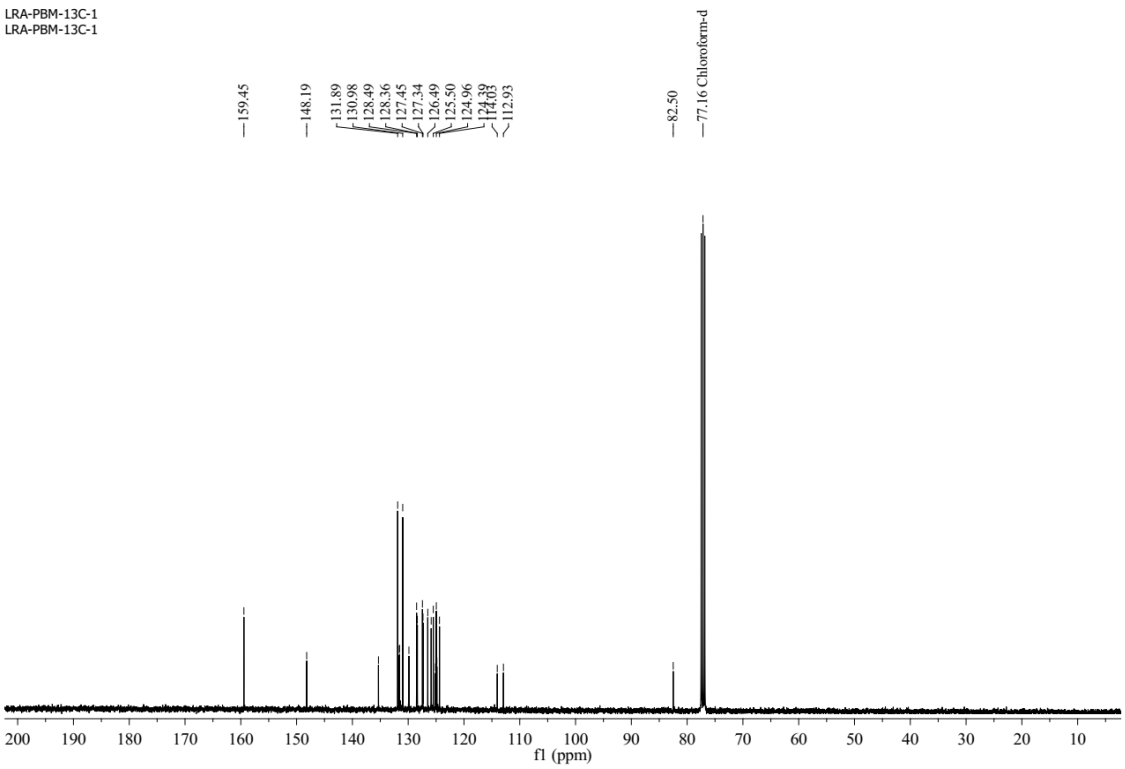

^{13}C NMR spectra of **PBM** in $CDCl_3$ solvent.

MALDI TOF spectra of pyrene derivatives

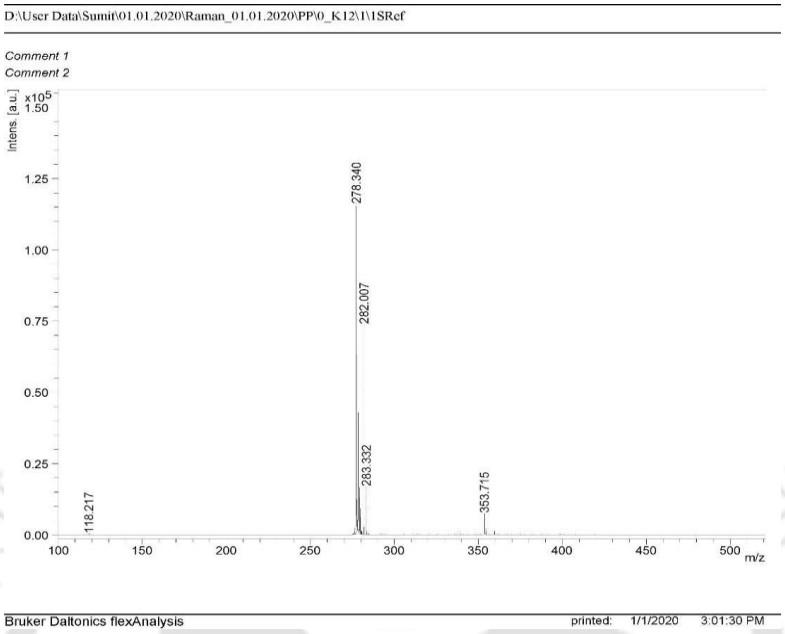

MALDI-TOF spectra of **PP**.

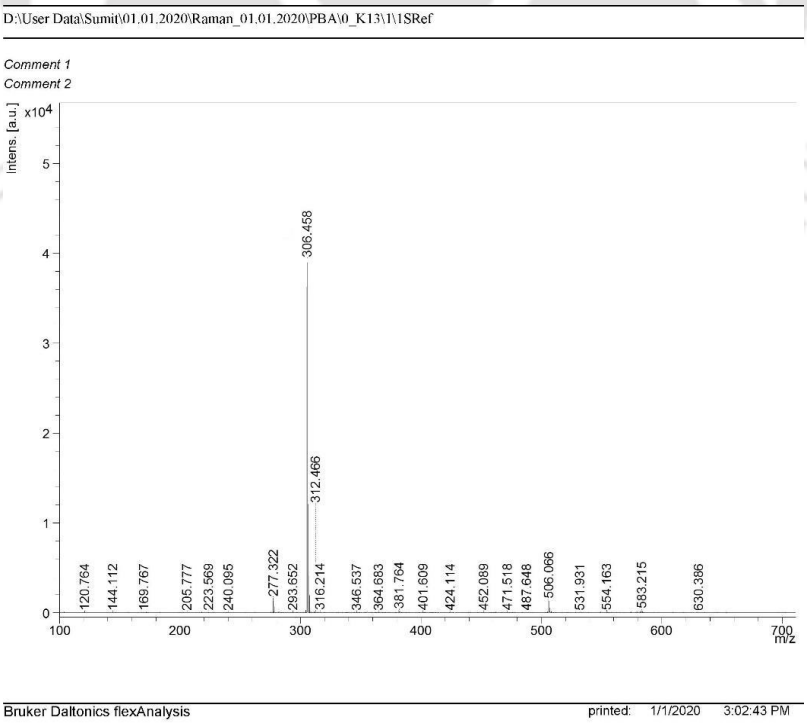

MALDI-TOF spectra of **PBA**.

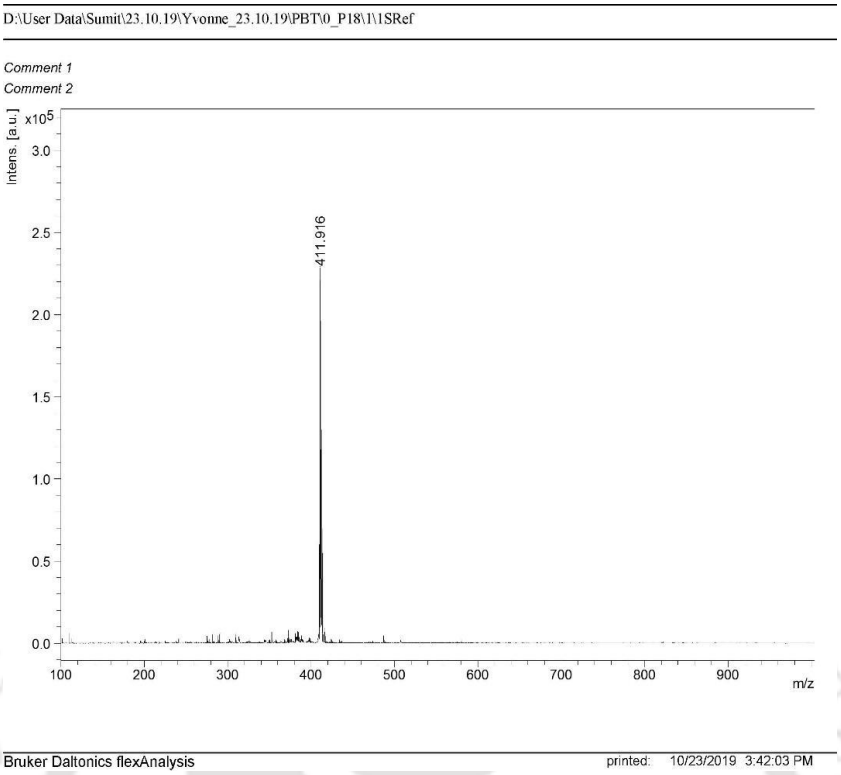

MALDI-TOF spectra of **PBT**.

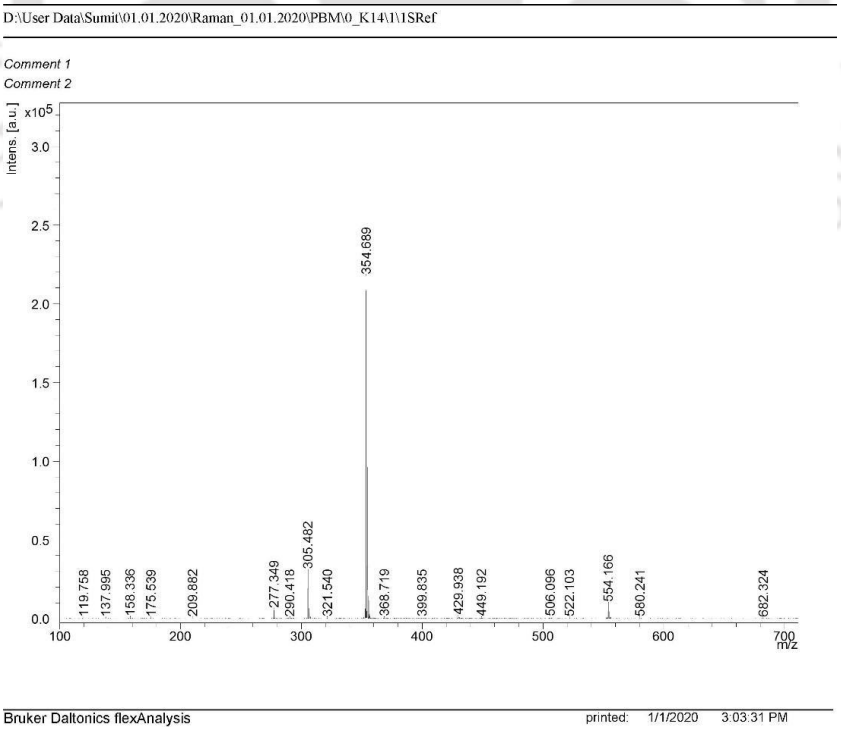

MALDI-TOF spectra of **PBM**.

CHAPTER 3

Receptor-Free Detection of Picric Acid: A New Structural Approach for Designing Aggregation-Induced Emission Probes

Adil, **L. R.;** Gopikrishna P.; Iyer, P. K. *ACS Appl. Mater. Interfaces*, 2018, **10**, 27260-27268

Abstract

A pristine aggregation-induced enhanced emission (AIEE) active monomer 2,5-bis((E)-4-bromostyryl)-3,4-diphenylthiophene (**TPBZ**) and its copolymer (**PFTPBZ**) with 9,9-dioctylfluorene-2,7-diboronic acid bis(1,3-propandiol) ester have been synthesized via Suzuki coupling polymerization. **PFTPBZ** that is devoid of any receptor showed AIEE property and demonstrated excellent and selective fluorometric recognition of TNT in aggregated state (aqueous medium) and PA in aggregated state and solution state (organic solvent) as well as in vapor phase via **PFTPBZ** dip-coated Whatman filter paper on a solid-phase platform in 1.86 ng level (naked eye). Limit of detection (LOD) for TNT in 95% water fraction (f_w) was 53.74 × 10^{-6} M, and at 40% f_w, it was 14.26 × 10^{-7} M PA detection in tetrahydrofuran solution was possible with a LOD of 28.16 × 10^{-7} M, 95% f_w with LOD of 10.47 × 10^{-6} M, and in 40% f_w with LOD of 47.39 × 10^{-8} M. As a unique example of structural design, the probe **PFTPBZ** surprisingly possesses no receptor, yet remarkably high selectivity was achieved via Förster resonance energy transfer (FRET) and photoinduced electron transfer from the copolymer **PFTPBZ** to PA and TNT. Detection of PA in the presence of various metal analytes and inorganic acids and in real water samples (lakes, rivers, and sea water) was also demonstrated using this concept of receptor-free conjugated polymer probe.

3.1 Introduction

Reliable, selective, rapid, and efficient detection of discharged nitro explosives from domestic establishments, transportation areas, and land mines are pressing concerns seeking increasing societal attention. Recently, rise in global terrorism is very crucial to homeland security and a high priority for counter terrorism applications and environment cleaning.[1-4] A variety of nitro aromatic compounds have been used as chemical explosives among which picric acid (PA), a fatal explosive, was used during world war extensively.[5,6] In small scale, PA is used as an antiseptic, treatment of burns, malaria, and small pox.[7] It is also used in leather, matches, dye, and fireworks industries as a result of which PA is released in unconfirmed amounts into environment. PA being highly soluble in water harms the soil and environment assets more than any other nitro explosives.[8-11] PA is highly toxic in nature, and according to material safety data sheet, it causes severe respiratory problems such as liver damage, anaemia, cancer, and strong skin, eye irritation, and so forth.[12-14] PA has greater explosive power than 2,4-dinitrotoluene (DNT) and 2,4,6-trinitrotoluene (TNT); thus, the violent and lethal nature of PA has drawn enormous attention for its sensitive detection to prevent damage of life and property because of its extensive misuse.[15-17] To detect PA, numerous methods such as liquid chromatography-mass spectrometry (LC-MS), gas chromatography-MS, solid-phase microextraction-LC, high-performance-LC proton transfer reaction-MS, surface-enhanced Raman spectroscopy, and ion mobility spectrometry have been developed.[18-23] However, these methods rely mainly on sophisticated and expensive instruments and usually are time consuming. Although the above-mentioned methods offer some advantages, abundant scope of improvement exists because of the vulnerability to false positive result interference from environmental contaminants and lack of portability in them. In addition, these instruments need costly maintenance and calibrations and therefore are not economical, thereby restricting their prevalent applications. Thus, reliable approaches are obligatory to detect explosives which must be robust, reasonably priced, easy to operate, and require least servicing.[24-26] Among various known detection methods, fluorometric and colorimetric detection have appealed conspicuous attention because of their sensitivity and ease in operation.[27, 28]

Aggregation-induced emission (AIE) and aggregation induced enhanced emission (AIEE)-based luminescent organic molecules and materials have received enormous attention since the early reports of AIE[29,30] because it changed the general anticipation

about the photophysical properties of any fluorophore. Traditional organic fluorophores are planar disc shaped, and they incline to aggregate via strong π-π stacking and become less or non-emissive in aggregated or solid state. This phenomenon is called aggregation-caused quenching (ACQ).[31,32] To rectify this consequence in the aggregation and solid state, various approaches, that is, physical, chemical, and engineering methods, have been applied.[33-38] AIE molecules precisely have opposite behavior than ACQ. AIE molecules are less emissive in solution but are highly emissive in solid and aggregated forms. AIE molecules have rotor groups, and their restriction in rotation (RIR) has caused this anomalous behavior.[39,40] AIEE fluorophores have opened up new possibilities in various applications such as chemo and biosensors, mechanochromism,[41] bioimaging,[42] organic light emitting diodes,[43] and molecular logic gates.[44] AIEE occurs via RIR, J-aggregation, and synergetic influence via spontaneous nanoparticle formation and intramolecular planarization. AIEE fluorophores show obvious fluorescence in solution, and the fluorescence is remarkably enhanced in aggregated state.[45] Phenothiazine,[46] silole,[47] and tetraphenylethelene[48] based AIE fluorophores have been elegantly utilized till date. Conjugated polymers (CPs) have higher sensitivity toward analytes than small molecules because of higher conjugation of π electrons that are delocalized along the entire chain length like electric current on a wire, a phenomenon called a "molecular wire effect".[49] To date many efficient CPs have been reported,[50-55] yet majority of them possess receptors to detect PA or any other analytes, they suffer from selectivity, poor sensitivity, and most importantly complex synthesis procedures to introduce specific receptor sites of choice. To overcome these multiple challenges, there is a necessity to design and synthesize new probes that do not require such tedious synthesis steps yet have high selectivity and sensitivity for desired analytes. In this paper, a new CP from an AIEE active monomer has been developed by a simple synthetic route. This newly synthesized AIEE active luminogen 2,5-bis((E)-4-bromostyryl)-3,4-diphenylthiophene (**TPBZ**) was utilized to prepare a new AIEE active copolymer **PFTPBZ** (Scheme 1). Nanoaggregates of **PFTPBZ** were successfully investigated for the sensitive detection of PA in tetrahydrofuran (THF) solution state, aggregated state 40% water fraction (f_w) and 95% f_w. Among the various f_w ratios, 40% f_w displayed highest sensitivity to PA detection. The current research mainly focused on the detection of TNT and PA because these are the most widely used nitro explosives. To date, numerous reports are available in literature based on receptor-free fluorophores for detection of PA and TNT with extremely higher sensitivity.[56-58] However, the

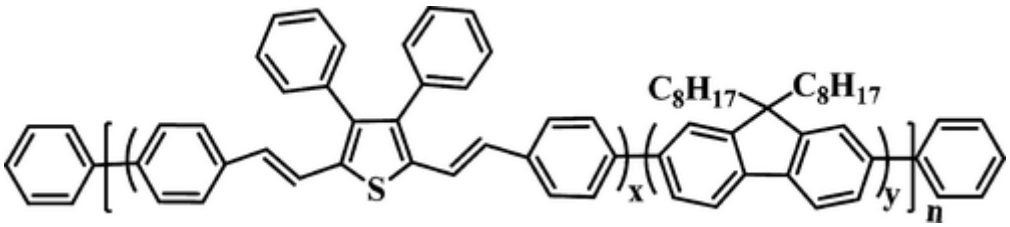

Scheme 3.1: Chemical Structure of a Newly Synthesized AIEE Active Copolymer **PFTPBZ** [Poly(2,7-(9,9-dioctylfluorene)-co-3,4-diphenyl-2,5-distyrylthiophene)]

selectivity is a very crucial factor for successful detection and very important for practical applications. Targeting specific analytes with strong electron affinity[59] and aggregation[60] can play a very important role to overcome the selectivity problem. The present work reports the sensitive and selective detection of PA and TNT. In addition, PA and TNT can be easily discriminated by using newly synthesized **PFTPBZ** polymer. Most of the available reports exhibited emission color in the blue region only; hence, there is still a large possibility to develop new materials in the longer emission wavelength region. More importantly, this **PFTPBZ** polymer showed the greenish-yellow color emission to provide less environment background interference compared with most of the PA sensors with blue fluorescence.

3.2 Results and Discussion

The **TPBZ** monomer was prepared by Suzuki coupling and Wittig-Horner reaction, and the **PFTPBZ** copolymer was prepared by Suzuki cross-coupling polymerization in high yield (Scheme 3.1). Monomer **TPBZ** was extensively analyzed by ^{1}H, ^{13}C NMR spectroscopy, MS, and single-crystal analysis.

3.2.1 Photophysical Properties

The absorption spectra were observed in solution and solid state for **TPBZ** and **PFTPBZ**. Broad absorption peak appeared at 409 and 433 nm (THF solution) and 422 and 454 nm (solid state) for **TPBZ** and **PFTPBZ**, respectively (Figure 3.1). The solution-state photoluminescence (PL) spectra of **TPBZ** measured by excitation of 410 nm showed two peaks at 456 and 481 nm, whereas in the solid state, it exhibited a single peak at 501 nm. Similarly, **PFTPBZ** displayed a single peak in both solution and solid state at 501 and 520 nm (430 nm excitation), respectively. There is a 19 nm red shift in the solid state as compared to the solution state because of the aggregation of **PFTPBZ**.

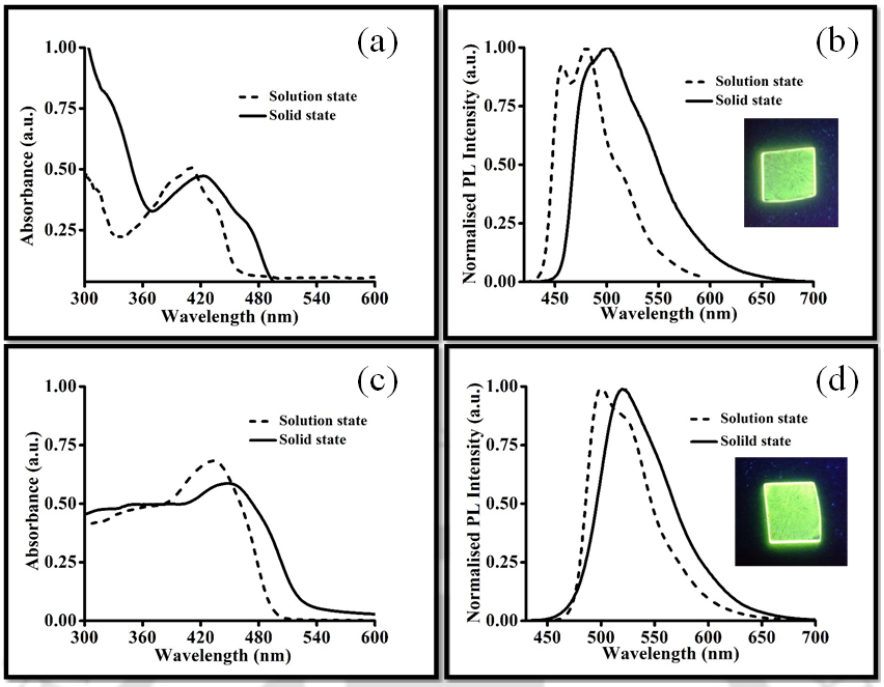

Figure 3.1: UV-visible and PL spectra of **TPBZ** (a,b) and **PFTPBZ** (c,d). The studies were performed at room temperature and the PL spectra recorded by the excitation of 410 nm for **TPBZ** and 430 nm for **PFTPBZ**.

3.2.2 AIEE Properties

For elucidating AIEE behavior associated with **TPBZ** and **PFTPBZ**, UV-vis and PL studies were performed in a binary solvent system. The binary solvents should contain a good solvent and a poor solvent that have to be miscible, and the fluorophores should not precipitate out. Hence, THF along with water was preferred as the binary solvent mixture. The UV-vis spectra (Figure 3.2a,b) of **TPBZ** and **PFTPBZ** were measured by changing the THF and water ratios with constant concentrations of 90 μM **TPBZ** and 90 μM **PFTPBZ**. A broad peak was observed in THF for both **TPBZ** and **PFTPBZ** at 410 and 433 nm, respectively. When f_w changes from 0 to 95%, the absorption peaks were slightly red shifted to 9 and 15 nm for **TPBZ** and **PFTPBZ**, respectively. This might be due to the solvent polarity or formation of J-type aggregation. The PL spectra were measured by increasing the f_w in THF solution at constant concentration (90 μM) of monomer **TPBZ**(Figure 3.2c,e). In THF, **TPBZ** showed greenish-blue color emission at 456 and 481 nm. When f_w reaches 60%, the emission intensity gradually increased to maximum. This is likely due to the RIR between thiophene and phenyl units and formation of nanoaggregates. Further, increasing the f_w from 60 to 95%, the emission intensity of the monomer decreased because of the agglomeration of **TPBZ** nanoparticles. Similarly, the PL studies were carried out for **PFTPBZ** at constant

concentration (90 μM) by changing the THF and water ratios (Figure 3d,f). In THF solution, **PFTPBZ** exhibited strong green color emission at 501 nm (Φ_F = 83.30%) and the emission intensity gradually increased by varying the f_w from 0 to 30%. When f_w reaches 40% (Φ_F = 88.50%), the emission intensity of polymer enhanced two times than that of 30% f_w. This is due to RIR effect and formation of nanoparticles. Furthermore,

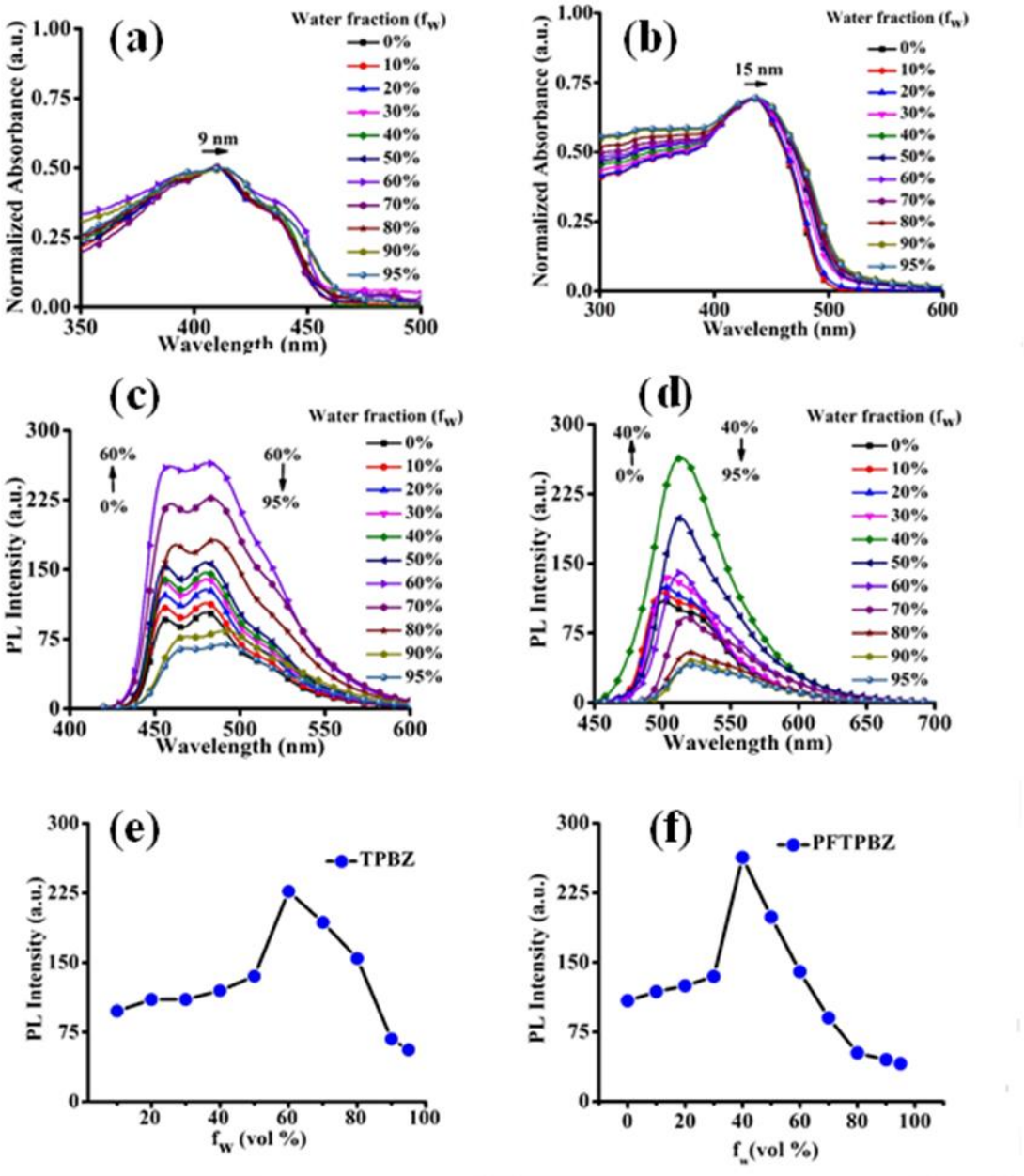

Figure 3.2: UV-visible, PL, and relative PL intensity of **TPBZ** (a,c), **PFTPBZ** (b,d), in THF-water mixtures. These studies were performed at room temperature and the PL spectra recorded by excitation at 410 nm for **TPBZ** and 430 nm for **PFTPBZ**. (e) **TPBZ** and (f) **PFTPBZ** fluorescent intensity ratio in different water fraction respectively.

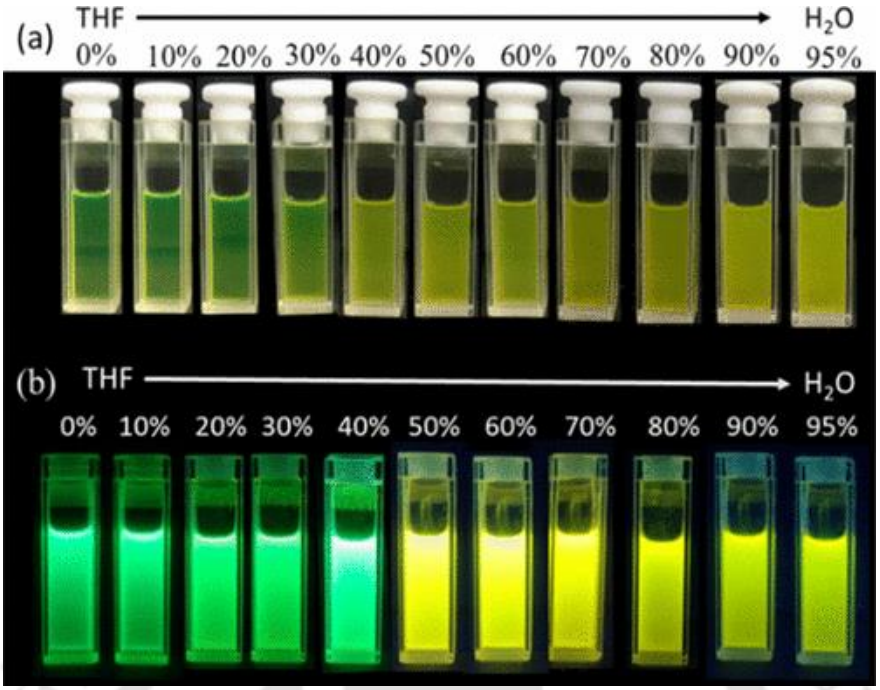

Figure 3.3: Visual change in emission color of **PFTPBZ** in THF and water mixtures under (a) normal light and (b) 365 nm UV lamp.

on increasing f_w from 40 to 95% (Φ_F = 66.06% in 95% f_w), the PL intensity of **PFTPBZ** gradually decreased with slight red shift in its emission spectra because of the polarity of the solvent and the formation of agglomeration of nanoparticles.

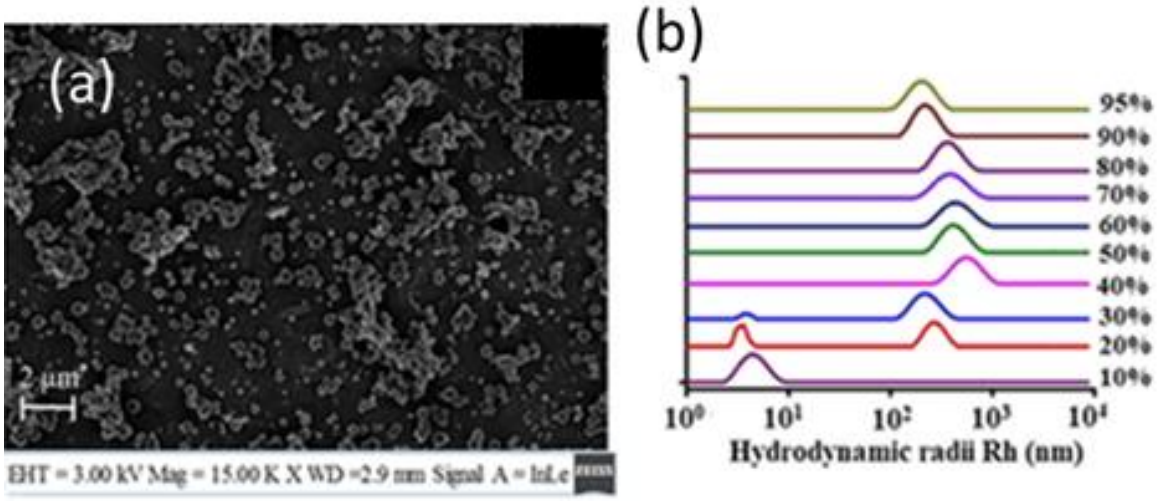

Figure 3.4: (a) FESEM image of **PFTPBZ** (40% f_w); (b) DLS curves of **PFTPBZ** in different THF and in different water fractions.

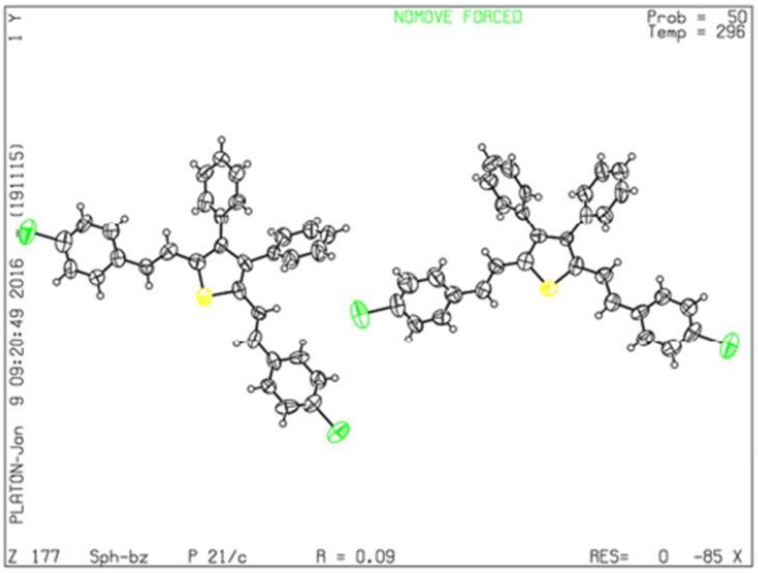

Figure 3.5: ORTEP diagram of **TPBZ**.

Figure 3.3a shows the photographs of **PFTPBZ** in 0-95% f_w in normal light and under UV hand held lamp (Figure 3.3b) and the nanoaggregates of **TPBZ** (60% f_w) (Figure A3.1) and **PFTPBZ** (40% f_w) were confirmed by TEM and FESEM images (Figure 3.4a) where the average size of nanoparticles was found to be ~10-15 and ~150-250 nm for **TPBZ** and **PFTPBZ**, respectively. The nanoparticle formation of **PFTPBZ** was confirmed by the DLS studies by changing f_w from 0 to 95% (Figure 3.4b). These results reveal that when f_w changes from 0 to 95%, the size of nanoparticles was also modified. The **TPBZ** single crystals were obtained by slow evaporation from 1:2 hexane and ethanol mixture. The single-crystal structure and packing of **TPBZ** were helpful to explain the AIEE and ACQ behavior of **TPBZ**. ORTEP diagram of **TPBZ** is presented in Figure 3.5 and Single Crystal data of 2,5-bis(4-bromostyryl)-3,4-diphenylthiophene (**TPBZ**) summarised in Table A3.1. Figure 3.6 shows the crystal arrangement and packing, in which two phenyl moieties act as rotors and are highly nonplanar, whereas the two 1-bromo-4-vinylbenzene moieties are in nearly planar position to the thiophene core. The torsion angles are of 51.72° and 61.23° for two phenyl units and 9.63° and 17.52° for 1-bromo-4-vinylbenzene units. These phenyl units and vinyl benzene units can restrict the intramolecular rotations (RIR) in the aggregated state. The two monomer units of **TPBZ** are packed by the intermolecular C-H···π (2.728 Å) interactions. However, the distance between two adjacent molecules is 4.034 Å with respect to thiophene cores, suggesting that these two molecules are weakly packed by intermolecular π-π interactions. Therefore, these nonplanar structures are highly

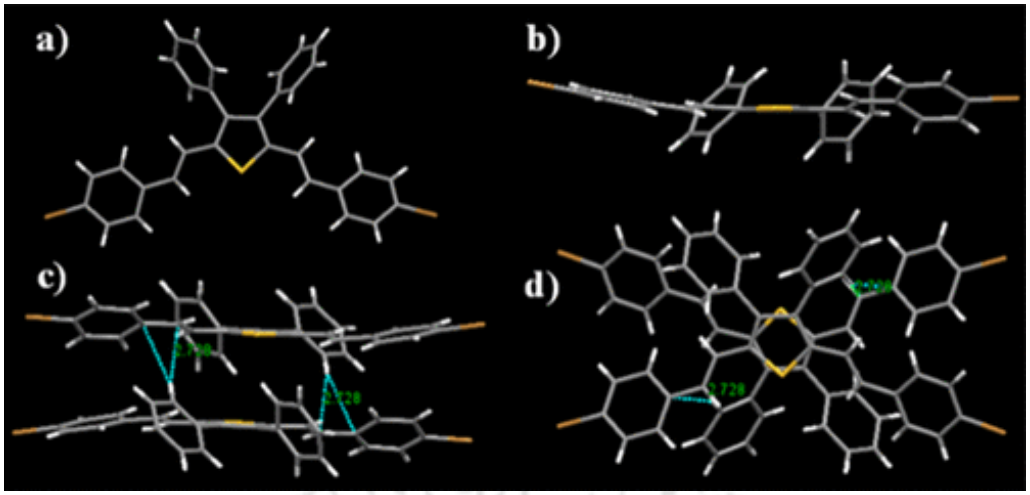

Figure 3.6: (a) Top view and (b) side view of **TPBZ**. (c) Side view and (d) top view of **TPBZ** dimer with C-H···π (2.728 Å) intermolecular structural interactions.

responsible for obtaining the strong solid-state emission and AIEE property

3.2.3 Density Functional Theory

To comprehend the molecular arrangement and the ground state geometry of **PFTPBZ**, the density functional theory (DFT) studies were carried out by Gaussian 09 A.02 software package[61] using B3LYP functional with 6-31G basis set. These DFT calculations were performed for copolymer model compound by introducing two alkyl

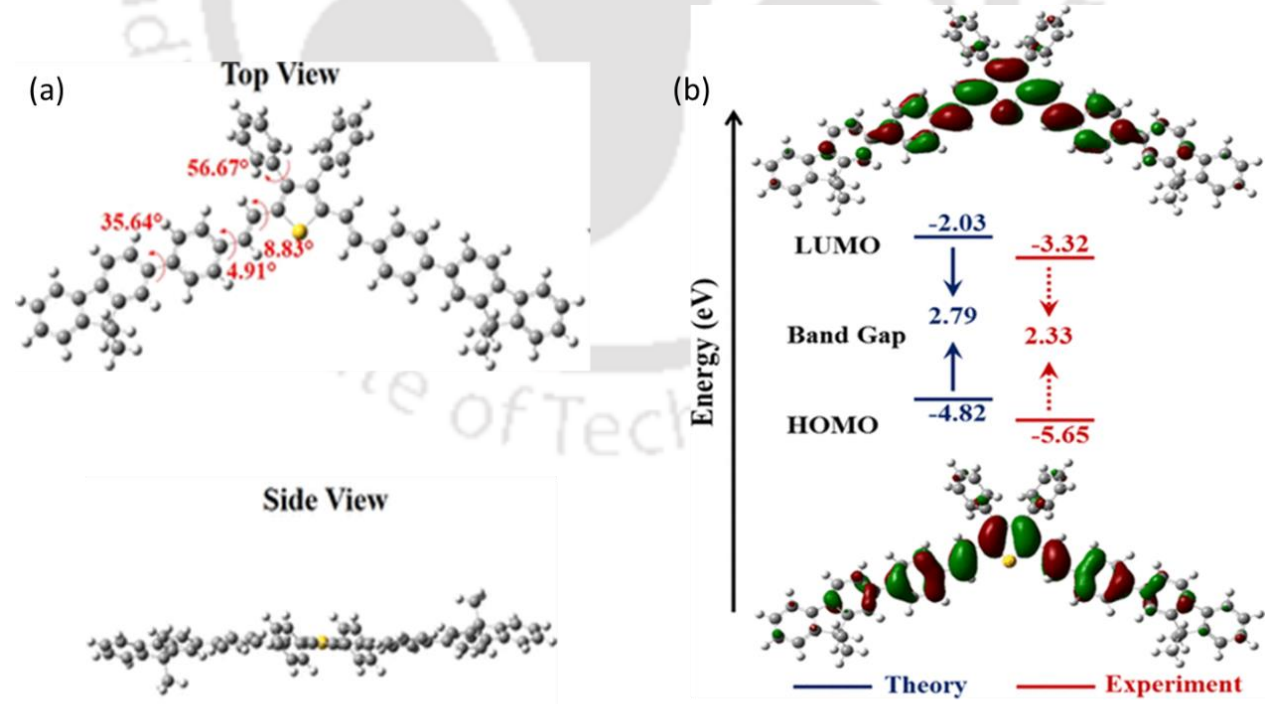

Figure 3.7: (a) Optimized structure of the model **PFTPBZ** copolymer (b) Molecular orbital amplitude plots for the LUMO and HOMO levels and the comparison of energy levels (iso_{value} = 0.02).

substituted fluorene moieties at the end of two vinylene phenyl para positions. Figure 3.7a shows the nonplanar optimized molecular structure. Except two phenyl units, the remaining compound is in one plane with dihedral angles of 56.67°, 8.83°, 4.91°, and 35.64°for thiophene-phenyl, thiophene double bond, double bond phenyl, and phenyl-fluorene, respectively, and the distributions of orbitals of the lowest unoccupied molecular orbital (LUMO) and highest occupied molecular orbital (HOMO) energy levels are displayed in Figure 3.7b. The LUMO and HOMO levels are mainly located on vinyl phenyl and thiophene units.

3.2.4 Analyte Detection and selectivity Studies

Considering the practical and various environmental applications, the stability of the probe was confirmed across the pH 2-13 range (Figure A3.2) thereby not requiring any buffering solution for sensing studies. In THF, 40 and 95% f_w **PFTPBZ** showed strong yellow fluorescence under an UV hand lamp and nitro-explosive detection experiments were done by varying the concentrations of nitro compounds. When PA of 44×10^{-5}, 32×10^{-5}, and 46×10^{-5} M was added in pure THF, 40% f_w and 95% f_w solutions of **PFTPBZ**, respectively, complete quenching of its emission was observed (Figure 3.8). The quenching of the yellow fluorescence of **PFTPBZ** after the addition of PA was easily visible under the UV hand lamp. Stern-Volmer graph was plotted between I_o/I versus [Q], where I_o is the intensity of **PFTPBZ** in the absence of PA, I represents the emission intensity of **PFTPBZ** in the presence of PA, and [Q] is the concentration of added PA. Quenching constant (K_{sv}) was found to be 4.960×10^3 for THF, 4.456×10^3 for 95% f_w, and 7.604×10^3 for 40% f_w (Figure A3.3). Fluorometric sensing studies were carried out by taking various nitro derivatives, viz., 4-NT, 2,4-DNT, 2,6-DNT, BA, 1,3-DNB, NB, and phenol, to the solution of **PFTPBZ** (90 μM) in THF, 40% f_w, and 95% f_w. Negligible changes were observed in the fluorescence intensity of **PFTPBZ** upon addition of these competitive nitro derivative analytes but when TNT was added in THF, 40% f_w, and 95% f_w solutions of **PFTPBZ**, the quenching was observed in the aggregated states (40 and 95% f_w). Furthermore, cations (Al^{3+}, Zn^{2+}, Co^{3+}, Ni^{2+}, Ca^{2+}, Cu^{2+}, Pb^{2+}, Cr^{2+}, and Hg^{2+}) and anions (PO_4^{3-}, F^-, I^-, NO_2^-, N_3^-, NO_3^-, HPO_4^{2-}, S_2^-, and BF_4^-) were titrated because some of these ions are usually present in real water samples.

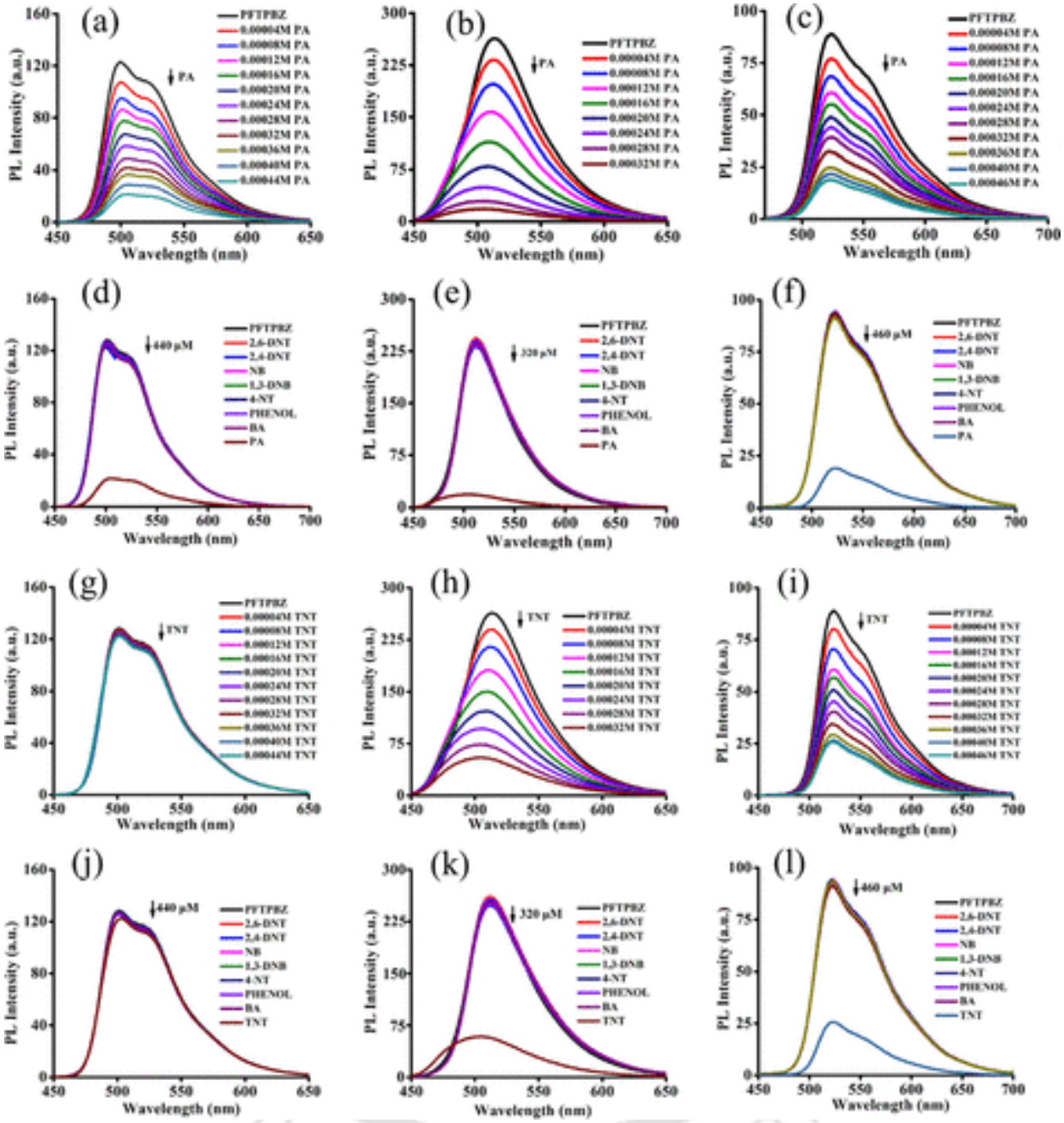

Figure 3.8: Fluorescence quenching experiment of PA and TNT in THF (a,d,g,j), 40% f_w (b,e,h,k), and 95% f_w (c,f,i,l).

Fortunately, they did not show any effect on the emission intensity of **PFTPBZ** (Figure 3.9), strongly suggesting the selectivity of **PFTPBZ** toward PA and TNT exclusively.

3.2.5 Time-Resolved PL Studies

Fluorescence decay studies of **PFTPBZ** (90 μM) were carried out without and with PA. The PA concentrations of 44×10^{-5}, 32×10^{-5}, and 46×10^{-5} M were added in THF, 40% f_w, and 95% f_w, respectively. Pulse excitation was 405 nm, and emission was measured at 500, 505 and 530 nm. The time-resolved PL (TRPL) curves obtained by biexponential

fitting, and the average lifetime was calculated (Figures A3.4-A3.6 and Tables A3.2-A3.4).

3.2.6 Electrochemical Analysis.

To find out the energy levels (HOMO and LUMO) of **PFTPBZ**, the cyclic voltammogram (CV) was carried out using ferrocene as a standard under inert atmosphere. Saturated $Ag/AgNO_3$ electrode, platinum wire, and glassy carbon electrode used as reference, counter, and working electrodes, respectively, and supporting electrolyte $TBAPF_6$ (0.1 M in CH_3CN) was used. **PFTPBZ** (1 mM) was drop casted from chloroform solution on a working electrode to record CV curves (Figure 3.10a). **PFTPBZ** exhibited only oxidation potential, and the HOMO energy level was estimated by substituting oxidation potential value into this formula [$E_{HOMO} = -[E_{(onset,\ ox\ vs\ Fc+/Fc)} + 4.8]$ (eV)]. The LUMO of **PFTPBZ** was estimated from the solid-state UV spectra.

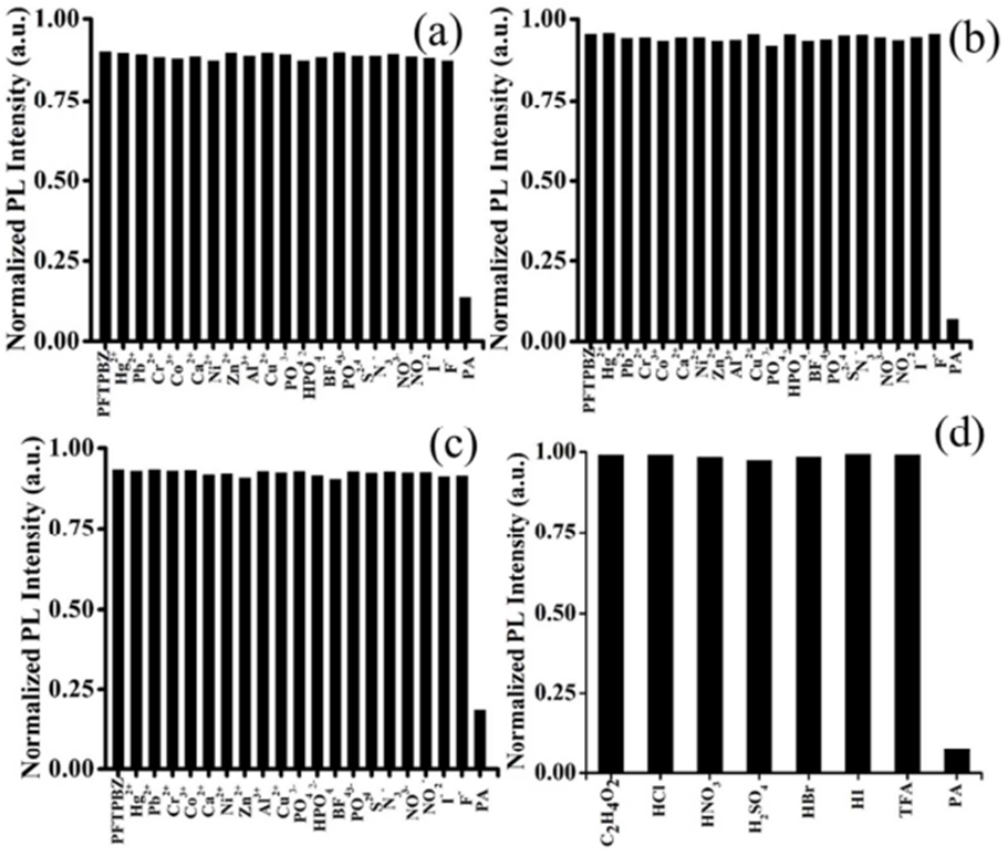

Figure 3.9: Change of fluorescence intensity of **PFTPBZ** in presence of various metal ions in (a) THF (b) 40% f_w (c) 95% f_w and (d) presence of inorganic acids.

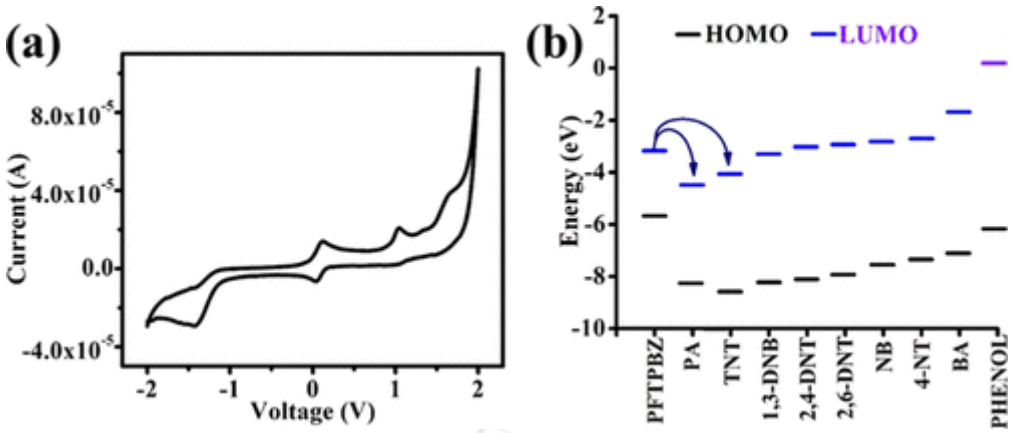

Figure 3.10: (a) CV of **PFTPBZ**. (b) HOMO and LUMO comparison of **PFTPBZ** with various nitro aromatics

3.2.7 Mechanism of Sensing.

On the basis of above detection experiment results, PA and TNT sensing by **PFTPBZ** could be possible via two mechanisms, photoinduced charge transfer (PET) and Förster resonance energy transfer (FRET) which were confirmed by CV analysis and TRPL experiments, respectively. The lifetime decay of **PFTPBZ** was examined without and with PA in THF, 40 and 95% f_w, respectively. The average lifetime of **PFTPBZ** in THF showed insignificant change (0.004 ns); however, in 40% f_w, significant changes (0.136 ns) and in 95% f_w moderate changes (0.076 ns) were obtained after adding PA (from equation A3.1). In the case of 40% f_w, there is FRET occurring while sensing PA because there is considerable overlap between the emission spectra of **PFTPBZ** and absorption spectra of PA. In addition, fluorophore and quencher should be at a specific distance (Förster distance) to enable efficient energy transfer. While detecting PA in the THF medium, there is a significant spectral overlap; however, quencher and fluorophore are not in the proximal distance so that energy transfer was not possible and hence no FRET. However, in 95% f_w, there is very little spectral overlap between quencher and fluorophore yet there is FRET because of high aggregation (Figures A3.7-A3.9). PET phenomenon is a recognized mechanism that found in various fluorescence sensor systems. For elucidating the plausible mechanism for PA and TNT, CV experiments were performed. Because the **PFTPBZ** energy level lies above the energy levels of PA and TNT, energy transfer from HOMO of **PFTPBZ** to LUMO of PA and TNT occurs. Because of the electron rich of **PFTPBZ**, the CV studies displayed only oxidation peak and the HOMO was found to be -5.65 eV. The LUMO energy level (-3.32 eV) of **PFTPBZ** was estimated from the optical band gap (2.33 eV) of the copolymer, which was obtained from the onset of solid-state absorption spectra. These results strongly

suggest that the PET takes place from LUMO of copolymer to the LUMO of PA and TNT. The quenching of other analytes does not follow this trend because LUMO level of other nitro explosives lies near or above the LUMO level of **PFTPBZ** (Figure 3.10b).

3.2.8 Calculating Detection Limit

Limit of detection (LOD) calculated in THF, 40% f_w, and 95% f_w by taking different **PFTPBZ** (90 μM) solutions and different concentrations of PA and TNT (1-6 μM) and recording fluorescence spectrum. To acquire the regression curve equation, a calibration curve was plotted between luminescence intensity of **PFTPBZ** and concentration of PA and TNT. The LOD was calculated by using the equation 3σ/k, wherein σ denotes the standard deviation for the emission intensity of **PFTPBZ** without PA or TNT and k represents the slope. In THF solution, the LOD for PA of 28.16×10^{-7} M, in 40% f_w the LOD of 47.39×10^{-8} M, and in 95% f_w 10.47×10^{-6} M and for TNT in 40% f_w 53.74×10^{-6} M and in 95% f_w 14.26×10^{-7} M LOD were obtained (Figures A3.10-A3.14 and Equations A3.2-A3.6)

3.2.9 Portable On-Site Detection of PA

Preparation of Paper Strips. To develop an easy and inexpensive tool for PA detection, the **PFTPBZ** fluorescent paper strip device was obtained by immersing the Whatman filter paper in the **PFTPBZ** solution (THF) and dried for 10 min. Then, the filter paper was cut into several 1 cm × 1 cm strips, and it successfully utilized for the simple on-site detection of PA. **PFTPBZ**-coated Whatman filter paper strips had fluorescence quenched dark spots observed under 365 nm hand held UV lamp after addition of different concentrations of PA. The Whatman filter papers were exposed to PA vapor for different time intervals to observe complete quenching of fluorescence of **PFTPBZ** within 18 min. Its reusability was checked by washing it by deionized water, drying, and reusing this filter paper for PA vapor sensing at different concentrations of PA solution. As shown in (Figure 3.11a), it is clearly indicating that the less quantity of PA has been detected by the bare eye and it was calculated as 1.86 ng concentration of PA. Detection of PA in real water samples, that is, lakes, river, and sea water, is very important because it is highly soluble in water and can very easily pollute them. Hence, it is essential to develop a sensitive probe that detect and evaluate trace amounts of PA in real water resource samples. Water samples were collected from various natural sources (Brahmaputra river, Shivanath river, Serpentine lake, and sea water). Water samples were centrifuged at 2500 rpm for half an hour and then passed through by a 0.2

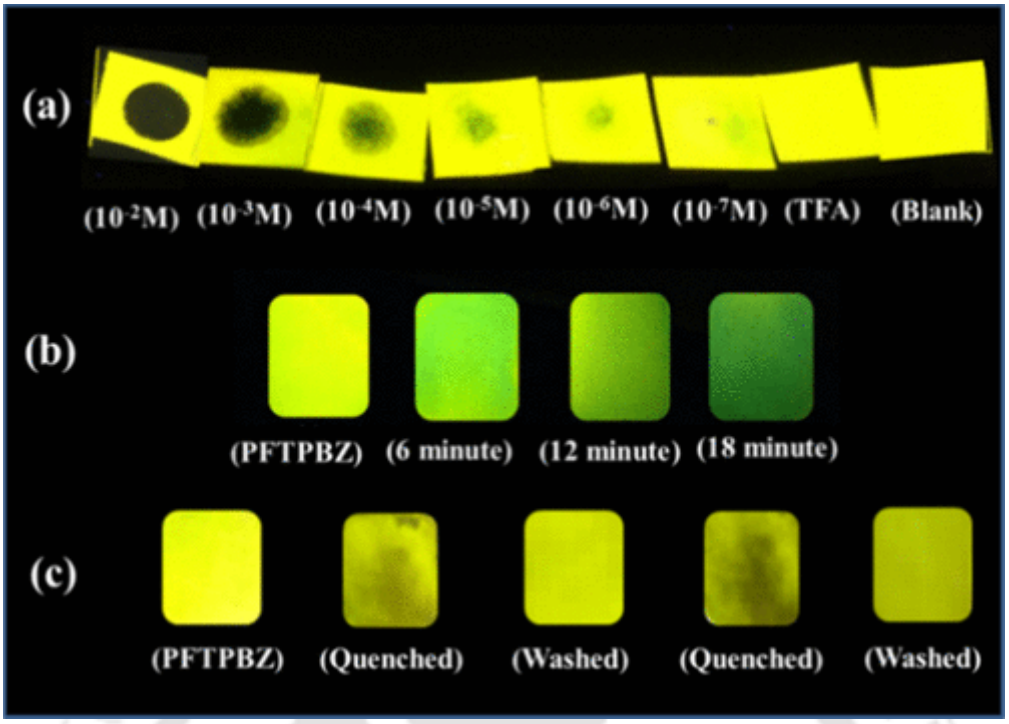

Figure 3.11: (a) Fluorescence of **PFTPBZ**-dipped Whatman filter paper was quenched by different concentrations of PA solution; (b) quenching of emission of **PFTPBZ**-dipped Whatman filter paper by introducing PA vapor for different times; (c) **PFTPBZ** Whatman filter paper after washing with water, reused for PA vapor sensing.

μm filter and used it for detection of PA studies. The amount of quenching was compared by a standard calibration curve (Figure A3.15 and Table A3.5).

3.3 Conclusions

In summary, a new "receptor-free" AIEE active monomer **TPBZ** and its copolymer **PFTPBZ** were synthesized by the reaction with 9,9-dioctylfluorene-2,7-diboronic acid bis(1,3- propandiol) ester. The receptor-free **PFTPBZ** showed excellent AIEE active nature and displayed bright yellow emission with high quantum yields of 83.30, 66.06, and 88.50% in THF, 95% f_w, and 40% f_w, respectively. **PFTPBZ** is highly stable under wide pH range of 2-13 and displayed high selectivity toward PA in different states, that is, soluble, AIEE, and ACQ state, and higher sensitivity was achieved in AIEE state (40% f_w) with lowest LOD of 47.39×10^{-8} M. Moreover, the selectivity study of PA was performed in the presence of various metal ions, inorganic acids, and real water samples. In addition, **PFTPBZ** was successfully demonstrated for sensing of PA vapor and its solution by simple **PFTPBZ**-dipped Whatman filter paper with 1.86 ng detection limit. **PFTPBZ** was also capable to perform detection of TNT in 40 and 95% f_w with LODs of 53.74×10^{-6} and 14.26×10^{-7} M, respectively, and discriminate it from the PA. The CV and TRPL studies strongly suggested that sensing of PA was realized via PET and

FRET mechanisms. The experimental results clearly indicated that **PFTPBZ**, a receptor-free polymer, selectively detects PA in competitive environment in solution, vapor form, and by a portable and economical reusable paper strip by naked eye visualization of the change in bright yellow color.

3.4 Experimental section

3.4.1 Materials and Measurements:

Caution! Nitroaromatic compounds are highly explosive and noxious in nature, we should work very sensibly with proper safety measures.

4-nitrotoluene (4-NT), 2,4-dinitrotoluene (2,4-DNT), 1,3-dinitrobenzene (1,3-DNB), phenol and 2,6- dinitrotoluene (2,6-DNT) were purchased from Sigma Aldrich India, picric acid was purchased from Loba Chemie Pvt. Ltd and were used as received without further purification and TNT was synthesized by reported method.[1] HPLC grade THF and Milli-Q water was used for preparing stock solutions as well as experiment purposes. ^{1}H NMR (400 MHz) and ^{13}C NMR (100 MHz) spectra were obtained on Varian-AS400 spectrometer. Gel permeation chromatography (GPC) was performed in Agilent Technologies instrument using polystyrene as standard and THF as a solvent. Photoluminescence (PL) and UV-visible spectra were recorded on a Horiba Fluoromax-4 and PerkinElmer Lambda-25 spectrofluorometer using 10 mm path length quartz cuvettes with a 3 nm slit width at 298 K. Time-resolved photoluminescence (TRPL) measurements carried out in Edinburgh Instrument Life Spec II. Paper strip sensing experiment was performed using Whatman qualitative filter papers, grade 1. Cyclic voltammogram (CV) was recorded using CH instrument model 700D series electrochemical workstation.

3.4.2 Preparation of standard solutions

Detection Studies. The standard solution of **TPBZ** and **PFTPBZ** was prepared at 1 mM concentration in HPLC-grade THF. The standard solution (10 mM) of 1,3-dinitrobenzene, 4-nitrotoluene, DNT, TNT, and 2,4-dinitrotoluene was prepared in HPLC-grade THF, and solutions of other analytes, viz., phenol, nitrobenzene (NB), PA, benzoic acid (BA), metal ions, were prepared in Milli-Q water

3.4.3 General Synthesis Procedure

Experimental sections:

Synthetic procedure of **TPBZ** and **PFTPBZ**:

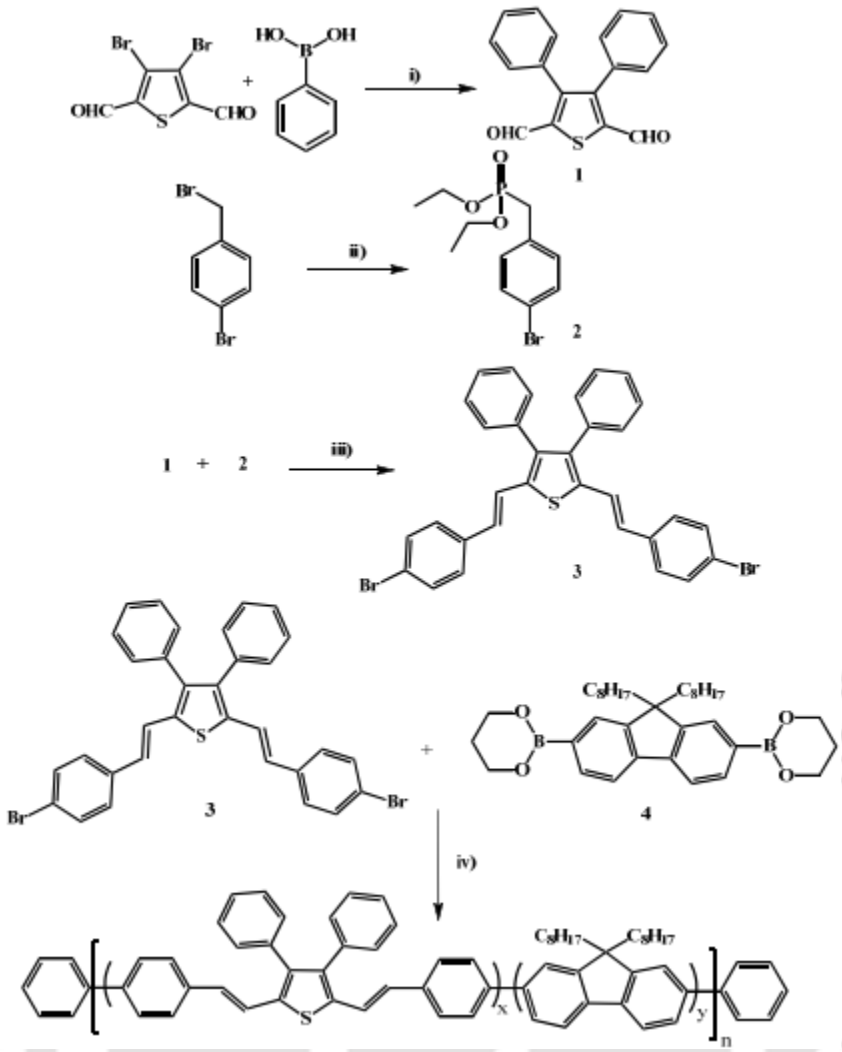

Scheme 3.2: (i) $Pd(PPh_3)_4$, K_2CO_3, THF:H_2O, 80 °C, 12 hr (ii) $P(OEt)_3$, 140 °C, 5 hr (iii) K^{t}BuO, THF, RT, 12 hr (iv) $Pd(PPh_3)_4$, K_2CO_3, THF:H_2O, 80 °C, 48 hr.

Synthesis of 3,4-diphenylthiophene-2,5-dicarbaldehyde (1): 3,4-dibromothiophene-2,5-dicarbaldehyde (0.675 mmol), phenyl boronic acid (1.5 mmol), 6 mL THF and tetrakis(triphenyl phosphine) palladium(0) (0.015 mmol) were taken into a dry round bottom flask and purged with argon gas and then aqueous K_2CO_3 (2M) were added into the flask and refluxed overnight. Then reaction was quenched and workup done using DCM and water washing. Pure product was collected after column chromatography as a white crystalline solid. (Yield-66%). ^{1}H NMR (400 MHz, $CDCl_3$, δ ppm) 7.13 (t, J = 8.0 Hz, 2H), 7.32 (t, J = 8.0 Hz, 4H), 7.38 (d, J = 8.0 Hz, 4H). ^{13}C NMR (100.00 MHz, $CDCl_3$, δ ppm) 128.47, 128.87, 130.51, 131.68, 144.07, 150.86, 185.27. HRMS (+ESI): Calculated for $C_{18}H_{12}O_2S$ 293.06 $[M]^+$ and Found. 293.70.

Synthesis of 2,5-bis(4-bromostyryl)-3,4-diphenylthiophene (2): Into a condenser fitted round bottom flask 1-bromo-4-(bromomethyl)benzene (2.054 mmol) and triethyl phosphite

(0.5 mL) in 7 mL of THF was refluxed for 5 hours then 3,4-diphenylthiophene-2,5-dicarbaldehyde (1 mmol) and potassium tertiary butoxide (2.5 mmol) was added and the reaction stirred at room temperature for 24 hours. Then the reaction mixture was quenched and workup performed by using DCM and water. Final product was collected by purifying it by using silica column chromatography. The yellow colored product was obtained in 57% yield. Needle shaped yellow crystals were grown in 1:2 hexane and ethanol mixture by slow evaporation. ^{1}H NMR (400 MHz, $CDCl_3$, δ ppm) 6.95 (d, J = 8.0 Hz, 2H), 7.09 (d, J = 8.0 Hz, 6H), 7.18 (t, J = 8.0 Hz, 2H), 7.23 (d, J=8.0Hz, 2H) 7.27 (d, J = 8.0 Hz, 8H), 7.42 (d, J = 8.0 Hz, 4H). ^{13}C NMR (100.00 MHz, $CDCl_3$, δ ppm) 114.20, 116.46, 121.50, 122.02, 127.38, 128.00, 128.14, 130.73, 131.93, 136.14, 139.43, 142.54. MALDI TOF: Calculated for $C_{32}H_{22}Br_2S$ 595.98, Found 595.90.

Synthesis of Poly[2,7-(9,9'-dioctylfluorene)-co-3,4-diphenyl-2,5-distyrylthiophene (PFTPBZ): 9,9-Dioctylfluorene-2,7-diboronic acid bis(1,3-propanediol)ester (1.0 eq.), 2,5-bis(4-bromostyryl)-3,4-diphenylthiophene (1.0 eq.) and tetrakis(triphenyl phosphine) palladium(0) (0.05 eq) were added into a dry round bottom flask in argon gas environment. 9 mL of THF and 3 mL of aqueous K_2CO_3 (2M) were added into the round bottom flask. The reaction mixture was degassed thrice by freeze- thaw cycle for complete removal of trace amount of oxygen present in reaction setup. The reaction mixture was refluxed for 48 hours then iodobenzene (0.1 eq.) was added as a end caper and 4 hours later phenyl boronic acid (0.1 eq.) was added as a 2nd end caper and reaction continued for 4 more hours. Then the reaction was quenched and workup performed by using DCM and water washings. The polymer (PFTPBZ) was collected by reprecipitation from methanol and acetone. Soxhlet filtration was performed by taking acetone as a solvent to remove oligomers and catalyst residue. ^{1}H NMR (400 MHz, $CDCl_3$, δ ppm) 0.07 (s, CH_2), 0.84 (br, CH_2), 1.09 (br, CH_2), 1.25 (br, CH_2), 1.56 (br, CH_2), 1.67 (br, CH_2), 2.04 (br, CH_2), 6.83 (br, Ar-H), 6.95 (br, Ar-H), 6.97 (br, Ar-H), 7.11 (br, Ar-H), 7.18 (br, Ar-H), 7.29 (br, Ar-H), 7.43 (br, Ar-H), 7.49 (br, Ar-H), 7.55 (br, Ar-H), 7.61 (br, Ar-H), 7.64 (br, Ar-H), 7.76 (br, Ar-H), 7.81 (br, Ar-H). Gel-permeation chromatography (GPC): M_n =22916, PDI = 1.25 (PMMA standards).

3.5 References

1 Salinas, Y.; Martinez- Máñez, R.; Marcos, M. D.; Sancenón, F.; Costero, A. M.; Parra, M.; Gil, S. *Chem. Soc. Rev.* **2012,** *41*, 1261-1296.

2 Ma, Y. X.; Li, H.; Peng, S.; Wang, L. Y. *Anal. Chem.* **2012,** *84*, 8415-8421.

3 Pushkarsky, M. B.; Dunayevskiy, I. G.; Prasanna, M.; Tsekoun, A. G.; Go, R.; Patel, C. K. N. *Proc. Natl. Acad. Sci. U.S.A.* **2006,** *103*, 19630-19634.

4 Germain, M. E.; Knapp, M. J. *Chem. Soc. Rev.* **2009,** *38*, 2543-2555.

5 Jenkins, T. F.; Leggett D. C.; Ranney, T. A. US Army Cold Regions Research and Engineering Laboratory *Special Report*, **1999.**

6 Peng, Y.; Zhang, A. J.; Dong, M.; Wang, Y. W. *Chem. Commun.* **2011,** *47*, 4505-4507.

7 Grunwald. E.; Price, E. *J. Am. Chem. Soc.* **1964,** *86*, 4517-4525.

8 Duraimurugan. K.; Siva, A. *J. Polym. Sci. Part A Polym. Chem.* **2016,** *54*, 3800-3807.

9 Shen, J. Y.; Zhang, J. F.; Zuo, Y.; Wang, L. J.; Sun, X. Y.; Li, J. S.; Han, W. Q.; He, R. *J. Hazard. Mater.* **2009,** *163*, 1199-1206.

10 Malik, A. H.; Hussain, S.; Kalita, A.; Iyer, P. K. *ACS Appl. Mater. Inter.* **2015,** *7*, 26968-26976.

11 King. E. J.; Lucas, C. C. *J. Am. Chem. Soc.* **1928,** *50*, 2395-2397.

12 Young, J. A. Picric Acid. *J. Chem. Edu.* **2008,** *85*, 492.

13 Pimienta, V.; Etchenique, R.; Buhse, T. *J. Phys. Chem. A* **2001,** *105*, 10037-10044.

14 Singh, S. *J. Hazard. Mater.* **2007,** *144*, 15-28.

15 Volwiler, E. H. *Ind. Eng. Chem.* **1926,** *18*, 1336-1337.

16 Cooper, P. W. Explosives Engineering; VCH, **1996.**

17 Hussain, S.; Malik, A. H.; Afroz, M. A.; Iyer, P. K. *Chem. Commun.* **2015,** *51*, 7207-7210.

18 Luggar, R. D.; Farquharson, M. J.; Horrocks, J. A.; Lacey, R. J. *X-Ray Spectrom.* **1998,** *27*, 87-94.

19 Håkansson, K.; Coorey, R. V.; Zubarev, R. A.; Talrose, V. L.; Håkansson, P. *J. Mass Spectrom.* **2000,** *35*, 337-346.

20 Berg, M.; Bolotin, J.; Hofstetter, T. B. *Anal. Chem.* **2007,** *79*, 2386-2393.

21 Chen, H. W.; Hu, B.; Hu, Y.; Huan, Y. F.; Zhou, Z. Q.; Qiao, X. F. *J. Am. Soc. Mass Spectr.* **2009,** *20*, 719-722.

22 Zhao, X. M.; Yinon, J. *J. Chromatogr. A* **2002,** *946*, 125-132.

23 Sulzer, P.; Petersson, F.; Agarwal, B.; Becker, K. H.; Jürschik, S.; Märk, T. D.; Perry, D.; Watts, P.; Mayhew, C. A. *Anal. Chem.* **2012,** *84*, 4161-4166.

24 Moore, D. S. *Rev. Sci. Instrum.* **2004,** *75*, 2499-2512.

25 Crippen, R. C. *Pergamon Press*; **1983.**

26 Sánchez, C.; Carlsson, H.; Colmsjö, A.; Crescenzi, C.; Batlle, R. *Anal. Chem.* **2003,** *75*, 4639-4645.

27 Lakowicz, J. R. Principles of Fluorescence Spectroscopy, Springer, 3rd Edn. **2006**.

28 Guan, W. J.; Zhou, W. J.; Lu, J.; Lu, C. *Chem. Soc. Rev.* **2015,** *44*, 6981-7009.

29 Luo, J. D.; Xie, Z. L.; Lam, J. W. Y.; Cheng, L.; Chen, H. Y.; Qiu, C. F.; Kwok, H. S.; Zhan, X. W.; Liu, Y. Q.; Zhu, D. B.; Tang, B. Z. *Chem. Commun.* **2001,** 1740-1741.

30 An, B. K.; Kwon, S. K.; Jung, S. D.; Park, S. Y. *J. Am. Chem. Soc.* **2002,** *124*, 14410-14415.

31 Yuan, W. Z.; Lu, P.; Chen, S. M.; Lam, J. W. Y.; Wang, Z. M.; Liu, Y.; Kwok, H. S.; Ma, Y. G.; Tang, B. Z. *Adv. Mater.* **2010,** *22*, 2159-2163.

32 Hong, Y. N.; Lam, J. W. Y.; Tang, B. Z. *Chem. Soc. Rev.* **2011,** *40*, 5361-5388.

33 Lee, S. H.; Jang, B. B.; Kafafi, Z. H. *J. Am. Chem. Soc.* **2005,** *127*, 9071-9078.

34 Grimsdale, A. C.; Chan, K. L.; Martin, R. E.; Jokisz, P. G.; Holmes, A. B. *Chem. Rev.* **2009,** *109*, 897-1091.

35 Setayesh, S.; Grimsdale, A. C.; Weil, T.; Enkelmann, V.; Müllen, K.; Meghdadi, F.; List, E. J. W.; Leising, G. R. *J. Am. Chem. Soc.* **2001,** *123*, 946-953.

36 Swager, T. M. *Acc. Chem. Res.* **2008,** *41*, 1181-1189.

37 Hecht, S.; Fréchet, J. M. J. *Angew. Chem. Int. Ed.* **2001,** *40*, 74-91.

38 Marsitzky, D.; Vestberg, R.; Blainey, P.; Tang, B. T.; Hawker, C. J.; Carter, K. R. *J. Am. Chem. Soc.* **2001,** *123*, 6965-6972.

39 Wu, J. S.; Liu, W. M.; Ge, J. C.; Zhang, H. Y.; Wang, P. F. *Chem. Soc. Rev.* **2011,** *40*, 3483-3495.

40 Mei, J.; Leung, N. L. C.; Kwok, R. T. K.; Lam, J. W. Y.; Tang, B. Z. *Chem. Rev.* **2015,** *115*, 11718-11940.

41 Jin, S. Y.; Tian, Y.; Liu, F.; Chen, J.; Deng, S. Z.; Xu, N. S. *J. Mater. Chem. C* **2015,** *3*, 8066-8073.

42 Zhao, N.; Li, M.; Yan, Y. L.; Lam, J. W. Y.; Zhang, Y. L.; Zhao, Y. S.; Wong, K. S.; Tang, B. Z. *J. Mater. Chem. C* **2013,** *1*, 4640-4646.

43 Huang, J.; Sun, N.; Chen, P. Y.; Tang, R. L.; Li, Q. Q.; Ma, D. G.; Li, Z. *Chem. Commun.* **2014,** *50*, 2136-2138.

44 Dong, Y. Q.; Lam, J. W. Y.; Tang, B. Z. *J. Phys. Chem. Lett.* **2015,** *6*, 3429-3436.

45 Würthner, F.; Kaiser, T. E.; Saha-Möller, C. R. *Angew. Chem. Int. Ed.* **2011,** *50*, 3376-3410.

46 Salimimarand, M.; La, D. D.; Al Kobaisi, M.; Bhosale, S. V. *Sci. Rep.* **2017,** *7*, 42898.

47 Xu, L. R.; Li, Y.; Li, S. H.; Hu, R. R.; Qin, A. J.; Tang, B. Z.; Su, B. *Analyst* **2014,** *139*, 2332-2335.

48 Zhu, Z. F.; Leung, C. W. T.; Zhao, X. Y.; Wang, Y. L.; Qian, J.; Tang, B. Z.; He, S. L. *Sci. Rep.* **2015,** *5*, 15189-15197.

49 Swager, T. M. *Acc. Chem. Res*., **1998,** *31*, 201-207.

50 Sun, X. C.; Wang, Y.; Lei, Y. *Chem. Soc. Rev.* **2015,** *44*, 8019-8061.

51 Hu, Z. C.; Deibert, B. J.; Li, J. *Chem. Soc. Rev.* **2014,** *43*, 5815-5840.

52 Ponnuvel, K.; Banuppriya, G.; Padmini, V. *Actuat. B-Chem.* **2016,** *234*, 34-45.

53 Tanwar, A. S.; Hussain, S.; Malik, A. H.; Afroz, M. A.; Iyer, P. K. *ACS Sensors* **2016,** *1*, 1070-1077.

54 Vij, V.; Bhalla, V.; Kumar, M. *ACS Appl. Mater. Inter*. **2013,** *5*, 5373-5380.

55 Xu, B. W.; Wu, X. F.; Li, H. B.; Tong, H.; Wang, L. X. *Macromolecules* **2011,** *44*, 5089-5092.

56 Liao, Y. Z.; Strong, V.; Wang, Y.; Li, X. G.; Wang, X.; Kaner, R. B. *Adv. Funct. Mater.* **2012,** *22*, 726-735.

57 Hu, R. R.; Lam, J. W. Y.; Liu, J. Z.; Sung, H. H. Y.; Williams, I. D.; Yue, Z. N.; Wong, K. S.; Yuen, M. M. F.; Tang, B. Z. *Polym. Chem.* **2012,** *3*, 1481-1489.

58 Zhou, H.; Wang, X. B.; Lin, T. T.; Song, J.; Tang, B. Z.; Xu, J. W. *Polym. Chem.* **2016,** *7*, 6309-6317.

59 Xu, B. W.; Wu, X. F.; Li, H. B.; Tong, H.; Wang, L. X. *Macromolecules* **2011,** *44*, 5089-5092.

60 Wang, T. S.; Zhang, N.; Bai, R. K.; Bao, Y. Y. *J. Mater. Chem. C* **2018,** *6*, 266-270.

61 Frisch, M. J.; Trucks, G. W.; Schlegel, H. B.; Scuseria, G. E.; Robb, M. A.; Cheeseman, J. R.; Scalmani, G.; Barone, V.; Mennucci, B.; Petersson, G. A.; Nakatsuji, H.; Caricato, M.; Li, X.; Hratchian, H. P.; Izmaylov, A. F.; Bloino, J.; Zheng, G.; Sonnenberg, J. L.; Hada, M.; Ehara, M.; Toyota, K.; Fukuda, R.; Hasegawa, J.; Ishida, M.; Nakajima, T.; Honda, Y.; Kitao, O.; Nakai, H.; Vreven, T.; Montgomery, J. A.; Peralta, Jr., J. E.; Ogliaro, F.; Bearpark, M.; Heyd, J. J.; Brothers, E.; Kudin, K. N.; Staroverov, V. N.; Keith, T.; Kobayashi, R.; Normand, J.; Raghavachari, K.; Rendell, A.; Burant, J. C.; Iyengar, S. S.; Tomasi, J.; Cossi, M.; Rega, N.; Millam, J. M.; Klene, M.; Knox, J. E.; Cross, J. B.; Bakken, V.; Adamo, C.; Jaramillo, J.; Gomperts, R.; Stratmann, R. E.; Yazyev, O.; Austin, A. J.; Cammi, R.; Pomelli, C.; Ochterski, J. W.; Martin, R. L.; Morokuma, K.; Zakrzewski, V. G.; Voth, G. A.; Salvador, P.; Dannenberg, J. J.; Dapprich, S.; Daniels, A. D.; Farkas, O.; Foresman, J. B.; Ortiz, J. V.; Cioslowski, J.; Fox, D. J. Gaussian, Inc., Wallingford CT, **2013**.

Appendix

Table A3.1 Single Crystal data of 2,5-bis(4-bromostyryl)-3,4-diphenylthiophene (**TPBZ**).

S No.	Compound	TPBZ
1	Empirical formula	$C_{32}H_{22}Br_2S$
2	CCDC NO	1448141
3	Formula weight	598.38
4	Temperature/K	293 K
5	Crystal system	monoclinic
6	Space group	P21/c
7	a/Å	32.3903(14)
8	b/Å	7.3832(3)
9	c/Å	24.0582(11)
10	α/°	90
11	β/°	109.684(2)
12	γ/°	90
13	Volume/$Å^3$	5417.2(4)
14	Z	8
15	ρcalcmg/mm^3	1.467
16	m/mm^{-1}	3.088
17	F(000)	2400.0
18	Crystal size/mm^3	0.30 × 0.25 × 0.21
19	2Θ range for data collection	1.34 to 47.78°
20	Index ranges	$-36 \le h \le 36$, $-8 \le k \le 8$, $-27 \le l \le 23$
21	Reflections collected	53126
22	Independent reflections	8417[R(int) = 0.1079]
23	Data/restraints/parameters	8417/0/632
24	Goodness-of-fit on F2	1.204
25	Final R indexes [I>=2σ(I)]	R1 = 0.0943, wR2 = 0.2051
26	Final R indexes [all data]	R1 = 0.2034, wR2 = 0.2331

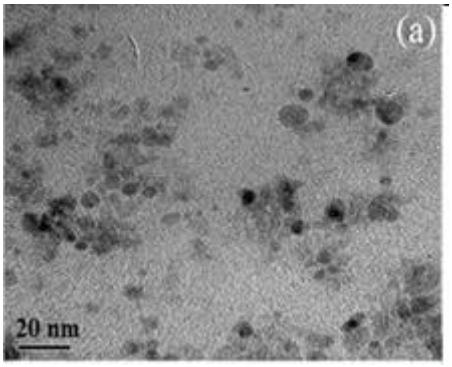

Figure A3.1: **(**a) TEM image of **TPBZ** (60% f_w).

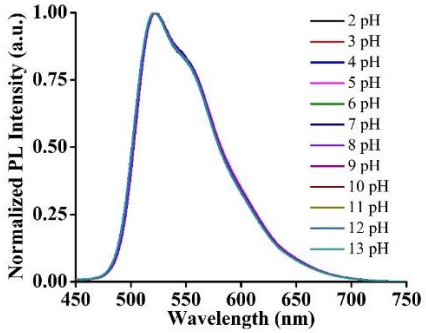

Figure A3.2: Change of fluorescence intensity of **PFTPBZ** in different buffer solutions.

K_{sv} calculation:

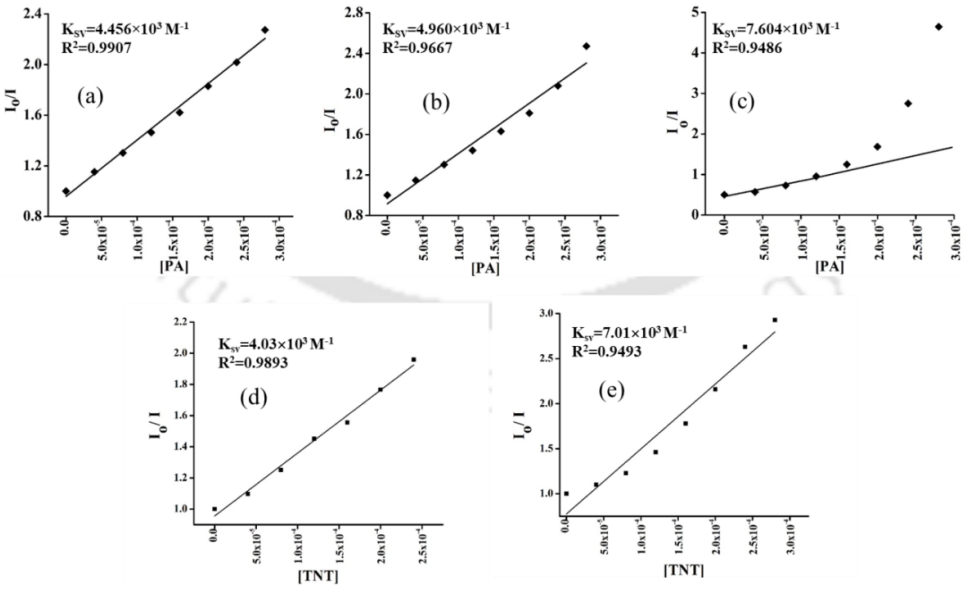

Figure A3.3: K_{sv} calculation for PA in 95% f_w (a), in THF (b) and in 40% f_w. K_{sv} calculation for TNT in 95% f_w (d) and in 40% f_w (e).

File: PFTPBZ THF 44uL PA ex 405 em 500 cnt 2500 ns 20.FL

❖ **Exponential Components Analysis (Reconvolution)**

Fitting range : [702; 2463] channels
χ^2 : 1.000

	B_i	ΔB_i	f_i (%)	Δf_i (%)	τ_i (ns)	$\Delta\tau_i$ (ns)
1	0.0067	0.0053	17.291	24.296	0.615	0.376
2	0.0220	0.0054	82.709	24.233	0.898	0.042

Shift : -0.196 ns(±1.914ns)
Decay Background: 0.991 (±0.155)
IRF background : 0.200

File: PFTPBZ THF ex 405 em 500 cnt 2500 ns 20.FL

❖ **Exponential Components Analysis (Reconvolution)**

Fitting range : [702; 2955] channels
χ^2 : 1.000

	B_i	ΔB_i	f_i (%)	Δf_i (%)	τ_i (ns)	$\Delta\tau_i$ (ns)
1	0.0265	0.0021	85.330	10.456	0.781	0.034
2	0.0029	0.0021	14.670	11.765	1.218	0.100

Shift : -0.169 ns(±1.107ns)
Decay Background: 0.791 (±0.120)
IRF background : 0.200

Figure A3.4: Fitting parameters and IRF values correspond to lifetime measurements in THF.

File: PFTPBZ 95% water 46uL PAex 405 em 530 cnt 2500 ns 50.FL

❖ **Exponential Components Analysis (Tail Fitting)**

Fitting range : [1025; 2500] channels
χ^2 : 0.999

	B_i	ΔB_i	f_i (%)	Δf_i (%)	τ_i (ns)	$\Delta\tau_i$ (ns)
1	2262.9146	13.2073	75.481	15.254	0.201	0.039
2	148.3885	5.7329	24.519	1.473	0.996	0.021

Shift : 0 ns (± 0 ns)
Decay Background : 0.741 (± 0.067)

File: PFTPBZ 95% water ex 405 em 530 cnt 2500 ns 50.FL

❖ **Exponential Components Analysis (Tail Fitting)**

Fitting range : [1025; 2680] channels
χ^2 : 1.000

	B_i	ΔB_i	f_i (%)	Δf_i (%)	τ_i (ns)	$\Delta\tau_i$ (ns)
1	2344.9890	12.9836	74.166	11.779	0.215	0.033
2	145.0541	4.4580	25.834	1.114	1.209	0.015

Shift : 0 ns (± 0 ns)
Decay Background : 0.925 (± 0.065)

Figure A3.5: Fitting parameters and IRF values correspond to lifetime measurements in 95% f_w.

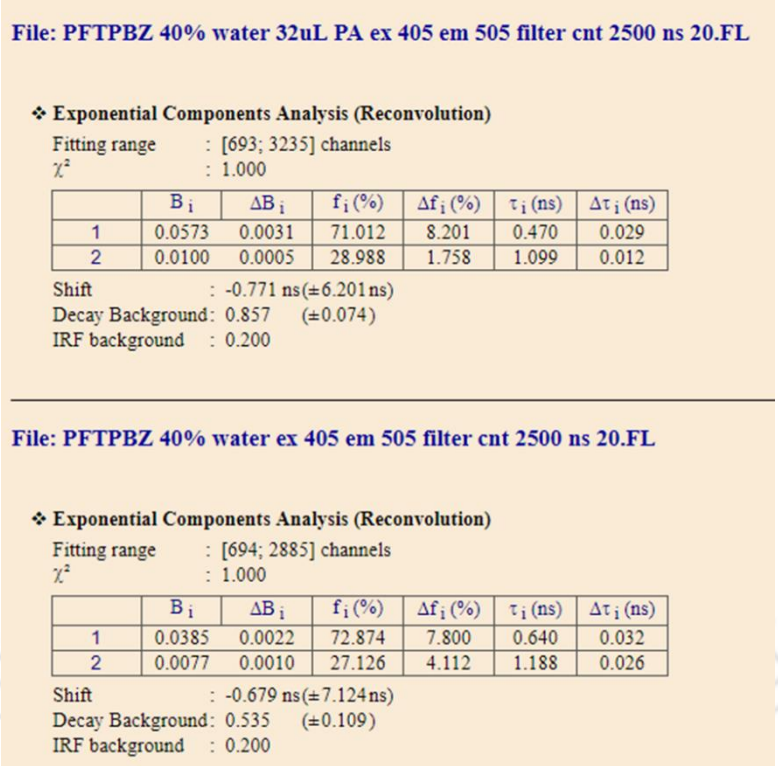

File: PFTPBZ 40% water 32uL PA ex 405 em 505 filter cnt 2500 ns 20.FL

❖ **Exponential Components Analysis (Reconvolution)**

Fitting range : [693; 3235] channels
χ^2 : 1.000

	B_i	ΔB_i	f_i (%)	Δf_i (%)	τ_i (ns)	$\Delta\tau_i$ (ns)
1	0.0573	0.0031	71.012	8.201	0.470	0.029
2	0.0100	0.0005	28.988	1.758	1.099	0.012

Shift : -0.771 ns (±6.201 ns)
Decay Background : 0.857 (±0.074)
IRF background : 0.200

File: PFTPBZ 40% water ex 405 em 505 filter cnt 2500 ns 20.FL

❖ **Exponential Components Analysis (Reconvolution)**

Fitting range : [694; 2885] channels
χ^2 : 1.000

	B_i	ΔB_i	f_i (%)	Δf_i (%)	τ_i (ns)	$\Delta\tau_i$ (ns)
1	0.0385	0.0022	72.874	7.800	0.640	0.032
2	0.0077	0.0010	27.126	4.112	1.188	0.026

Shift : -0.679 ns (±7.124 ns)
Decay Background : 0.535 (±0.109)
IRF background : 0.200

Figure A3.6: Fitting parameters and IRF values correspond to lifetime measurements in 40% f_w.

Average life time calculation

We calculate average life time of **PFTPBZ** in absence of PA (a,c,e) presence of PA (b,d,f) by using formula below-

<tau> = { (B*t)2}/{(Bi*t)} **Equation A3.1**

B- Amplitude of lifetime component

t- Respective lifetime value

Table A3.2: Average lifetime calculation in THF.

(a)	B	t	tsquare	B*tsquare	B*t
1	0.0265	0.781	0.609961	0.016163967	0.020697
2	0.0029	1.218	1.483524	0.00430222	0.003532
(b)	B_i	t	tsquare	B*tsquare	B*t
1	0.0067	0.615	0.378225	0.002534108	0.004121
2	0.022	0.898	0.806404	0.017740888	0.019756

Table A3.3: Average lifetime calculation in 40% f_w.

(c)	B	t	tsquare	B*tsquare	B*t
1	0.0385	0.64	0.4096	0.0157696	0.02464
2	0.0077	1.188	1.411344	0.010867349	0.009148

(d)	B_i	t	tsquare	B*tsquare	B*t
1	0.0573	0.47	0.2209	0.01265757	0.026931
2	0.01	1.099	1.207801	0.01207801	0.01099

Table A3.4: Average lifetime calculation in 95% f_w.

(e)	B	t	tsquare	B*tsquare	B*t
1	2344	0.215	0.046225	108.3514	503.96
2	145	1.209	1.461681	211.943745	175.305

(f)	B_i	t	tsquare	B*tsquare	B*t
1	2262.9146	0.201	0.040401	91.42401275	454.8458
2	148.3885	0.996	0.992016	147.2037662	147.7949

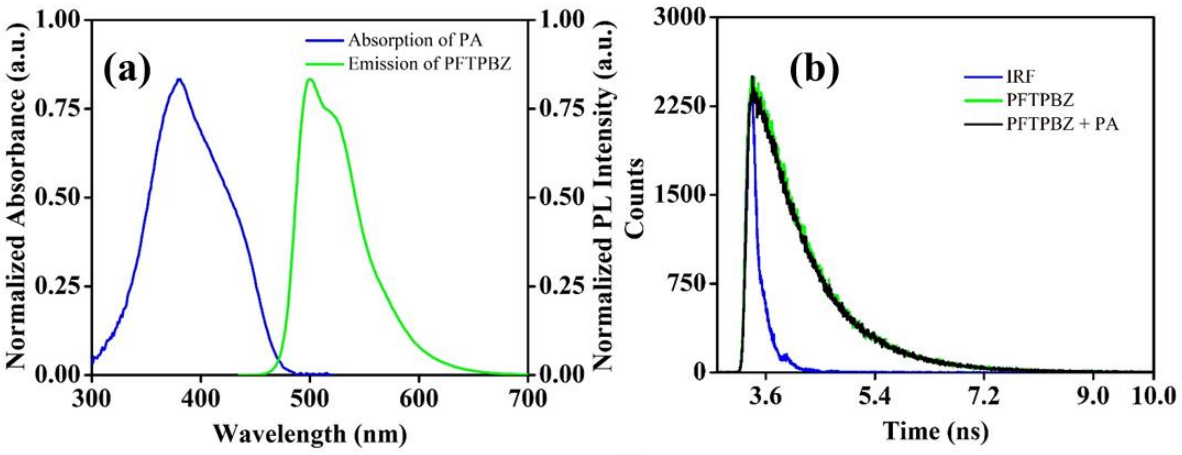

Figure A3.7: (a) UV-vis of PA and PL spectra of **PFTPBZ** overlapping (b) TRPL of **PFTPBZ** in presence and absence of PA in THF.

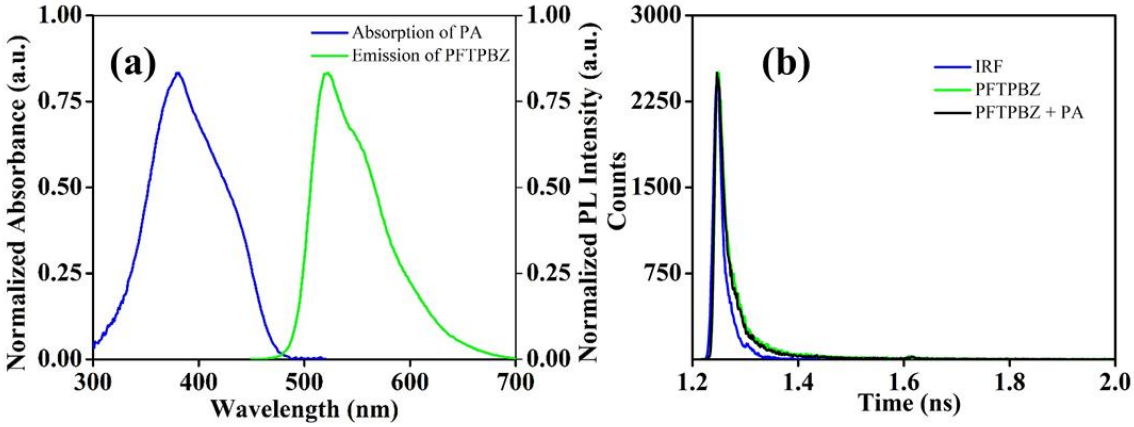

Figure A3.8: (a) UV-vis of PA and PL spectra of **PFTPBZ** overlapping (b) TRPL of **PFTPBZ** in presence and absence of PA in 95% f_w.

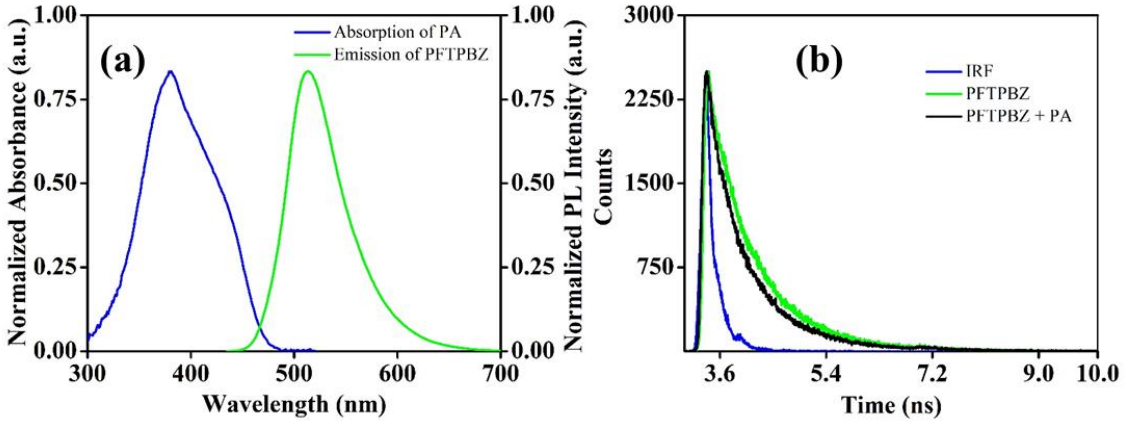

Figure A3.9: (a) UV-vis of PA and PL spectra of **PFTPBZ** overlapping (b) TRPL of **PFTPBZ** in presence and absence of PA in 40% f_w.

Limit of detection calculation

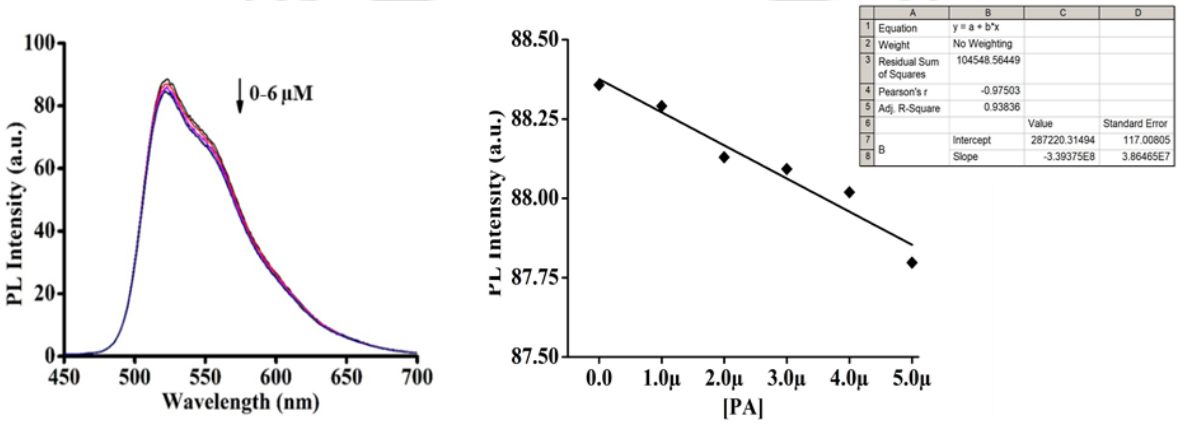

Figure A3.10: Change of fluorescence intensity of **PFTPBZ** in lower concentration of PA in 95% f_w.

Equation A3.2: LOD = 3 × S.D. / k

LOD for PA= 3 × 1184.40 / 3.39 × 10^{7}

= 10.47 × 10^{-6} M (23.98 ppm)

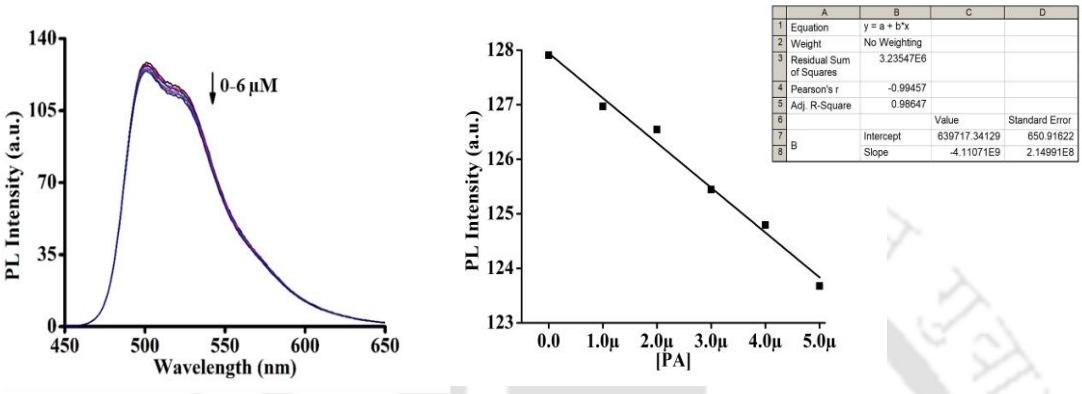

Figure A3.11: Change of fluorescence intensity of **PFTPBZ** in lower concentration of PA in THF.

Equation A3.3: LOD = 3 × S.D. / k

LOD for PA = 3 × 3858.40 / 4.11 × 10^{9}

= 28.16 × 10^{-7} M (6.45 ppm)

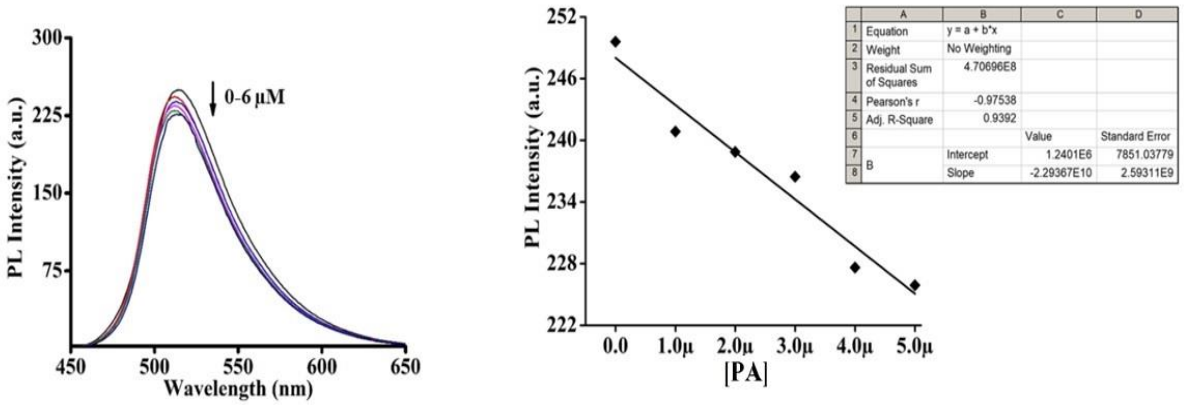

Figure A3.12: Change of fluorescence intensity of **PFTPBZ** in lower concentration of PA in 40% water.

Equation A3.4: LOD = 3 × S.D. / k

LOD for PA = 3 × 3617.911 / 2.29 × 10^{10}

$= 47.39 \times 10^{-8}$ M (1.08 ppm)

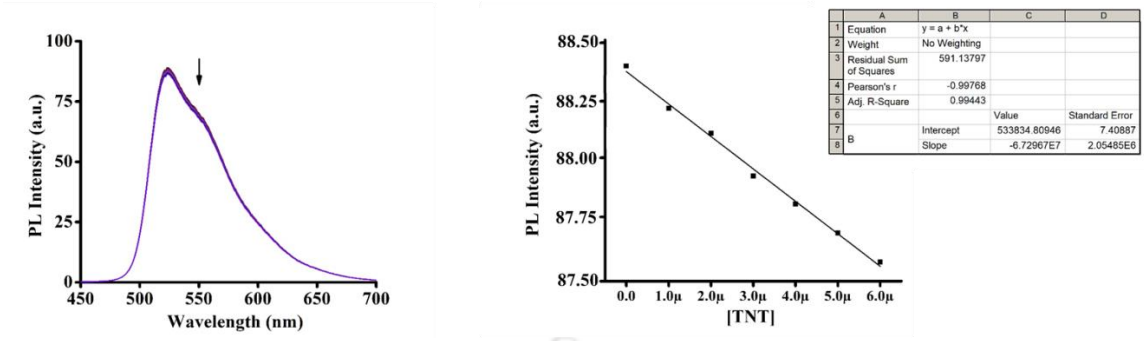

	A	B	C	D
1	Equation	y = a + b*x		
2	Weight	No Weighting		
3	Residual Sum of Squares	591.13797		
4	Pearson's r	-0.99768		
5	Adj. R-Square	0.99443		
6			Value	Standard Error
7	B	Intercept	533834.80946	7.40887
8		Slope	-6.72967E7	2.05485E6

Figure A3.13: Change of fluorescence intensity of **PFTPBZ** in lower concentration of TNT in 95% f_w.

Equation A3.5: LOD = 3 × S.D. / k

LOD for PA = $3 \times 1203.91 / 6.72 \times 10^{7}$

$=53.74 \times 10^{-6}$ M (123.11 ppm)

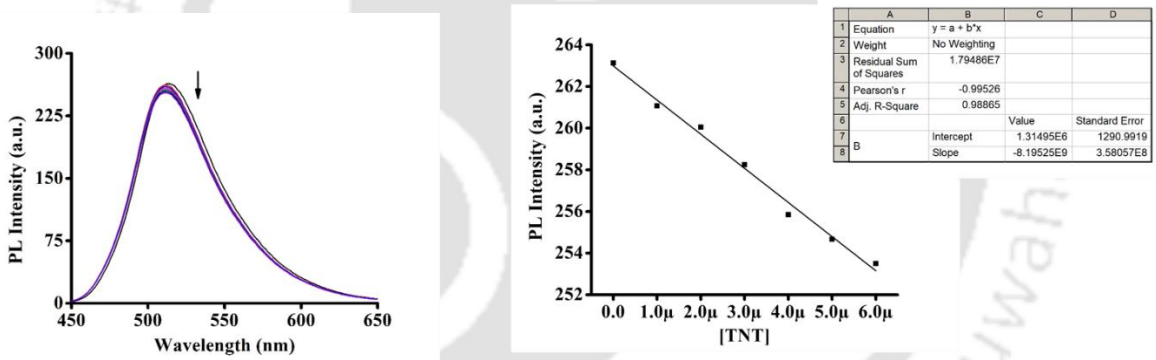

	A	B	C	D
1	Equation	y = a + b*x		
2	Weight	No Weighting		
3	Residual Sum of Squares	1.79486E7		
4	Pearson's r	-0.99526		
5	Adj. R-Square	0.98865		
6			Value	Standard Error
7	B	Intercept	1.31495E6	1290.9919
8		Slope	-8.19525E9	3.58057E8

Figure A3.14: Change of fluorescence intensity of **PFTPBZ** in lower concentration of TNT in 40% f_w.

Equation A3.6: LOD = 3 × S.D. / k

LOD for PA = $3 \times 3892.40 / 8.19 \times 10^{9}$

$=14.26 \times 10^{-7}$ M (3.26 ppm)

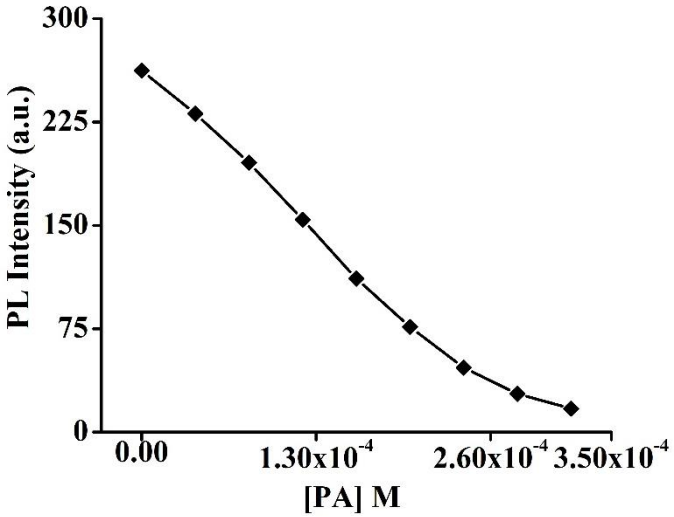

Figure A3.15: Calibration plot obtained by addition of different concentration of PA in **PFTPBZ** in 40% f_w for estimation of PA in different water resources.

Table A3.5: Estimation of PA in various natural water resources

S. No.	Water Samples	Sample added (10^{-5} M)	Found (10^{-5} M)	Recovered (%)
1	Lake 1	3	2.8	93.3
2	Lake 2	6	5.7	95.0
3	River 1	9	8.6	95.5
4	River 2	15	14.8	98.6
5	Sea water	20	18.4	92.0

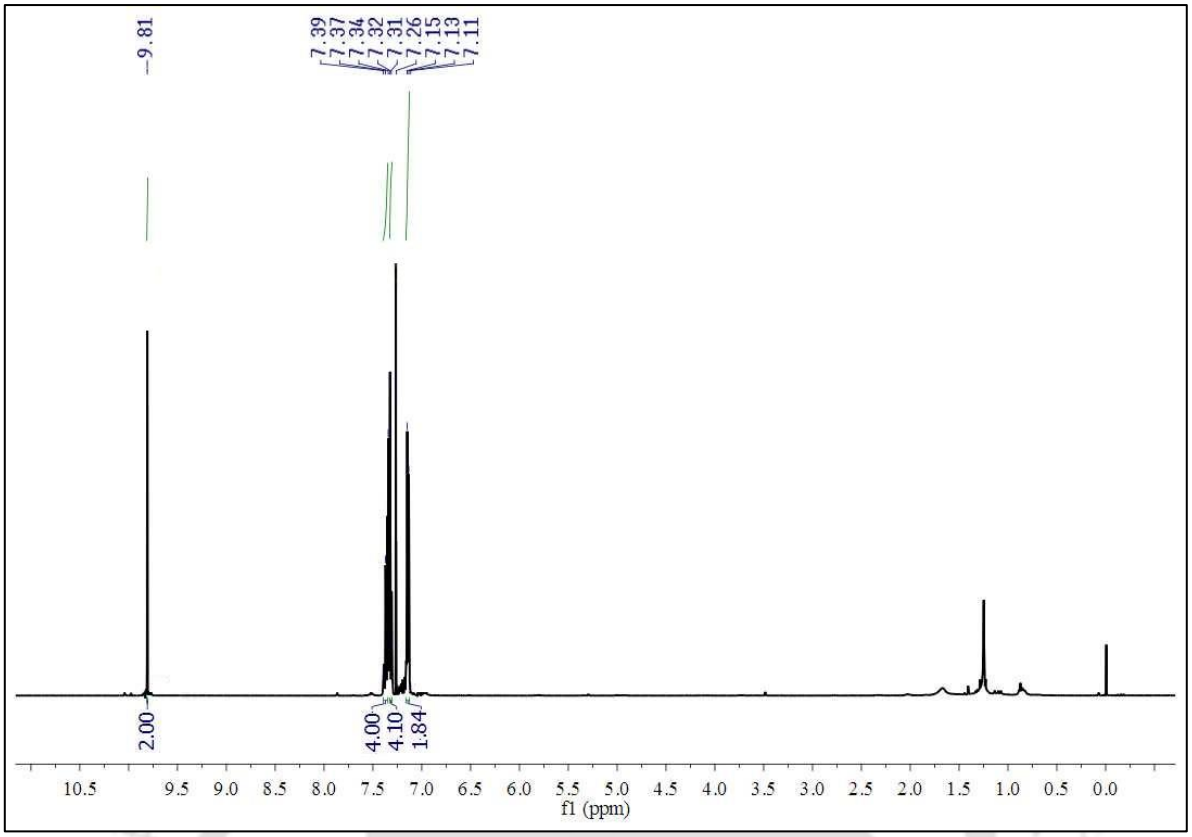

^{1}H NMR Spectra of 3,4-diphenylthiophene-2,5-dicarbaldehyde.

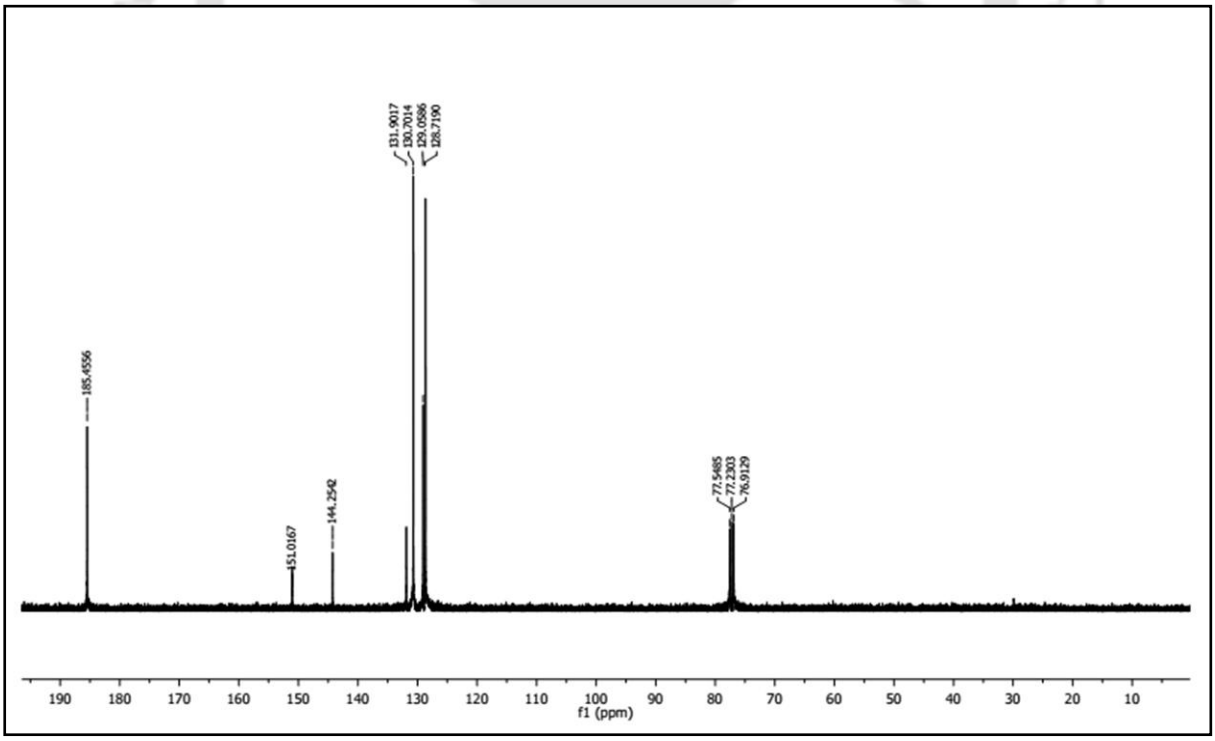

^{13}C NMR Spectra of 3,4-diphenylthiophene-2,5-dicarbaldehyde.

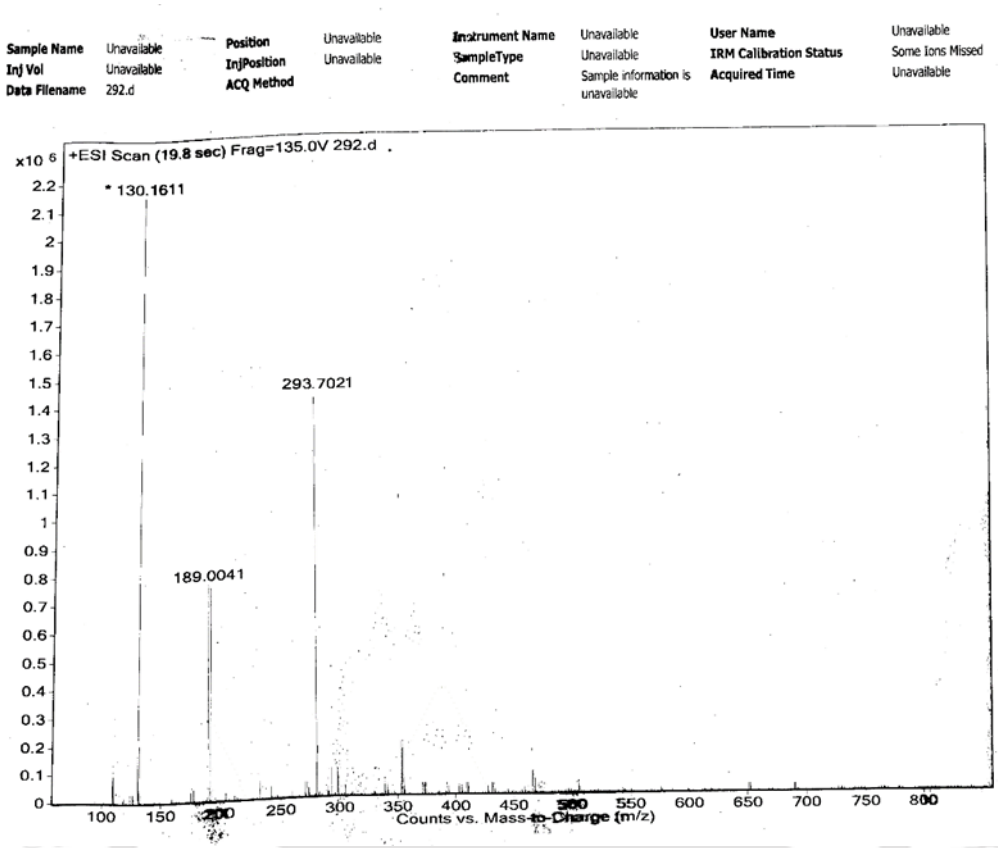

HRMS of 3,4-diphenylthiophene-2,5-dicarbaldehyde.

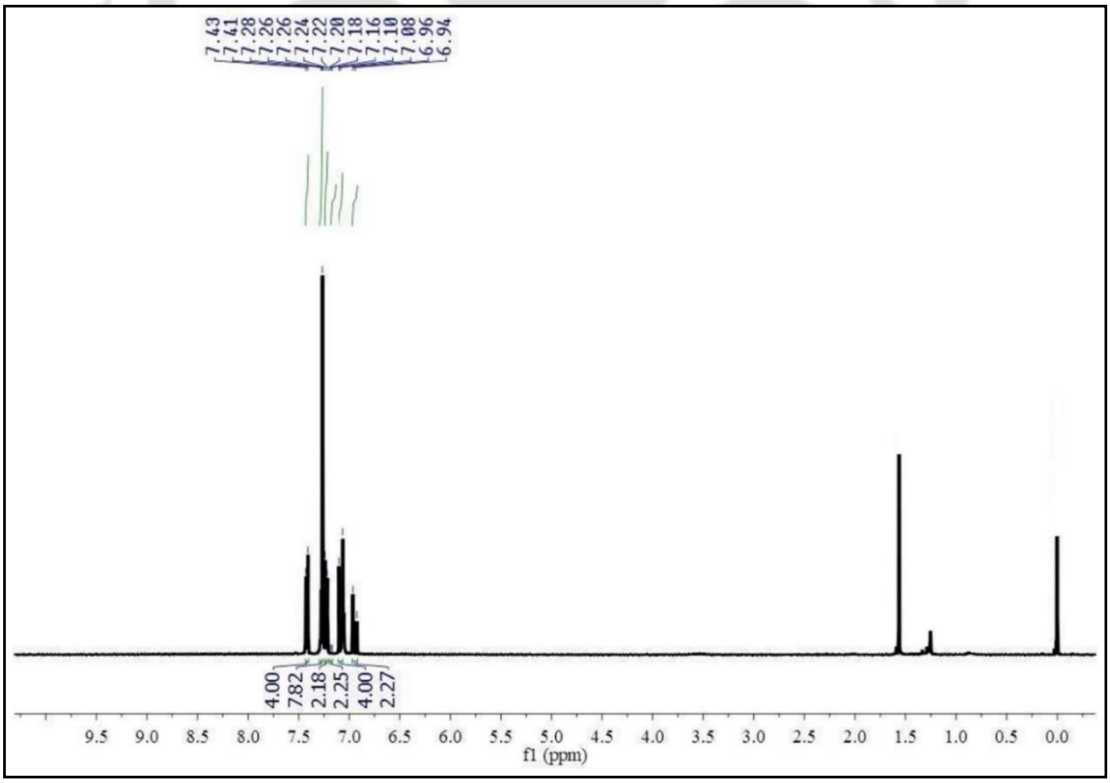

^{1}H NMR Spectra of 2,5-bis(4-bromostyryl)-3,4-diphenylthiophene.

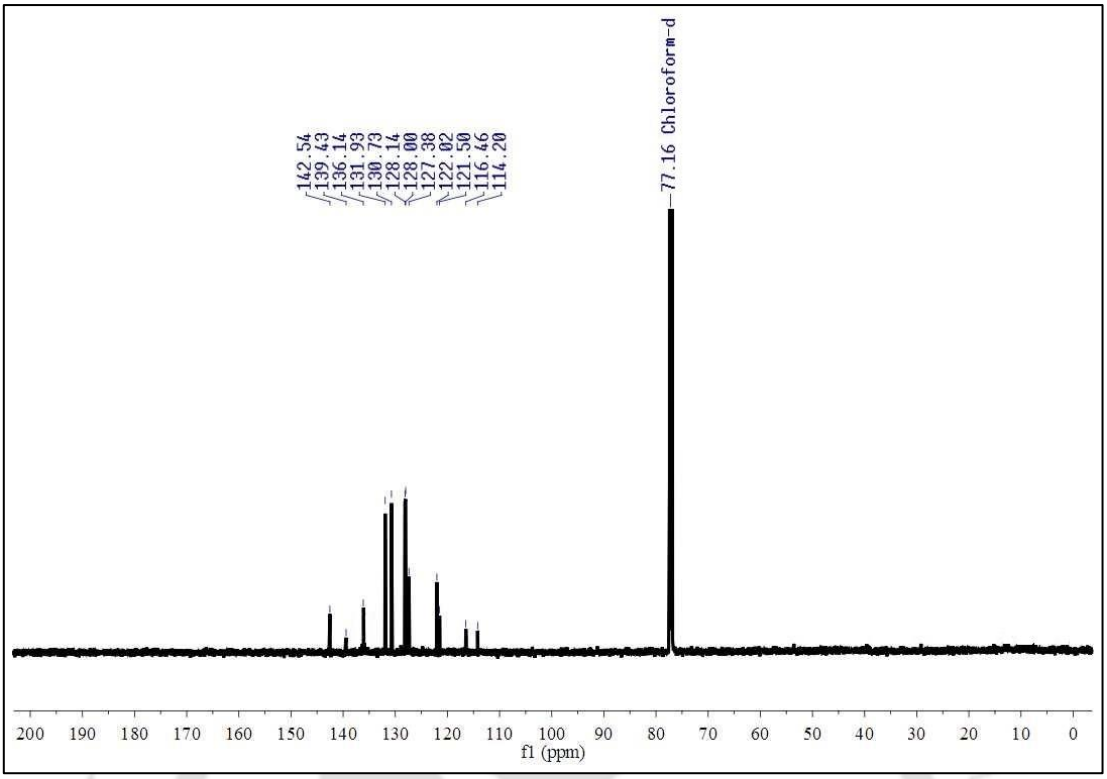

^{13}C NMR Spectra of 2,5-bis(4-bromostyryl)-3,4-diphenylthiophene.

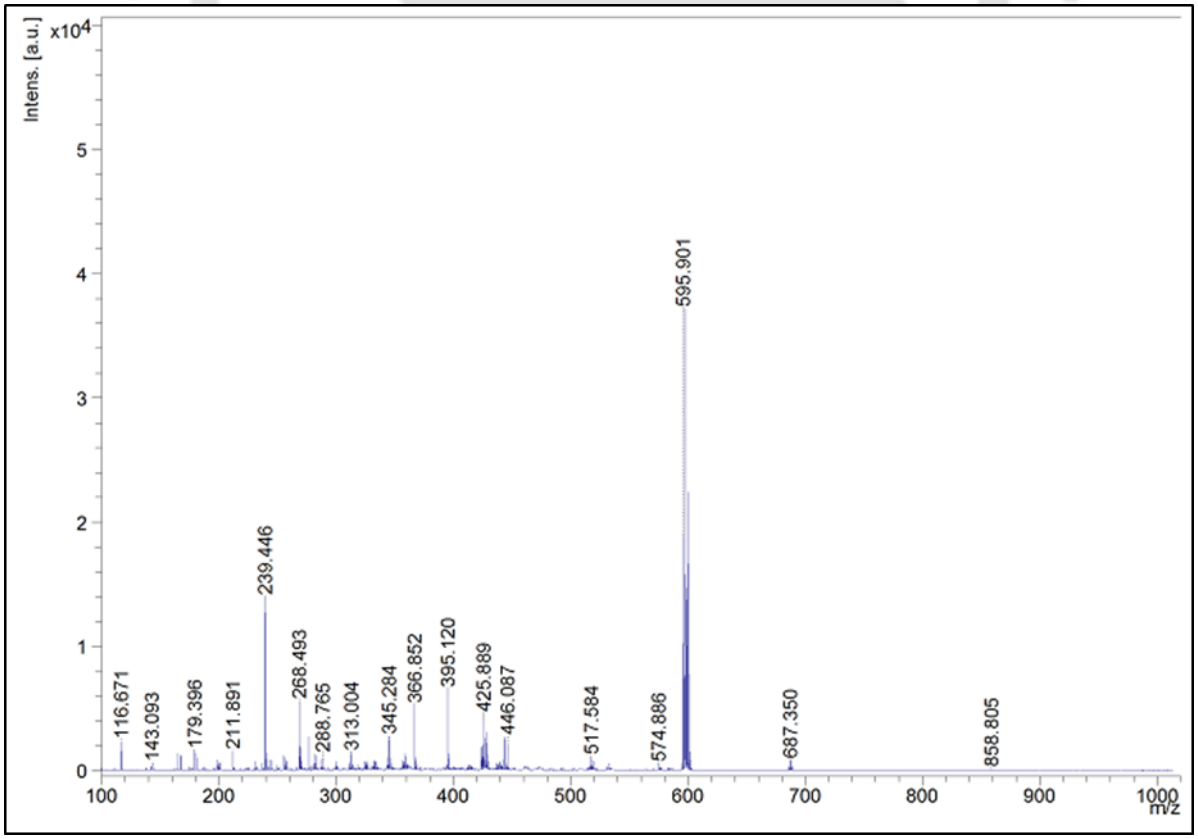

MALDI TOF of 3,4-diphenylthiophene-2,5-dicarbaldehyde.

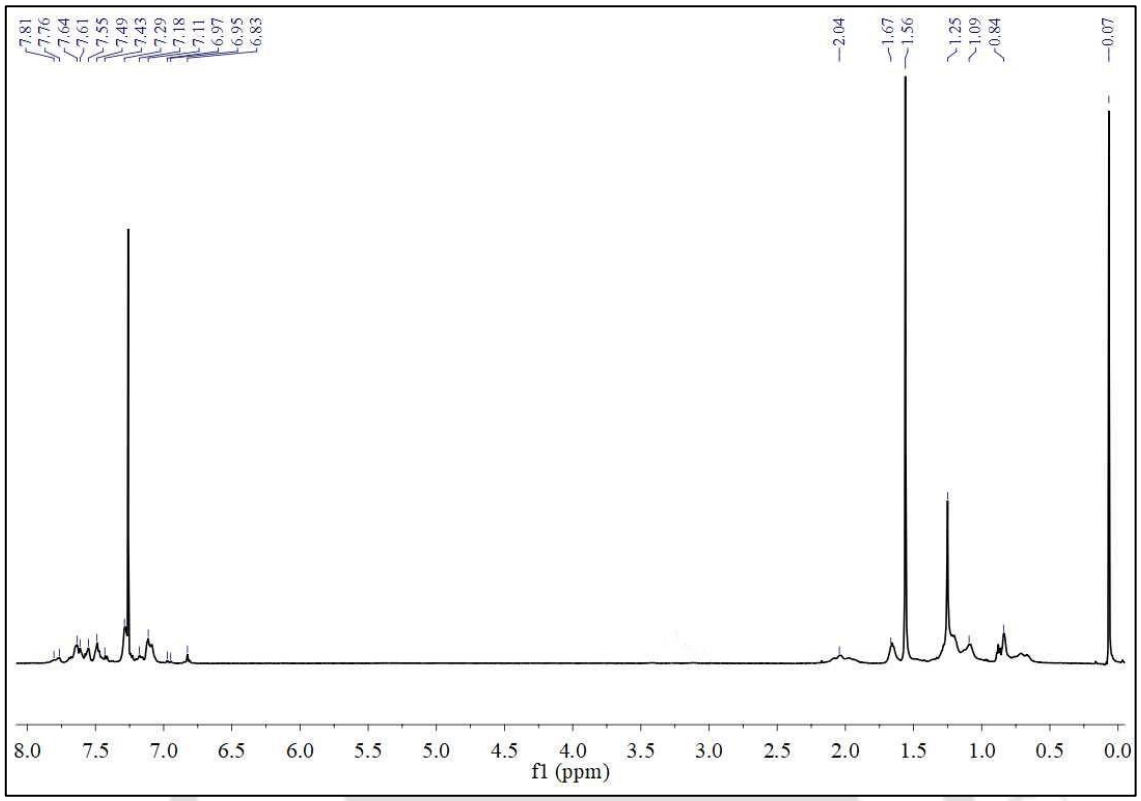

^{1}H NMR Spectra of **PFTPBZ**.

Reference

1. Dennis, W. H.; Rosenblatt, D. H.; Blucher, W. G.; Coon, C. L. *J. Chem. Eng. Data.* **1975,** *20*, 202-203

CHAPTER 4

Effects of incorporating regioisomers and flexible rotors to direct aggregation-induced emission to achieve stimuli-responsive luminogens, security inks and chemical warfare agent sensors

Adil, L. R.; Iyer, P. K. *Chem. Commun.*, 2020, **56**, 7633-7636.

Abstract

Fluorophores having aggregation-induced emission (AIE) and solid-state emission are intriguing molecules since they display higher fluorescence in the condensed or aggregate state since they do not suffer from the notorious aggregation-caused quenching (ACQ) effect. The three molecules presented here are the first examples of efficient transformation of ACQ molecule into an AIE system strategically using a simple design principle of C-C bond removal. Consequently, the bond link, bond position and their effects on optical properties have been carefully deliberated and shown to have a conceptually very close and profound relationship. To study these combined effects three fluorophores 4-(4-((9*H*-fluoren-9-ylidene)methyl)phenyl)pyridine (**1PN**), 4-(2-((9*H*-fluoren-9-ylidene)methyl)phenyl)pyridine (**1PON**) and 4-(4-(2,2-diphenylvinyl)phenyl)pyridine (**3PN**) were designed and synthesized *via* Knoevenagel condensation, Wittig-Horner reaction, Suzuki coupling reaction and their unique optical properties were compared. Consequently, the bond link, position and packing influence the photophysical properties that can be utilized in erasable secret inks, pressure sensors and chemical warfare sensors.

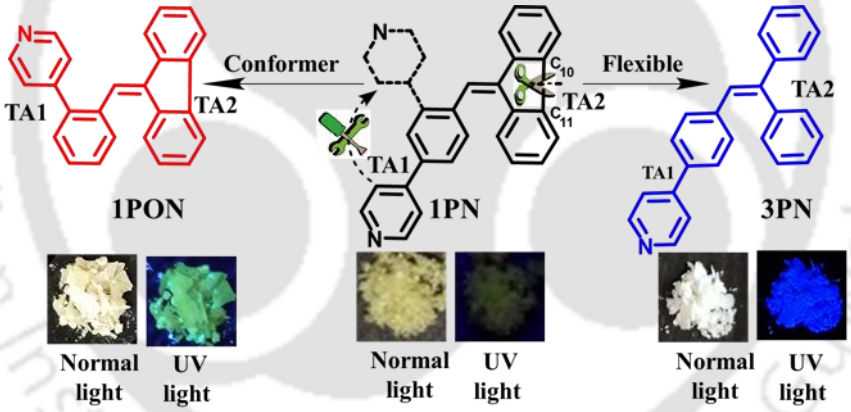

4.1 Introduction

The design of conceptually new AIE materials, including identifying precise structures, and finding apt avenues for utilizing them are important research themes. The progress in molecular fluorescence, especially in AIE luminogens, has led to significant leaps in the field of imaging, diagnosis, sensors and optoelectronics because of higher selectivity, sensitivity, quantum yield, condensed state property and tunable structural design. Classical organic luminogens have planar aromatic rings and exhibit enormous emission in the dilute solution state but show much less or nearly quenched emission at a higher concentration, in the aggregated state or in the solid-state.[1] Aggregates, ''a whole formed by combining several separate elements'' are also an ensemble or a cluster.[2] In fluorescence, the emission of a luminogen in solution is quenched at a higher concentration and is called concentration quenching (CQ). The CQ phenomenon is referred to as aggregation-caused quenching (ACQ) and typically classical aromatic compounds suffer from this ACQ effect.[3,4] While the ACQ effect can be limited to some extent by reducing the concentration, the diluted luminogen has much less emission, thereby the problem of faint emission remains unsolved, hence limiting their practical utility. Tang *et al*.[5] reported a few non-planar aromatic compounds which have exactly opposite emission properties to classical ACQ, and are the most fascinating because of their broad applications. These non-classical (non-planar) compounds have enabled extensively bright emission due to the formation of aggregates, and hence are referred to as aggregation-induced emission (AIE).[6] In the individual state, they were weakly emissive due to the intramolecular rotation or vibration, but in the aggregated state, they have a higher emission because of the restriction of the intramolecular rotation (RIR) or vibration (RIV).[7] AIE compounds have a wide range of applications such as in chemosensing,[8] bioimaging,[9] photodynamic therapy,[10] drug delivery[11] and OLED devices.[12] The effective emission of these compounds in the aggregated state is ascribed to their nonplanarity that hampers the π-p stacking and prevents ACQ.[13] This non-planarity and rotor groups are especially required for emission in aggregated and solid states. Yet generating the AIE effect by designing positional isomers and varying the bonding pattern has remained elusive and not been previously examined.

In the present work, three novel non-planar molecules (**1PN**, **1PON** and **3PN**) are designed and synthesized *via* Knoevenagel condensation, Wittig-Horner and Suzuki

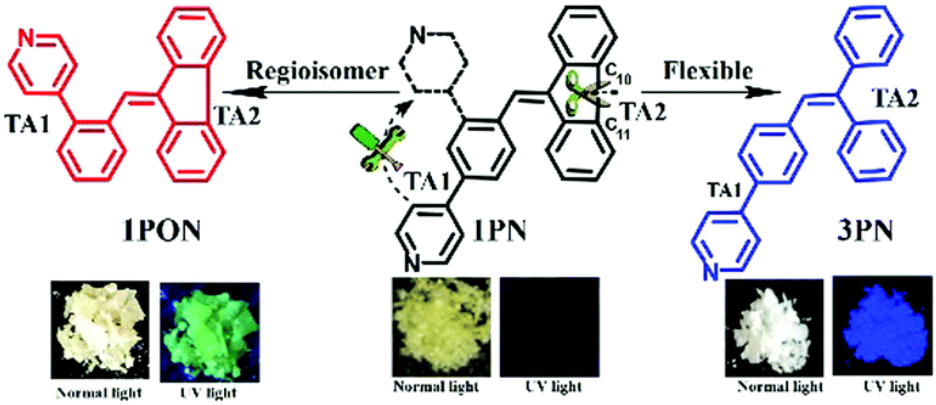

Figure 4.1: Chemical structure of **1PN**, **1PON** and **3PN** with important twist angles (TA). Picture of PN luminogens under a UV lamp, respectively.

coupling reactions. **1PN** and **1PON** molecules are regioisomers, while **3PN** is an analogue of **1PN** and it is devoid of one C-C bond, thus altering their packing behaviour and endowing them with profoundly diverse photophysical properties. The connectivity difference between **1PN** and **3PN** is a bond between the two carbons (C_{10}, C_{11}) in fluorene, while the difference between **1PN** and **1PON** is the position of the pyridine group (positional isomers) (Figure 4.1). These minor structural changes enormously impact their packing behaviour thereby influencing their fluorescence properties, which have been utilized for sensing chemical warfare agents (CWAs).[14,15] CWAs are the less anticipated and more horrific race extermination agents used during combat and can be possessed by terrorists. There are different categories of CWAs *viz.* asphyxiate, blister and nerve agents (NAs). NAs inhibit the cholinesterase enzyme, found in the central nervous system (CNS), that hydrolyses the neurotransmitter acetylcholine.[16] Diethyl

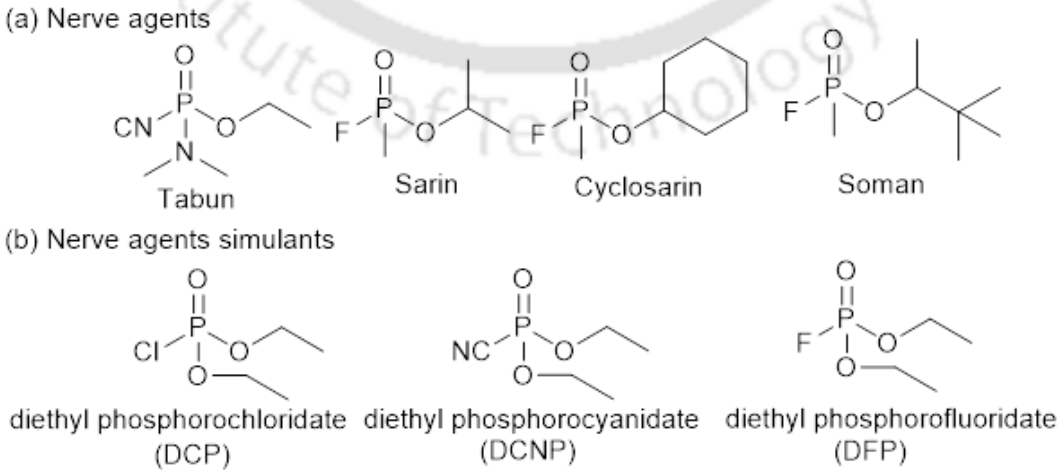

Figure 4.2: Chemical structure of tabun, sarin, cyclosarin, soman (nerve agents) and DCP, DCNP, DFP (nerve agent simulants).

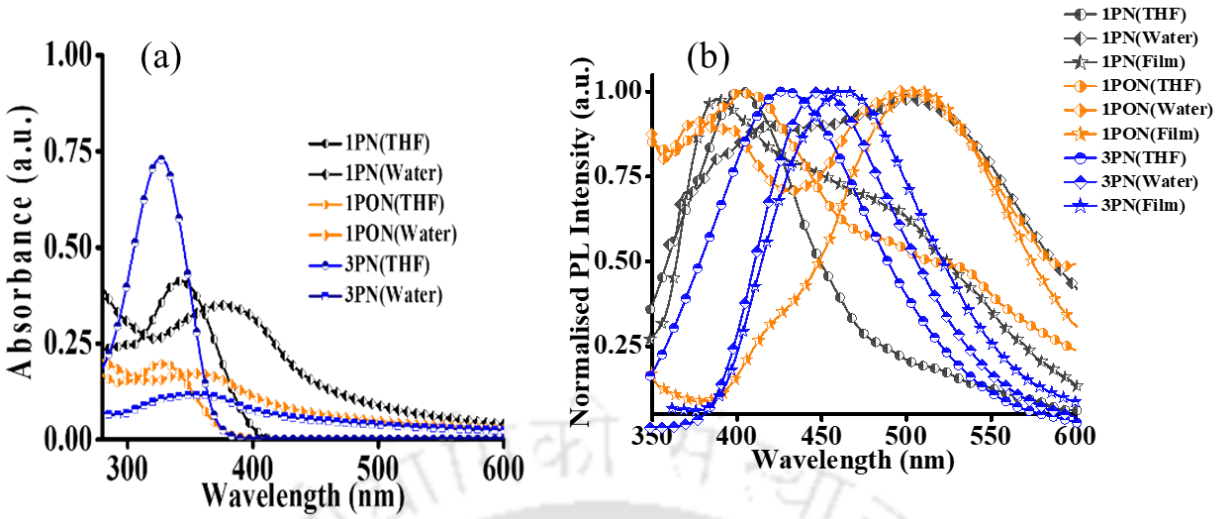

Figure 4.3: (a) UV-vis. spectra of PN derivatives in THF, 99% f_w and (b) PL spectra **1PN**, **1PON** and **3PN** in THF, 99% f_w and in the solid film at room temperature.

chlorophosphate (DCP) is used to mimic NA because it has the chemical activity similar to sarin, soman and tabun but has less acute toxicity (Figure 4.2). To date, NA sensing (mainly DCP) has been reported using electrochemistry,[17] high performance liquid chromatography (HPLC),[18] gas chromatography (GC)[19] and enzyme assays.[20] However these conventional methods suffer from multiple limitations such as tedious sample preparation, long response times, difficulties in portability and handling, cost efficiency, complexity, expensive instrumentation, etc. In contrast, fluorescent sensing of NAs is popular because of the quick response, high selectivity, simple handling and easy operation.[21]

4.2 Results and Discussion

4.2.1 Photophysical studies

The UV-vis (Figure 4.3a) and PL spectra (Figure 4.3b) of PN derivatives showed that the λ_{max} of the luminogens was in the order **3PN** < **1PON** < **1PN** since the two phenyl rings (P_1, P_2) of the fluorene in **1PN** (and **1PON**) are in the same plane, which

Table 4.1 1PN, **1PON** and **3PN** (a) UV-vis. spectra in THF, 99% f_w & (b) PL spectra in THF, 99% f_w, and as solid film, quantum yield in 99% f_w at room temperature at 10 µM concentration. [a]Quinine sulfate in 0.1 M H_2SO_4 (reference). [b] fluorescence was very low therefore quantum yield could not measure.

Compound	λ_{max} abs (nm) THF	λ_{max} abs (nm) H_2O	λ_{max} PL (nm) THF	λ_{max} PL (nm) H_2O (99% f_w)	λ_{max} PL (nm) Solid	Φ_f[a] (%) THF	Φ_f[a] (%) H_2O
1PN	343	379	403,520	419,503	389,492	b	b
1PON	329	358	406,528	388,500	507	b	11.6
3PN	326	354	428	450	464	b	73.2

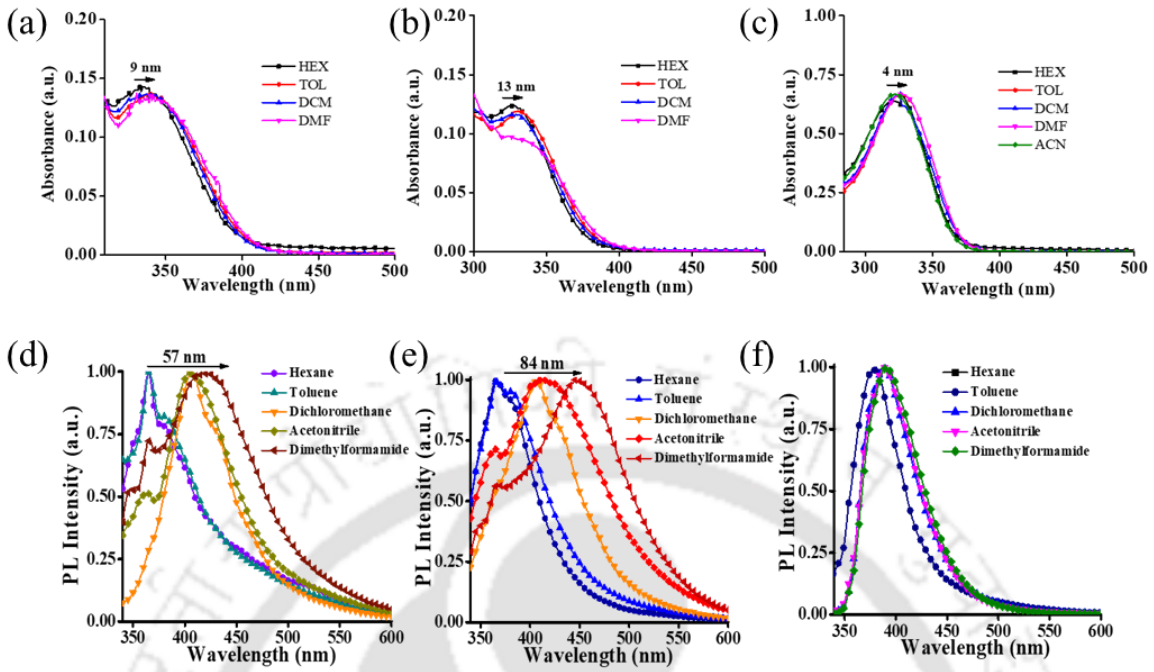

Figure 4.4: UV vis. spectra of (a) **1PN** (b) **1PON** (c) **3PN** and pl spectra of (d) **1PN** (e) **1PON** (f) **3PN** in different polar solvents, all spectra were taken at room temperature.

influences the effective conjugation length and absorbs at higher wavelength as compared to **3PN** with rotatable phenyl rings. The PL spectra of **1PN** showed two peaks at 403 and 520 nm in the THF solution, 419 and 503 nm in the aggregate state and 389 and 492 nm in the thin films. **1PON** had two peaks at 406 and 528 nm in the THF solution, 388 and 500 nm in the aggregated state and 388 and 500 nm in the thin film (Table 4.1).[22]

The UV-vis and PL spectra (Figure 4.4)of the PN luminogens were studied by varying the polarity of the solvents. In UV-vis studies **1PN**, **1PON** and **3PN** showed 9, 13 and 4 nm red shift, while, in the PL spectra there were 57, 84 and 6 nm red shift for **1PN**, **1PON** and **3PN**, respectively. These results confirmed that except for **3PN**, both **1PN** and **1PON**, drastically suffered from the TICT effect.[23] The first peak is due to the local excitation state (LE) and the second peak is because of the twisted intramolecular charge transfer (TICT). **3PN** exhibited emissions at 428, 450 and 431 nm in THF solution, in the aggregate state, and in the crystal state, respectively. The PL spectra of **3PN** (Figure A4.1) showed a decrease in intensity at an acidic pH.

4.2.2 AIE studies

The AIE behaviour of **1PN**, **1PON** and **3PN** were studied by using PL spectroscopy in the THF-water mixtures. PN luminogens (10 mM) were taken in the THF solution and

the f_w was increased from 0% to 99% in the THF solution. Aggregates are likely to form when PN luminogens are introduced to the anti-solvent (water in this case). As shown in Figure 4.5a, **1PN** had a much lower emission in the soluble form (THF) and the emission further decreased on increasing the f_w. **1PON** showed less emission (Figure 4.5b) up to 60% f_w, but the enhancement in emission was at its maximum at 99% f_w, due to the RIR effect. 3PN (Figure 4.5c) was non-emissive in the THF solution but when the f_w increased to 95%, the emission recovery was huge and reached its maximum [73.2% Equation-A4.1] at 99% f_w again due to the RIR effect.[24] The PL spectra of 1PN crystals (Figure 4.5d) did not exhibit any emission, whereas, its isomer **1PON** (Figure 4.5e) exhibited a weak green emission, while the **3PN** (Figure 4.5f) exhibited an intense blue emission.

4.2.3 Nanoparticle formation studies

Nanoparticles of PN luminogens were formed by increasing f_w and their size was expressed as an average size distribution.

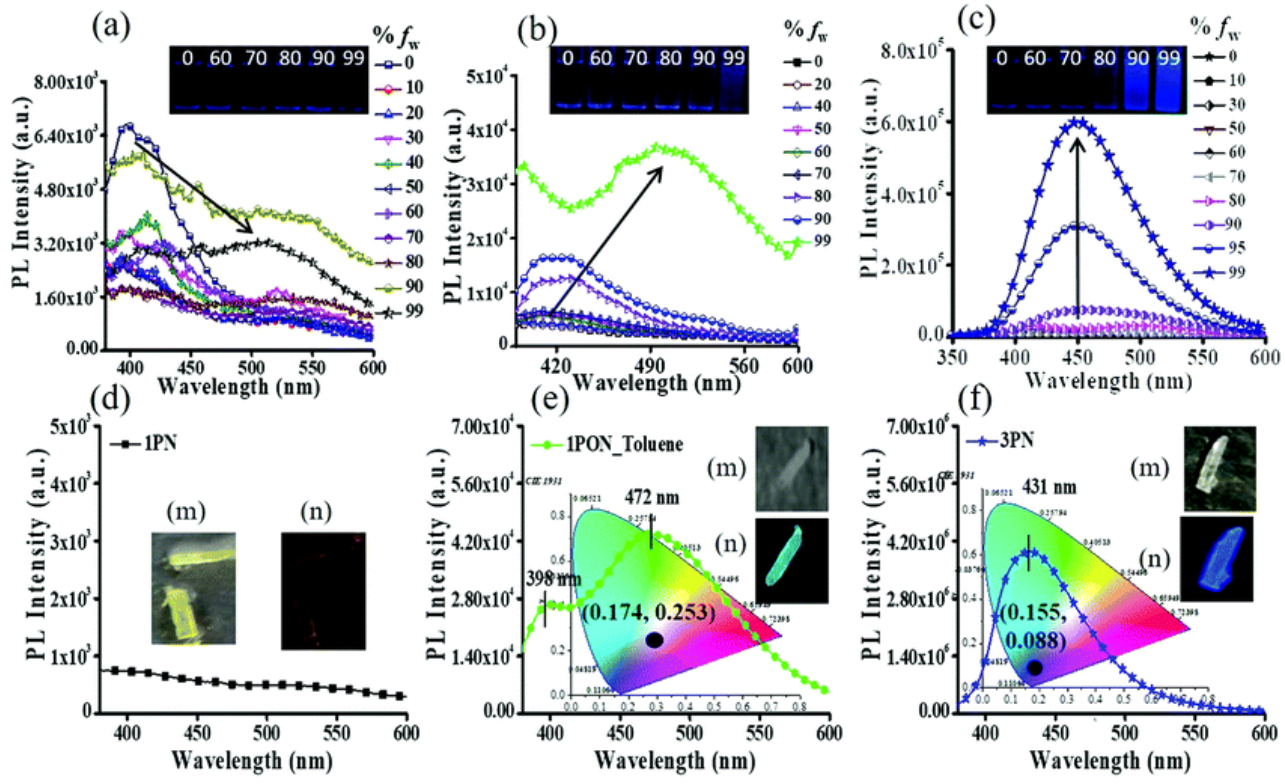

Figure 4.5: AIE studies of (a) **1PN**, (b) **1PON** and (c) **3PN** in the THF/water mixture (% f_w). PL spectra of a single crystal and the respective CIE coordinates of (d) **1PN**, (e) **1PON** and (f) **3PN**. Photos of the single crystal were taken under (m) normal light and (n) a UV lamp (365 nm).

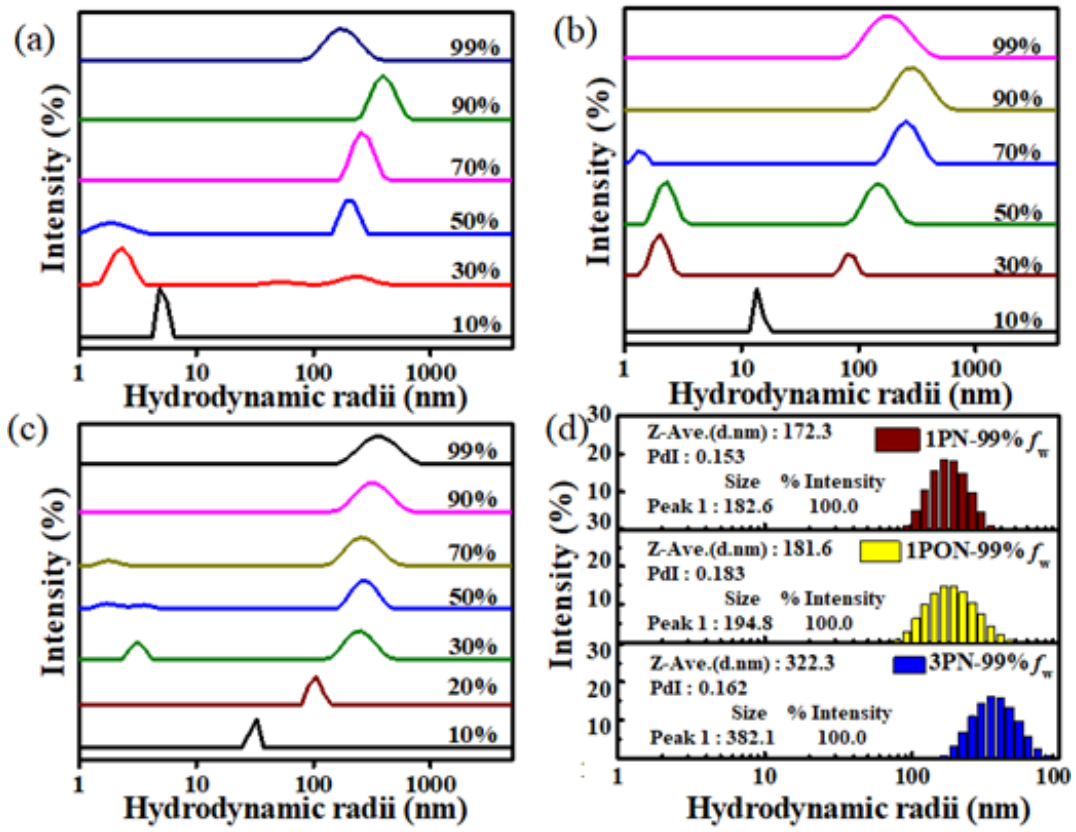

Figure 4.6: Study of nanoparticle formation of PN derivatives by DLS spectroscopy with increasing %f_w in THF (a) **1PN** (b) **1PON** (c) **3PN**. (d) Average nanoparticle size in the 99% f_w at room temperature (10 µM solution).

The DLS spectra suggested that the average sizes of **1PN**, **1PON** and **3PN** were 172.3, 181.6 and 322.3 nm, respectively (Figure 4.6), which revealed no nanoparticle formation of the PN luminogens in the organic solvents but the nanoparticles size increased with increasing fw. Nanoparticle formation was also confirmed by using FESEM (Figure A4.2) and AFM image analyses (Figure A4.3- Figure A4.5).

4.2.4 Theoretical calculation studies

The molecular structure parameters of the PN luminogens were considered from the single crystal X-ray diffraction (SCXRD) data and the theoretical calculations were carried out by using density functional theory (DFT) using the B3LYP/ 6-311G(d,p) basis set in Gaussian 09W software.[25] The LUMO electron cloud was found all over the molecule in **3PN** but localised mainly towards the pyridine in **1PN** and **1PON**. The HOMO electron cloud was mainly located on fluorene for **1PN** and **1PON** but for the **3PN**, the HOMO electron cloud was located all over the molecule (Figure 4.7). This strong donating nature originates from the fluorene group that induces robust charge transfer in isomers **1PN** and **1PON**. HOMO and LUMO orbitals in polymorphic **1PON_DCM** were more separated compared to the **1PON_Tol**, since single crystals

formed in a more polar solvent have a more twisted structure leading to a better HOMO-LUMO gap.

4.2.5 Single crystal X-ray structure

SCXRD establishes the relationship between molecular packing, conformation and optical properties.[26] Efforts to grow high-quality crystals of the PN luminogens paid off when slow evaporation of DCM in methanol resulted in quality crystals of **1PN** and **3PN** luminogens. The polymorphic crystals of **1PON** were obtained from both DCM and toluene solvents. The fluorescence properties of the PN luminogens were governed by twist angles (TAs), viz. TA1 and TA2 (Figure 4.1). The PN luminogens have distorted conformation leading to a highly twisted geometry, and their optical properties are governed by these TAs. In **1PN**, the dihedral angle between fluorene and phenyl, in the different planes, was 68.491°, whereas, the dihedral angle between phenyl and pyridine was 0.791° (TA1), hence they were in the same plane. In **1PON_Tol**, fluorene and phenyl were at 126.991° and the torsional angle between phenyl and pyridine was 42.031° (TA1). The dihedral angle between fluorene and phenyl in **1PON_DCM** was increased to 127.361° and the dihedral angle between phenyl and pyridine was increased to 43.191° (TA1). This higher TA between the donor and the acceptor results in increased nonplanarity. The **3PN** has three phenyl rings. Phenyl-1 (P_1) had a dihedral angle of 32.191°, phenyl-2 (P_2) had a dihedral angle of 74.651°, and phenyl-3 (P_3) had a dihedral angle of 16.321° w.r.t. the vinyl group, while pyridine had a dihedral

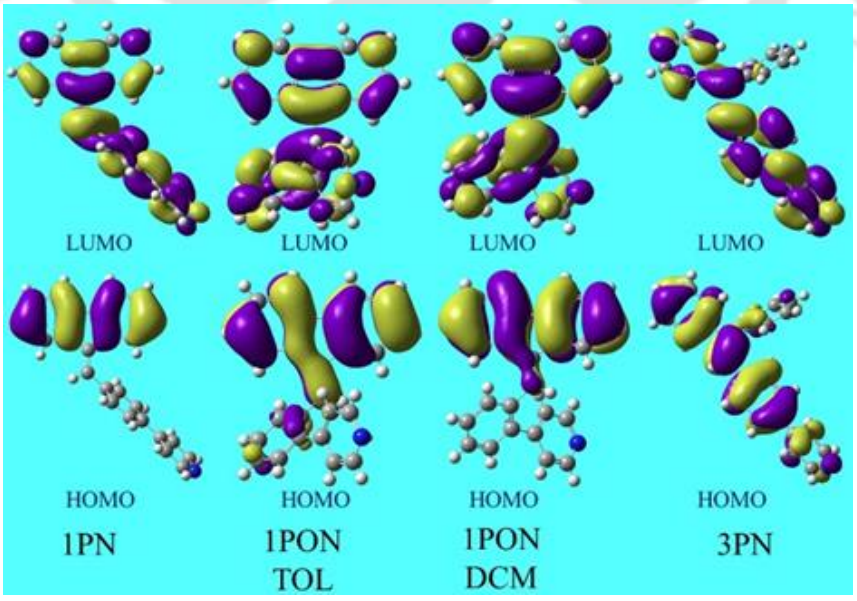

Figure 4.7: Frontier molecular orbitals (FMO) amplitude plots of **1PN, 1PON_Tol, 1PON_DCM** and **3PN** calculated by B3LYP/6-31G(d, p).

angle of 28.801° (TA1) w.r.t. P_3. **1PN** had pyridine attached to the para position of benzene and its TA1 was much less (0.791°); hence, it was not able to prevent π-π stacking. **1PN** was arranged in an antiparallel head to head manner and two **1PN** molecules were stacked by having a 0° planar angle and the distance between the two molecules was 3.519 Å (Figure 4.8$a_{1–3}$). The **3PN** molecule had 28.801° (TA1) between benzene (P_3) and pyridine which prevented their π-π stacking. The **3PN** displayed a head to tail arrangement with a 0° plane angle of the pyridine plane and the distance between the two planes was 2.894 Å, which is less than **1PN**, although there is no π-π stacking in **3PN**. As shown in Figure 4.8$b_{1–3}$, the non-planar P_3 ring made it impossible to allow co-facial π-π stacking. The rotatable non-planar benzene rings resulted in an intense blue solid-state emission in **3PN**. The **1PON** molecule had pyridine attached to the ortho position of benzene and had higher TA1, thereby inducing steric hindrance in this confirmation and preventing the facial approach of the isomer and making **1PON** completely non-planar. **1PON_Tol** (Figure 4.8$c_{1–}c_3$) and **1PON_DCM** (Figure 4.8$d_{1–}d_3$) molecules were arranged in a head to head manner with 39.971° and 39.981° planar angles and the distance of pyridine in the **1PON** molecules was 4.730 and 4.733 Å. **1PN** and **1PON** had TA2 of 0°; hence, it worked as a donor (fluorene) acceptor (pyridine) system and was influenced by the TICT effect. However, 3PN with a higher TA2 did not behave as a typical donor acceptor system; hence, 3PN did not suffer from the TICT effect. The difference between **1PN** and **3PN** is only one bond at the C_{10} and C_{11} positions. The **3PN** molecule was designed by modifying this C_{10}-C_{11} single bond in **1PN** which plays a very crucial role in generating its photophysical properties since it keeps the two phenyl rings (fluorene, TA2) in one plane. Hence, TA modifications in the three PN luminogens gave rise to a very unique condensed state and structural packing arrangements (Figure A4.6–A4.9). The summary of all four crystals of the PN molecules are given in Table A4.1-A4.4

4.2.6 Mechanochromic luminescenc

The disorder in packing arrangements or its reorganization on applying external stimuli such as mechanical force is the origin of mechanochromism (MC).[27] Surprisingly, the **1PON** crystal which was grown in the polar solvent DCM has more TICT, thus displaying a weak yellow emission (Figure 4.9a, CIE: 0.250, 0.344) under UV lamp illumination, which upon gentle grinding (mortar and pestle) turns blue in color (Figure 4.9b, CIE: 0.204, 0.263) with a clear emission increment.

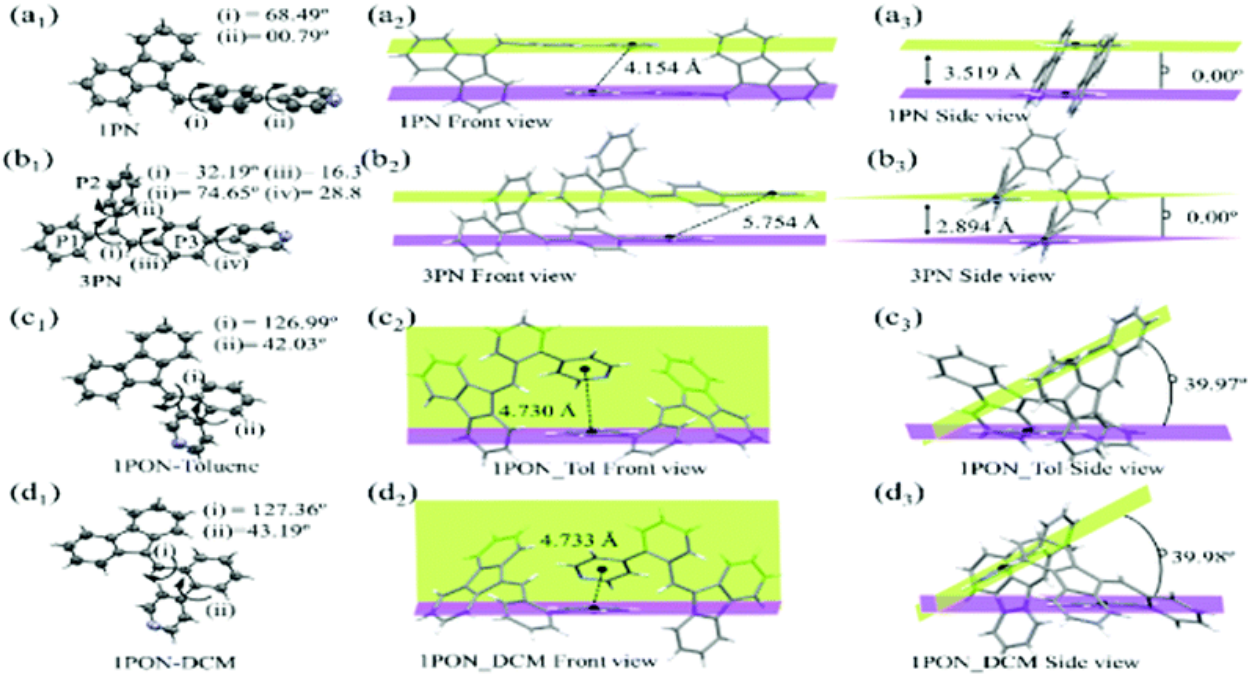

Figure 4.8: SCXRD: molecular structures and torsion angles of (a_1) **1PN**, (b_1) **3PN**, (c_1) **1PON_Toluene**, and (d_1) **1PON_DCM**. SCXRD: molecular arrangements of **1PN** (a_2,a_3), **3PN** (b_2, b_3), **1PON_Tol** (c_2,c_3), and **1PON_DCM** (d_2,d_3).

In non-crystalline form the weakening of the intermolecular interaction results in the loss of crystallinity that affects the electronic state delocalization causing a blue shifted emission enhancement after grinding, with a huge 90 nm emission shift. Such mechanochromic emission with hypsochromic shift in AIE regioisomers (**1PON**) systems is indeed unique.[28] However, no significant emission changes were found in the **1PN** and **3PN** crystals under external stimuli. In the case of **1PN** the strong π-π interaction prevents any disorder on applying a mechanical force. In case of **3PN**, despite the high crystallinity, it does not show any mechanochromic response due to the compact structural packing.[29]

A pressure responsive polymer thin-film doped **1PON** based system was also developed by using poly(dimethylsiloxane) (PDMS) membranes. The **1PON** doped PDMS free standing thin-film showed an excellent response towards pressure stimuli (Figure 4.9c and Figure A4.10). **3PN** and **1PON** also showed thermal-stimuli influenced fluorescence on-off in the solid state. When solid samples (powder) of **3PN** and **1PON** were heated, their emission faded very fast which on cooling was reversed multiple times. This reversible thermoresponsive behaviour was due to the recovery of the molecular arrangement after repeated heating-cooling cycles (Figure 4.9d).

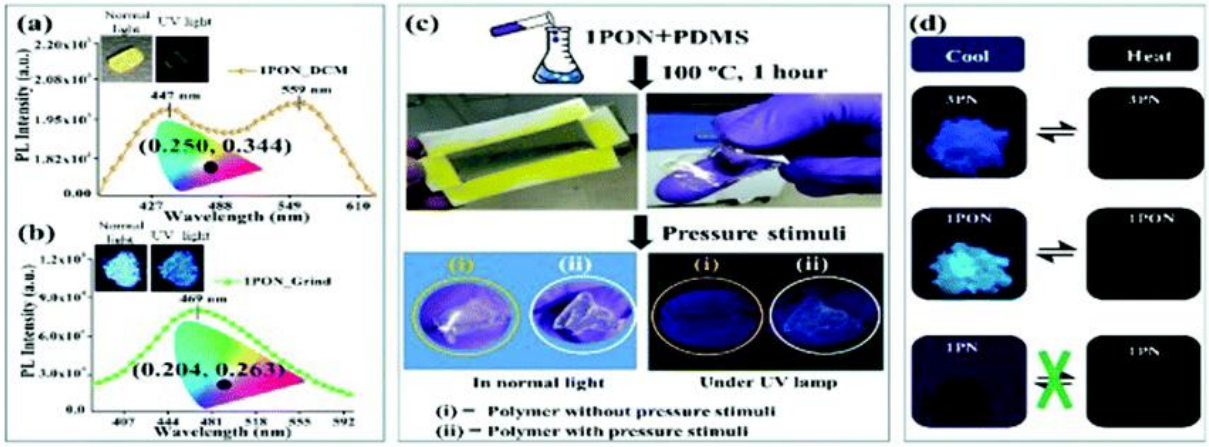

Figure 4.9: (a) PL spectra of the **1PON_DCM** crystal with CIE diagram (inset: picture of **1PON_DCM** crystal captured in daylight and under UV lamp illumination). (b) PL spectra of **1PON_DCM** after grinding to a powder with CIE diagram (inset: picture of **1PON_DCM** powder captured in daylight and under UV lamp illumination). (c) Pressure responsive thin-films made using PDMS doped **1PON** and a demonstration of the pressure stimuli. (d) Thermoresponsive emission studies of the PN luminogens (pictures taken under UV light 365 nm).

Additionally, **1PON** was also used as security inks and in message encryption, where he written message can be erased or read very secretly by using mechanical pressure and selective organic solvent fuming confirming their MC property (Figure 4.10).

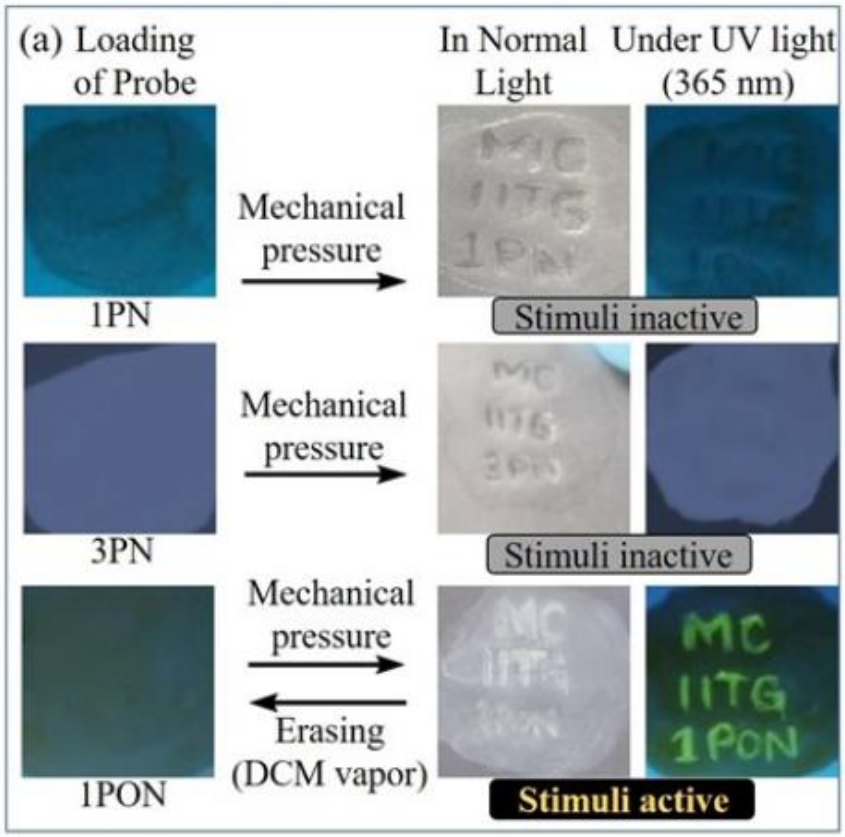

Figure 4.10: Mechanochromic emission study of PN derivatives in weighing paper and developing erasable secret ink using **1PON**.

4.2.7 Detection of CWAs

3PN has the highest emission in the solid state and in aqueous medium among all the PN luminogens, thus making it the best candidate for DCP sensing. The colorimetric and fluorometric detection of CWAs was performed by the exposure of diethyl chlorophosphate (DCP) vapors to the **3PN** probe in solution and in the solid phase. The aqueous phase detection of DCP by using **3PN** is very challenging, yet this probe showed a rapid response to different amounts of DCP in the range of 0-24 mM and its emission peak at 450 nm was quenched. Furthermore, after 12 mM addition, the colorimetry response was also observed that did not have any interference with the emission of the **3PN** probe (Figure 4.11a,b).

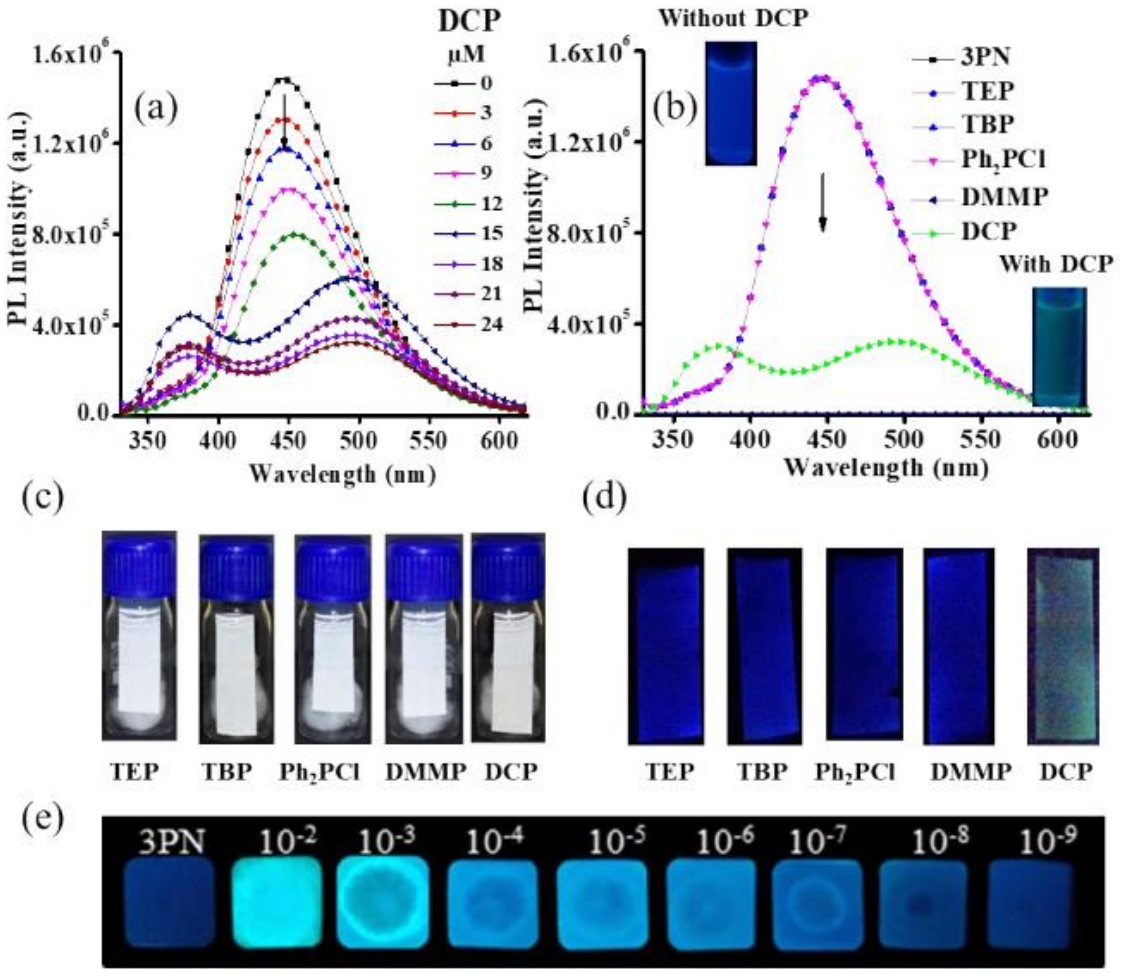

Figure 4.11: (a) PL spectra of **3PN** (10 μM) in 99% fw upon gradual addition of DCP (0-24 μM) (b) PL spectra of **3PN** 99% f_w after addition of different guest analytes (30 μM). Portable device made by **3PN** dipped Whatman filter paper for sensing CWAs vapors and similar analytes (100 μM) exposed (1 min) in (c) normal light (d) UV lamp (e) Whatman filter paper based device pictures sensing various CWA concentration by **3PN** under UV lamp.

These remarkable results with **3PN** in the aqueous phase encouraged us to develop a portable and inexpensive sensing system for DCP vapors and solution. Hence, the **3PN** dip-coated Whatman filter paper was exposed to DCP and its competing analytes for 1 minute. The emission of this handy and cost-efficient device was quenched only in the presence of DCP with very high selectivity (Figure 4.11c-e). The lowest limit of detection (LoD) was calculated to be 70.88 $x10^{-7}$ in water and 8.6 ng on a solid platform (Figure A4.11). Furthermore, the sensing mechanism was elucidated by using ^{1}H NMR (Figure A4.12) which confirmed that **3PN** emission was quenched because of the protonation in the presence of DCP.

4.3 Conclusions

In summary, three rotor incorporated, nonplanar compounds **1PN**, **1PON**, and **3PN** were engineered to conceptually generate AIE molecules in structural isomers as well as by modulating minor structural variations in three key twist angles in these three compounds. Despite all the three luminogens being non-planar, only **1PON** and **3PN** showed AIE property. The photophysical properties of these PN molecules were governed clearly by their core moiety. The effect of one ring (pyridine) position (ortho and para) and one carbon-carbon bond had profound impact on the photophysical and mechanochromic response of these compounds. We demonstrated that on altering the pyridine ring position, the π- π stacking is prevented yet it had less emission because of TICT effect. However, when we introduce a molecule that is devoid of a carbon-carbon bond in fluorene, i.e. to have two phenyl rings (in **3PN**), it no longer has π - π stacking, it becomes TICT inactive with remarkable AIE properties and with huge increase in quantum yields. We employed **1PON** as invisible ink because it has a different arrangement in the crystalline phase as seen in the amorphous phase. **3PN** has bright blue emission in aggregated and solid state and has broader applications. This contribution delivers a simple idea to design new potent AIE molecules, which have prominent applications as smart materials for sensors, security inks and optoelectronic devices. The simple molecules presented in this work provide ways to design luminogens, that not only have AIE properties but are useful as highly sensitive chemical sensors on multiple platform, mechano and pressure responsive materials as thin films. The **3PN** molecule has higher selectivity, sensitivity and fast response that makes them appropriate for developing economical nerve agents sensor. The condensed state properties of these luminogens are shown to be governed by the bond link, bond

position, bond pattern and not necessarily only by the restriction of rotation and can be applied as sensors for a much wider group of analytes beyond nerve agents. Hence, **1PON** and **3PN** molecules could be very interesting as smart fluorescence materials due to their easy accessibility and numerous properties.

4.4 Experimental Section

4.4.1 Materials

Fluorene, benzophenone, 4-pyridinylboronic acid, potassium tert-butoxide, 4-bromobenzaldehyde, 2-bromobenzaldehyde, 4-bromobenzyl bromide, triethylphosphite (TEP), dimethyl methylphosphonate (DMMP), diethylchlorophosphate (DCP), tributylphosphate (TBP), chlorodiphenylphosphine (Ph_2PCl) were purchased from Sigma Aldrich. All mentioned chemicals were received commercially and used without any further purification. THF was used for the preparation of stock solutions and photophysical experiments were performed by using THF and

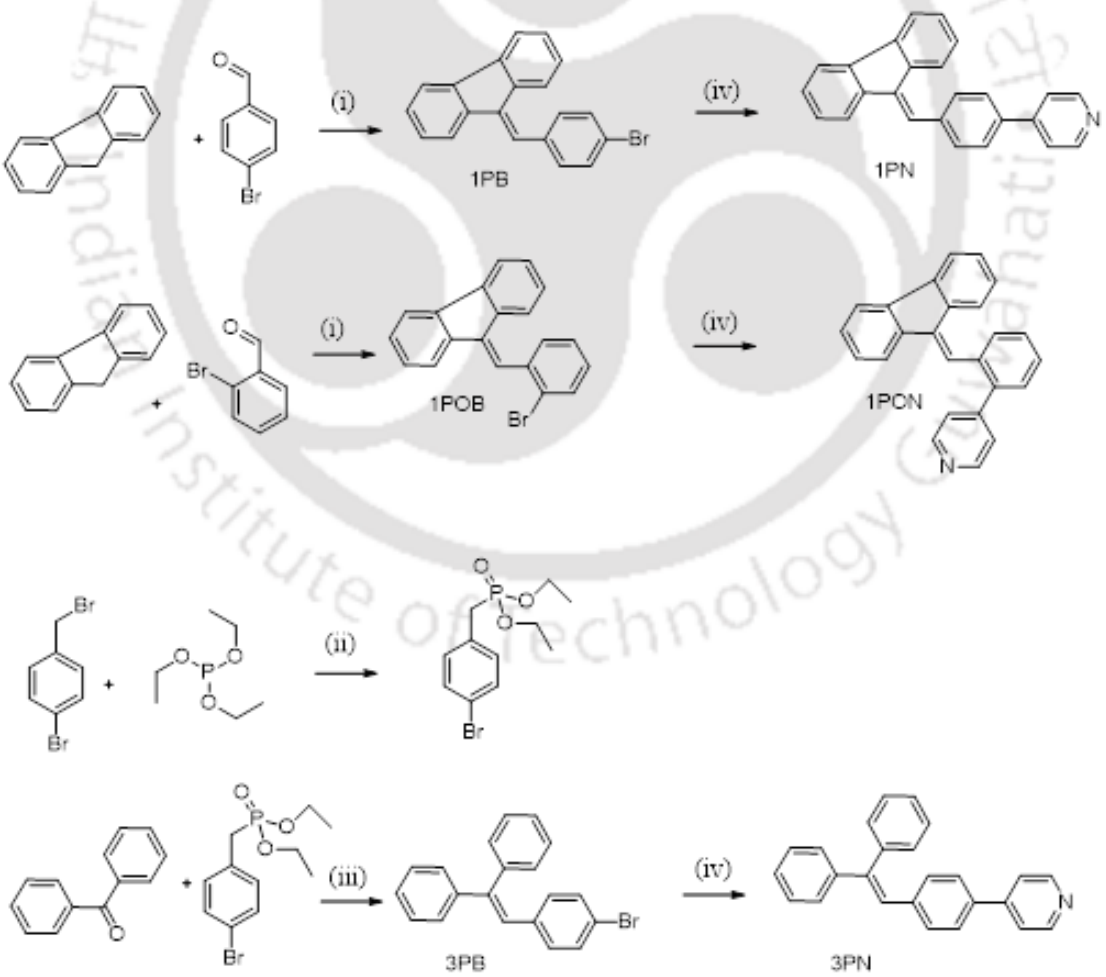

Scheme S1: (i) K^{t}Bu, Ethanol, 80°C, 12 h (ii) THF, 80°C, 10 h (iii) K^{t}BuO, THF, RT, 12 h (iv) 4-pyridinyl boronic acid, $Pd(PPh_3)_4$, K_2CO_3, THF:H_2O, 80°C, 24 h.

Milli-Q water. All the reactions which were moisture and air sensitive were performed under argon atmosphere by using the standard technique. ^{1}H NMR (400 MHz) and ^{13}C NMR (100 MHz) spectra were obtained on Varian-AS400 spectrometer. The photophysical studies of PN derivatives were done in HPLC grade solvents (DCM, DMSO, THF, Toluene) and Milli-Q water. The standard solution of **1PN**, **1PON** and **3PN** were prepared at a one mM concentration in THF solvent. UV-vis. spectra and Photoluminescence (PL) were recorded on PerkinElmer Lambda and Horiba Fluoromax-4 using 10 mm path length quartz cuvettes with a 3 nm slit width at 298 K.

4.4.2 General Synthesis Procedure

Synthesis Methods

The synthesis procedure of 1PBr

A mixture of fluorene (0.166 g, 1eq.) and potassium tert-butoxide (0.137 g, 1.2 eq.) was dissolved in 10 mL absolute ethanol and refluxed for 1 hour. 4 bromo benzaldehyde (0.185 g, 1 eq.) was added into resulting mixture then it was refluxed for 24 hours. The solvent was removed by rotary evaporator and the compound was extracted with dichloromethane (DCM) and water. Pure compound 1PBr was collected from silica column chromatography by taking hexane as eluent. (yellow solid, 0.245 g, 73% yield).

1PBr ^{1}H NMR (400 MHz, $CDCl_3$, δ ppm): 7.08 (t, 1H), 7.32 (t, 2H), 7.39 (t, 1H) 7.45 (d, 2H), 7.51 (d, 1H) 7.58 (m, 3H), 7.70 (d, 2H) 7.76 (d, 1H).

1PBr ^{13}C NMR (100 MHz, $CDCl_3$, δ ppm) 119.77, 119.97, 120.39, 122.17, 124.43, 125.78, 126.88, 127.19, 128.56, 128.92, 131.07, 131.84, 135.86, 136.35, 137.12, 139.31, 141.47.

The synthesis procedure of 1POBr

1POBr was synthesized by the above prescribed method. (yellow solid, 0.260 g, 78.07% yield).

1POBr ^{1}H NMR (400 MHz, $CDCl_3$, δ ppm): 7.17 (t, 1H), 7.39 (m, 6H), 7.61 (d, 1H) 7.70 (d, 1H), 7.77 (m, 2H) 7.92 (m, 1H), 8.03 (d, 1H).

1POBr ^{13}C NMR (100 MHz, $CDCl_3$, δ ppm) 141.25, 139.61, 139.24, 137.25, 136.77, 136.35, 133.54, 129.65, 128.31, 128.23, 127.81, 127.40, 127.17, 126.87, 125.26, 124.59, 120.46, 120.18, 119.82.

The synthesis procedure of 3PBr

Into condenser fitted round bottom flask 1-bromo-4-(bromomethyl)benzene (0.249 g, 1 mmol), triethyl phosphite (0.5 mL) in 10 mL of THF refluxed for 10 hours then benzophenone (0.182 g, 1 mmol) and potassium tertiary butoxide (0.112 g, 1 mmol) added and the reaction stirred at

room temperature for 12 hours. The reaction mixture was quenched and workup performed by using DCM and water. Pure product 3PBr was collected by silica column chromatography by taking hexane an eluent. (white solid, 0.215 g, 64.56% yield).

3PBr ^{1}H NMR (400 MHz, $CDCl_3$, δ ppm): 6.87 (m, 1H), 6.89 (m, 2H), 7.19 (m, 2H), 7.24 (m, 1H) 7.32 (m, 8H).

3PBr ^{13}C NMR (100 MHz, $CDCl_3$, δ ppm) 120.70, 126.93, 127.73, 127.78, 127.88, 128.40, 128.90, 130.40, 131.19, 131.23, 136.47, 140.08, 143.20, 143.58.

The synthesis procedure of 1PN

9-(4-bromobenzylidene)-9*H*-fluorene (0.332 g, 1 eq.), phenylboronic acid (0.134 g, 1.1 eq.), tetrakis(triphenylphosphine) palladium (0) (0.015 mmol) were taken in inert medium (argon gas) then 10 ml THF and aqueous K_2CO_3 (2M) was added. The reaction was refluxed for overnight. The reaction was quenched and workup performed by DCM and water. Pure product collected by silica column chromatography (yellow crystalline solid, 0.214 g,64.56% yield). Yellow color crystals with block shape were grown in 9:1 methanol and DCM by slow evaporation.

1PN ^{1}H NMR (400 MHz, $CDCl_3$, δ ppm): 7.08 (t, 1H), 7.36 (m, 3H), 7.61 (m, 3H), 7.74 (m, 7H), 7.79 (m, 1H), 8.70 (d, 2H).

1PN ^{13}C NMR (100 MHz, $CDCl_3$, δ ppm) 119.80, 119.99, 120.45, 121.58, 124.49, 126.27, 126.85, 127.19, 127.23, 128.59, 128.95, 130.30, 136.46, 137.25, 137.64, 137.96, 139.35, 139.46, 141.54, 147.77, 150.51.

The synthesis procedure of 1PON

Synthesis of **1PON** was done by the above prescribed method. (Yellow solid, 0.225 g, 67.56% yield). Yellow color crystals with rectangular shaped were growth in toluene and DCM by slow evaporation.

1PON ^{1}H NMR (400 MHz, $CDCl_3$, δ ppm): 7.09 (t, 1H), 7.27 (m, 1H), 7.36 (m, 5H), 7.54 (m, 4H), 7.58 (d, 1H), 7.73 (t, 2H), 7.77 (d, 1H).

1PON ^{13}C NMR (100 MHz, $CDCl_3$, δ ppm) 119.72, 120.01, 120.54, 124.42, 124.46, 126.52, 126.88, 127.18, 128.50, 128.68, 128.87, 129.00, 129.74, 131.34, 135.15, 136.63, 137.38, 138.65, 139.07, 139.16, 141.47, 148.42, 149.76.

The synthesis procedure of 3PN

Synthesis of **3PN** was done by the above prescribed method. (white solid, 0.220 g, 66.06% yield). Colorless crystals with needle-shape were grown in 9:1 methanol and DCM mixture by slow evaporation.

3PN ^{1}H NMR (400 MHz, $CDCl_3$, δ ppm): 7.00 (s, 1H), 7.12 (d, 2H), 7.24 (m, 2H), 7.35 (m, 8H), 7.44 (d, 4H), 8.60 (d, 2H).

3PN ^{13}C NMR (100 MHz, $CDCl_3$, δ ppm): 121.31, 121.75, 126.57, 127.10, 127.26, 127.74, 127.77, 127.89, 128.37, 128.89, 129.17, 129.22, 130.32, 130.40, 136.02, 138.47, 140.23, 143.18, 143.84, 247.73, 150.29.

4.5 References

1. Fu, B.; Huang, J.; Bai, D.; Xie, Y.; Wang, Y.; Wang, S.; Zhou, X. *Chem. Commun*., **2015**, *51*, 16960–16963.
2. Würthner, F.; Kaiser, T. E.; Saha-Möller, C. R. *Angew. Chem., Int. Ed.*, **2011**, *50*, 3376–3410.
3. Birks, J. B. Photophysics of Aromatic Molecules, Wiley, London, **1970**.
4. Feng, X.; Xu, Z.; Hu, Z.; Qi, C.; Luo, D.; Zhao, X.; Mu, Z.; Redshaw, C.; Lam, J. W. Y.; Ma, D.; Tang, B. Z. *J. Mater. Chem. C*, **2019**, *7*, 2283–2290.
5. Luo, J.; Xie, Z.; Lam, J. W. Y.; Cheng, L.; Chen, H.; Qiu, C.; Kwok, H. S. Zhan, X.; Liu, Y.; Zhu, D.; Tang, B. Z. *Chem. Commun*., **2001**, 1740–1741.
6. Meher, N.; Iyer, P. K. *Nanoscale*, **2017**, *9*, 7674–7685.
7. Zhang, H.; Liu, J.; Du, L.; Ma, C.; Leung, N. L. C.; Niu, Y.; Qin, A.; Sun, J.; Peng, Q.; Sung, H. H. Y.; Williams, I. D.; Kwok, R. T. K.; Lam, J. W. Y.; Wong, K. S.; Phillips, D. L.; Tang, B. Z. *Mater. Chem. Front*., **2019**, *3*, 1143–1150.
8. Adil, L. R.; Gopikrishna, P.; Iyer, P. K. *ACS Appl. Mater. Interfaces*, **2018**, *10*, 27260–27268.
9. Zhang, X.; Wang, K.; Liu, M.; Zhang, X.; Tao, L.; Chena, Y.; Wei, Y. *Nanoscale*, **2015**, *7*, 11486–11508.
10. Alifu, N.; Dong, X.; Li, D.; Sun, X.; Zebibula, A.; Zhang, D.; Zhang, G.; Qian, J. *Mater. Chem. Front*., **2017**, *1*, 1746–1753.
11. Wang, L.; Wang, W.; Xie, Z. *J. Mater. Chem. B*, **2016**, *4*, 4263–4266.
12. Zhan, X.; Wu, Z.; Lin, Y.; Xie, Y.; Peng, Q.; Li, Q.; Ma, D.; Li, Z. *Chem. Sci*., **2016**, *7*, 4355–4363.

13. Wang, J.; Gu, X.; Zhang, P.; Huang, X.; Zheng, X.; Chen, M.; Feng, H.; Kwok, R. T. K.; Lam, J. W. Y.; Tang, B. Z. *J. Am. Chem. Soc*., **2017**, *139*(46), 16974–16979.
14. Wu, X.; Wu, Z.; Han, S. *Chem. Commun*., **2011**, *47*, 11468–11470.
15. Chen, L.; Wu, D.; Yoon, J. *ACS Sens*., **2018**, *3*, 27–43.
16. Sambrook, M. R.; Notman, S. *Chem. Soc. Rev.*, **2013**, *42*, 9251–9267.
17. Cinti, S.; Valdés-Ramírez, G.; Gao, W.; Li, J.; Palleschi, G.; Wang, J. *Chem. Commun*., **2015**, *51*, 8668–8671.
18. Chen, L.; Wang, X.; Lu, W.; Wu, X.; Li, *J. Chem. Soc. Rev.*, **2016**, *45*, 2137–2211.
19. Steiner, W. E.; Klopsch, S. J.; English, W. A.; Clowers, B. H. Hill, H. H. *Anal. Chem.*, **2005**, *77*, 4792–4799.
20. Joshi, K. A.; Prouza, M.; Kum, M.; Wang, J.; Tang, J.; Haddon, R.; Chen, W.; Mulchandani, A. *Anal. Chem.*, **2006**, *78*, 331–336.
21. Wu, D.; Sedgwick, A. C.; Gunnlaugsson, T.; Akkaya, E. U.; Yoon, J.; James, T. D. *Chem. Soc. Rev.*, **2017**, *46*, 7105–7123.
22. Venkataraman, L.; Klare, J. E.; Nuckolls, C.; Hybertsen, M. S.; Steigerwald, M. L. *Nature*, **2006**, *442*, 904–907.
23. Zhang, G.-F.; Aldred, M. P.; Gong, W.-L.; Li, C.; Zhu, M.-Q. *Chem. Commun.*, **2012**, *48*, 7711–7713.
24. Liu, J.; Evrard, M.; Cai, X.; Feng, G.; Tomczak, N.; Ng, L. G. and Liu, B. *J. Mater. Chem. B*, **2018**, *6*, 2630–2636.
25. Becke, D. *J. Chem. Phys.*, **1993**, *98*, 1372–1377.
26. Hughes, E.; Reddy, G. N. M.; Masiero, S.; Brown, S. P.; Williams, P. A.; Harris, K. D. M. *Chem. Sci*., **2017**, *8*, 3971–3979.
27. Zhu, X.; Liu, R.; Li, Y.; Huang, H.; Wang, Q.; Wang, D.; Zhu, X.; Liu, S. Zhu, H. *Chem. Commun.*, **2014**, *50*, 12951–12954.
28. Chen, M.; Chen, R.; Shi, Y.; Wang, J.; Cheng, Y.; Li, Y.; Gao, X.; Yan, Y.; Sun, J. Z.; Qin, A.; Kwok, R. T. K.; Lam J. W. Y.; Tang, B. Z. *Adv. Funct. Mater.*, **2018**, *28*, 1704689- 1704698.
29. Dong, Y. Q.; Lam, J. W. Y.; Tang, B. Z. *J. Phys. Chem. Lett.*, **2015**, *6*, 3429–3436.

Appendix

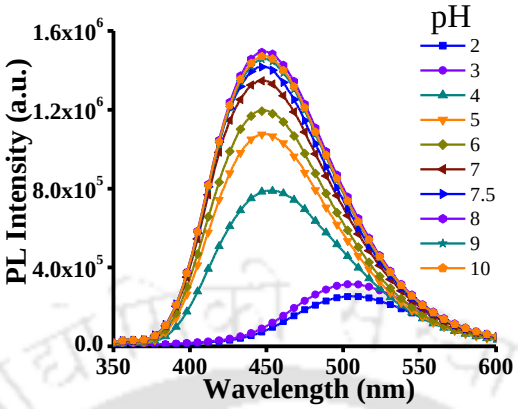

Figure A4.1: PL spectra of **3PN** in different pH medium, all spectra were taken at room temperature.

Quantum yield calculations for PN derivatives

PN derivatives quantum yield (Φ_s) was calculated in aqueous medium by using following equation and quinine sulfate (Φ_s = 0.57 in 0.1 M H_2SO_4) was taken as reference dye.

$$\Phi_s = \Phi_r (A_r F_s / A_s F_r) (\eta_s^2 / \eta_r^2) \ldots\ldots\ldots\ldots\ldots \text{Equation-A4.1}$$

Where, s and r represent sample and reference, Φ signifies the quantum yield, A denotes absorbance, F signifies relative integrated fluorescence intensity, and η represents the refractive index of the medium.

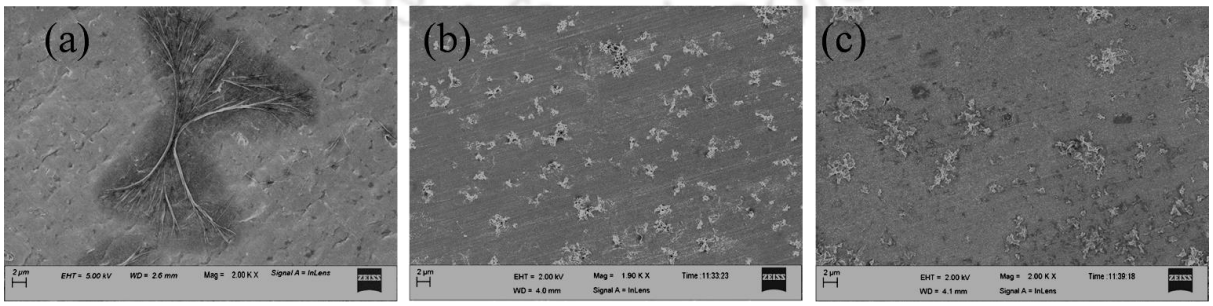

Figure A4.2: FESEM images of (a) **1PN** (b) **1PON** (c) **3PN** nanoparticles formed in 99% f_w by simple drop-casting technique (10 µM).

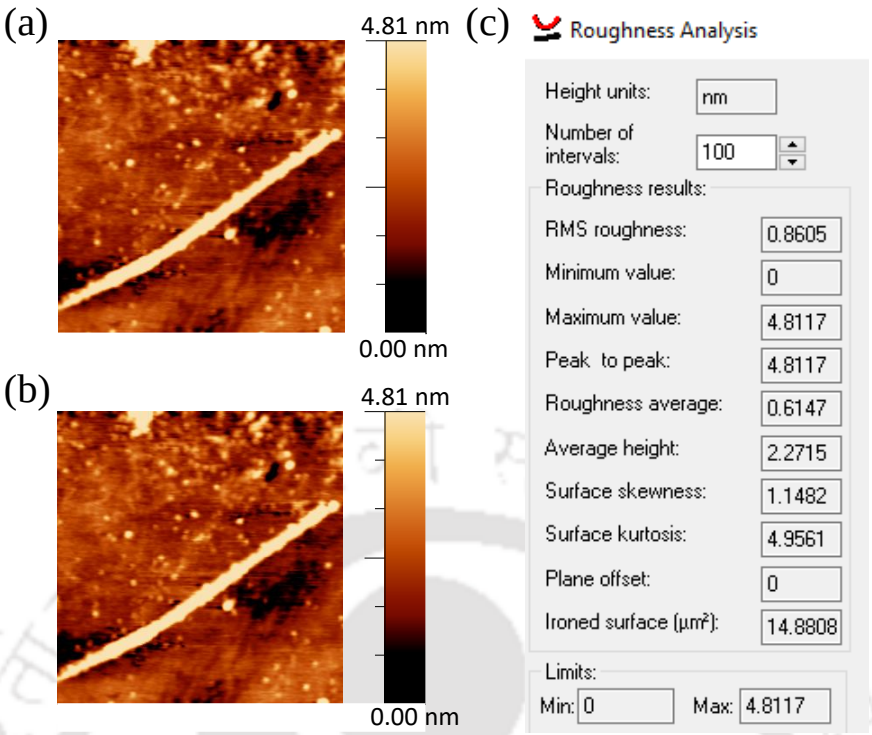

Figure A4.3: AFM images of **1PN** derivative nanoparticles formed in 99% f_w by simple drop-casting on glass slide (10 µM).

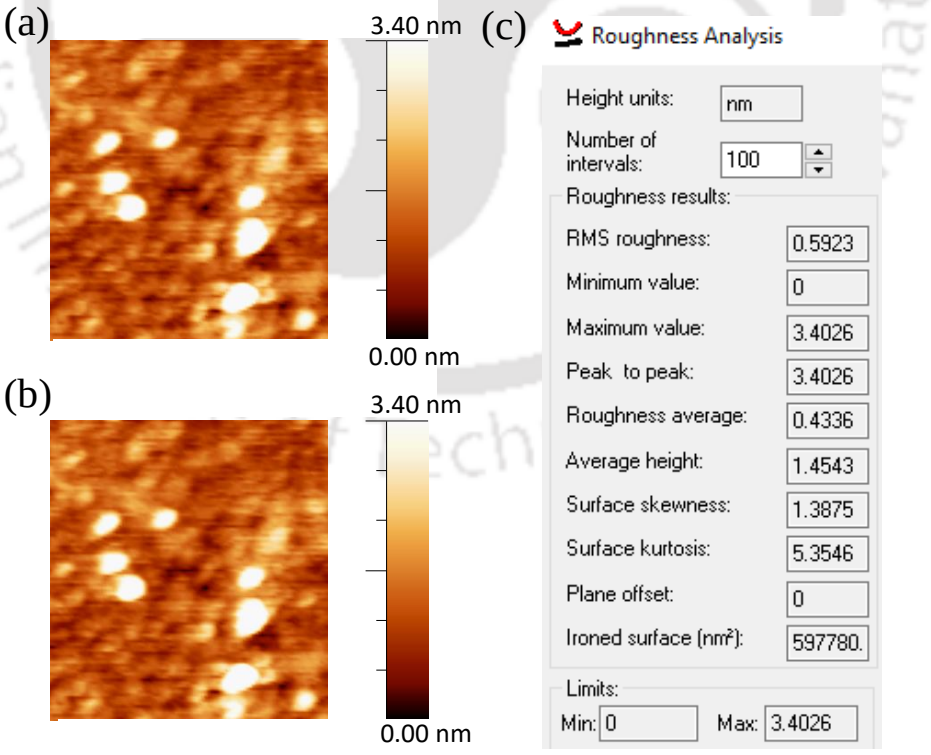

Figure A4.4: AFM images of **1PON** derivative nanoparticles formed in 99% f_w by simple drop-casting on glass slide (10 µM).

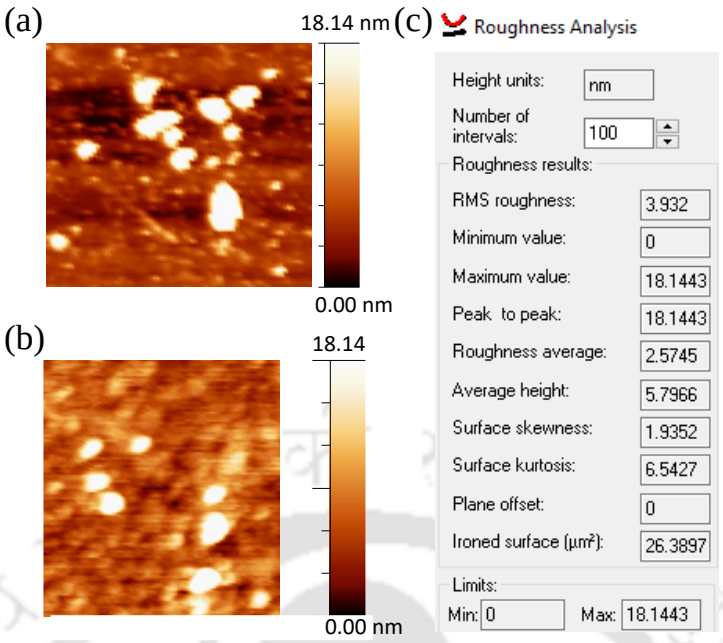

Figure A4.5: AFM images of **3PN** derivative nanoparticles formed in 99% f_w by simple drop-casting on glass slide (10 µM).

Molecular packing and arrangement

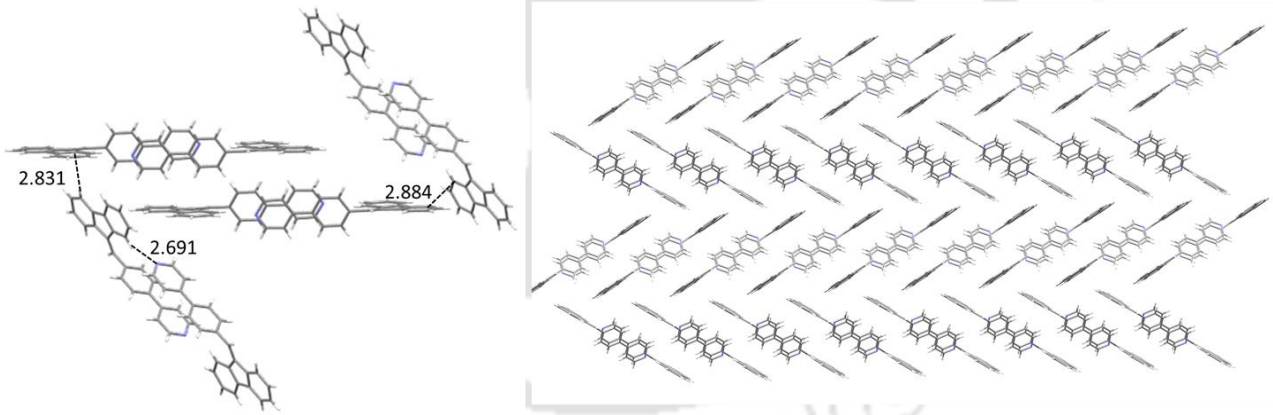

Figure A4.6: 1PN molecular packing and arrangement from SCXRD.

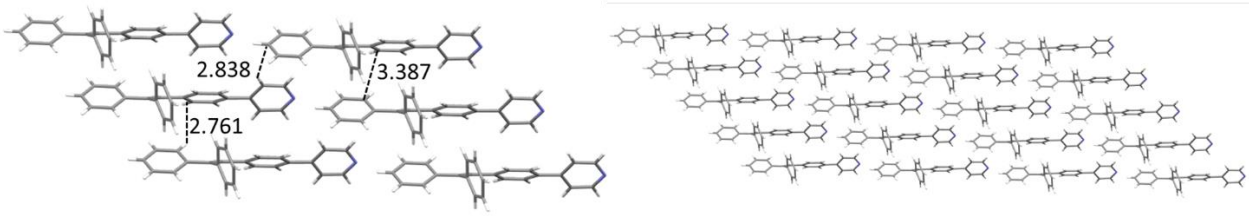

Figure A4.7 3PN molecular packing and arrangement from SCXRD.

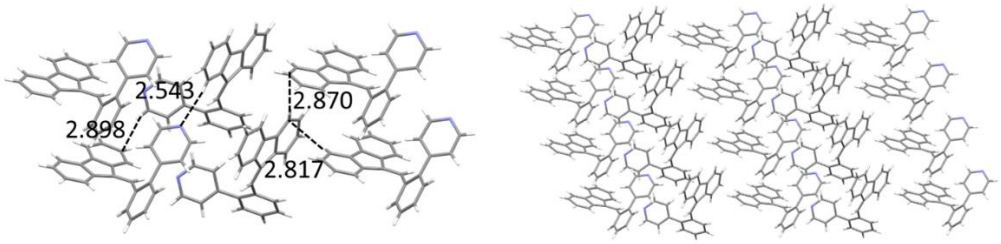

Figure A4.8: 1PON_Tol molecular packing and arrangement from SCXRD.

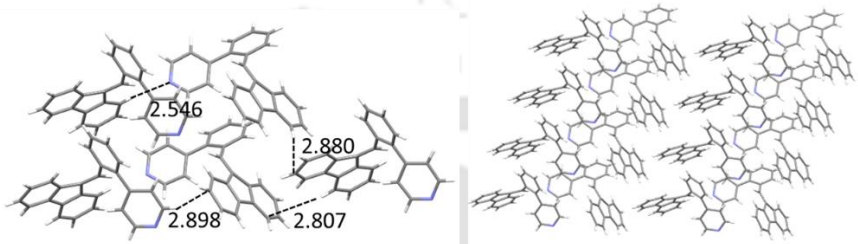

Figure A4.9: 1PON_DCM molecular packing and arrangement from SCXRD.

Table A4.1: Single crystal X-ray diffraction data of **1PN**.

S No.	Compound	1PN
1	Empirical formula	C_{25} H_{17} N
2	CCDC NO	1850300
3	Formula weight	331.40
4	Temperature/K	298 K
5	Crystal system	Monoclinic
6	Space group	P2(1)/c
7	a/Å	8.3412(4)
8	b/Å	20.3704(9)
9	c/Å	10.3467(5)
10	α/°	90.00
11	β/°	95.383(3)
12	γ/°	90.00
13	Volume/$Å^3$	1750.29(14)
14	Z	4
15	ρ**calc**mg/mm^3	1.258
16	m/mm^{-1}	0.073
17	F(000)	696.00
18	Crystal size/mm^3	0.28 × 0.23 × 0.17
19	2Θ range for data collection	2.00 to 47.78°
20	Index ranges	$-9 \leq h \leq 9$, $-24 \leq k \leq 24$, $-12 \leq l \leq 12$
21	Reflections collected	18868

22	Independent reflections	3102[R(int) = 0.0432]
23	Data/restraints/parameters	3102/0/235
24	Goodness-of-fit on F2	0.954
25	Final R indexes [I>=2σ(I)]	R1 = 0.0508, wR2 = 0.1366
26	Final R indexes [all data]	R1 = 0.0975, wR2 = 0.1670

Table A4.2: Single crystal X-ray diffraction data of **3PN**.

S No.	Compound	3PN
1	Empirical formula	C_{25} H_{19} N
2	CCDC NO	1850519
3	Formula weight	333.41
4	Temperature/K	296 K
5	Crystal system	Monoclinic
6	Space group	P 21/n
7	a/Å	5.7544(7)
8	b/Å	11.1791(13)
9	c/Å	28.221(3)
10	α/°	90.00
11	β/°	95.062(2)
12	γ/°	90.00
13	Volume/$Å^3$	1808.4(4)
14	Z	4
15	ρ**calc**mg/mm^3	1.225
16	m/mm^{-1}	0.071
17	F(000)	704
18	Crystal size/mm^3	0.26 × 0.21 × 0.15
19	2Θ range for data collection	1.44 to 25.00°
20	Index ranges	$-6 \le h \le 6$, $-13 \le k \le 13$, $-33 \le l \le 33$
21	Reflections collected	58468
22	Independent reflections	58468 [R(int) =0.0379]
23	Data/restraints/parameters	58468/0/235
24	Goodness-of-fit on F2	1.078
25	Final R indexes [I>=2σ(I)]	R1 = 0.0388, wR2 = 0.1026
26	Final R indexes [all data]	R1 = 0.0474, wR2 = 1.078

Table A4.3: Single crystal X-ray diffraction data of **1PON_Toluene**.

S No.	Compound	1PON_Toluene
1	Empirical formula	C_{25} H_{17} N
2	CCDC NO	1938858
3	Formula weight	331.39
4	Temperature/K	296 K
5	Crystal system	Monoclinic
6	Space group	P21/n

7	a/Å	16.8262(9)
8	b/Å	6.0687(3)
9	c/Å	18.6754(10)
10	α/°	90.00
11	β/°	110.396(6)
12	γ/°	90.00
13	Volume/Å^3	1787.45(17)
14	Z	4
15	ρ**calc**mg/mm^3	1.231
16	m/mm^{-1}	0.071
17	F(000)	696
18	Crystal size/mm^3	0.34 × 0.21 × 0.13
19	2Θ range for data collection	2.327 to 28.948 °
20	Index ranges	-22 ≤ h ≤ 9, -8 ≤ k ≤ 5, -24 ≤ l ≤ 24
21	Reflections collected	7893
22	Independent reflections	4110[R(int) = 0.0269]
23	Data/restraints/parameters	7893/0/235
24	Goodness-of-fit on F2	1.080
25	Final R indexes [I>=2σ(I)]	R1 = 0.0552, wR2 = 0.1129
26	Final R indexes [all data]	R1 = 0.0988, wR2 = 0.1382

Table A4.4: Single crystal X-ray diffraction data of **1PON_DCM**.

S No.	**Compound**	**1PON (DCM)**
1	Empirical formula	C_{25} H_{17} N
2	CCDC NO	1941127
3	Formula weight	331.39
4	Temperature/K	296 K
5	Crystal system	Monoclinic
6	Space group	P21/n
7	a/Å	16.8722(15)
8	b/Å	6.0689(4)
9	c/Å	18.7149(19)
10	α/°	90.00
11	β/°	110.549(11)
12	γ/°	90.00
13	Volume/Å^3	1794.4(3)
14	Z	4
15	ρ**calc**mg/mm^3	1.227
16	m/mm^{-1}	0.071
17	F(000)	696
18	Crystal size/mm^3	0.30 × 0.24 × 0.17
19	2Θ range for data collection	3.54 to 25.75°
20	Index ranges	-9 ≤ h ≤ 20, -7 ≤ k ≤ 6, -22 ≤ l ≤ 21
21	Reflections collected	6493
22	Independent reflections	1982[R(int) = 0.0345]
23	Data/restraints/parameters	6493/0/235

24	Goodness-of-fit on F2	1.185
25	Final R indexes [I>=2σ(I)]	R1 = 0.0832, wR2 = 0.2526
26	Final R indexes [all data]	R1 = 0.1180, wR2 = 0.3373

Mechanoresonsive studies and secret ink

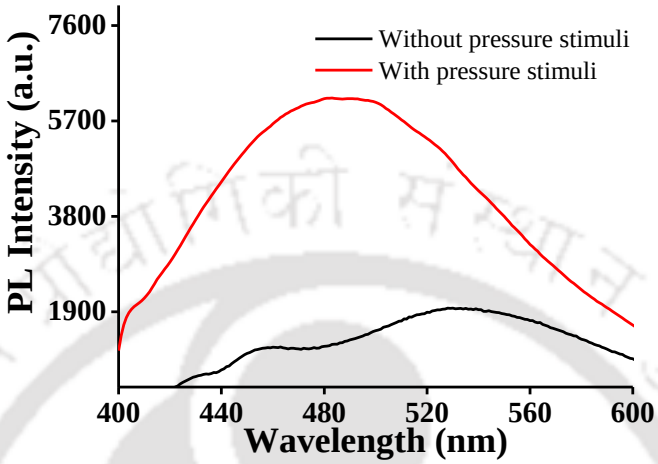

Figure A4.10: Enhancement of emission of PDMS thin film after pressure stimuli**.**

Limit of detection calculation

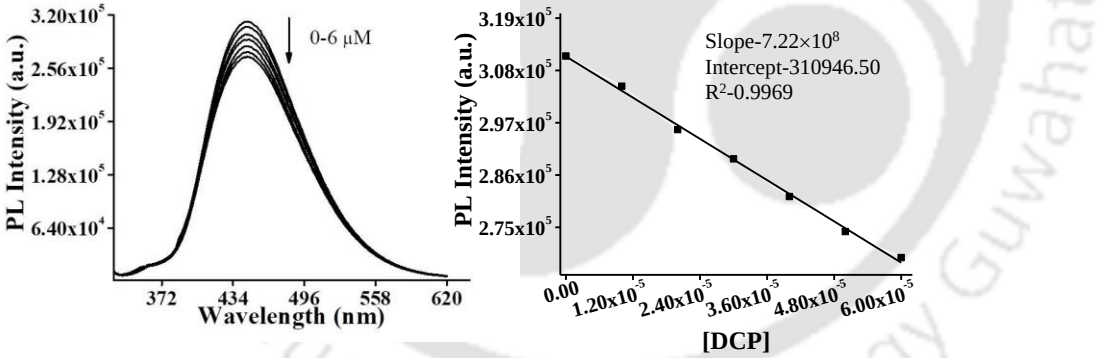

Figure A4.11: Change of fluorescence intensity of **3PN** in lower concentration of DCP in 99% f_w.

$$LOD = 3 \times S.D. / k$$

$$LOD \text{ for DCP} = 3 \times 1653.90 / 7.22 \times 10^8$$

$$= 70.88 \times 10^{-7} \text{ M}$$

Determination of nerve agents sensing mechanism by 3PN

3PN fluorescence response of towards DCP is due to the pyridine group because it has stronger nucleophilicity (pKa = 5.17). Hence the pyridine group will be first electrophilically attacked by the phosphonyl group of DCP, forming an unstable intermediate, whose N–P bond is easily further attacked by a weak nucleophilic reagent like oxygen atoms from H_2O (either form the aqueous medium or from vapor) ultimately be rapidly hydrolyzed into pyridinium salt.As a result fluorescence changes due to push–pull electron effect can be observed. Meanwhile, the nerve agent mimic DCP will transform into non-toxic neutral phosphate. This sensing mechanism was confirmed by ^{1}H NMR.

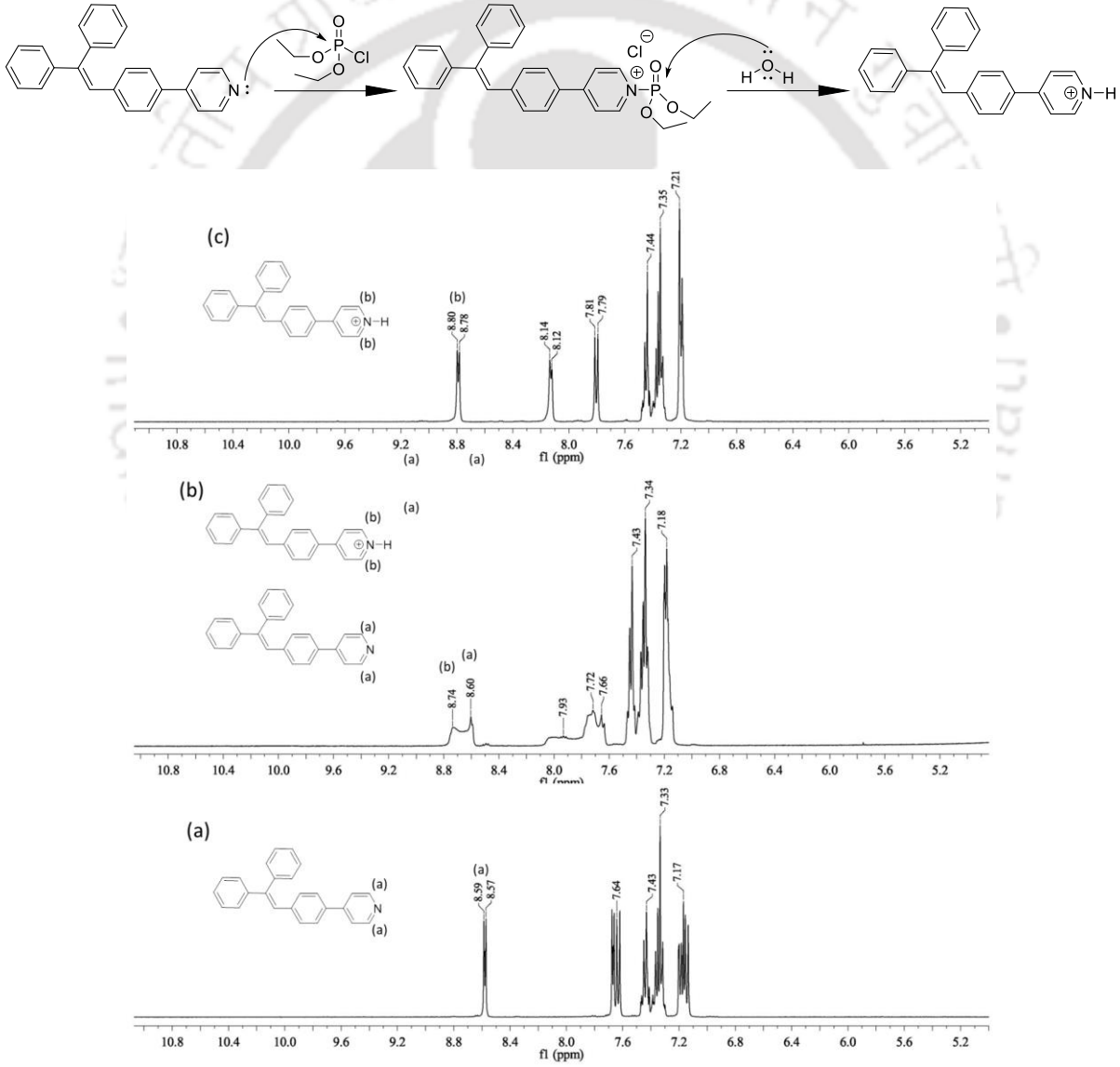

Figure A4.12 Proposed mechanism of sensing and shift of ^{1}H NMR peaks of **3PN** in (a) absence of DCP (b) 0.5 equivalent of DCP (c) 1 equivalent of DCP in DMSO-d_6 solvent.

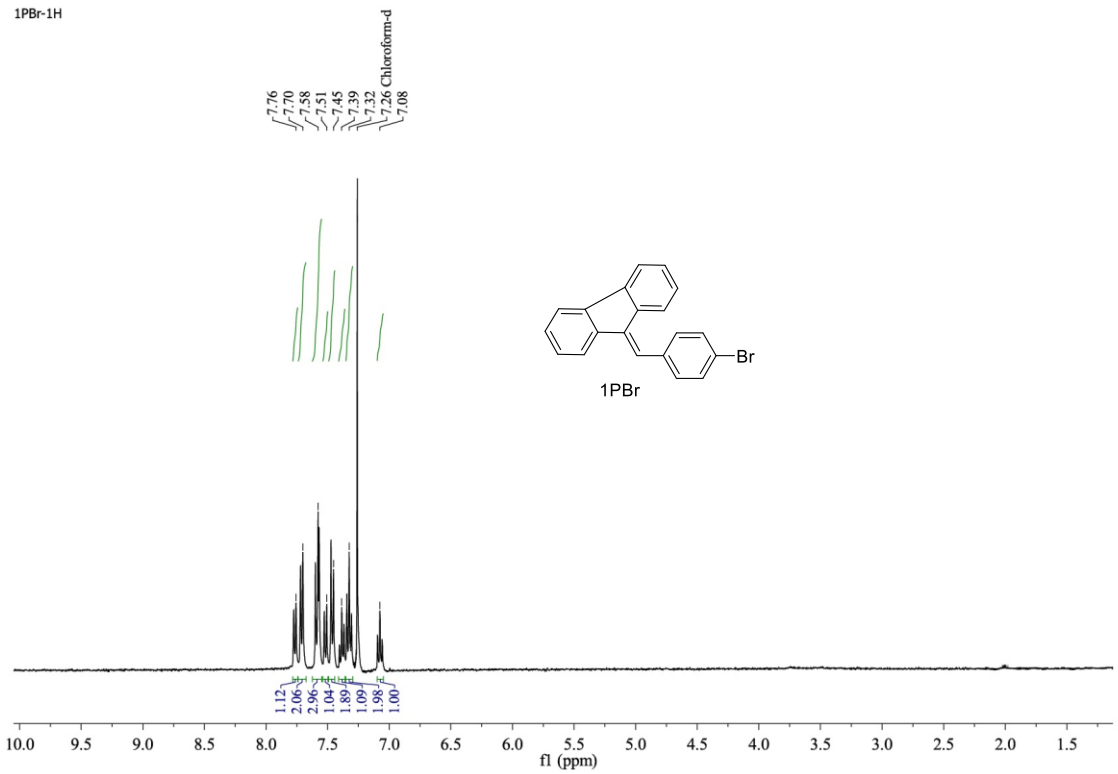

^{1}H NMR spectra of **1PBr** in $CDCl_3$ solvent.

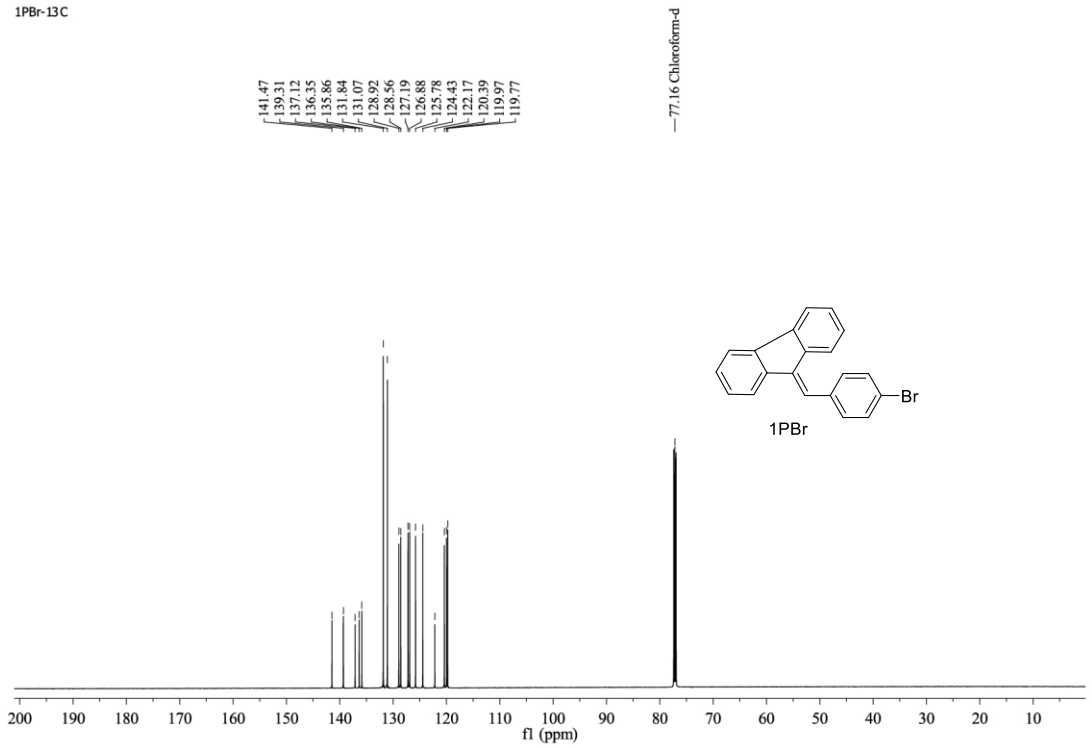

^{13}C NMR spectra of **1PBr** in $CDCl_3$ solvent.

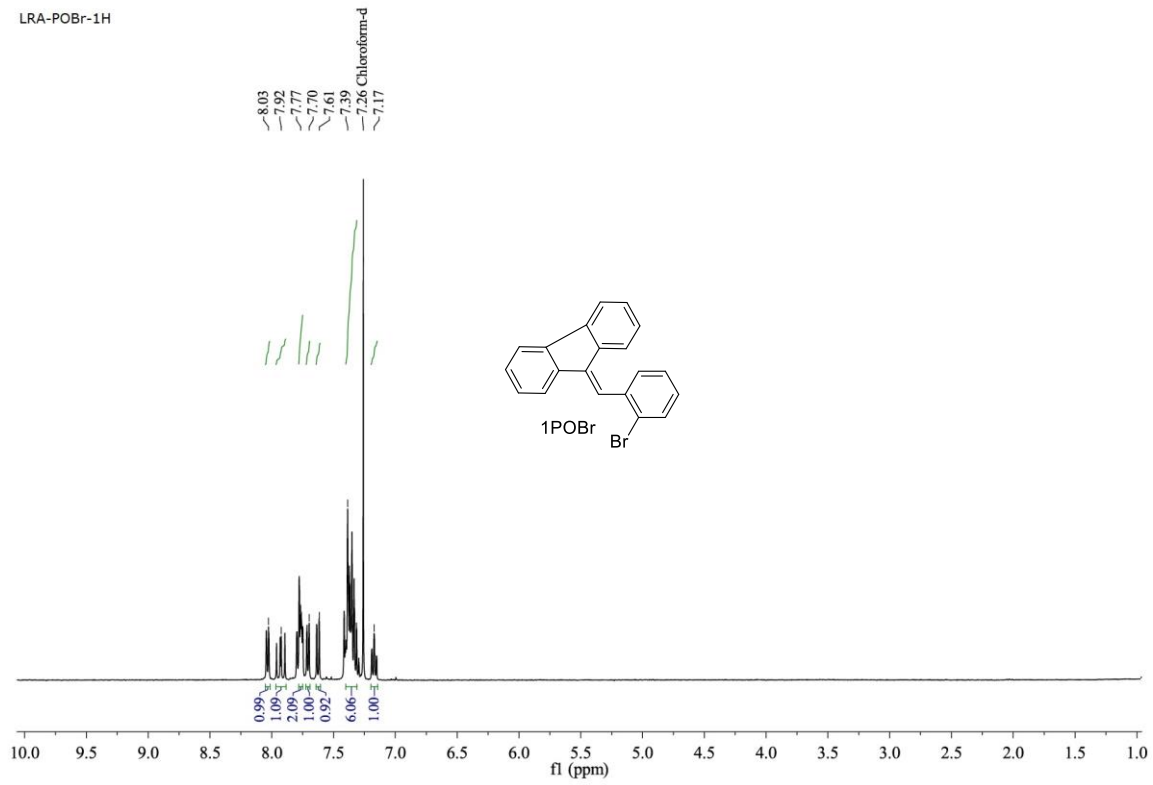

^{1}H NMR spectra of **1POBr** in $CDCl_3$ solvent.

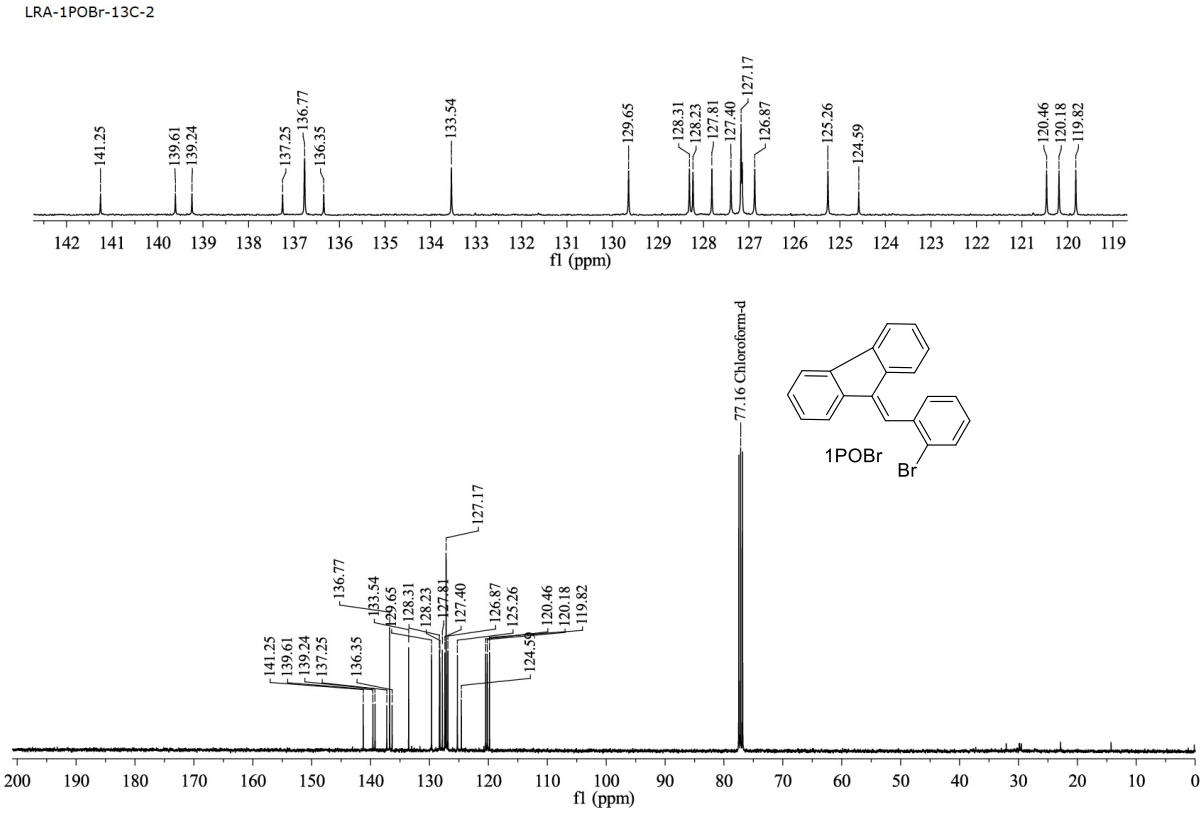

^{13}C NMR spectra of **1POBr** in $CDCl_3$ solvent.

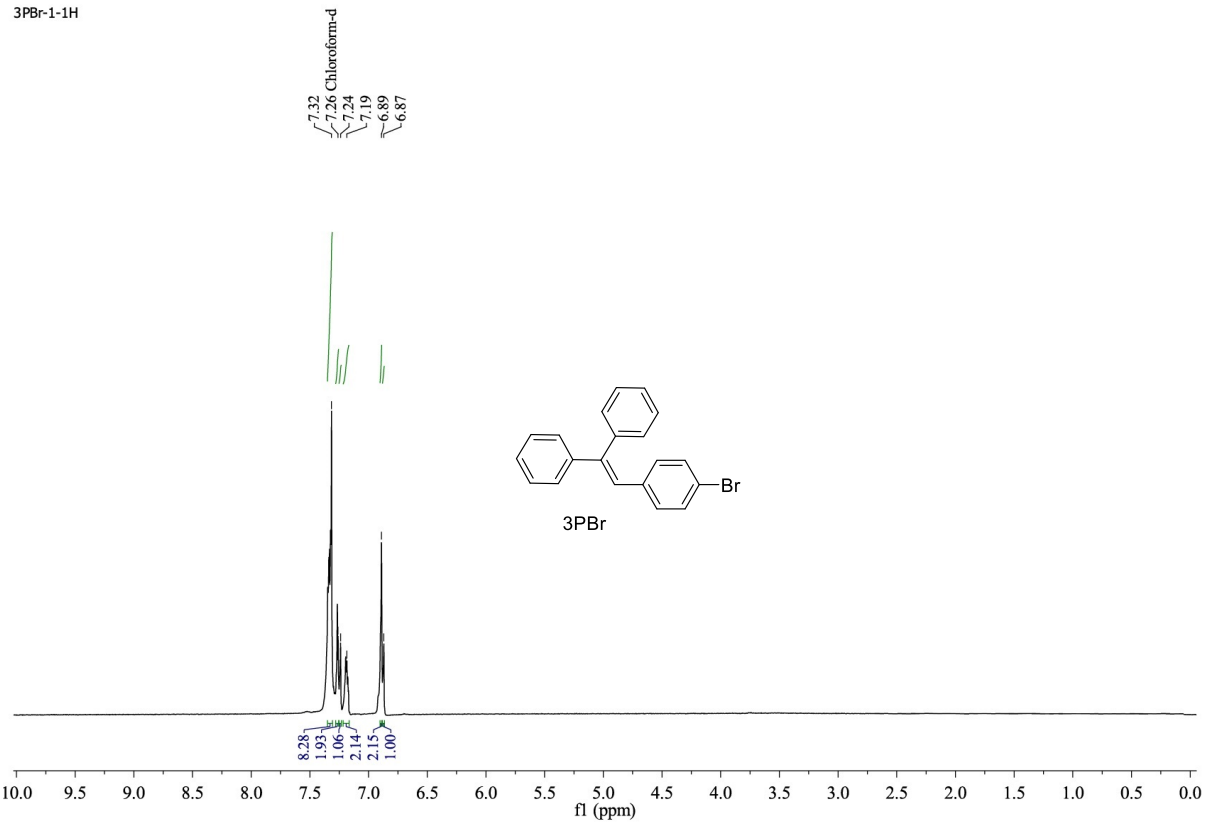

^{1}H NMR spectra of **3PBr** in $CDCl_3$ solvent.

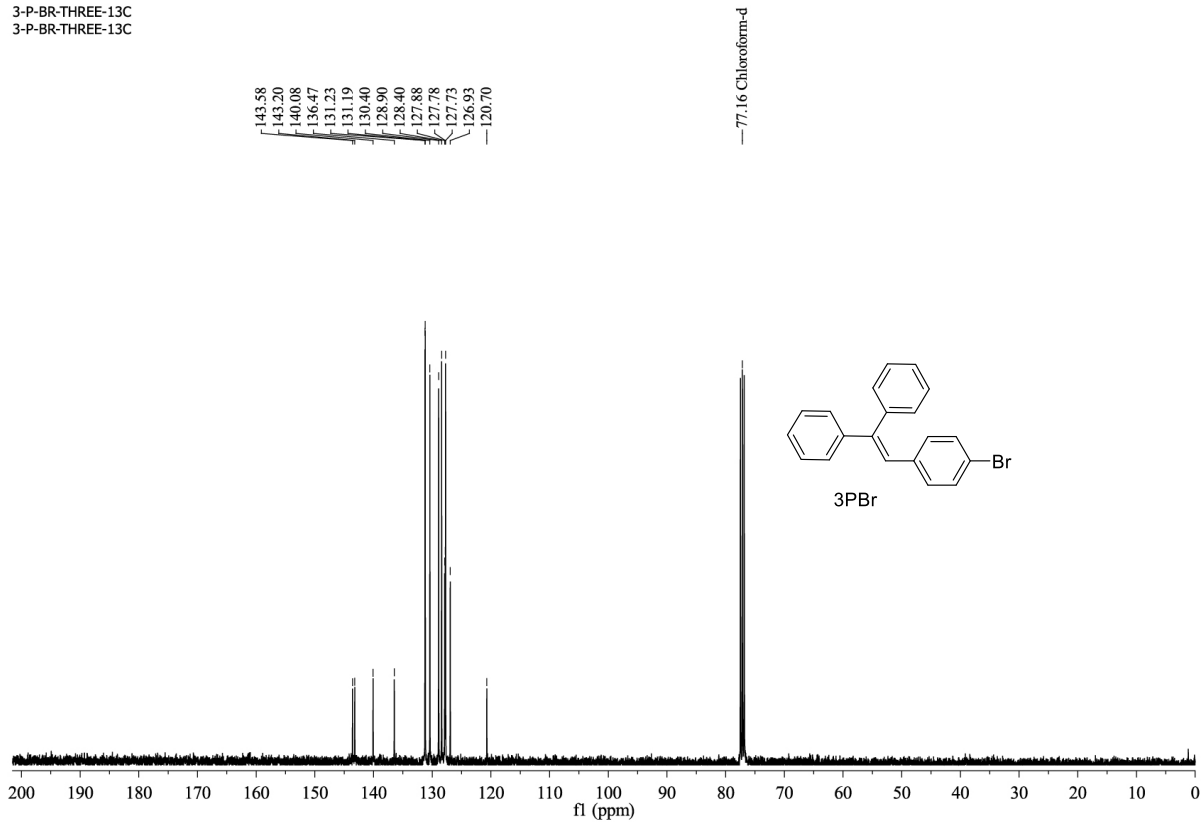

^{13}C NMR spectra of **3PBr** in $CDCl_3$ solvent.

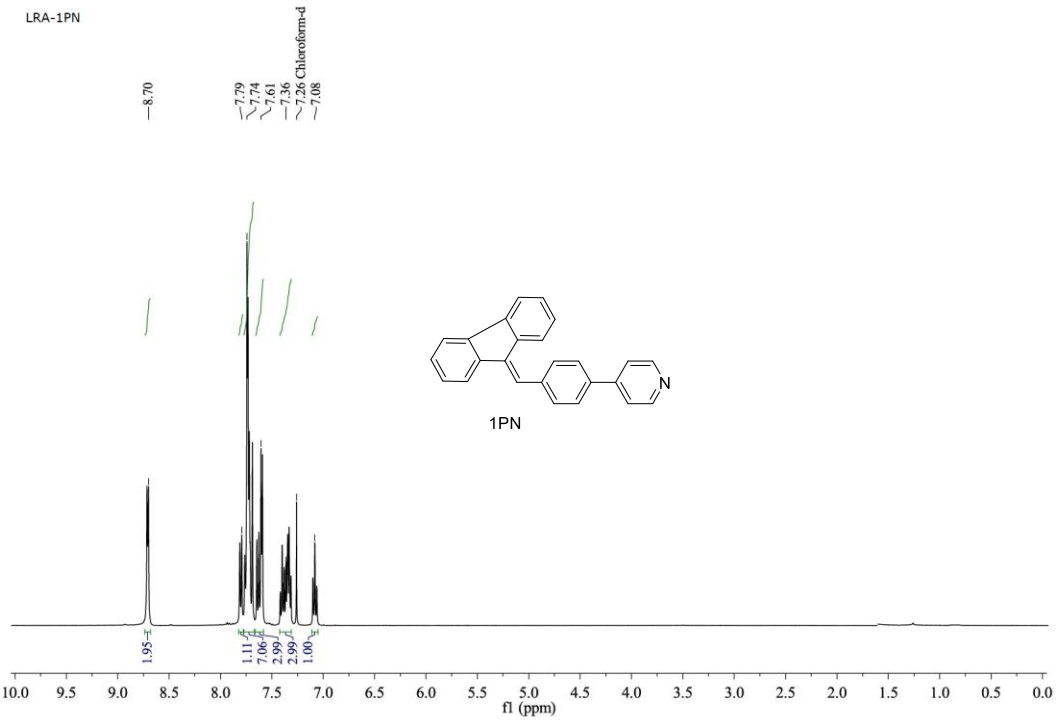

^{1}H NMR spectra of **1PN** in $CDCl_3$ solvent.

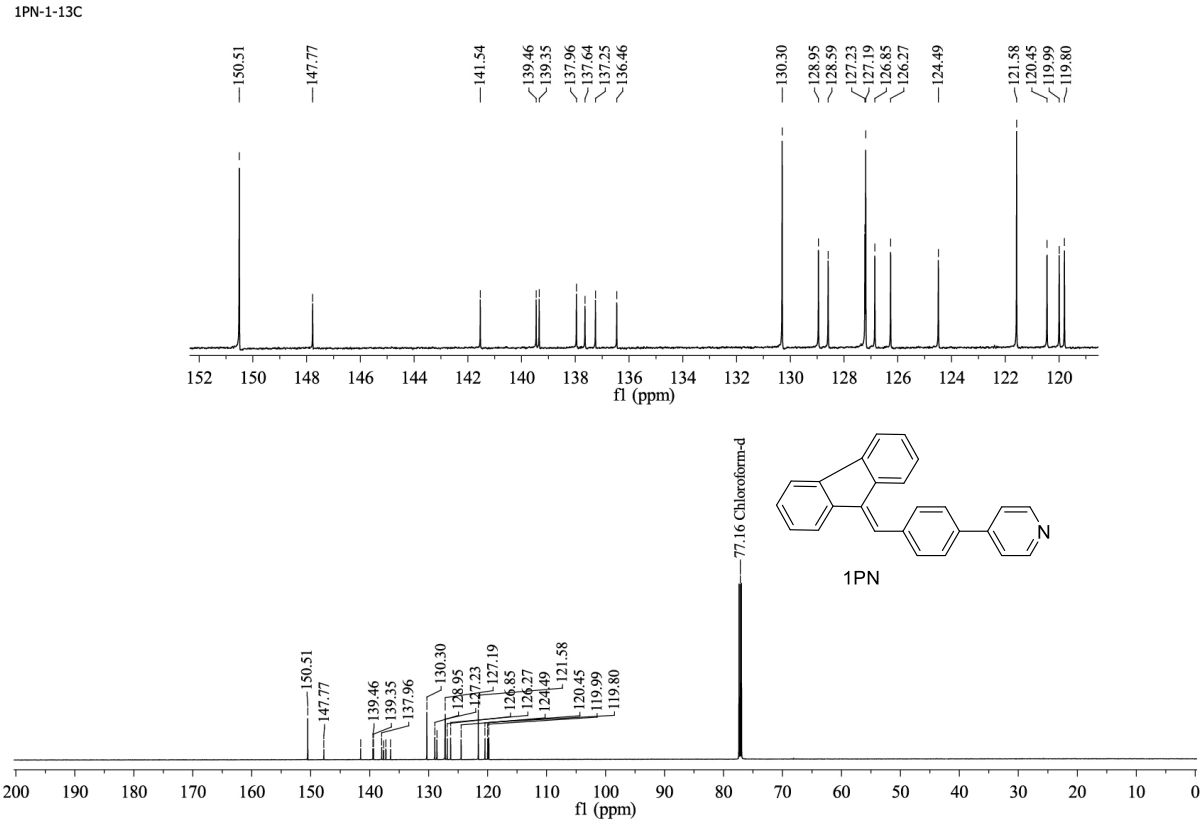

^{13}C NMR spectra of **1PN** in $CDCl_3$ solvent.

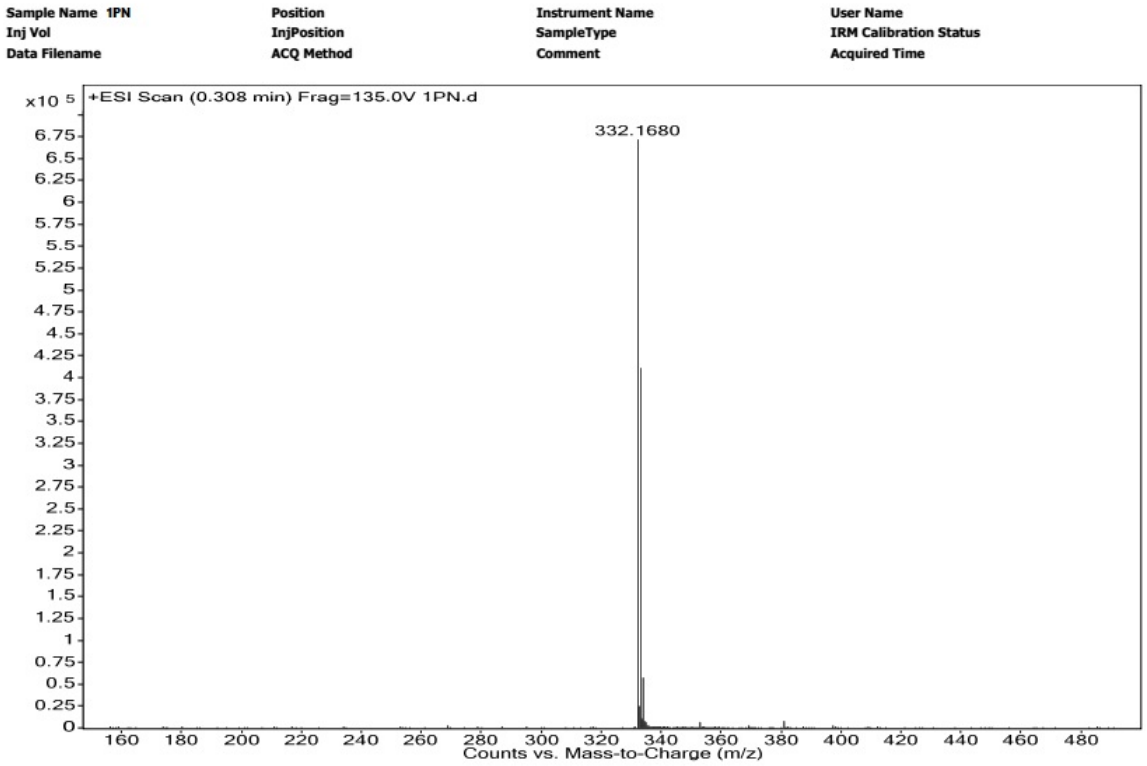

HRMS of **1PN**.

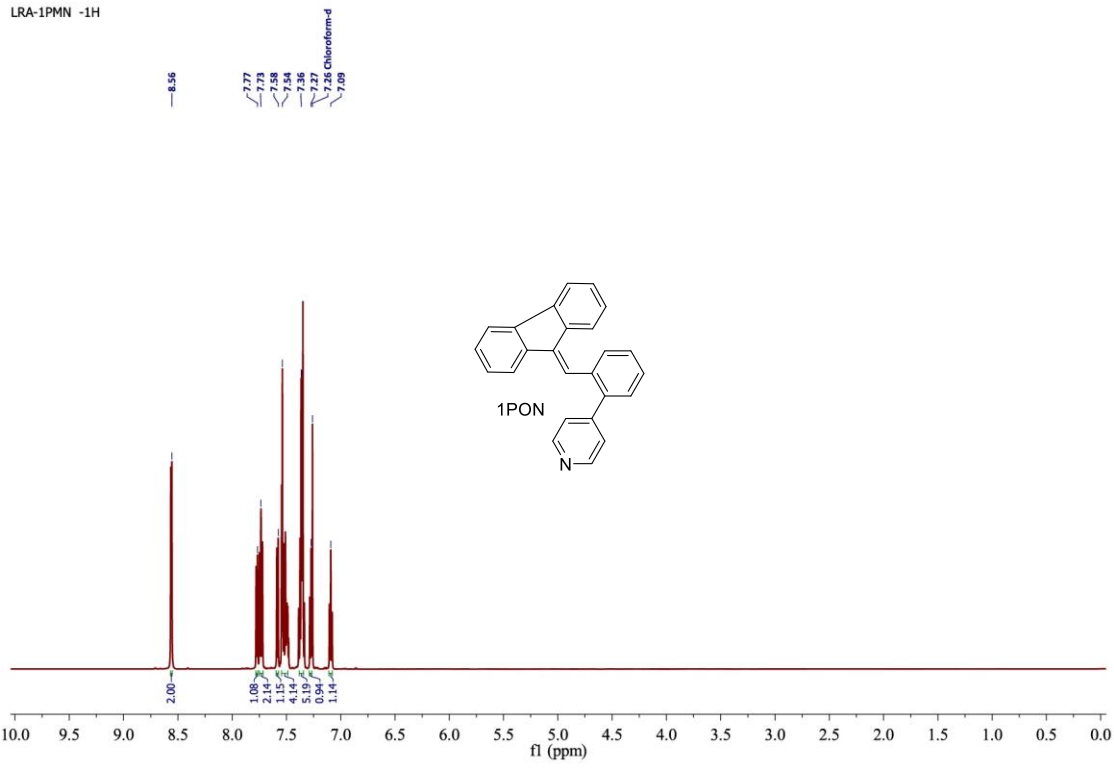

^{1}H NMR spectra of **1PON** in $CDCl_3$ solvent.

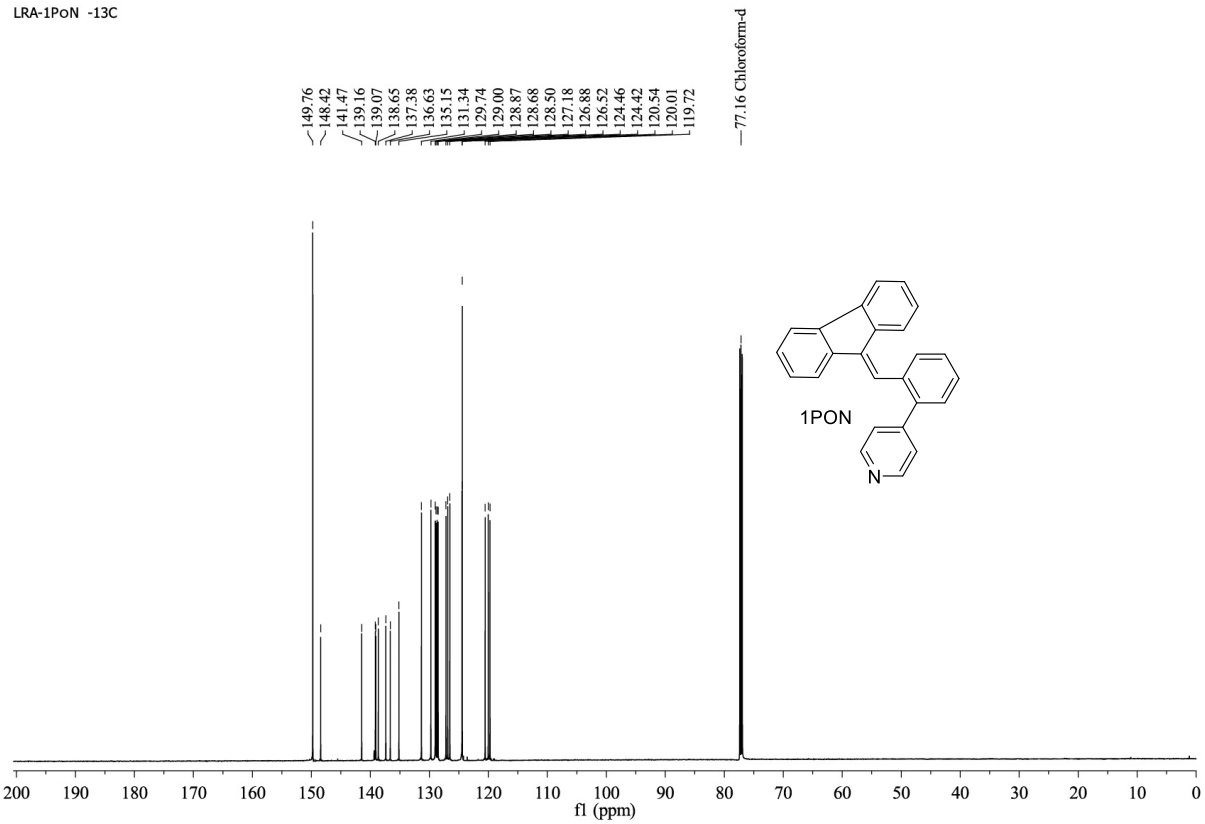

^{13}C NMR spectra of **1PON** in $CDCl_3$ solvent.

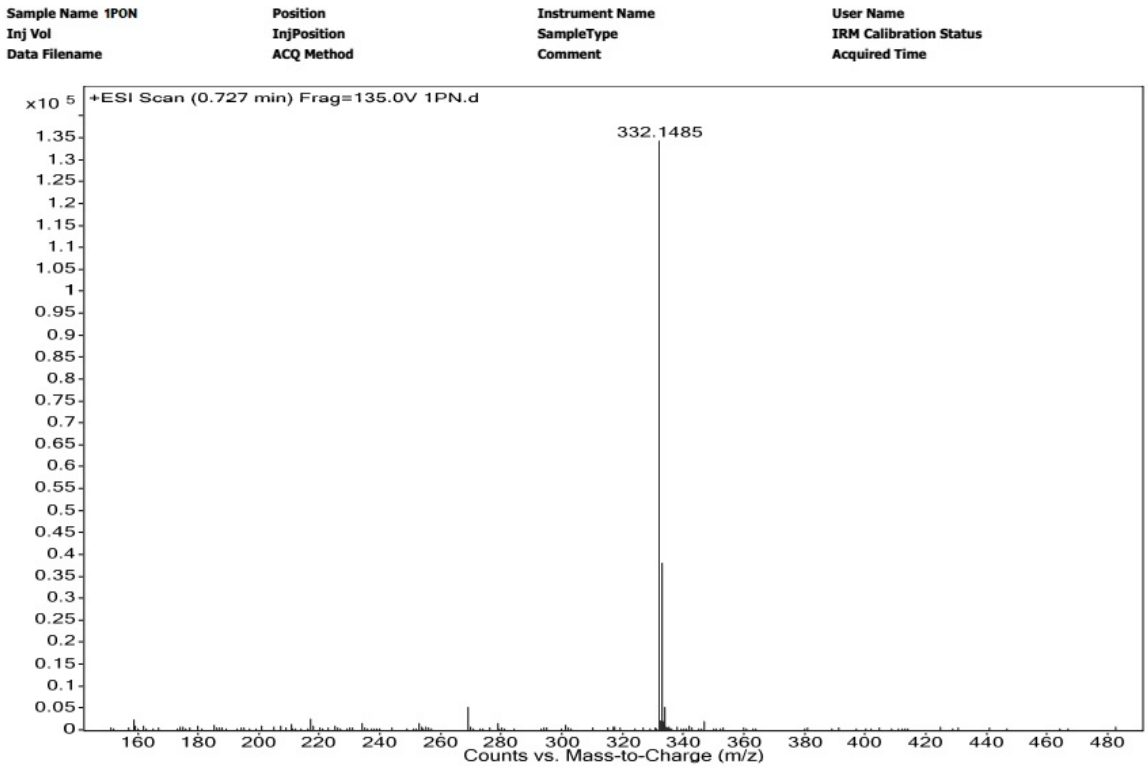

HRMS spectra of **1PON**.

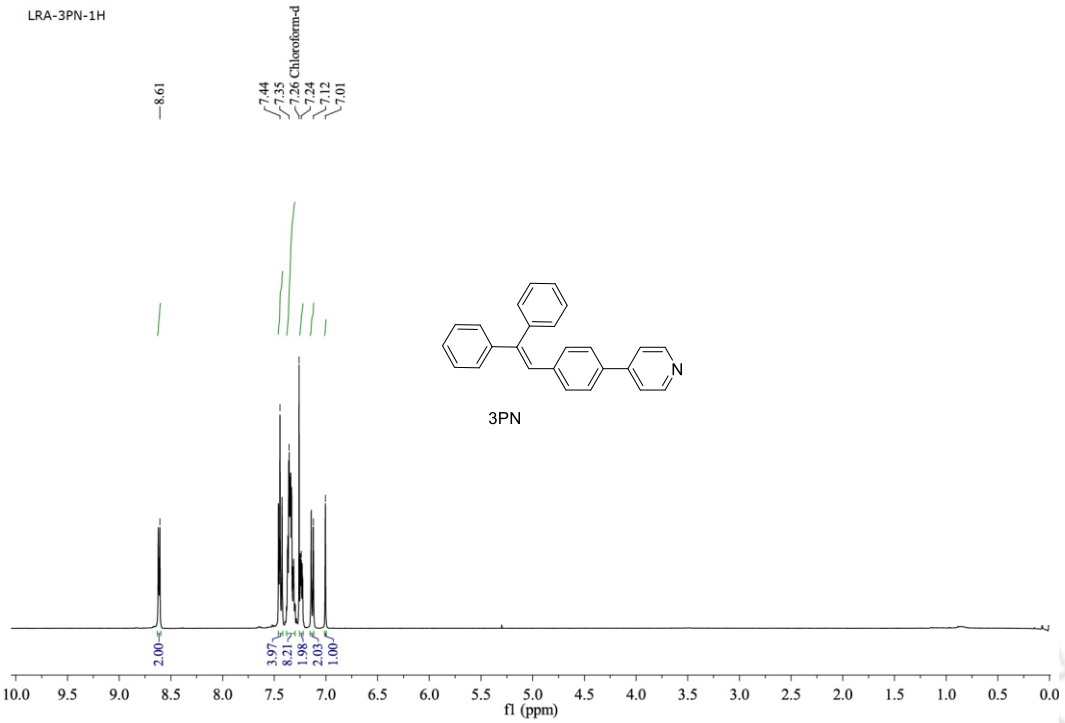

^{1}H NMR spectra of **3PN** in $CDCl_3$ solvent.

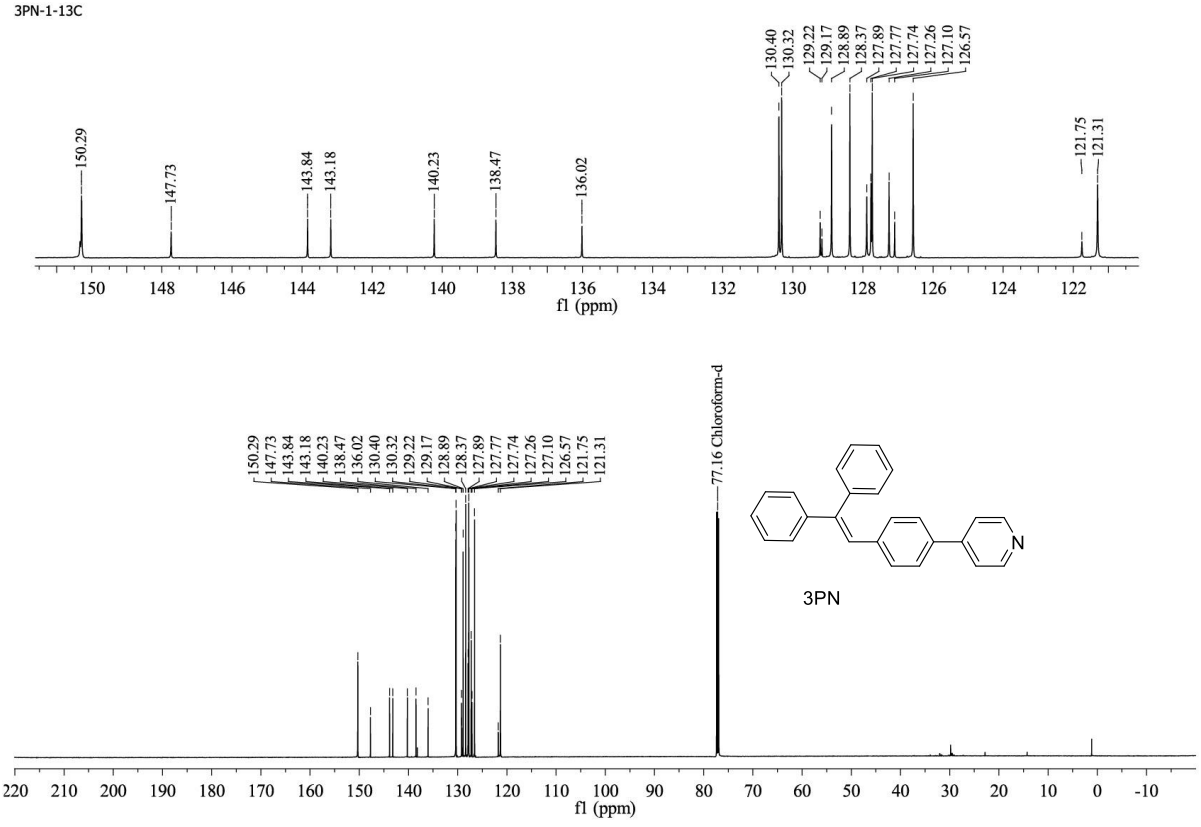

^{13}C NMR spectra of **3PN** in $CDCl_3$ solvent.

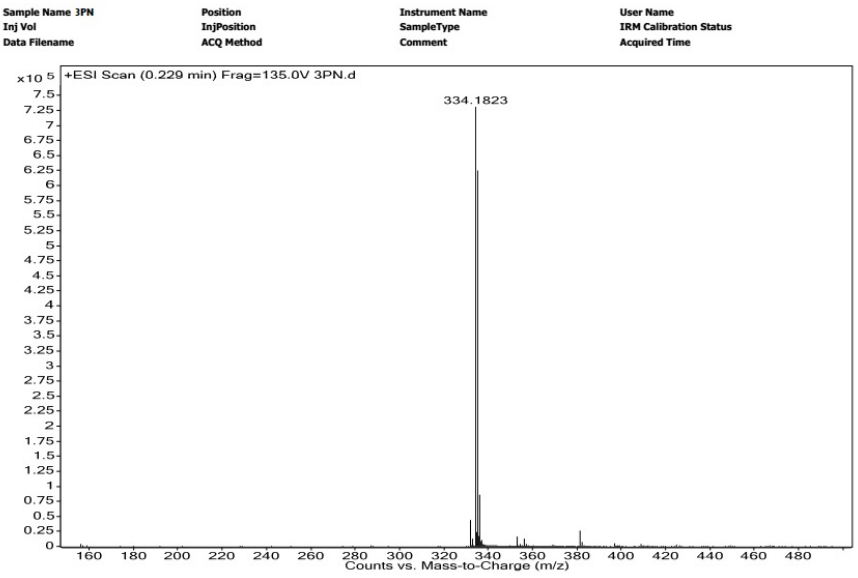

HRMS spectra of **3PN**.

CHAPTER 5

Aggregation-induced emission active luminogens for wash free imaging and antimicrobial application against pathogenic bacteria and fungus

Adil, L. R.; Patra, A.; Bidkar, A.; Ghosh, S. S.; Iyer, P. K. (under communication).

Abstract

The enhancement in microbial antibiotic resistance and their increase in infection have posed severe threat to human health. In this work **PNH**, **PNM** and **PNB** AIEgen are reported, that demonstrated wash-free imaging of bacteria (S. aureus, E.coli) and fungus (C. albicans). **PNM** could also be used for discrimination between gram-negative and gram-positive bacteria. **PNB** molecules facilitates visualizing all microbes in confocal laser scanning microscopy. Hence, the present work displays an unprecedented tool for the imaging and antimicrobial application against microbes (fungus, gram-positive and gram-negative bacteria).

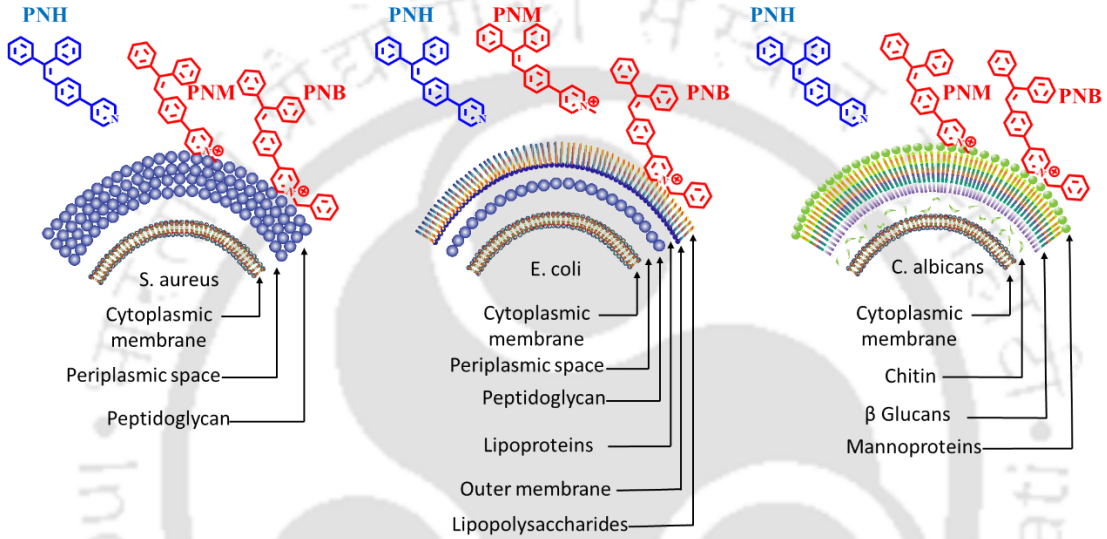

5.1 Introduction

Bacteria are utmost abundant microorganism that can be found in every habitat on the earth, such as plants, water, soil, glacier, hot springs, living body (human and animals), international space station (ISS), etc.[1,2] They are beneficial and harmful for human and animal health. Infectious diseases mostly are caused by microorganisms viz. Cholera, tuberculosis, anthrax, leprosy, plague, athlete's foot, Jock itch, ringworm etc.[3,4] Microbes such as bacteria and fungus pose serious threats to civic health due to lack of effective drugs microbes killing and emergence of antibiotic resistance.[5,6]

In the past decades, significant number of bacterial infections have been reported this leads to attracted the immense attention of research scientists to develop materials for antimicrobial applications.[7,8] To address this issue, various peptides, antibiotics, inorganic nanoparticles (NPs), organic NPs and hydrogels have been established.[9.12] Although these materials showed their individual effectiveness but they have been elusive in clinical applications. Therefore, more research efforts are required to design and develop a cost effective, sensitive and simple technique for microbe identification and antimicrobial application. The standard technique for bacterial classification is gram staining. This method is solely based on a variation on the cell wall of bacteria.[13] The fluorescence-based material is an alternative approach for the staining of gram-positive and gram-negative bacteria. Real-time or in situ monitoring of microbes can be possible by fluorescence microscopy. [14]

Fluorescence materials have attracted great attention in sensor, optoelectronic devices, cellular imaging in biomedicine and life science research areas.[15-18] However, conventional fluorescent materials experience some serious drawbacks, their emission is decreased in higher concentrations, this phenomenon is termed as concentration quenching. Classical fluorescent materials are disc-shaped, they tend to form aggregate via π-π interaction, this phenomenon is called aggregation caused quenching (ACQ).[19,20] To prevent organic fluorescent materials from notorious ACQ, various strategies such as chemical and physical methods were employed but received limited success. In 2001, Tang et al. reported non-planar materials, that showed completely opposite emissive properties to the ACQ fluorescent materials. These non-planar materials have emissive aggregates and therefore, these behaviours are referred to as aggregation-induced emission (AIE).[21] AIE active materials have less emission in solution or less concentration, but emission enhances in the aggregates state or higher concentration due to restriction in intramolecular rotation (RIR) and intramolecular vibration (RIV).[22]

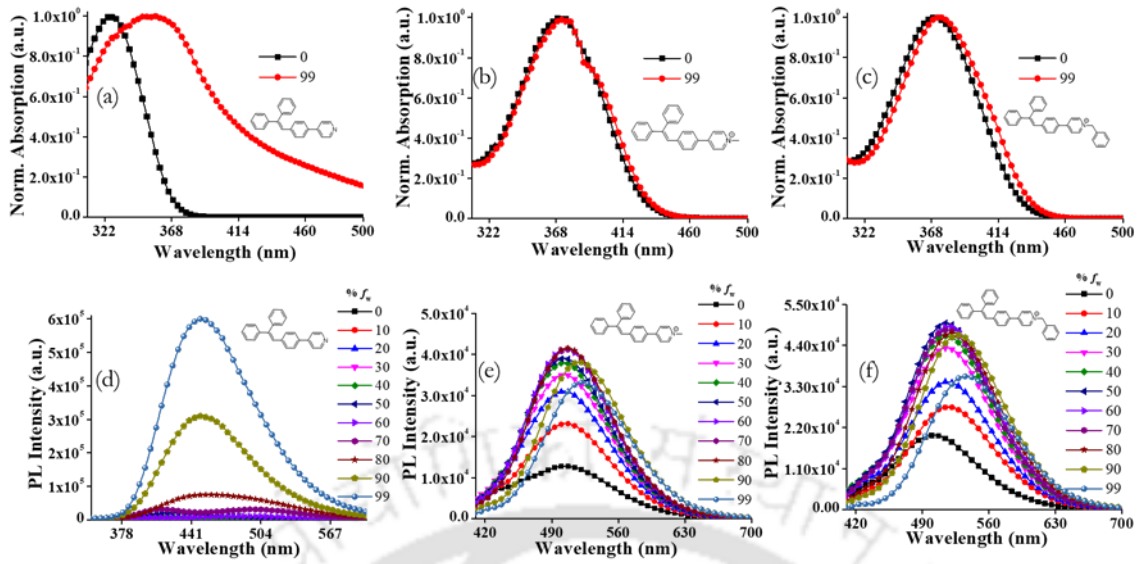

Figure 5.1: UV vis. spectra of (a) **PNH**, (b) **PNM** and (c) **PNB** in DMSO and 99% f_w . PL spectra of (d) **PNH**, (e) **PNM** and (f) **PNB** with increasing % f_w in DMSO.

Fluorescent emissive materials having AIE properties are noble materials for bioimaging applications. The development of new AIE active material is an emerging field of research as they possess high brightness, good photostability, higher bioactivity.[23,24] Scientists have explored many fluorescent dyes for imaging of bacteria, but AIE based fluorescent dye for imaging and killing of microorganisms is less studied and now it is a hot topic for the research field.

5.2 Results and Discussion

5.2.1 Photophysical studies

All synthesized materials **PNH**, **PNM** and **PNB** are soluble in chloroform and Dimethyl sulfoxide (DMSO). The standard solution was prepared in DMSO in 1 mM concentration. **PNH**, **PNM** and **PNB** maximum absorbance (max) were observed at 325,368, 369 in DMSO and 354, 373, 374 nm in water, respectively. AIE studies were performed using binary solvent, DMSO (as good solvent) and water (as bad solvent). Initially, in 0-70% f_w (in DMSO) **PNH** is non-emissive, it becomes emissive at 80% f_w and shows maximum emission at 99% f_w whereas **PNM** and **PNB** have less emission in 0% f_w and their emission enhances with the enhancement of water fraction from 10-70% f_w **PNM** and **PNB** have maximum emission at 80 % f_w, but further increased water fraction leads to emission decrease due to the formation of less emissive agglomeration (Figure 5.1.

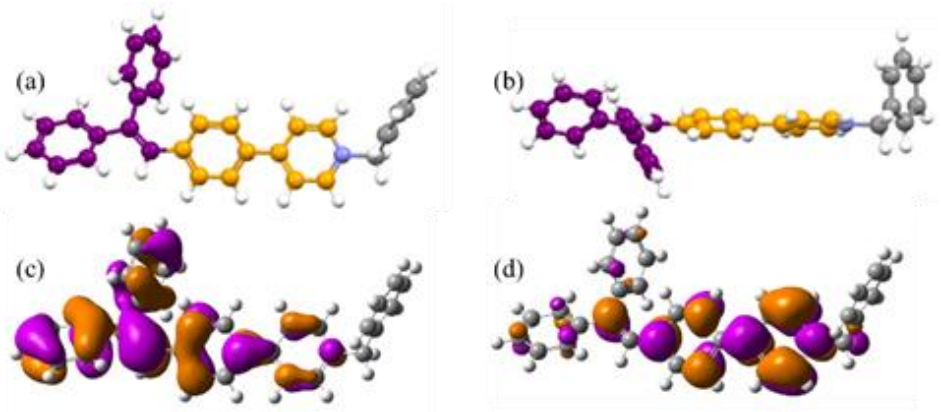

Figure 5.2: Optimized structure (a) front view (b) side view and theoretical calculation of electron cloud distribution (c) HOMO (d) LUMO of PNB. by using B3LYP/6-31G (d,p) basis set

5.2.2 Theoretical calculation studies

In order to elucidate the electronic distribution in **PNH**, **PNM** and **PNB** theoretical calculations were performed using Gaussian09 A.02 software. The molecular structure of **PNH**, **PNM**, **PNB** was optimized, and energy calculation was carried out by density functional theory (DFT) using B3LYP/6-311G (d, p) as a basis set.[25] As shown in Figure 5.2 and A5.1 optimized structure of **PNH, PNM** and **PNB** have non-planar geometry. For **PNH**, the highest occupied molecular orbital (HOMO) and lowest unoccupied molecular orbital (LUMO) electron cloud are located throughout the molecule, whereas for **PNM** and **PNB** HOMO electron clouds are found towards the triphenylethylene moiety and LUMO electron clouds located towards the pyridinium part.

5.2.3 Antibacterial susceptibility assessment

Antibacterial susceptibility assessment of compounds **PNH**, **PNM** and **PNB** against S. aureus (gram-positive bacteria) and Escherichia coli (gram-negative bacteria) has been investigated according to the CLSI M-07 broth microdilution method.[26] S. aureus and E. coli strains were propagated and maintained in sterile brain heart infusion (BHI) medium and Luria Bertani (LB) medium, respectively and the same medium was used to assay the antibacterial activity. Overnight grown bacterial cultures were counted using a Neubauer counting chamber (hemocytometer) and the inoculum was diluted at 2x strength of $5x10^5$ CFU/mL in respective growth medium. 0.05 mL of diluted bacterial cultures were added in each well of a 96 healthy microtiter plate containing 0.05 mL of test compounds of respective concentration (prepared at 2x final strength). Compound free control wells were also included. The microtiter plates were incubated at 37.0 °C for 16 hours. All assays were performed in triplicate and repeated thrice. The minimum inhibitory concentration (MIC) of each compound was determined by

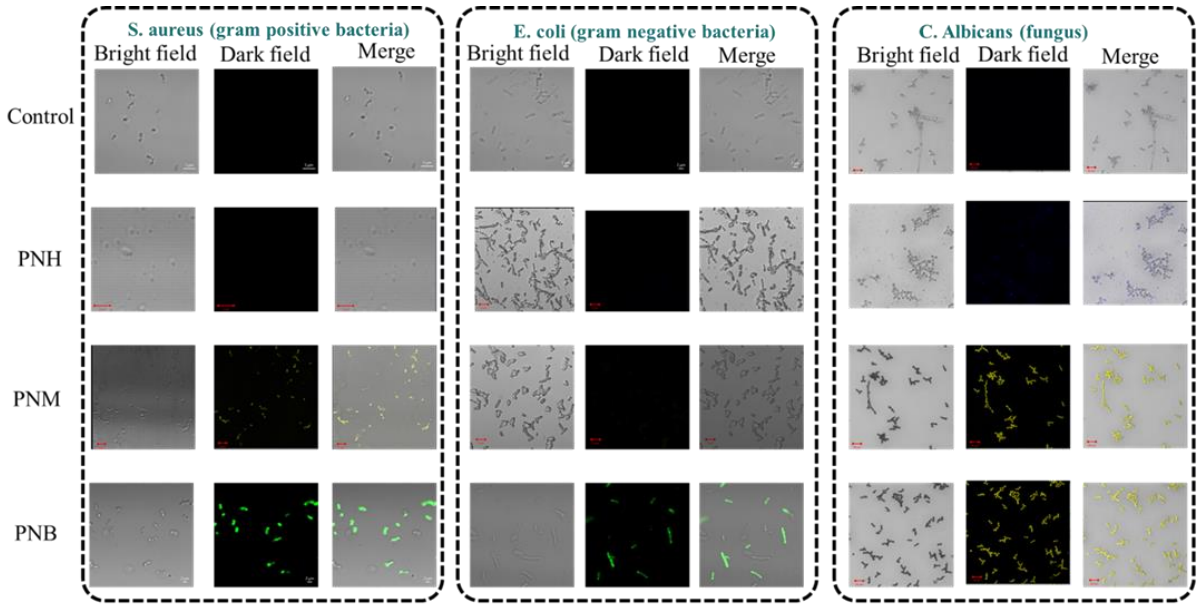

Figure 5.3: Confocal laser scanning fluorescence images of pathogens by **PNH**, **PNM** and **PNB.**

identifying the lowest concentration at which visible growth of the test organism was prevented. The absorbance of the wells was also determined at 600 nm for quantitative estimation of the bacterial growth. The absorbance values were converted and represented in terms of viability (%) using equation 1.

5.2.4 Antifungal susceptibility assessment

Qualitative antifungal susceptibility assessment was performed by the well diffusion method. Candida albicans (MTCC183 equivalent to ATCC2091) was grown overnight in yeast extract peptone dextrose (YEPD) medium at 30.0 °C temperature and 180 rpm. 100 µL of overnight grown culture was spread over each YEPD agar plates, and wells were punctured using sterile tips. Different dilutions of the test compounds were prepared in a sterile YEPD medium and added to the respective wells, where the control well was inoculated with a sterile YEPD medium. Plates were incubated at 35 °C temperature for 48 hours and observed for the appearance of a clear zone. Antifungal susceptibility assessment of compounds **PNH**, **PNM** and **PNB** against Candida albicans (MTCC183 equivalent to ATCC2091) has been investigated according to the CLSI M-27A2 broth microdilution method. 27 C. albicans strain was propagated and maintained in sterile yeast extract peptone dextrose (YEPD) medium. The assay was performed in sterile RPMI-1640 medium containing L-glutamine, buffered with 0.165M 3-morpholinopropane-1-sulfonic acid (MOPS), pH 7.0. C. albicans culture was grown in YEPD broth medium at 30°C temperature and 180 rpm for 24 hours. The yeast cells were harvested by centrifugation at 5000 rpm for 10 minutes, washed twice with PBS and finally

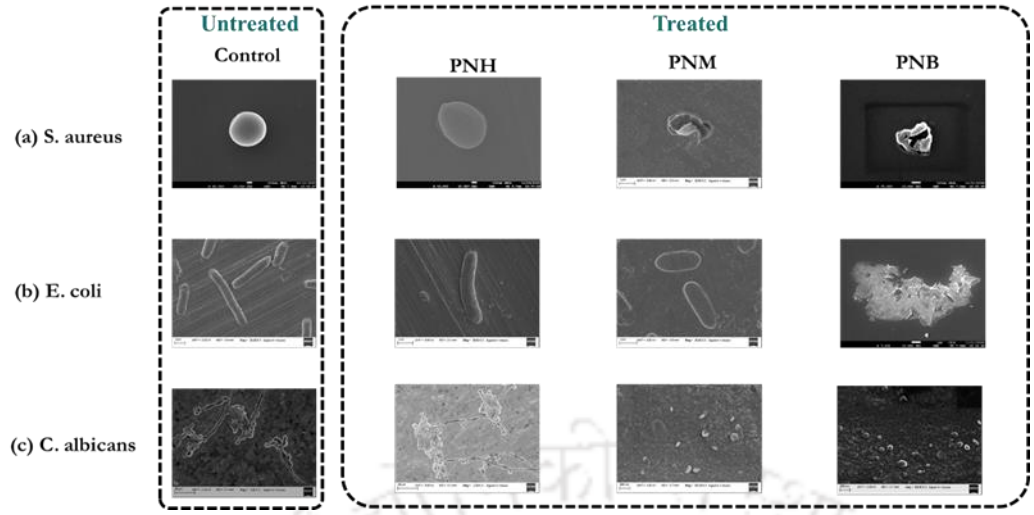

Figure 5.4: FESEM images for antimicrobial activity of **PNH**, **PNM**, **PNB**.

resuspended in RPMI-1640 assay medium. The cells were counted using a Neubauer counting chamber (hemocytometer), and the inoculum was diluted at 2x concentration of 0.5 McFarland standard (0.5-2.5 x 10^3 cells/mL) in RPMI-1640 medium. 50 µL of diluted yeast cells were added in each well of 96 well microtiter plate containing 50 µL of test compounds of respective concentration (prepared at 2x final concentration). Compound free control wells were also included. The microtiter plates were incubated at 35.0 °C for 48 hours. All assays were performed in triplicate and repeated thrice. The minimum inhibitory concentration (MIC) of each compound was determined by identifying the lowest concentration at which visible growth of the test organism was prevented. The absorbance of the wells was also determined at 600 nm for quantitative estimation of the yeast growth. The absorbance values were converted and represented in terms of viability (%) using the following equation 1.

$$\text{Viablity (\%)} = \frac{\text{Average } A_{600} \text{ of test wells}}{\text{Average } A_{600} \text{ of control wells}} \times 100 \ldots\ldots\ldots \text{Equation 1}$$

5.2.5 Visualisation of microbes

To study the practicability of synthesized materials for visualization of microbes live confocal laser scanning microscopy (CLSM) has been performed. **PNH** was not able to stain any of the microbes. Yet, **PNH** successfully stained the S aureus and C. albicans but not E. Coli. Whereas a very interesting **PNB** was able to visualize all microbes after incubation at MIC for 5 minutes (Figure 5.3).

5.2.6 The antimicrobial activity and mechanism of killing

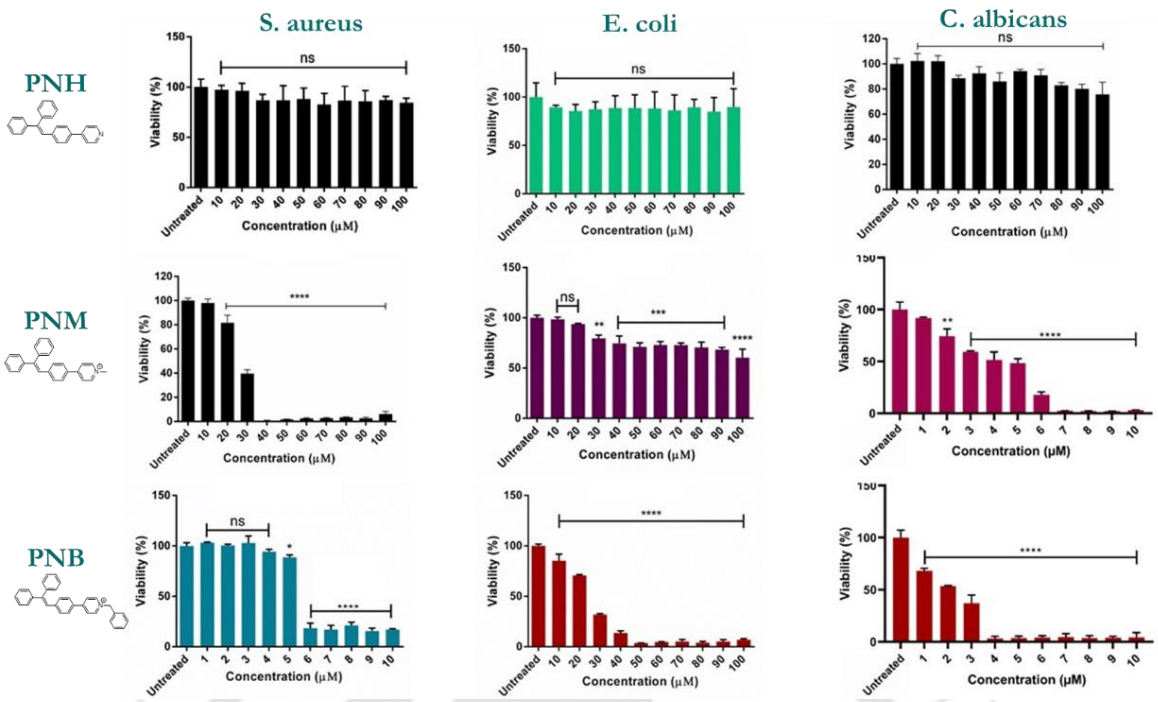

Figure 5.5: Antimicrobial susceptibility assessment of S. aureus, E. coli, C. albicans by **PNH**, **PNM** and **PNB**

The antimicrobial activity of **PNH**, **PNM** and **PNB** mechanism was confirmed by FESEM images (Figure 5.4). If the cell surface area of the microbe is clear and smooth with regular edges after incubation with materials, it indicates the viable state of microbe else they would have died. FESEM images of suggested that there is no membrane disruption of S. aureus, E. coli and C. albicans after incubation with **PNH** molecule. Whereas disruption in the membrane was observed for S. aureus and C. albicans after incubation with the **PNM** but no change was observed for E coli. Most interesting all microbe's membrane was disrupted after incubation with the **PNB**. Microbes' selective visualize and killing is based on the electrostatic interaction between the microbes and synthesized materials. As we know that due to the presence of teichoic acids with thick peptidoglycan layer, lipopolysaccharide and mannoprotein in S. aureus E. coli and C. albicans respectively have a negative net charge. Therefore, neutral **PNH** does not interact with the negative charge microbes, hence microbes are not visualized by **PNH**. S. aureus and C. albicans are electron negative compared to E. coli, hence **PNM** and **PNB** can interact by electrostatic interaction with them, but due to less net charge **PNM** is not interacting with E. coli, but interestingly **PNB** is interacting. The reason behind the selectivity is referred to E. coli membrane consisting of long alkyl chain and benzyl group attached with the molecule that enhanced its hydrophobicity and lipophilic, that helps **PNB** interact with the E. coli as well, hence all microbes can be visualized and killed with the PNB (Figure 5.5).

5.3 Conclusions

In summary, AIE materials **PNH**, **PNM** and **PNB** have been developed for wash-free imaging and as well as antimicrobial application. Selectivity visualization of S. aureus and C. albicans over E. coli. is achieved due to electrostatic interaction with **PNM**. Whereas enhanced lipophilic character due to benzyl functionalisation help **PNB** to interact with E. coli and due to positive charge, it can able to visualize S. aureus and E. coli. Also **PNM** showed selective killing towards S. aureus and C. albicans and **PNB** showed towards all microbes via disruption of the outer layer which was confirmed by FESEM images. AIE luminogens are paying towards solving this dilemma and deliver great prospective for microbes imaging and killing.

5.4 Experimental Section

In the presented work, we designed and synthesized AIE active material **PNH**, **PNM** and **PNB** (Scheme S1) and it was well characterized by NMR and MALDI TOF.

5.4.1 Materials and instruments

Benzophenone, 4-pyridinylboronic acid, 4-bromobenzyl bromide, triethylphosphite (TEP), methyl iodide, tetrakis(triphenylphosphine)palladium(0), potassium carbonate, potassium tert-butoxide were purchased from Sigma Aldrich and used without further purification. ^{1}H NMR (400 MHz) and ^{13}C NMR (100 MHz) spectra were obtained on Bruker (Model: AVANCE 400). For mass determination Matrix-assisted laser desorption/ionization (MALDI-TOF) spectrometer was used (Make: BRUKER, Model: AUTOFLEX SPEED). Photoluminescence (PL) and UV-visible spectra were recorded on a Horiba Fluoromax-4 and PerkinElmer Lambda-25 spectrofluorometer using 10 mm path length quartz cuvettes with a 3 nm slit width at 298 K. Nano particle size was measured using Malvern Zetasizer Nano ZS90. FE-SEM-images were obtained on Sigma Carl ZEISS field emission scanning electron microscope. The morphological features as well as the fluorescence of the treated cells were recorded in LSM 880 (Zeiss).

5.4.2 General Synthesis Procedure

The synthesis procedure of **3PBr**

Into condenser fitted round bottom flask 1-bromo-4-(bromomethyl)benzene (1 mmol), triethyl phosphite (0.5 ml) in 10 ml of THF refluxed for 10 hours then benzophenone (1 mmol) and potassium tertiary butoxide (1 mmol) added and the reaction stirred at room temperature for 12 hours. The reaction mixture was quenched and workup performed by DCM and water. Pure

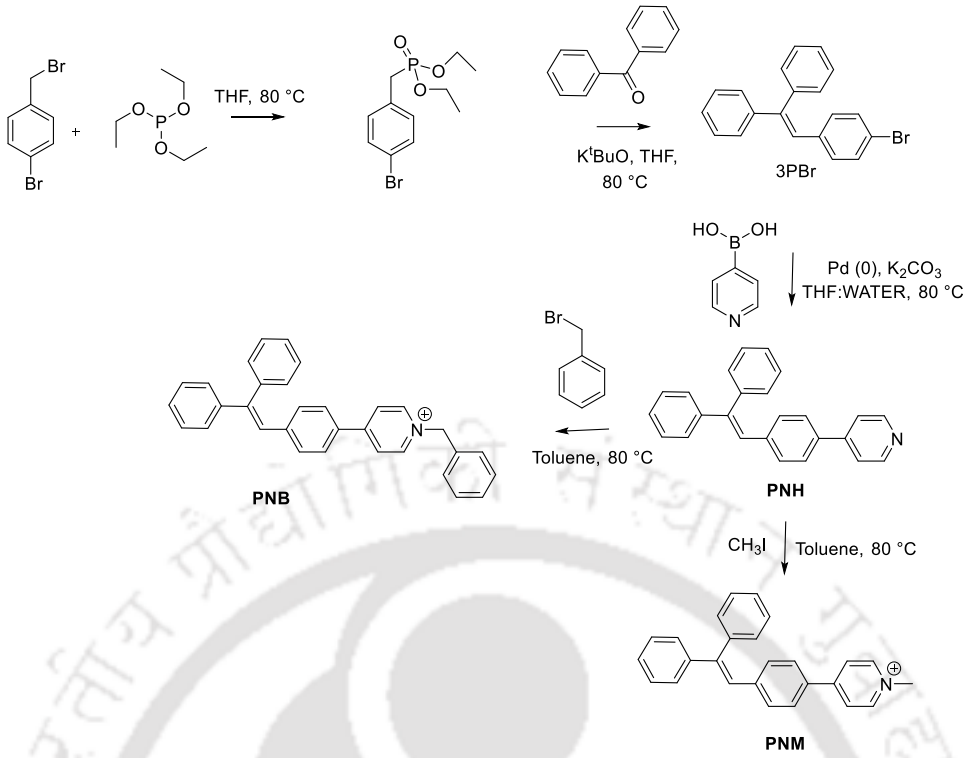

Scheme S1: Synthesis scheme of **PNH**, **PNM** and **PNB**.

product 3PBr was collected by silica column chromatography by taking hexane an eluent. (white solid, 64.56% yield.

3PBr ^{1}H NMR (400 MHz, CDCl3, δ ppm): 6.87 (m, J = 8.0 Hz, 1H), 6.89 (m, J = 8.0 Hz, 2H), 7.19 (m, J = 8.0 Hz, 2H), 7.24 (m, J = 8.0 Hz, 1H) 7.32 (m, J = 8.0 Hz, 8H).

3PBr ^{13}C NMR (100.00 MHz, CDCl3, δ ppm) 120.70, 126.93, 127.73, 127.78, 127.88, 128.40, 128.90, 130.40, 131.19, 131.23, 136.47, 140.08, 143.20, 143.58.

The synthesis procedure of **PNH**

3PBr (1 mmol), 4-Pyridinylboronic acid (1.1 mmol), tetrakis(triphenylphosphine) palladium(0) (0.015 mmol) were taken in inert medium (argon gas) then 10 ml THF and aqueous K2CO3 (2M) was added. The reaction was refluxed for overnight. The reaction was quenched and workup performed by DCM and water. Pure product collected by silica column chromatography by DCM and hexane as eluent (white solid, 60.00% yield).

PNH ^{1}H NMR (400 MHz, CDCl3, δ ppm): 7.00 (s J = 8.0 Hz, 1H), 7.12 (d, J = 8.0 Hz, 2H), 7.24 (m, J = 8.0 Hz, 2H), 7.35 (m, J = 8.0 Hz,8H), 7.44 (d, J = 8.0 Hz, 4H), 8.60 (d, J = 8.0 Hz, 2H).

PNH ^{13}C NMR (100.00 MHz, CDCl3, δ ppm): 121.31, 121.75, 126.57, 127.10, 127.26, 127.74, 127.77, 127.89, 128.37, 128.89, 129.17, 129.22, 130.32, 130.40, 136.02, 138.47, 140.23, 143.18, 143.84, 247.73, 150.29.

The synthesis procedure of **PNM**

PNH (1 mmol) and Iodomethane (MeI) (20 mmol) were taken in inert medium (argon gas) then 10 ml Toluene was added. The reaction was refluxed for overnight. The reaction was quenched and workup performed by chloroform and water. Pure product collected by precipitation on ether. (yellow color solid, 84.00 % yield).

PNM ^{1}H NMR (400 MHz, CDCl3, δ ppm): δ 9.12(d, 2H), 8.10(d, 2H), 7.55(d, 2H), 7.34(m, 8H), 7.19 (m, 4H), 7.00(s, 1H), 4.61(s, 3H).

PNM ^{13}C NMR (100.00 MHz, DMSO): 153.29, 145.41, 144.28, 141.92, 140.83, 139.55, 131.30, 130.25, 129.59, 129.18, 128.46, 128.14, 128.04, 127.71, 127.21, 126.46, 123.47, 47.31.

The synthesis procedure of **PNB**

PNH (1 mmol) and 4-Bromobenzyl bromide (1.3 mmol) were taken in inert medium (argon gas) then 10 ml Toluene was added. The reaction was refluxed for overnight. The reaction was quenched and workup performed by chloroform and water. Pure product collected by precipitation on ether. (yellow color solid, 80.00 % yield).

PNB ^{1}H NMR (400 MHz, CDCl3, δ ppm): 9.40(d, 2H), 8.02(d, 2H), 7.62(d, 2H), 7.48(d, 2H), 7.36(m, 11H), 7.17(m, 4H), 6.98 (s, 1H), 6.20 (s, 2H).

PNB ^{13}C NMR (100.00 MHz, DMSO): 154.11, 144.59, 144.38, 141.91, 141.00, 139.53, 134.53, 131.24, 130.24, 129.67, 129.58, 129.20, 129.18, 128.71, 128.46, 128.15, 128.05, 127.90, 127.22, 126.46, 124.96, 124.29, 62.22.

5.5 References

1. Adnani, N.; Rajski, S. R.; Bugni, T. S. *Nat. Prod. Rep.* **2017,** *34* (7), 784-814.
2. Bijlani, S.; Singh, N. K.; Eedara, V. V. R.; Podile, A. R.; Mason, C. E.; Wang, C. C. C.; Venkateswaran, K. *Frontiers in Microbiology* **2021,** *12, 639396-639409.*
3. Maglangit, F.; Yu, Y.; Deng, H. *Nat. Prod. Rep.* **2021,** *38* (4), 782-821.
4. Kell, D. B.; Pretorius, E. *Integr. Biol.* **2015,** *7* (11), 1339-1377.
5. Gupta, A.; Mumtaz, S.; Li, C.-H.; Hussain, I.; Rotello, V. M. *Chem. Soc. Rev.* **2019,** *48* (2), 415-427.

6. Petchiappan, A.; Chatterji, D. *ACS Omega* **2017,** *2* (10), 7400-7409.
7. Gao, W.; Zhang, L. *Nat Rev Microbiol.* **2021,** *19* (1), 5-6.
8. Miller, K. P.; Wang, L.; Benicewicz, B. C.; Decho, A. W. *Chem. Soc. Rev.* **2015,** *44* (21), 7787-7807.
9. Ray, P. C.; Khan, S. A.; Singh, A. K.; Senapati, D.; Fan, Z. *Chem. Soc. Rev.* **2012,** *41* (8), 3193-3209.
10. Rai, A.; Ferrão, R.; Palma, P.; Patricio, T.; Parreira, P.; Anes, E.; Tonda-Turo, C.; Martins, M. C. L.; Alves, N.; Ferreira, L. *J. Mater. Chem. B* **2022**, DOI:10.1039/D1TB02617H 10.1039/D1TB02617H.
11. Chen, Q.-W.; Qiao, J.-Y.; Liu, X.-H.; Zhang, C.; Zhang, X.-Z. *Chem. Soc. Rev.* **2021,** *50* (22), 12576-12615.
12. Ju, E.; Li, Z.; Li, M.; Dong, K.; Ren, J.; Qu, X. *Chem. Commun.* **2013,** *49* (79), 9048-9050.
13. Coico, R. *Current Protocols in Microbiology* **2006,** *00* (1), A.3C.1- A.3C.2.
14. Müller, V.; Sousa, J. M.; Ceylan Koydemir, H.; Veli, M.; Tseng, D.; Cerqueira, L.; Ozcan, A.; Azevedo, N. F.; Westerlund, F. *RSC Adv.* **2018,** *8* (64), 36493-36502.
15. Hosokawa, M.; Ando, M.; Mukai, S.; Osada, K.; Yoshino, T.; Hamaguchi, H.-o.; Tanaka, T. *Anal. Chem.* **2014,** *86* (16), 8224-8230.
16. Law, G.-L.; Wong, K.-L.; Man, C. W.-Y.; Wong, W.-T.; Tsao, S.-W.; Lam, M. H.-W.; Lam, P. K.-S. *J. Am. Chem. Soc.* **2008,** *130* (12), 3714-3715.
17. Nasu, Y.; Shen, Y.; Kramer, L.; Campbell, R. E. *Nat Chem Biol* **2021,** *17* (5), 509-518.
18. Salehi, A.; Dong, C.; Shin, D.-H.; Zhu, L.; Papa, C.; Thy Bui, A.; Castellano, F. N.; So, F. *Nat. Commun.* **2019,** *10* (1), 2305-2313.
19. Ricchelli, F.; Gobbo, S.; Moreno, G.; Salet, C.; Brancaleon, L.; Mazzini, A. *European Journal of Biochemistry* **1998,** *253* (3), 760-765.
20. Ma, X.; Sun, R.; Cheng, J.; Liu, J.; Gou, F.; Xiang, H.; Zhou, X. *J. Chem. Educ.* **2016,** *93* (2), 345-350.
21. Luo, J.; Xie, Z.; Lam, J. W. Y.; Cheng, L.; Chen, H.; Qiu, C.; Kwok, H. S.; Zhan, X.; Liu, Y.; Zhu, D. and B. Z. Tang. *Chem. Commun.* **2001**, 18, 1740-1741.
22. Hong, Y.; Lam, J. W. Y.; Tang, B. Z. *Chem. Commun.* **2009**, 29, 4332-4353.
23. Wang, B.; Liu, S.; Liu, X.; Hu, R.; Qin, A.; Tang, B. Z. *Adv. Healthcare Mater.* **2021,** *10* (24), 2101067-2101084.
24. Wang, H.; Liu, G. *J. Mater. Chem. B* **2018,** *6* (24), 4029-4042.

25. Frisch, M. J.; Trucks, G. W.; Schlegel, H. B.; Scuseria, G. E.; Robb, M. A.; Cheeseman, J. R.; Scalmani, G.; Barone, V.; Mennucci, B.; Petersson, G. A. et al. Gaussian 09, revision D.01; Gaussian, Inc., Wallingford, CT, **2013.**

26. Humphries, R. M.; Ambler, J.; Mitchell, S. L.; Castanheira, M.; Dingle, T.; Hindler, J.; Sei, C. M. *J Clin Microbiol*, 2018, **56**, 1934-1917.

27. Wayne, P. A. CLSI document, M27, 4th Ed., **2002**.

Appendix

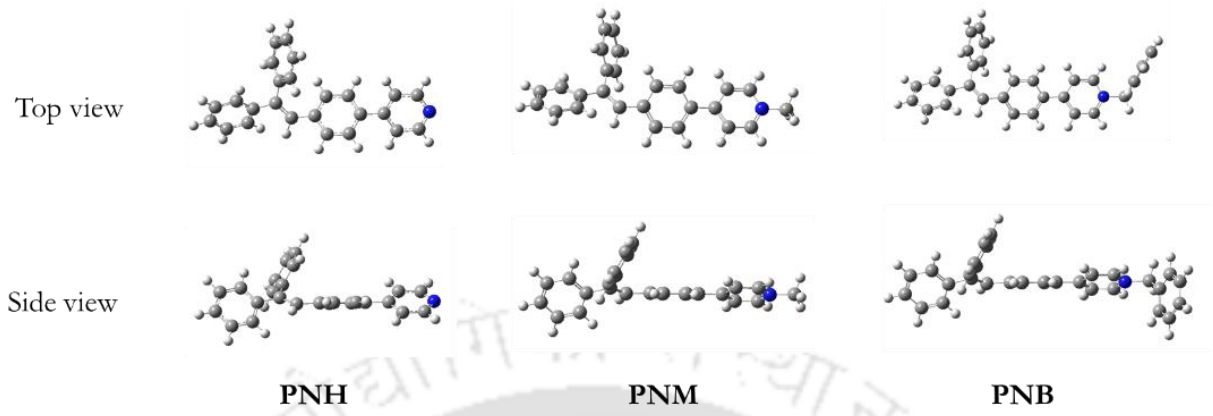

Figure A5.1: Optimized structure of **PNH**, **PNM** and **PNB**.

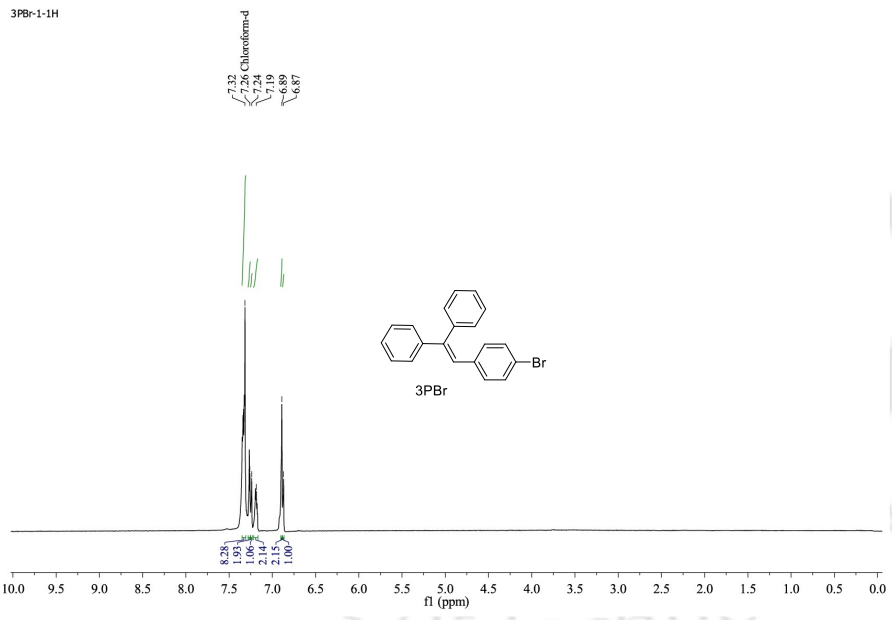

^{1}H NMR spectra of **3PBr** in $CDCl_3$ solvent.

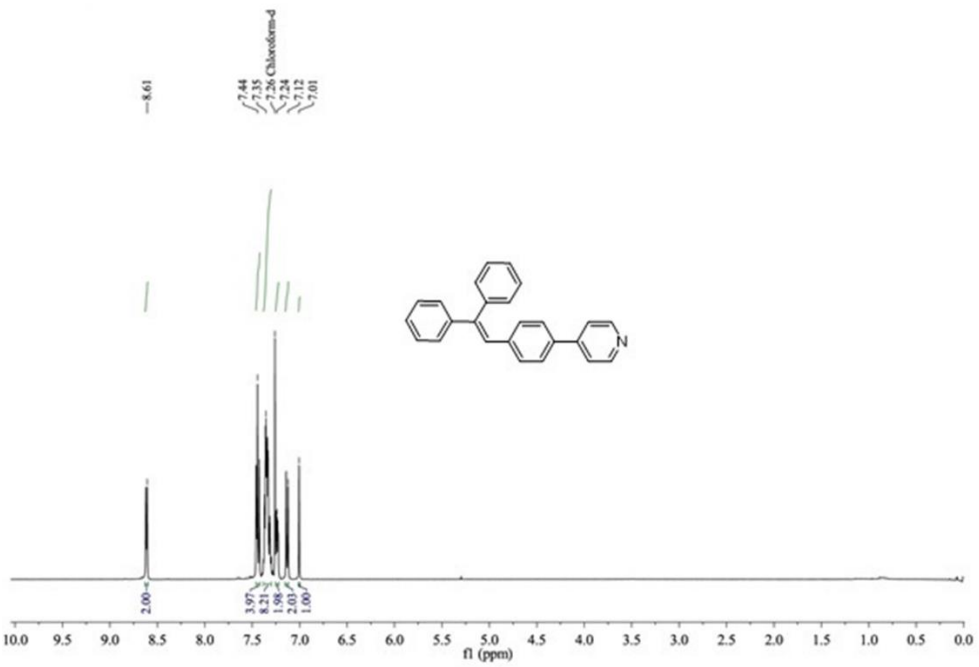

^{1}H NMR spectra of **PNH** in $CDCl_3$ solvent.

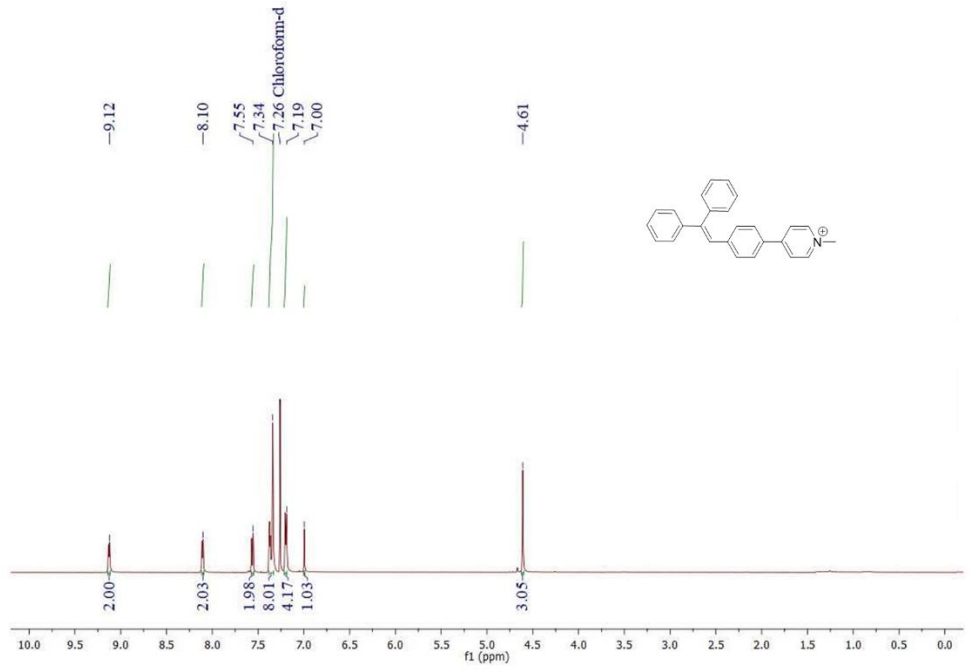

^{1}H NMR spectra of **PNM** in $CDCl_3$ solvent.

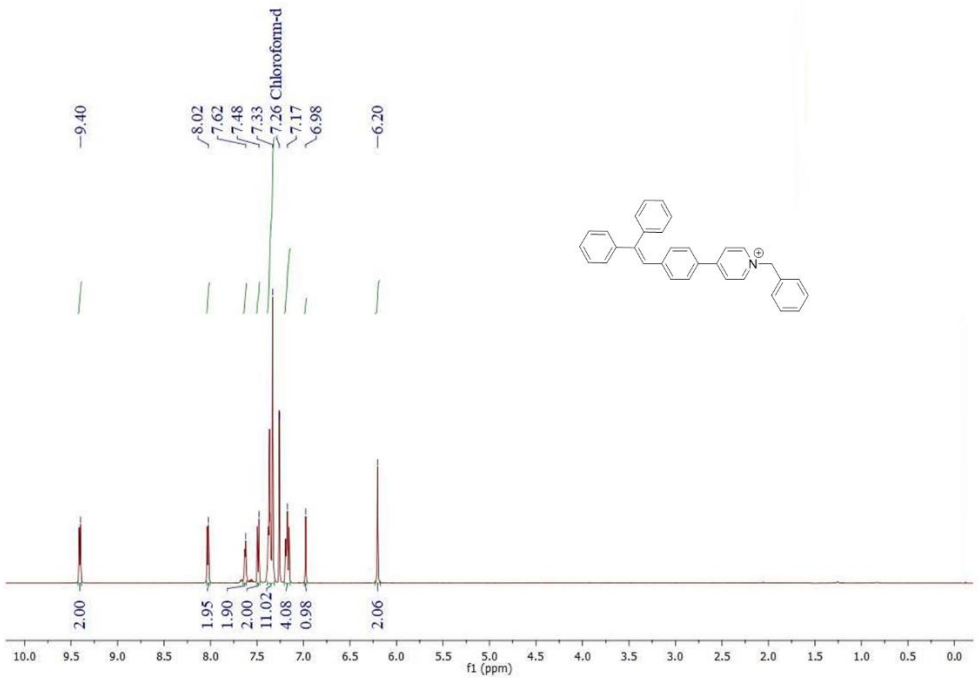

^{1}H NMR spectra of **PNB** in $CDCl_3$ solvent.

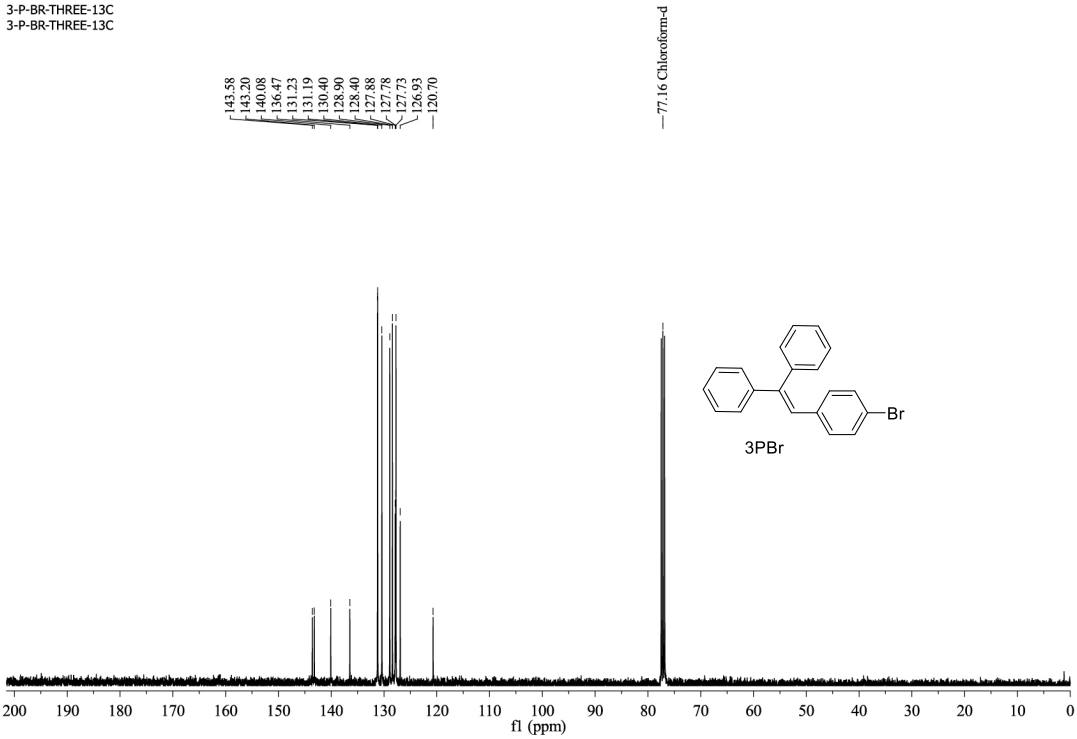

^{13}C NMR spectra of **3PBr** in $CDCl_3$ solvent.

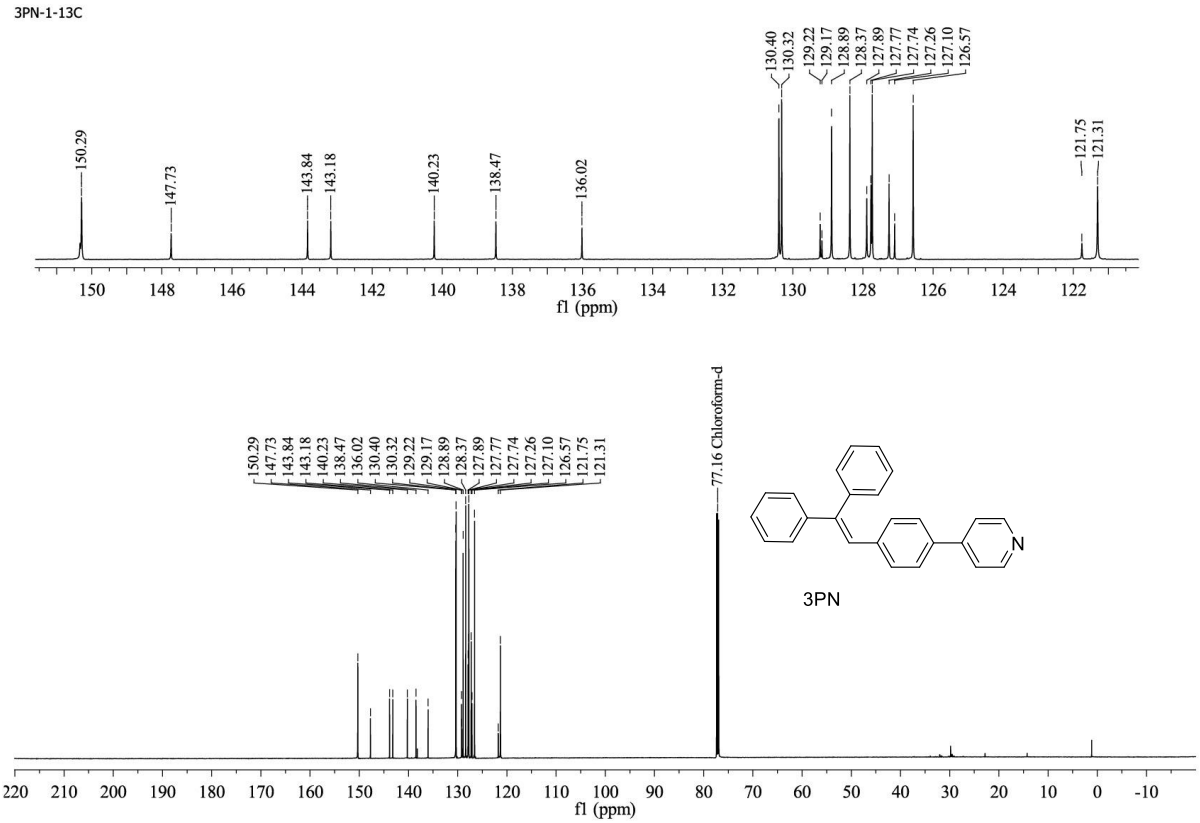

^{13}C NMR spectra of **PNH** in $CDCl_3$ solvent.

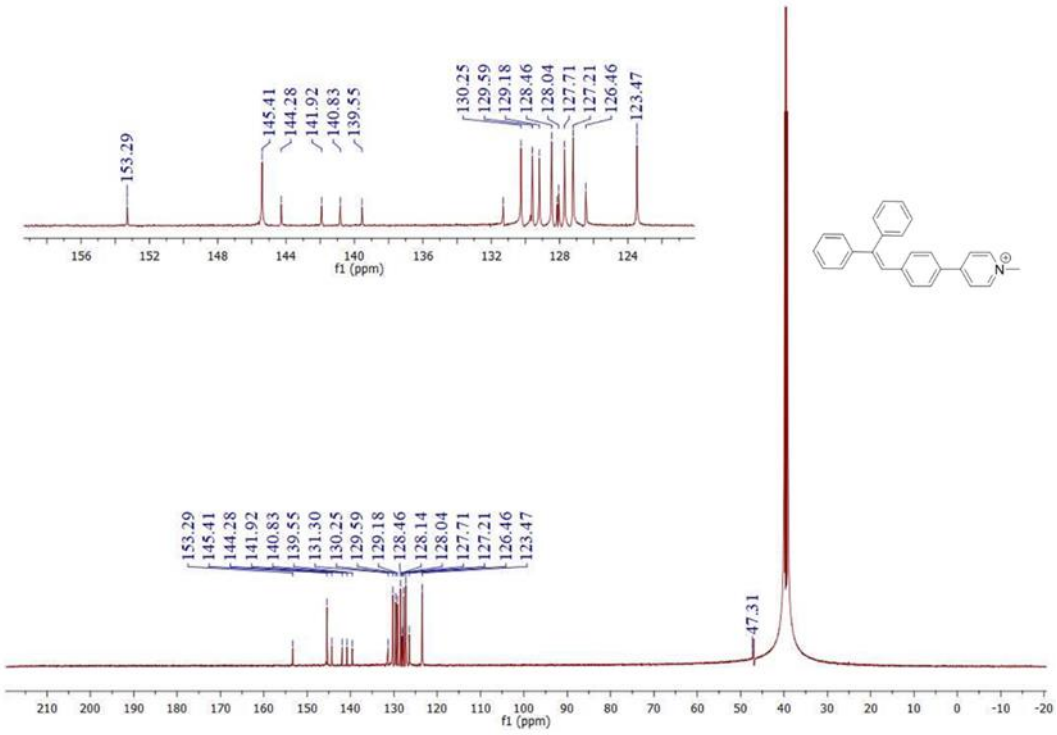

^{13}C NMR spectra of **PNH** in DMSO solvent.

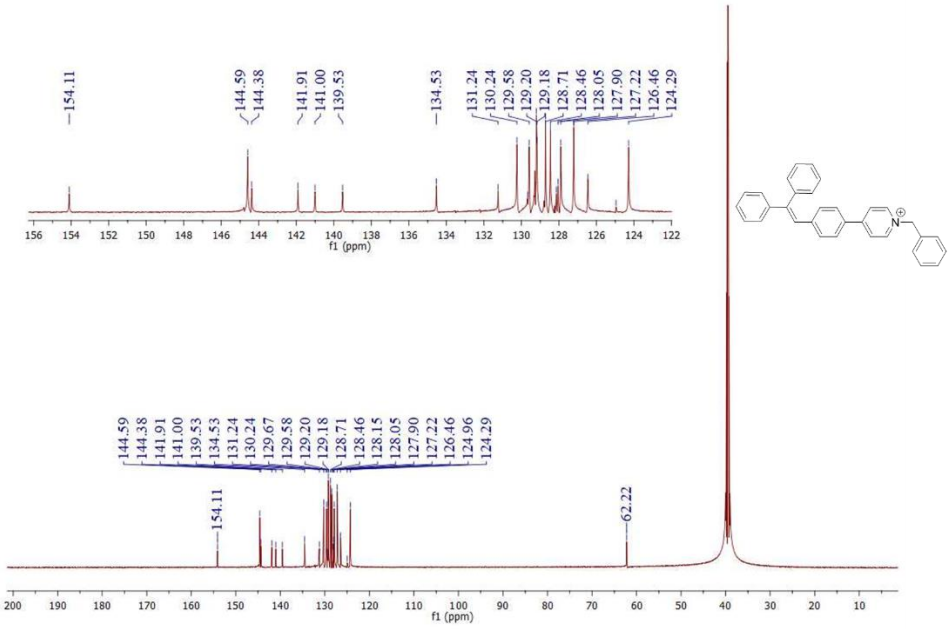

^{13}C NMR spectra of **PNB** in DMSO solvent.

Mass spectra PN derivatives

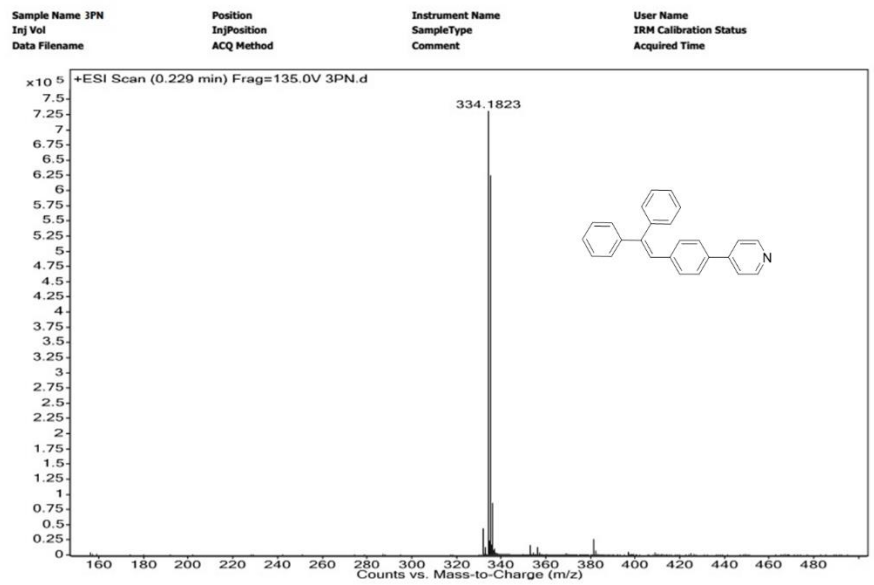

HRMS spectra of **PNH**.

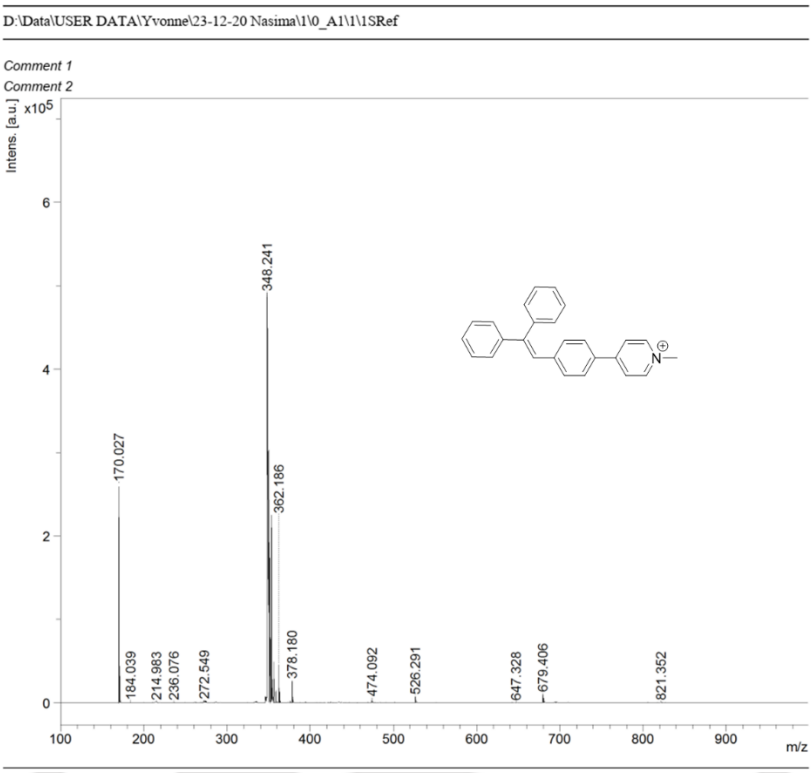

MALDI-TOF spectra of **PNM**.

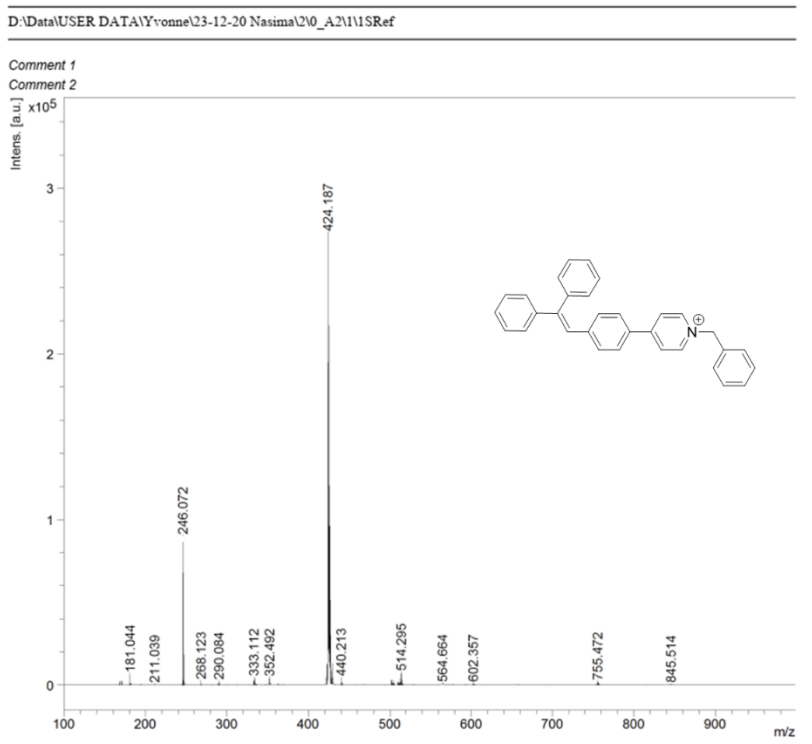

MALDI-TOF spectra of **PNB**.

Thesis overview

Chapter 1-Introduction to Aggregation Induced Emission (AIE) and its applications

Chapter 5-Aggregation induced emission active luminogens for wash free imaging and antimicrobial application against pathogenic bacteria and fungus

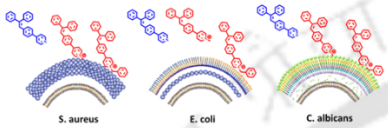

Chapter 2-Suppression of aggregation caused quenching in pyrene by push-pull, planar–rotor architecture further used as a multi-responsive probe and photodynamic therapy

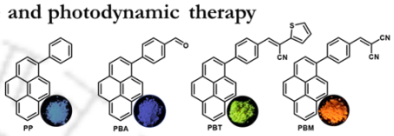

Thesis Summary

Chapter 4-Effects of incorporating regioisomers and flexible rotors to direct aggregation induced emission to achieve stimuli-responsive luminogens, security inks and chemical warfare agent sensors

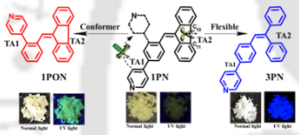

Chapter 3-Impact of Aggregation on Receptor Free Sensing of Picric Acid by AIEE active Copolymer

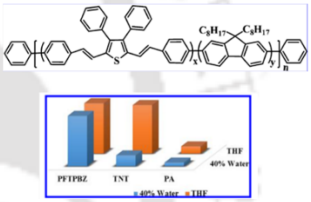

List of publications

1. Gopikrishna, P.; Das, D.; **Adil, L. R**.; Iyer, P. K. Saturated and stable white electroluminescence from linear single polymer systems based on polyfluorene and mono-substituted dibenzofulvene derivatives. *J. Phys. Chem. C*., **2017**, 121, 18137-18143.
2. Gopikrishna, P.; **Adil, L. R**.; Iyer, P. K. Bridge-driven aggregation control in dibenzofulvene-naphthalimide based donorBridge-acceptor systems: enabling fluorescence enhancement, blue to red emission and solvatochromism. *Mater. Chem. Front.*, **2017**, 1, 2590-2598.
3. Tanwar, A. S.; **Adil, L. R**.; Afroz, M. A.; Iyer, P. K. Inner filter effect and resonance energy transfer based attogram level detection of nitroexplosive picric acid using dual emitting cationic conjugated polyfluorene. *ACS Sens.*, **2018**, 3, 1451-1461.
4. **Adil, L. R**.; Gopikrishna, P.; Iyer, P. K. Receptor-free detection of picric acid: a new sructural approach for designing aggregation-induced emission probes. *ACS Appl. Mater. Interfaces*, **2018**, 10, 27260-27268.
5. Tanwar, A. S.; **Adil, L. R**.; Iyer, P. K. Stepwise elucidation of fluorescence based sensing mechanisms considering picric acid as a model analyte. *Analyst*, **2020**,145, 4753-4767.
6. **Adil, L. R**.; Iyer, P. K. Effects of incorporating regioisomers and flexible rotors to direct aggregation induced emission to achieve stimuli-responsive luminogens, security inks and chemical warfare agent sensors. *Chem. Commun.*, **2020**, 56, 7633-7636.
7. **Adil, L. R**.; Bidkar, A. P.; Ghosh S. S.; Iyer, P. K. Suppression of aggregation caused quenching in pyrene by introducing push-pull dipolar rotor groups and used as a multiresponsive probe and photodynamic therapy (communicated).
8. **Adil, L. R.;** Bidkar, A. P.; Ghosh S. S.; Iyer, P. K. Aggregation-induced emission active luminogens for wash free imaging and antimicrobial application against pathogenic bacteria and fungus (communicated).

BOOKS

1. Zehra, N.; Tanwar, A. S.; Khatun, M. N.; **Adil, L. R**.; Iyer, P. K. *In progress in molecular biology and translational science*; Bhosale, R. S.;Singh, V., Eds.; Academic Press, **2021**, 137-177.
2. Zehra, N.; **Adil, L. R**.; Tanwar, A. S.; Mondal, S.; Krishnan Iyer, P. In chemical solution synthesis for materials design and thin film device applications; Das, S.;Dhara, S., Eds.; Elsevier, **2021,** 369-405.
3. **Adil, L. R.;** Zehra, N.; Parui, R.; Iyer, P. K. Nanomaterials for sensors: synthesis and applications (under communication).

Awards

1. Awarded the National Research Fellowship from University Grants Commission (NET-UGC-June-78) New Delhi, Govt. of India.
2. Best poster presentation award received at International Conference on Emerging Trends in Chemical Sciences 2020 (ETCS-2020), organized by Department of Chemistry, Gauhati university, Guwahati, India.
3. Best paper award received at North-East Research Conclave 2022 (NERC-2022), organized by Indian Institute of Technology Guwahati, India.

Conference/Workshop attended

1. Participated in North-East Research Conclave (NERC-2022) organized by Indian Institute of Technology Guwahati, India. (20-22 May, 2022).
2. Participated in International Conference on Emerging Trends in Chemical Sciences (ETCS-2020) organized by Department of Chemistry at Gauhati University, India. (13-15 Feb., 2020).
3. Participated in 6th International Conference on Advanced Nanomaterials and Nanotechnology (ICANN2019) is organized by Centre for Nanotechnology at the Indian Institute of Technology Guwahati (IITG), India. (18-21 Dec., 2019).
4. Participated in National Conference On Recent Advances in Chemistry (RAC 2019), Organized by Department of Chemistry, National Institute of Technology Meghalaya, India. (14-15 Oct., 2019).
5. Participated in International Conference on Synthetic Potent Molecule and Its Applications (ICSPMIA-2018) Organised by Sikkim Manipal Institute of Technology, Sikkim. (30-31 Oct., 2018).
6. Participated in 5th International Conference on Advanced Nanomaterials and Nanotechnology organized by Center for Nanotechnology IIT Guwahati, Assam (18-21 Dec., 2017).
7. Participated in the Workshop on Biomedical Device Technology Organized by Center for Nanotechnology IIT Guwahati, Assam (18 Dec., 2017).
8. Participated in International Conference on Sophisticated Instruments in Modern Research Organized by Central Instrument Facility IIT Guwahati, Assam (30-1 July, 2017).
9. Participated in 3rd National Workshop on MEMS/NEMS and Theranostic Devices Organized by Center for Nanotechnology, IIT Guwahati, Assam (21-23 Feb., 2017).
10. Participated in the 20th CRSI National Symposium in Chemistry Organized by Department of Chemistry, Gauhati University (3-5 Feb., 2017).
11. Participated in the Workshop on ACS on Campus Organized by American Chemical Society at IIT Guwahati Assam (16 Jan., 2017).